The clustering of galaxies and groups

Lorrimer, Stephen John

THE CLUSTERING OF GALAXIES AND GROUPS

Stephen John Lorrimer

Dept of Physics & Trevelyan College

July 1993

An account of research undertaken at the Department of Physics, submitted to the University of Durham in accordance with the regulations for admission to the degree of Doctor of Philosophy.

ABSTRACT

We show that there are typically 8 satellites in the magnitude range $-16 \geq M_{B_T} \geq -18$ within a projected distance of $1h^{-1}$Mpc of a bright galaxy, their surface density being described by a power law of slope ~ 0.8. If the clustering of the bright galaxies is accounted for this corresponds to 4 satellites and a steeper slope. The satellite distributions around late and early type galaxies are significantly different. The bright-faint cross-correlation function has a lower amplitude than the bright autocorrelation function. However, we also find that faint satellites are more strongly clustered around bright galaxies than brighter satellites are, contradicting theoretical expectations.

We look at the dynamics of satellites around Milky Way-like galaxies. The observations are consistent with galaxies having isothermal dark halos, containing $\sim 10^{12} M_{\odot}$ out to at least $150h^{-1}$kpc. The circular velocity of the halo is equal to the circular velocity of the inner parts of the bright galaxy. We place a 95% lower limit on the density of the Universe, $\Omega > 0.024$ by assuming that all the mass in the Universe is within $150h^{-1}$kpc of bright galaxies. We confirm the Holmberg effect: an excess of satellites close to the minor axis of the bright galaxy.

We show that Low Surface Brightness (LSB) galaxies have fewer close companions than High Surface Brightness galaxies. Since LSB galaxies have a low star formation rate, this is consistent with theories in which star formation is tidally triggered.

We develop a method for estimating the clustering of objects of particular masses, based on the statistics of a gaussian field. This allows the clustering to be estimated in the mildly non-linear regime, giving results which are in good agreement with the results of numerical simulations. Our results lead us to suggest that objects of above and below the average mass exist in separate regions of the Universe. We demonstrate the potential

of the technique by looking at the redshift evolution of clustering and the clustering of groups of galaxies.

PREFACE

The work described in this thesis was undertaken between 1989 and 1993 whilst the author was a research student under the supervision of Dr. C.S.Frenk, in the Department of Physics at the University of Durham. This work has not been submitted for any other degree at the University of Durham or at any other University.

The work presented in Chapters 2 and 3 was undertaken in collaboration with Dr. C.S. Frenk, Dr. R.M. Smith (University of Wales, Cardiff), Dr. S.D.M. White (IOA, Cambridge) and Dr. D. Zaritsky (Observatories of the Carnegie Institution, Pasadena). The work in Chapter 4 was carried out in collaboration with Dr. Zaritsky alone and the work in Chapter 5 in collaboration with Dr. R.G. Bower (MPE, Munchen). However, the major part of the work described here is the author's own work.

A number of the results described here have appeared in the following papers:

Lorrimer, S.J. & Bower, R.G., 1991. in *Cluster & Superclusters of Galaxies: Contributed papers*, ed. Colless, M.M. *et al* (Cambridge University).

Zaritsky, D. & Lorrimer S.J., 1992. in *The Third Teton Summer School: Evolution of Galaxies and Their Environment – The Contributed Papers*, ed. Hollenbach, D. (Universities of Colarado & Wyoming).

Pooh sat down on a large stone and tried to think this out. It sounded to him like a riddle, and he was never much good at riddles, being a Bear of Very Little Brain.

Winnie-the-Pooh, A.A. Milne

... a great cause of the night is lack of the sun.

As You Like it, Act III, Sc II

CONTENTS

1 Introduction

1.1 Faint galaxies

Observed galaxy luminosities cover more than 7 magnitudes. These range from the massive cD galaxies which dominate the cores of rich clusters, such as the Coma and Virgo clusters, to the faintest smudges on photographic plates. Two good examples of these faint galaxies are the Large and Small Magellanic Clouds (LMC and SMC). These objects are beautiful southern sky objects and are easily observed with the naked eye. However, it is only because of their proximity that they can be so easily observed. The brighter of the pair, the LMC, is, in fact, about 5 times fainter than a typical galaxy. This means that they can only be observed at less than half the distance of their more typical counterparts.

The cosmological importance of faint galaxies lies in their prevalence. Studies of the field luminosity function, $\phi(L)dL$, (the number of galaxies with luminosities between L and $L + dL$) suggest that for the faintest galaxies $\phi(L) \sim L^{-1}$, although with large errors (Efstathiou *et al* 1988a; Loveday *et al* 1992a). Studies of rich clusters give more extreme results, suggesting that $\phi(L) \sim L^{-1.5}$ (*eg*, Irwin *et al* 1990). So, as fainter magnitudes are reached the number of galaxies increases rapidly. An undersatnding of faint galaxies is therefore a key part of understanding the Universe. However, paradoxically, it is the

relative scarcity of faint galaxies that conflicts with currently favoured theoretical models. These models suggest that for the faintest galaxies $\phi(L) \sim L^{-2}$ (Cole 1990; Lacey & Silk 1991; White & Frenk 1992; Cole *et al* 1993; Kaufmann *et al* 1993). The combination of the numerous population of faint galaxies with our poor understanding of them makes the study of faint galaxies a key element in improving cosmological theories.

The difficulties which arise in studying faint galaxies are mainly due to lack of depth: only the most local faint galaxies can be effectively surveyed. To some extent this limitation can be bypassed by surveying dense clusters, such as the Virgo and Fornax clusters, (Sandage *et al* 1985; Impey *et al* 1988; Irwin *et al* 1990 and references therein) allowing the distances of the faint galaxies to be estimated without the need for spectroscopic observations. In such studies the area of sky corresponding to the cluster is surveyed. It is assumed that in these areas there is a sufficiently large number of faint cluster galaxies to overwhelm any contribution from intrinsically bright, but more distant, galaxies. The contribution made by such background galaxies can be estimated from the number counts. In addition some attempt can be made to reject background galaxies (*eg*, Binggeli *et al* 1985). However, the rejection criteria are ambiguous. For instance, based on the surface brightness-luminosity relation (Bingelli *et al* 1984; Impey *et al* 1988), Binggeli *et al* (1985) regard objects of low surface brightness as intrinsically faint. However, Davies *et al* (1988) and Phillipps *et al* (1988) find no evidence for a surface brightness-luminosity relation. This problem aside, these studies have shown that the number of faint galaxies in clusters exceeds the number expected from simply extrapolating the distribution of galaxies found in the field (*eg*, Efstathiou *et al* 1988a). However, one must bear in mind that clusters represent especially dense environments. Thus, one of two conclusions follows – either there are disproportionately more faint galaxies in clusters or there are more faint galaxies in general than is suggested by a naive extrapolation of the field galaxy distribution, which is only poorly determined at the faint end.

Studies of the clustering of faint galaxies are beset by similar difficulties. It is not possible to probe large enough volumes to have a 'fair' sample of the Universe whilst an accurate estimate of the number of galaxies per unit luminosity is required to estimate the clustering strength accurately. These difficulties have lead to confusing and contradictory results. For instance White *et al* (1988) detected an increase in the clustering strength of nearby dwarf galaxies as a function of their 21cm line width, but this was based on a survey of a relatively small volume and so selection effects may have affected the result. In contrast, Eder *et al* (1989) failed to detect any difference in the apparent distributions of 102 dwarf irregulars and a sample of bright galaxies in the vicinity of a nearby void. We will address this problem in Chapter 2. In this Chapter we quantify the way in which faint galaxies are clustered around bright galaxies. Our method offers a number of advantages over previous work, such as that of Phillipps & Shanks (1987a, 1987b). Firstly, our datasets are significantly larger and secondly we develop a bootstrap method for calculating the surface density of faint satellite galaxies. The bootstrap method allows us to use non-contiguous Schmidt plates and bright galaxies with recession velocities as low as 1000km s^{-1}(a factor of 10 closer than the Phillipps & Shanks studies). We are thus able to make the most efficient use of the data available to us. This then allows us to divide the bright galaxies into different morphologies and the faint satellites into a number of ranges in magnitude: we can then consider in detail the effect of environment on satellites and how the clustering strength varies with the luminosity of the satellites.

Studies of rich clusters have also lead to the recognition of two new classes of galaxy – low surface brightness (LSB) and very low surface brightness (VLSB) galaxies (Bothun *et al* 1986; Phillipps *et al* 1987; Davies *et al* 1989). It was once believed that all galaxies had the same central surface brightness (*eg*, Freeman 1970). However, this myth has now been dispelled and it is clear that galaxies have a range of central surface brightnesses (*eg*, Schombert *et al* 1990; Peletier & Wilner 1992). The properties of LSB and VLSB galaxies

are particularly poorly understood, mainly because the selection effects in catalogues of this nature are difficult to take account of (Disney & Phillipps 1987). There is, however, speculation that only the 'tip of the iceberg' has yet been observed. This was emphasised by Disney (1976). We will look in detail at the small scale clustering properties of LSB galaxies in Chapter 4. We use here the same technique as in Chapter 2 to quantify the nature of the small scale environment of LSB galaxies. Making use of an unpublished LSB redshift survey (supplied by D.Sprayberry and C.Impey) we are able to probe the environment of LSB galaxies to significantly fainter luminosities than previous studies, such as that of Bothun *et al* (1992). This work may have a significant impact on models in which the star formation rate is affected by the local environment of the galaxy. In particular, we here consider those models, proposed by Lacey & Silk (1991), in which star formation is triggered by tidal interactions with nearby companions.

The clustering and abundance of faint galaxies is an important constraint for models of galaxy formation. The standard hierarchical models (such as that described in §1.3) predict a steeper increase in the number of galaxies with decreasing luminosity than is observed (Cole 1990; Lacey & Silk 1991; White & Frenk 1992; Cole *et al* 1993; Kaufmann *et al* 1993). 'Natural biasing' (White *et al* 1987b; Bertschinger & Gelb 1991) and 'statistical biasing' (Kaiser 1984; Kashlinsky 1986) predict that faint galaxies should be less strongly clustered than bright galaxies. However, making this prediction is beset with difficulties. The masses of faint galaxies are too low for them to be easily studied using N-body codes and previous analytical work simply identifies objects with peaks in the density field (Kaiser 1984; Bardeen *et al* 1986). In Chapter 5 we aim to improve on previous analytical studies by identifying regions which have undergone gravitational collapse using the formalism proposed by Press & Schechter (1974). Our work is similar to the work of Kashlinsky (1986, 1991), but we develop the method further in order to allow it to be applied to galaxies with a range of masses, rather than a single mass; a significant

improvement over Kashlinsky's work since this makes comparisons with observational catalogues straightforward. We also make a detailed comparison of these analytical results with the results of N-body codes in order to test the reliability of the method. Whilst this Chapter is motivated by a wish to understand the clustering of faint galaxies in different cosmological models, the technique we develop can also be applied to larger objects, for which the rarity of the object becomes a problem when using an N-body approach. This makes our technique useful for studying areas such as the cluster-cluster correlation function.

As well as being of interest in their own right, faint galaxies have also proved to be useful tools for dynamical studies. The LMC and SMC are both satellites of the Milky Way and satellite galaxies have also been found around other galaxies – initially by Holmberg (1969). As satellite galaxies are much less massive than the galaxies around which they orbit they make ideal dynamical tracers, allowing the properties of galactic halos to be determined at distances far greater than those which can be reached by direct observation of the kinematics of the parent galaxy. This was done for the Milky Way by Little & Tremaine (1980) and by Zaritsky *et al* (1989). For external galaxies this approach was used by Zaritsky *et al* (1993). In this study they observed the area around many bright galaxies to search for satellites. The properties of the bright galaxies are tightly controled; all the satellites can then be regarded as a single system. In Chapter 3 we extend the sample used by Zaritsky *et al* (1993), although bad weather prevented us extending it by more than 10 satellites. However, our analysis differs from that of Zaritsky *et al* in a number of key areas. Firstly, we use an alternative method for rejecting faint galaxies which are close to the bright galaxy simply because of a chance projection (interlopers). This criterion is motivated by N-body results and so, we believe, is significantly better than that used by Zaritsky *et al* (1993). We also look in more depth at the way in which the velocities of the satellites (relative to the bright galaxy) are related to the properties

of the central galaxy. Zaritsky *et al* (1993) suggested that velocities of the satellites are uncorrelated with the circular velocities of the bright galaxies. If this turned out to be correct it would have worrying implications for the Tully-Fisher relation (Tully & Fisher 1977). The mass estimates we are able to make are broadly similar to those of Zaritsky *et al* , but we also attempt to use these place lower limits on the density of the Universe, Ω.

In §1.2 of this chapter we review some statistical tools of which we will make extensive use in later chapters. Section 1.3 describes the standard Cold Dark Matter model and finally in §1.4 we describe the structure of the rest of this thesis.

1.2 Useful Statistics

1.2.1 The luminosity function

The luminosity function, $\phi(L)$, is defined such that $\phi(L)\ dL$ is the number of galaxies per unit volume in the luminosity range $L \rightarrow L+dL$. It may be a function of environment, perhaps via some dependence on the morphology of the galaxies on environment(see Binggeli *et al* 1988 for a review). The field luminosity function can be conveniently described using a function proposed by Schechter (1976):

$$\phi(L)\ dL = \phi_\star \left(\frac{L}{L_\star}\right)^{-\alpha} \exp\left(-\frac{L}{L_\star}\right)\ d\left(\frac{L}{L_\star}\right) \tag{1.1}$$

where α is the faint end slope, $L_\star$ is the characteristic luminosity and $\phi_\star$ is a normalisation constant. This function can also be expressed conveniently using magnitudes. If $M_\star$ is the absolute magnitude corresponding to $L_\star$ then

$$\phi(M)\ dM = 0.92\phi_\star x^{1-\alpha} \mathrm{e}^{-x}\ dM, \qquad x \equiv 10^{0.4(M_\star - M)}. \tag{1.2}$$

Efstathiou *et al* (1988a) found that the field luminosity function is well described by $\alpha = 1.07$, $M_\star^{B_T} = -19.68$ and $\phi_\star = 1.56 \times 10^{-2} \mathrm{h}^3\,\mathrm{Mpc}^{-3}$.* Note that the Schechter function has the property that $\int_L^\infty \phi(L)\, dL \rightarrow \infty$ as $L \rightarrow 0$. Clearly, the number density of galaxies must be finite and so the Schechter function will not provide an acceptable fit to the luminosity function for arbitrarily faint luminosities. However, it does reflect the large number of faint galaxies observed. Disney & Phillipps (1983) and Phillipps & Disney (1986) have suggested that the luminosity function should be a function of the surface brightness of the galaxy as well.

1.2.2 The correlation function

A clustering pattern can be described in many ways. In this Thesis we will use only some of these descriptions. However, since they will be used in a number of chapters it is useful to review them here. More comprehensive reviews can be found in Fall (1979) and Peebles (1980, 1993). The statistics could refer to the clustering of galaxies, groups of galaxies, clusters of galaxies, *etc.* However, in all these cases the statistical tools are the same and so in this section we will use 'galaxies' to stand for all of these possibilities.

In particular, we will use the correlation approach, the basic statistic of which is the autocorrelation function, ξ, defined such that

$$\delta p(\mathbf{r}) \equiv n^2(1 + \xi(\mathbf{r}))\delta v_1\ \delta v_2 \tag{1.3}$$

where δp is the joint probability of finding galaxies in the elemental volumes δv_1 and δv_2 separated by the vector $\mathbf{r}$ and n is the mean spatial density of galaxies. Clearly if

* Throughout this Thesis we express the Hubble constant as $H_0 = 100\mathrm{h}\ \mathrm{km\,s^{-1}\,Mpc^{-1}}$. When writing absolute magnitudes we will suppress the H_0 dependence. An extra factor of $5\log_{10}\mathrm{h}$ should be added to these.

the galaxies were distributed in a random uncorrelated (or Poisson) fashion then $\delta p = n^2 \delta v_1 \delta v_2$. Deviations from this distribution lead to a non-zero value of ξ. The definition of δp as a joint probability is something of misnomer. It is clearly possible for $\delta p > 1$ for anything other than infinitesimal δv_1 and δv_2, even when $\xi(\mathbf{r}) = 0$ for all $\mathbf{r}$. Nevertheless, it is still reasonable to interpret ξ as an excess probability if δv is small compared with $1/n$ so that the volume will typically contain one or no galaxies. In general ξ is taken to be only a function of the amplitude of the separation vector, $r \equiv |\mathbf{r}|$. This assumption follows from the cosmological principle – that the universe is homogeneous and isotropic on large scales.

The spatial autocorrelation function also has an angular analogue, ω. This is defined such that

$$\delta p(\theta) \equiv \mathcal{N}^2 (1 + \omega(\theta)) \delta\sigma_1 \, \delta\sigma_2 \tag{1.4}$$

where $\delta p(\theta)$ is the joint probability of finding galaxies in the elemental solid angles $\delta\sigma_1$ and $\delta\sigma_2$, separated by angle θ and $\mathcal{N}$ is the mean surface density of galaxies. Similar comments apply to this expression as for equation (1.3).

An underlying assumption of the correlation approach is that ξ is universal, allowing the construction of samples large enough to allow its measurement. Thus, the autocorrelation function found in different samples should agree, to within statistical uncertainties. However, ω will vary from sample to sample if the sampling depth changes (*ie*, if the limiting magnitude changes). This is demonstrated by Limber's equation (Limber 1953) which relates ξ and ω. For small θ ('the narrow angle approximation') this is given by

$$\omega(\theta) = \frac{\int_0^\infty dx \; x^4 \phi^2(x) \; \int_{-\infty}^\infty dy \; \xi(\{x^2\theta^2 + y^2\}^{1/2})}{\left(\int_0^\infty dx \; x^2 \phi(x) \right)^2}. \tag{1.5}$$

In this expression $\phi(x)$ is the selection function, which gives the mean fractional number of galaxies in the sample at distance x. For instance, if the sample has a magnitude limit m,

then the selection function is given by the integral luminosity function $\Phi(M)$ (the number of galaxies brighter than some absolute magnitude, M).

$$\phi(x) = \Phi(m - 5\log_{10}(x/\,\mathrm{Mpc}) - 25) \tag{1.6}$$

The autocorrelation function is often approximated by a power law, $\xi(r) = Br^{-\gamma}$. Limber's equation then gives $\omega(\theta) = A\theta^{1-\gamma}$ with

$$B = A\frac{\Gamma(\frac{\gamma}{2})}{\sqrt{\pi}\Gamma(\frac{\gamma-1}{2})}\frac{\left(\int_0^\infty dx\ x^2\phi(x)\right)^2}{\int_0^\infty dx\ x^{5-\gamma}\phi^2(x)} \tag{1.7}$$

where A, B and γ are constants. The strength of the spatial correlation function is commonly expressed as a clustering length, r_0, such that

$$\xi(r) = \left(\frac{r}{r_0}\right)^{-\gamma}. \tag{1.8}$$

For a fixed γ a longer clustering length indicates stronger clustering.

The correlation function approach can be generalised in many ways. Firstly, we have described so far only two-point correlation functions. It can be generalised to 3 or more points. For instance, the three point correlation function is defined such that

$$\delta p \equiv n^3(1 + \xi(r_{12}) + \xi(r_{23}) + \xi(r_{31}) + \zeta(r_{12}, r_{23}, r_{31}))\delta v_1\ \delta v_2\ \delta v_3 \tag{1.9}$$

where δp is the joint probability that a galaxy will be found in each of the volumes δv_1, δv_2 and δv_3 separated by distances r_{12}, r_{23} and r_{31} . We will make no further use of these higher order correlation functions and further details can be found in Peebles (1980,1993). Of more interest to us is the cross-correlation function. This allows us to describe the clustering of one class of objects around another. The cross-correlation of objects in category a (mean density n_a) relative to those in category b (mean density n_b), $\xi_\mathrm{ab}(r)$ is given by

$$\delta p(r) = n_\mathrm{a} n_\mathrm{b}(1 + \xi_\mathrm{ab}(r))\delta v_\mathrm{a}\ \delta v_\mathrm{b} \tag{1.10}$$

where $\delta p(r)$ gives the joint probability of finding an object of category a in volume $\delta v_{\rm a}$ and one of category b in volume $\delta v_{\rm b}$. The two volumes are a distance r apart. An example of the use of this statistic is the galaxy-cluster cross correlation function, ξ_{cg} (*eg*, Lilje & Efstathiou 1988).

1.2.3 The power spectrum

We may regard the distribution of galaxies as a random realisation of a smooth fluctuating mass density field. The correlation function is then given by

$$\xi(r) = \langle \delta(\mathbf{x}) \delta(\mathbf{x}+\mathbf{r}) \rangle_{\mathbf{x}} - \frac{\delta_D(|\mathbf{r}|=0)}{\overline{\rho}} \tag{1.11}$$

where $\delta(\mathbf{x})$ is the density contrast at $\mathbf{x}$, defined as

$$\delta(\mathbf{x}) = \frac{\rho(\mathbf{x})}{\overline{\rho}} - 1. \tag{1.12}$$

In this expression $\rho(\mathbf{x})$ is the density of galaxies at $\mathbf{x}$ and $\overline{\rho}$ is the mean density. The second term in equation (1.11) is a Dirac delta function which takes into account the self correlation of discrete points. It must be interpreted as vanishing in the continuum limit (*ie*, when considering the correlation function of the underlying density field). All the averages are over large volumes.

It is now possible to define a quantity which is closely related to the correlation function, the power spectrum, $P(k)$. This is the fourier transform of $\delta(\mathbf{x})$. In the case where the fluctuations depend only on the magnitude of k and their phases are uncorrelated, the power spectrum is a function only of the the amplitudes of the fourier components, $|\delta_k|^2$. The power spectrum is related to the correlation function by

$$P(k) = 1 + 4\pi\overline{\rho} \int_0^\infty dr\ r^2 \xi(r) \frac{\sin(kr)}{kr}. \tag{1.13}$$

The first term is again a discreteness term and should be omitted in the case of the continuum limit. *

In the linear regime, *ie*, where gravitational collapse has not occurred, the power spectrum of the underlying density field is simply proportional to that present after recombination. However on smaller scales, where collapse has occurred (and where $\xi > 1$) this is no longer the case. For a simple power law model of the correlation function, $\xi(r) = Br^{-\gamma}$,

$$P(k) = \frac{2\pi^2 \overline{\rho} B}{\Gamma(\gamma - 1)\sin(\pi\frac{\gamma-1}{2})} k^{\gamma-3} \tag{1.14}$$

in the linear regime.

1.2.4 Other clustering estimators

Many other measures of clustering could in principle be used, *eg*, counts-in-cells (Efstathiou *et al* 1990) or the 'minimal spanning tree' (Barrow *et al* 1985). However, in this Thesis we will use only one other estimator – the number of galaxies within a distance r of a randomly chosen galaxy. The number by which this exceeds the Poisson count is given by

$$\Xi(r) = 4\pi n \int_0^r ds\ s^2 \xi(s). \tag{1.15}$$

The total number within r is $\Xi(r) + \frac{4}{3}\pi r^3 n$.

1.3 The Cold Dark Matter cosmological model

Recent observations have placed much pressure on the standard cosmological model – biased cold dark matter (CDM) (Efstathiou *et al* 1990; Maddox *et al* 1990; Saunders

* In some texts, especially older ones, $P(k)$ is referred to as the structure function, $S(k)$, and then $S(k) = 1 + P(k)$.

et al 1991; Davis *et al* 1992). However, it remains the model against which observations and other models are gauged. Also, it is becoming apparent that much of the observed discrepancies may be accommodated within a CDM framework (Efstathiou *et al* 1992). So, a discussion of the CDM model remains of great relevance.

Big bang nucleosynthesis sets limits on the amount of baryonic matter which could have emerged from the primeval fireball. These are expressed as the density relative to the density required to just prevent the Universe from recollapsing in a 'big crunch', Ω. For instance calculations by Walker *et al* (1991) suggest that the density of the Universe in baryons is $\Omega_b h^2 = 0.013 \pm 0.003$. However, theoretical bias favours a total density corresponding to $\Omega = 1$, since, if in the early Universe the density varied from this by only a small amount, the density now would be many orders of magnitude away from the critical density. There is also now some observational evidence for this assumption (Kaiser *et al* 1991; Nusser & Dekel 1993). A model producing a critical density universe and providing a physical mechanism for the generation of gravitational seeds is the inflationary model (Guth 1981). Combining inflation with standard cosmological nucleosynthesis we are forced to accept a universe in which $> 90\%$ of its density is made up by non-baryonic particles. It is now believed that the best candidate for these non-baryonic particles are a group with non-relativistic velocities, collectively known as CDM. None of the CDM particles have yet been detected, although a variety of particle physics results have restricted the range of properties the particle could have. The aim of this model (and any other cosmological model) is to predict the observable characteristics of galaxies and other large scale structures.

The linear density fluctuation field is usually specified in terms of $\delta(r)$ or δ_k as we discussed above. In the absence of any physical processes which could have introduced a scale this is usually assumed to have a power law form, $|\delta_k|^2 \propto k^n$. The inflationary model produces fluctuations which have random phase and a power spectrum close to the scale-invariant

(Harrison-Zeldovich) spectrum, $n = +1$. As fluctuations of a particular wavelength come within the horizon, physical processes can affect the shape of $P(k)$ on those scales. At late times, the power spectrum thus deviates from a power law form. The deviation depends on the nature of the particles and the physical processes by which they are affected. CDM particles are either very heavy or slow moving and so the shape of the CDM spectrum is defined in the radiation dominated era (Mezaros 1974). The spectrum is bent at a scale $\sim 13\Omega^{-1}h^{-2}$ Mpc towards $n = -3$ at large k.

The results of the Cosmic Background Explorer (COBE) satellite (Smoot *et al* 1992) have offered the prospect of directly determining the power spectrum via the fluctuations measured in the temperature of the Cosmic Microwave Background (CBR). The COBE satellite measures the intensity of the CBR at 31, 53 and 90 GHz. It has detected fluctuations in the CBR temperature on angular scales of 10° ($\Delta T/T \simeq 5 \times 10^{-6}$). However, the COBE satellite does not, independently, provide very strong constraints on standard CDM. The fluctuations it detects do have a somewhat larger amplitude than would be expected in standard CDM, but only by a factor of ~ 2, corresponding to a $\sim 2\sigma$ discrepancy. However, the satellite is still operating and improving its signal-to-noise and so the significance of this discrepancy should be better determined in due course. It is also unclear at present what fraction of the fluctuations detected by COBE are in fact due to gravitational waves, rather than to density variations in the last scattering surface.

Much of the early quantitative work on the CDM model was carried out using N-body simulations by 'the gang of four' (Davis *et al* 1985; White *et al* 1987a,1987b; Frenk *et al* 1985, 1988, 1990). They parameterised the power spectrum by

$$P(k) \propto \frac{k}{(1 + 1.7Lk + 9.0L^{3/2}k^{3/2} + L^2k^2)^2} \tag{1.16}$$

where $L = \Omega^{-1}h^{-2}\,\mathrm{Mpc} = 100\Omega^{-1}h^{-1}\,\mathrm{km\,s^{-1}}$. There are two free parameters in the power spectrum – the amplitude and the length scale, L. In the standard model, $\Omega = 1$ and

h = 0.5, thus determining L. This has recently been generalised to a family of 'CDM-like' power spectra:

$$P(k) \propto \frac{k}{(1+(ak+(bk)^{3/2}+(ck)^2)^{1.13})^{2/1.13}} \tag{1.17}$$

where $a = (6.4/\Gamma)\,\mathrm{h^{-1}Mpc}$, $b = (3.0/\Gamma)\,\mathrm{h^{-1}Mpc}$ and $c = (1.7/\Gamma)\,\mathrm{h^{-1}Mpc}$ (Efstathiou *et al* 1992). This fits the standard CDM, $\Omega = 1$ spectrum with $\Gamma = \mathrm{h}$ for a small baryon density (Bond & Efstathiou 1984). However, in addition, many other models can also be fitted by varying Γ. These are summarised by Efstathiou *et al* (1992). These authors combine the COBE results with conventional clustering results. As COBE probes extremely large scales compared to conventional studies this gives a very large lever-arm with which to constrain the shape of the power spectrum. Their results favour $\Gamma \sim 0.3$.

In Figure 1.1 we show the power spectra for $0.1 \leq \Gamma \leq 1.0$ in steps of $\Delta\Gamma = 0.1$. The curves have been normalised to have the same amount of power on small scales. It is clear from these that the main effect of lowering Γ is to increase the amount of power on large scales. We will return to the effect of the shape of the power spectrum on the correlation function in Chapter 5.

An essential feature of the CDM model is biasing as it is only in this way that the dynamical estimates of $\Omega = 0.2$ (*eg*, Davis & Peebles 1983a; Bean *et al* 1983; Yahil 1985; Colless & Hewett 1987), which assume that the light traces the mass, can be reconciled with the $\Omega = 1$ prediction of inflation. It is still not clear how biasing arises, but several processes have been suggested (*eg*, Dekel & Rees 1987; White *et al* 1987a; White & Frenk 1992; Bower *et al* 1993). Galaxy clusters and galaxies of different morphologies all exhibit different clustering strengths, although their autocorrelation functions have broadly similar shapes (*eg*, Davis & Geller 1976; Bahcall & Soneira 1983). Thus only one type of object at most could be truly tracing the underlying mass distribution of the Universe in both shape

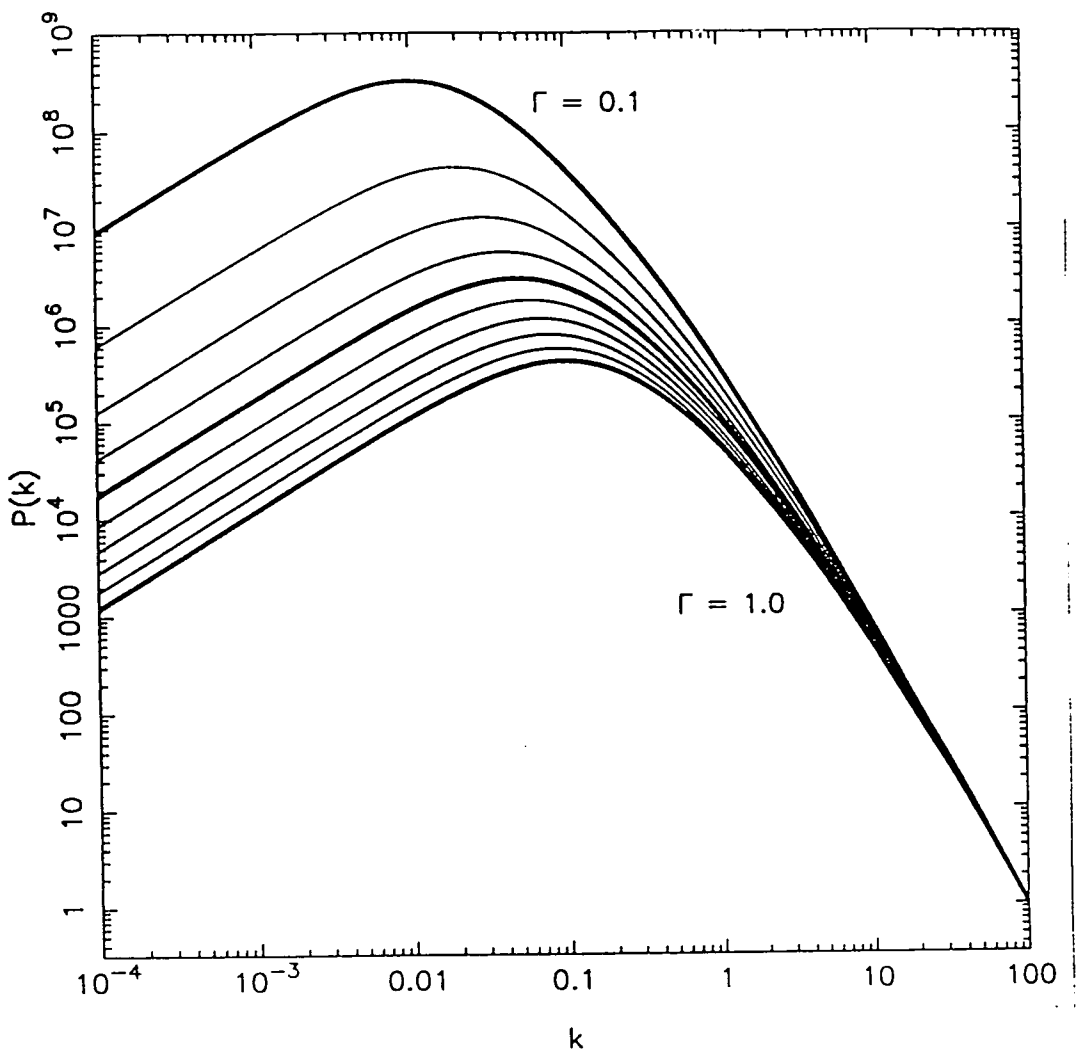

Figure 1.1. The 'CDM-like' power spectrum (equation (1.17)) for $\Gamma = 0.1$ to $\Gamma = 1.0$. The curves have arbitrary normalisation such that $P(100) = 1$.

and amplitude. It is more probable that none of these objects provides a true reflection of the clustering of the underlying mass field, and each is a biased tracer.

Kaiser (1984) (and Rice 1954 in a different context) showed that the highest peaks in a Gaussian random field are more strongly clustered than the field itself. This offers a possible explanation for the differences in the clustering strengths of different objects. For instance, if the rich Abell clusters are associated with higher peaks in the field than the galaxies, this would explain why Abell clusters are more strongly clustered than galaxies. This bias is commonly expressed as the biasing parameter b such that

$$\sigma_{\rm gal} = b\sigma_\rho \tag{1.18}$$

where $\sigma_{\rm gal}$ is the rms overdensity in, say, galaxies and σ_ρ is the rms overdensity in the mass. For galaxies $\sigma_{\rm gal} = 1$ when their distribution is smoothed using a top hat filter of radius $8{\rm h}^{-1}$Mpc. The identity $b = 1/\sigma_8$ is therefore often used, where σ_8^2 is the variance of the density field when similarly smoothed on a scale of $8{\rm h}^{-1}$Mpc. In the past b has often been taken to be a constant for any particular class of objects. Consideration is now being given to the possibility that b may also be a function of position (Bower *et al* 1993).

1.4 Outline

In this Thesis we will address several problems related to the clustering of galaxies and groups of galaxies. We will concentrate especially on the clustering of faint galaxies.

In Chapter 2 we investigate the clustering of faint galaxies around bright galaxies in a way which is not biased towards particularly extreme environments. We also consider the effect of the morphology of the bright galaxies. By assuming a luminosity function we are able to deduce the bright-faint cross-correlation function, $\xi_{\rm bf}$.

In Chapter 3 we extend the work of Zaritsky *et al* (1993) on the satellites of isolated, Milky Way like galaxies. Bad weather has prevented us expanding the sample of satellites significantly, but we are able to extend the work of Zaritsky *et al* (1993), developing an alternative method for interloper rejection, placing a lower limit on Ω and considering the dynamics of the optical part of the central spiral galaxy relative to the dynamics of its dark halo.

In Chapter 4 we use the techniques developed in Chapter 2 to look at the small scale environment of LSB galaxies. We then consider the implications of our results for models of how star formation is triggered.

In Chapter 5 we develop a method for estimating the clustering of objects of a particular mass or masses. This method is analytical, extending the formalism introduced by Press & Schechter (1974) and requiring a knowledge of only the shape of $P(k)$. We compare the results of this analytical work with numerical N-body work and illustrate the technique by addressing some simple astrophysical problems.

Finally in Chapter 6 we summarise our main results and conclusions and consider the future for studies of this kind.

2 A statistical study of satellite galaxy distributions around bright galaxies

2.1 Introduction

Faint satellite galaxies are often found in the vicinity of bright galaxies. Prime examples are The Large and Small Magellanic clouds, which are satellites of the Milky Way. However, satellite systems have also been detected around other bright galaxies, initially by Holmberg (1969). Such systems are of interest in a variety of contexts. For instance, Zaritsky *et al* (1993) have shown that they can be effectively used as dynamical tracers of the outer parts of dark galactic halos, probing regions which other techniques, such as optical rotation curves or HI line widths, cannot reach. For a detailed discussion of this topic see Chapter 3. The abundance and clustering of intrinsically faint galaxies, of which satellite galaxies are an example, are important constraints on models of galaxy formation. For example, current models have difficulty explaining why so few faint galaxies are observed, generally predicting that the faint end slope of the luminosity function (equation (1.1)) produced in the models should be much steeper than that observed (White & Frenk 1992, Cole 1990, Cole *et al* 1993, Lacey & Silk 1991, Kaufmann *et al* 1993). Also, the question of whether or not intrinsically faint galaxies are less clustered than their intrinsically bright counterparts remains unanswered. This is predicted by the mechanism of 'natural biasing' (White *et al* 1987a; Bertschinger & Gelb 1991) although, as we discuss in Chapter 5, the clustering amplitude may begin to increase again for very faint objects. In this chapter we

address these issues by investigating the projected distribution of satellites around bright galaxies of different morphological types.

Redshift surveys of faint galaxies are limited to relatively small distances. Consequently, determinations of their luminosity function tends to be based on photometry of nearby clusters such as Virgo and Fornax (Sandage *et al* 1985; Impey *et al* 1988; Irwin *et al* 1990). There are indications from this work that the faint end slope of the luminosity function may be somewhat steeper than is expected from simply extrapolating the intermediate behaviour of the field luminosity function ($\alpha \sim 1.5$, rather than $\alpha \sim 1$). However, the errors are still large (*eg* Loveday *et al* 1992a) and the clusters represent a particularly rich environment which may affect the luminosity function. Studying the spatial distribution of faint galaxies is plagued by similar difficulties. White *et al* (1988) detected an increase in the clustering strength of nearby dwarf galaxies as a function of their 21cm line width, but this was based on a survey of a relatively small volume and so sampling effects may have affected the result. In contrast, Eder *et al* (1988) failed to detect any difference between the apparent distributions of 102 dwarf irregulars and a sample of bright galaxies in the vicinity of a nearby void. Studies based on redshift surveys of flux limited samples are restricted to a limited range of intrinsic luminosities around L_* and detections of differences in the clustering of different populations are, at best, marginal. This leads to contradictory results (Alimi *et al* 1988; Hamilton 1988; Loveday *et al* 1992b, Moore *et al* 1993).

In this chapter we aim to bypass some of the problems mentioned above by concentrating on faint galaxies which are satellites of bright galaxies. We are then able to determine their statistics by cross-correlating deep maps of the projected galaxian distribution with a catalogue of bright galaxies of known redshift. Since the bright galaxy redshifts can be measured for galaxies at large distances we are able to survey a large volume. Also, by choosing our sample of bright galaxies in an unbiased fashion we avoid focussing on

extreme environments such as rich clusters. As with all clustering studies we cannot determine both the luminosity function and the clustering strength of the faint galaxies, but only a combination of both. In addition we are also restricted to estimating the bright-faint cross correlation function. The faint galaxy autocorrelation function can only be obtained by assuming a bright galaxy autocorrelation function and a cosmological model.

Our method of analysis is based on the work of Holmberg (1969) who used Palomar Observatory Sky Survey (POSS) plates. He counted the number of faint galaxies which were within $40h^{-1}$kpc of a sample of bright spiral galaxies for which distance moduli were known. After correcting for the background, using the counts at much greater projected distances, he concluded that spirals typically have between 1 and 5 satellites brighter than -10.5 within $40h^{-1}$kpc. This compares well with the Milky Way, for which only one satellite lies within $40h^{-1}$kpc. In this study he also discovered the 'Holmberg effect': an apparent excess of satellites close to the minor axis of the spirals. Recently Vader & Sandage (1991) estimated the frequency of early type dwarves around early type bright galaxies. They determined the projected density profile of the dwarves, $\Sigma_s \propto r^{-1.22\pm0.05}$, on scales of (12.5–200)h^{-1}kpc. They also found a dependence of the dwarf frequency within $200h^{-1}$kpc on the average galaxian density, increasing from ~ 0.25 around 'isolated' early type galaxies to ~ 8 in the Virgo cluster (Ferguson & Sandage 1991).

Lake & Tremaine (1980) used Holmberg's own data to estimate the satellite-bright galaxy cross correlation function for separations of (5–40)h^{-1}kpc. They then fitted this to a power law of the usual form (equation (1.8)). Using the luminosity function which Holmberg had estimated for the field they found $\gamma = 1.52 \pm 0.19$ and $r_0 = (3.8 \pm 1.5)\,h^{-1}$Mpc. Since these values are consistent with the autocorrelation function of bright galaxies at larger separations (Davis & Peebles 1983) they concluded that the correlation function is independent of luminosity. The density profile subsequently found by Vader & Sandage

is significantly different from that of Lake & Tremaine. This discrepancy may be due to the different morphological types of the bright galaxies considered in each case. This is an important point, to which we will return later.

Phillipps (1985) used a procedure analogous to the derivation of Limber's equation to find the relationship between the projected satellite surface density and the satellite-bright galaxy spatial cross-correlation function (see also Lilje & Efstathiou 1988 for a related derivation in a different context). Phillipps & Shanks (1987a, 1987b) applied this formalism to a sample constructed from POSS plates and the Durham-AAT redshift survey. Assuming a standard field galaxy luminosity function they were unable to detect any significant difference between the clustering of faint galaxies around bright galaxies and the clustering of bright galaxies amongst themselves. However, due to the limited amount of data available to them their estimates had large uncertainties. In this chapter we apply this type of analysis to a considerably larger data set, so obtaining an improved determination of the amplitude of the satellite-bright galaxy cross-correlation function.

The rest of this chapter is organised as follows. In §2.2 we describe our data sets; in §2.3 we develop new statistical methods to estimate the radial distribution of satellites around bright galaxies and in §2.4 we discuss the clustering properties of the faint galaxies. Finally, in §2.5 we summarise and discuss our main results.

2.2 The Data

The method is based on the comparison of two data sets: a large catalogue of galaxies with positional information and luminosities (the 'faint galaxies') and a less numerous catalogue of galaxies with distance estimates (the 'primary galaxies'). The sample of

primary galaxies must be homogeneous, but need not be complete. We estimate the distance of our primaries using their redshifts.

The primaries are drawn from the CfA redshift survey (Davis *et al* 1982) with morphological types drawn from the Huchra catalogue (Huchra 1990). Only those primaries which have magnitudes brighter than $M_{B_T} = -18.5$ are considered as potential primaries. Although not all of the CfA galaxies are used the sample of primaries is homogeneous in as much as it is drawn from a flux limited sample. All recessional velocities are corrected for virgocentric infall (*eg*, Davis & Peebles 1983b). The redshift distribution of the the primaries is shown in Figure 2.1.

The faint galaxies are drawn from 45 POSS plates scanned using the Automated Plate Measuring (APM) machine at Cambridge (Kibblewhite 1980; Kibblewhite *et al* 1984) which were analysed using standard techniques (Irwin 1985). The plates are predominantly close to the galactic poles, but are not necessarily contiguous. To minimise the effects of vignetting only the central $5^o \times 5^o$ of each plate is used. The positions of these plates, and all the galaxies in the CfA survey, are shown in Figure 2.2. Also shown are the positions of eight additional plates used for devignetting (see below).

For the faint galaxies we require luminosity information as well as positional information. The APM machine gives accurate relative magnitudes within each plate, but these need to be externally calibrated. We achieve this by first ordering the APM galaxies according to their APM magnitudes. Their number density is then matched against the number density found in the Lick galaxy catalogue (Shane & Wirtanen 1967) for that plate area. The magnitude of the galaxy for which a match is obtained is then set equal to $m_{pg} = 18.9$, which is the limit of the Lick catalogue (Groth & Peebles 1977). The same adjustment is made to all the faint galaxy magnitudes for the plate. This photographic magnitude can now be converted to total blue magnitude using the relationship $m_{B_T} = m_{pg} + 0.08$ (Lilje

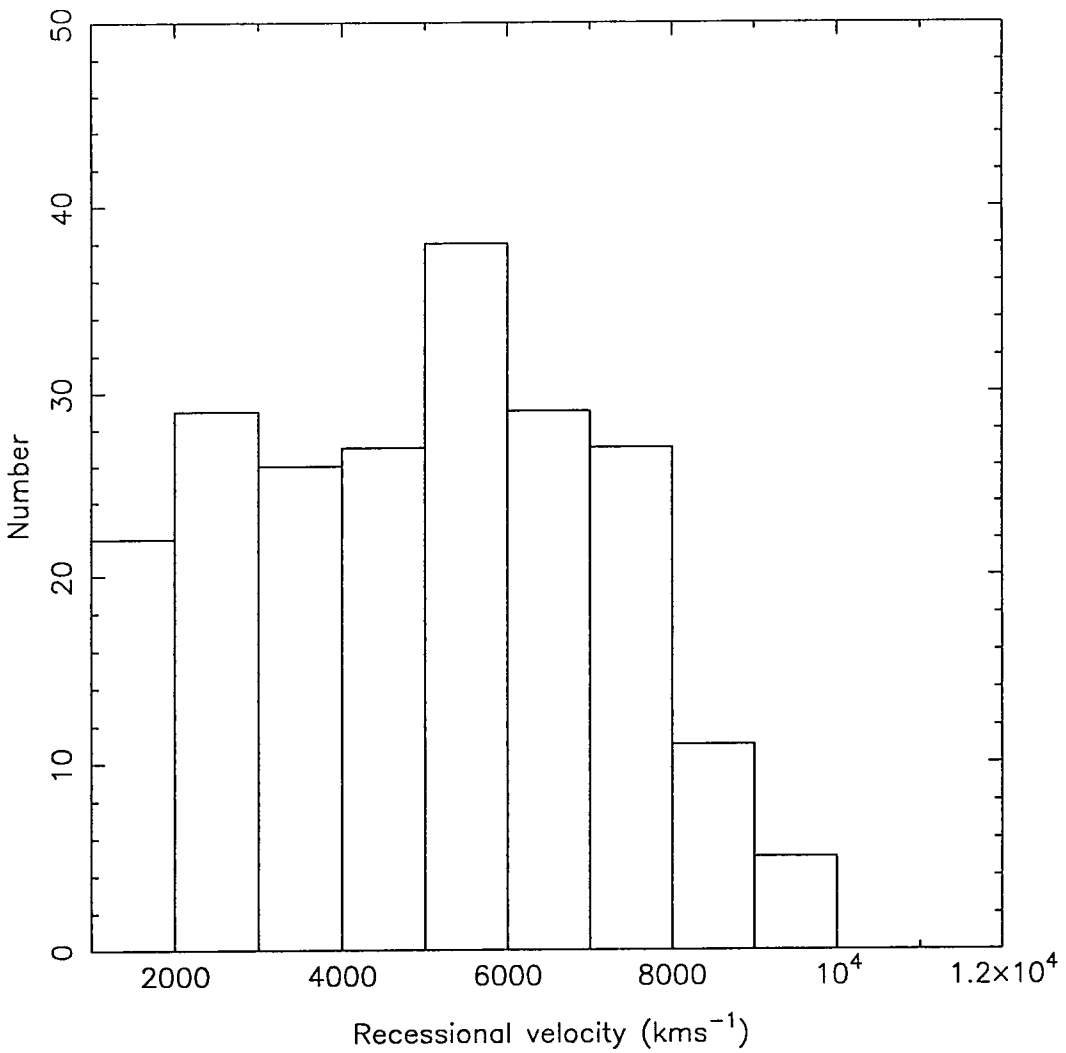

Figure 2.1. The redshift distribution of primaries drawn from the CfA Catalogue. This is prior to any target selection on the basis of distance or morphological type.

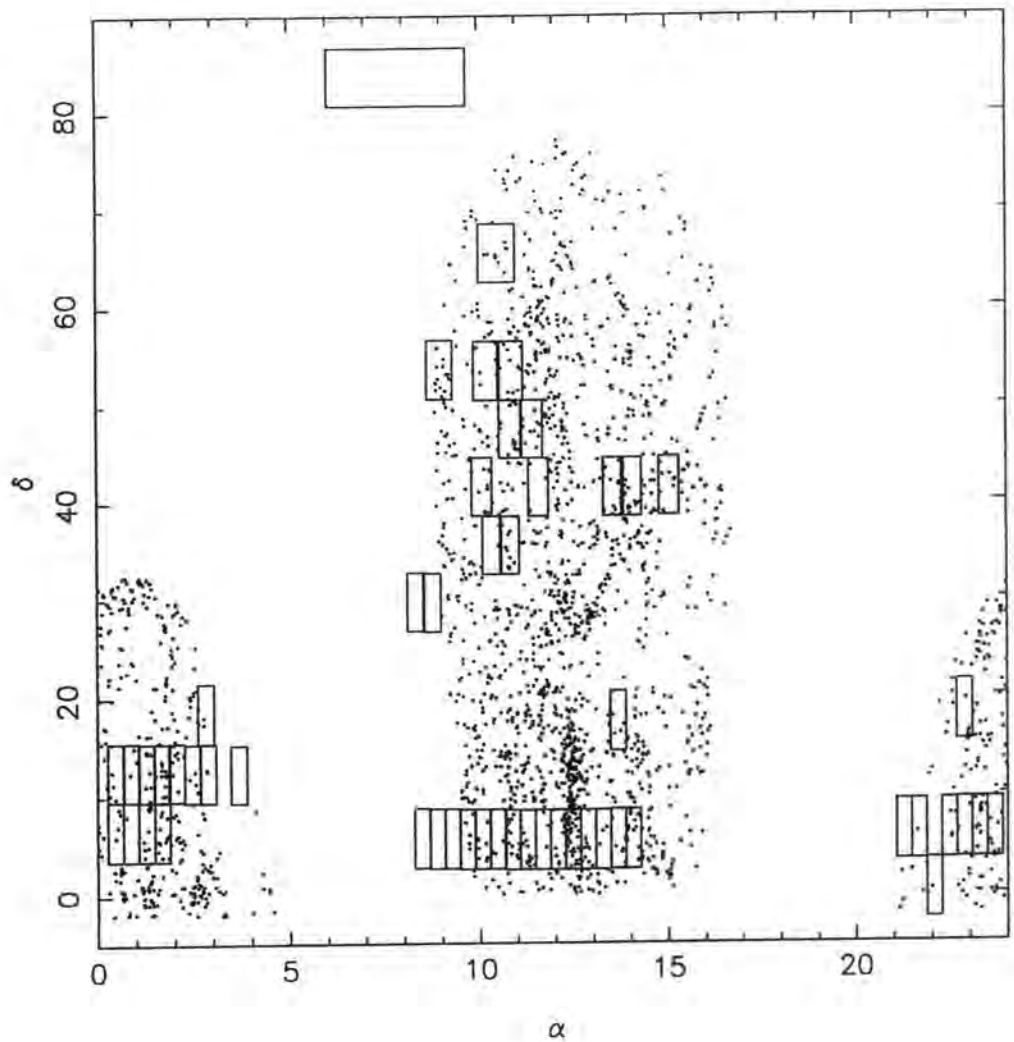

Figure 2.2. The spatial distribution of the APM scanned Palomar plates used in the analysis (solid boxes) and the positions of the the galaxies in the CfA redshift survey (dots). The apparent change in shape of the Palomar plates with changing declination is a projection effect.

& Efstathiou 1988). It has been claimed that the Lick catalogue contains artificial large scale gradients (Geller *et al* 1984; de Lapparent *et al* 1986). Using the Lick catalogue to calibrate our magnitudes could lead to similar gradients in our data. Groth & Peebles (1986a, 1986b) however showed that these gradients do not have a significant effect on $\omega(\theta)$ for $\theta < 3^o$. The linear scale to which 3^o corresponds varies from primary to primary. Figure 2.1 shows that the distribution of primary recession velocities peaks at $\sim 2000\,\mathrm{km\,s^{-1}}$. At this redshift 3^o corresponds to $\sim 1\,\mathrm{h^{-1}Mpc}$. We can justify our use of the Lick catalogue *a posteriori* by noting that most of the signal we observe is for separations which are smaller than this.

Having set the plate zero point in this way we now applied a devignetting correction. We stacked the plates (the original 45 plus a further 8 from outside the CfA region) and sorted by magnitude in a 22×22 grid. The expected count of faint galaxies in each cell is 120. A zero point correction equal to the difference between the magnitude of the 120^{th} galaxy and 18.9 is applied in each pixel. Only faint galaxies brighter than $m_{pg} = 18.9$ are then retained. The typical correction in a pixel was ~ 0.1 magnitudes and this correction increased the number of faint galaxies from the number found in the Lick catalogue, from 58047 to 58082. The mean absolute change in the number of galaxies on a single plate was $< 1\%$. The properties of each plate are summarised in Table 2.1. Finally, tests were made for significant extinction. One plate had already been rejected because the area it covered showed significant structure on the IRAS 100μm map. We estimated the mean extinction on each of the remaining plates by checking the extinction of ~ 150 galaxies from the Burstein & Heiles (1984) compilation. The worst plate mean was < 0.1 magnitudes. This is similar to the devignetting corrections and less than the typical uncertainties in the magnitudes. We therefore made no further correction for extinction. This is as we expected, most of the plates being close to the galactic poles.

POSS plate	RA (1950)	Dec (1950)	N_L	N_c	N_c/N_L	N_p
1019	$13^h40^m35^s$	17°31′14″	1376	1374	1.00	4
1032	$10^h21^m30^s$	35°31′10″	1184	1188	1.00	2
104	$12^h52^m49^s$	05°29′02″	1258	1279	1.02	7
1146	$22^h04^m52^s$	00°27′47″	1103	1105	1.00	2
1157	$22^h28^m47^s$	06°29′17″	808	785	0.97	4
1161	$22^h52^m40^s$	18°30′22″	831	827	1.00	3
1201	$01^h16^m57^s$	06°29′59″	1280	1265	0.99	7
1202	$02^h05^m14^s$	18°27′12″	730	722	0.99	4
1274	$00^h52^m58^s$	12°30′58″	1304	1287	0.99	3
1300	$02^h29^m09^s$	12°25′21″	799	828	1.04	5
1331	$10^h14^m09^s$	53°31′33″	1046	1036	0.99	5
1351	$08^h19^m52^s$	29°41′52″	933	925	0.99	0
1358	$08^h53^m02^s$	05°38′25″	668	664	0.99	0
1359	$10^h04^m59^s$	05°32′19″	1184	1179	1.00	9
1371	$15^h03^m32^s$	41°37′46″	947	949	1.00	7
1386	$14^h03^m58^s$	41°31′48″	1264	1267	1.00	15

Table 2.1 Table showing summary of properties of plates used in this analysis. The columns give the following information: column 1 shows the POSS plate number; columns 2 and 3 give the position of the centre of the plate; column 4 gives N_L, the number of galaxies in the central $5^o \times 5^o$ of the plate, as predicted by the Lick Map; column 5 gives N_c, the number of galaxies on the plate after applying a devignetting correction; column 6 gives the ratio N_c/N_L and column 7 gives the number of primaries in the plate area, N_p. The details of the primaries on each plate is given in the appendix.

POSS plate	RA (1950)	Dec (1950)	N_L	N_c	N_c/N_L	N_p
1392	$11^h16^m54^s$	$05°28'48''$	1237	1243	1.00	9
1399	$10^h28^m57^s$	$05°30'50''$	1259	1278	1.02	3
14	$01^h41^m04^s$	$12°28'50''$	959	969	1.01	13
15	$02^h53^m11^s$	$12°23'22''$	875	874	1.00	2
154	$13^h34^m07^s$	$41°30'54''$	1236	1240	1.00	9
1560	$12^h28^m51^s$	$05°28'29''$	1452	1455	1.00	31
1561	$13^h16^m48^s$	$05°29'58''$	1077	1075	1.00	3
1611	$12^h04^m52^s$	$05°28'15''$	1590	1601	1.01	12
209	$02^h03^m54^s$	$12°33'12''$	902	915	1.01	7
21	$01^h41^m10^s$	$06°32'00''$	1133	1133	1.00	10
233	$09^h41^m02^s$	$05°33'49''$	1099	1106	1.01	5
28	$09^h17^m03^s$	$05°35'31''$	854	835	0.98	0
316	$23^h16^m49^s$	$06°31'11''$	1094	1092	1.00	14
495	$11^h40^m53^s$	$05°28'23''$	1943	1965	1.01	2
552	$21^h16^m48^s$	$06°24'00''$	875	876	1.00	0
635	$01^h17^m01^s$	$12°30'00''$	1183	1195	1.01	7
642	$08^h29^m03^s$	$05°40'50''$	527	531	1.01	0
662	$10^h30^m40^s$	$65°30'40''$	774	776	1.00	8

Table 2.1 continued.

POSS plate	RA (1950)	Dec (1950)	N_L	N_c	N_c/N_L	N_p
673	$10^h51^m45^s$	53°29′43″	1984	1989	1.00	9
692	$07^h52^m22^s$	83°44′22″	349	342	0.98	0
700	$11^h25^m14^s$	47°28′39″	1167	1163	1.00	12
709	$10^h51^m34^s$	47°29′43″	1390	1400	1.01	11
711	$10^h05^m47^s$	41°32′10″	1377	1349	0.98	7
719	$11^h35^m04^s$	41°28′31″	926	919	0.99	2
722	$10^h52^m56^s$	05°29′37″	1282	1270	0.99	13
731	$10^h49^m21^s$	35°29′49″	1191	1195	1.00	12
796	$23^h40^m51^s$	06°31′38″	641	632	0.99	6
821	$22^h52^m48^s$	06°30′23″	1198	1194	1.00	1
823	$00^h28^m55^s$	12°31′31″	999	1020	1.02	3
860	$21^h40^m44^s$	06°25′57″	621	627	1.01	1
877	$00^h52^m55^s$	06°30′57″	1163	1137	0.98	1
90	$13^h40^m47^s$	05°31′08″	1429	1420	0.99	4
915	$00^h28^m54^s$	06°31′30″	1327	1339	1.01	4
924	$08^h45^m47^s$	29°39′04″	1155	1169	1.01	0
940	$03^h41^m15^s$	12°18′19″	428	438	1.02	0
96	$14^h04^m45^s$	05°32′46″	1527	1518	0.99	13
982	$08^h58^m54^s$	53°37′45″	1109	1122	1.01	14
Total			58047	58082	1.00	325

Table 2.1 continued.

Our final sample consists of 45 plates with 325 primaries in their inner $5^o \times 5^o$. Of these 245 primaries are brighter than $M_{B_T} = -18.5$. None of the plates are in the region of the Coma cluster, but Virgo is included. The primaries on a single plate are frequently at similar redshifts. For all the faint galaxies we calculated (x, y) positions which were binned in annuli around each primary. We then imposed the following restrictions on the primaries:

i) The primary must have a recessional velocity of at least $1000\,\mathrm{km\,s^{-1}}$, in order that its redshift be a reliable estimator of its distance (Twenty five primaries rejected);

ii) For the given absolute magnitude threshold, M_t, the corresponding apparent magnitude threshold, m_t, at the distance of the primary is calculated. If this is fainter than the apparent magnitude limit of the Lick catalogue, the primary is rejected. By imposing this condition we ensure that we count all faint galaxies which would be brighter than M_t if they were at the distance of the primary ($M_t = -16$, 7 rejections,$M_t = -17$, 1 rejection);

iii) The outermost annulus must correspond to a projected radius, $r > 500\,\mathrm{h^{-1}kpc}$ at the distance of the primary. The outermost annulus is defined to be the most distant annulus for which at least 25% of its total area lies on the plate (No rejections).

2.3 The radial distribution of satellites

In this section we develop, test and apply statistical tools to estimate the surface density of satellites as a function of projected separation from their primaries.

2.3.1 The surface density estimator

To translate the radial counts into the mean surface density of satellites around the primaries, the background needs to be subtracted. This background is due to faint galaxies which are not associated with the primary, but are projected into similar positions on the sky. For a set of disjoint plates this is particularly problematic. Consider, for example, the case where around the $i^{\rm th}$ primary, the surface density of satellites is given by a power law superimposed on the mean plate background of density, Σ_i^b. The mean background varies from primary to primary for two reasons. Firstly, different primaries may be on different plates. Secondly, since we are measuring the projected surface density, it is also a function of the distance to the primary. So, around this primary the surface density of faint galaxies, $\Sigma_i(r)$, is given by

$$\Sigma_i(r) = \Sigma_i^b + \Sigma_0 r^{-\epsilon} \tag{2.1}$$

where Σ_0 (the surface density at $r = 1\,{\rm h}^{-1}{\rm Mpc}$)and ϵ are constants. Now, consider an infinitesimal annulus around the primary, $r \to r + dr$. The total number of galaxies in such an annulus is given by

$$dN_i = \Sigma_i(r) 2\pi r\, dr \tag{2.2}$$

So, if a finite bin has inner radius r and width Δr then the total number of galaxies in that bin is

$$\begin{aligned} N_i(r) &= \int_r^{r+\Delta r} \Sigma_i(r) 2\pi r\, dr \\ &= \pi\Sigma_i^b(2r + \Delta r)\Delta r + \frac{2\pi\Sigma_0}{2-\epsilon}((r+\Delta r)^{2-\epsilon} - r^{2-\epsilon}) \end{aligned} \tag{2.3}$$

Now, suppose that due to the finite size of the plates the maximum projected separation at which a faint galaxy can be observed around the $i^{\rm th}$ primary is D_i. If we assume that all of the annuli are complete, *ie*, none of their area falls off the plate, then the total number

of faint galaxies within D_i is

$$\begin{aligned} N_i^{ex}(D_i) &= \int_0^{D_i} \Sigma_i(r) 2\pi r \, dr \\ &= \pi \Sigma_i^b D_i^2 + \frac{2\pi\Sigma_0}{2-\epsilon} D_i^{2-\epsilon} \end{aligned} \tag{2.4}$$

and the expected mean surface density is

$$\Sigma_i^{ex}(D_i) = \Sigma_i^b + \frac{2\Sigma_0}{2-\epsilon} D_i^{-\epsilon}. \tag{2.5}$$

We can use this surface density to calculate the background correction for a bin $r \rightarrow r+\Delta r$ giving:

$$N_i^{ex}(r) = \pi\Sigma_i^b(2r+\Delta r)\Delta r + \frac{2\Sigma_0}{2-\epsilon} D_i^{-\epsilon}\pi(2r+\Delta r)\Delta r. \tag{2.6}$$

So, a background corrected surface density can be found, given by

$$\Sigma_i^{corr}(r) = \frac{N_i(r) - N_i^{ex}(r)}{A(r)} \tag{2.7}$$

where $A(r)$ is the area of the bin, given by $A(r) = \pi(2r+\Delta r)\Delta r$. Substituting from equations (2.3) and (2.4) this gives:

$$\begin{aligned} \Sigma_i^{corr}(r) &= \frac{2\pi\Sigma_0}{2-\epsilon} \frac{(r+\Delta r)^{2-\epsilon} - r^{2-\epsilon} - D_i^{-\epsilon}(2r+\Delta r)\Delta r}{\pi(2r+\Delta r)\Delta r} \\ &\simeq \Sigma_0 r^{-\epsilon} - \frac{2}{2-\epsilon}\Sigma_0 D_i^{-\epsilon}; \end{aligned} \tag{2.8}$$

where the latter expression is for $\Delta r \ll r$. Now averaging over all M primaries for which $D_i > r$ we have:

$$\langle \Sigma_i^{corr}(r) \rangle_i = \Sigma_0 r^{-\epsilon} - \frac{2}{2-\epsilon}\Sigma_0 \langle D_i^{-\epsilon} \rangle_i. \tag{2.9}$$

The number of primaries which contribute to the average varies as a function of r, and so the second term is also a function of r. Hence the correct power law is only recovered if $\frac{2}{2-\epsilon}\langle D_i^{-\epsilon}\rangle_i \ll r^{-\epsilon}$. We might typically expect $\epsilon \sim 1$ and so we require $\langle D_i \rangle_i \gg 2r$. The typical projected plate size is $1h^{-1}$Mpc and so it would be impractical to make this requirement and to investigate all the separations of interest. This difficulty would not

arise at all when using a large, homogeneous and contiguous survey such as that of Maddox (1988) as then $\langle D_i \rangle_i \gg 2r$ for almost all interesting choices of r.

A similar calculation shows that measuring the background at some projected distance from the primary poses similar problems if the projected distance does not remain fixed. Previous authors (*eg*, Phillipps & Shanks 1987a, 1987b) have simply required that for all primaries a certain projected distance be within the limits of the plate. However, if this projected distance is to be large enough only relatively distant primaries can be used. For instance, if we required that for all primaries a projected separation of $5\,\mathrm{h}^{-1}$Mpc was accessible, primaries with recession velocities of $< 5000\,\mathrm{km\,s^{-1}}$ could not be used. This would exclude most of our primaries. Phillipps and Shanks (1987b) required that a circle of radius $1\mathrm{h}^{-1}$Mpc around each primary should not 'cover too large a fraction' of their UKSTU plates. This lead them to exclude primaries with recession velocities $< 10000\,\mathrm{km\,s^{-1}}$. By contrast, condition *(iii)* above only requires that projected separations of $\leq 500\,\mathrm{h}^{-1}$kpc are accessible. This allows all primaries with recession velocities $> 500\,\mathrm{km\,s^{-1}}$ to be used, well within the limit of condition *(i)*. We therefore devised a 'bootstrap' method to remove the background in a consistent way, whilst still making the optimal use of all our data.

Let us label by j the annulus at projected separation r_j around the i^{th} primary; by $j_{\mathrm{max},i}$ the most distant annulus for which at least a quarter of its area lies on the plate of the i^{th} primary; and by j_{max} the most distant annulus for the sample as a whole. Note that j_{max} should be chosen to be somewhat less than the maximum possible since it is this bin which will be used to estimate the background so a significant number of faint galaxies is still required in bin j_{max}. Let us define:

$$N_j = \text{Number of primaries for which } j_{max,i} > j;$$

$$A_{ij} = \text{Area of } j^{\mathrm{th}} \text{ bin around } i^{\mathrm{th}} \text{ primary;}$$

$$n_{ij} = \text{Number of faint galaxies in the } j^{\mathrm{th}} \text{ bin around the } i^{\mathrm{th}} \text{ primary;}$$

$$A_j = \sum A_{ij} \text{ over primaries for which } j_{\max,i} \geq j;$$

We estimate the mean surface density of *satellites* at projected separation r_j by

$$\widetilde{\Sigma}_s(r_j) = \Delta_j + \Delta_{j+1} + \ldots + \Delta_{j_{\max}-1}, \tag{2.10}$$

where

$$\Delta_j = \frac{1}{A_j} \sum_i \left(n_{ij} - A_{ij} \frac{n_{ij+1}}{A_{ij+1}} \right); \tag{2.11}$$

and the sum is over all galaxies which contribute to the $(j+1)^{\text{th}}$ bin.

Each term in equation (2.11) gives the mean difference in the surface densities between a pair of adjacent annuli, weighted by the area of the inner annulus. Since as many primaries as possible are used for this calculation, this procedure removes the background in an optimal fashion. Estimating uncertainties in $\widetilde{\Sigma}_s(r_j)$ is not trivial however as the background galaxies are themselves clustered and there is typically more than one primary per plate with overlapping annuli. To estimate the uncertainties it is therefore necessary to use the Monte Carlo techniques described below.

The usefulness of this expression can be verified using the same model as before (equation (2.1)). Assuming that the width of the bins is much less than their radius of curvature ($\Delta r \ll r$) we have

$$A_{ij} = 2\pi r_j \Delta r_j$$

$$n_{ij} = 2\pi r_j \Delta r_j \Sigma_i^b + 2\pi \Sigma_0 r_j^{1-\epsilon} \Delta r_j$$

$$A_j = N_j 2\pi r_j \Delta r_j$$

Substituting these in equation (2.11) we have

$$\Delta_j = \Sigma_0 (r_j^{-\epsilon} - r_{j+1}^{-\epsilon}) \tag{2.12}$$

and substituting into equation (2.10) we have

$$\widetilde{\Sigma}_s(r_j) = \Sigma_0 r^{-\epsilon} - \Sigma_0 r_{j_{\max}}^{-\epsilon}. \tag{2.13}$$

This is much easier to interpret. In the case of a finite bin size we have

$$\tilde{\Sigma}_s(r_j) \equiv \overline{\Sigma_s}(r_j) - \overline{\Sigma_s}(r_{j_{max}}) = \Sigma_0 \frac{2}{2-\epsilon}\left(\frac{r_{j,u}^{2-\epsilon} - r_{j,l}^{2-\epsilon}}{r_{j,u}^2 - r_{j,l}^2} - \frac{r_{j_{max},u}^{2-\epsilon} - r_{j_{max},l}^{2-\epsilon}}{r_{j_{max},u}^2 - r_{j_{max},l}^2}\right). \qquad (2.14)$$

where the subscripts l and u indicate the lower and upper radii of the j^{th} bin respectively and the overbar indicates the integral over the bin of equation (2.1). All projected distances are in units of h^{-1}Mpc.

We used 10 logarithmic spaced bins from $20h^{-1}$kpc to $5h^{-1}$Mpc. The region (0 - 20)h^{-1}kpc was excluded to guard against the possibility that the APM machine might have misclassified a galactic HII region as a separate galaxy or that a mismatch in the positions given by the APM scans and the CfA survey may have caused a galaxy to be counted as a satellite of itself. We consider only those faint galaxies which, at the distance of the primary, would be fainter than $M_{B_T} = -18$. Since our primaries are by definition brighter than $M_{B_T} = -18.5$ this ensures that each primary is always brighter than it satellites and that the primaries and faint galaxies form distinct sets.

2.3.2 Monte-Carlo tests

We carried out a variety of Monte-Carlo simulations designed to test our method and estimate the uncertainties. The first is a null test, designed to check for possible systematic errors in our catalogues of faint and primary galaxies. It consisted of swapping the positions of primaries between plates. We replaced the primaries on each of our 45 plates with a set of primaries located at the positions of those on a different, randomly chosen plate. Each set of primaries was used only once in each simulation. For each set of swapped plates we calculated $\tilde{\Sigma}_s(r_j)$ using equation (2.10). The procedure was repeated 50 times. The mean over these realisations and the error in the mean are plotted in Figure 2.3. This null test shows that no detectable systematic effects are introduced by either our statistical methods or our data sets.

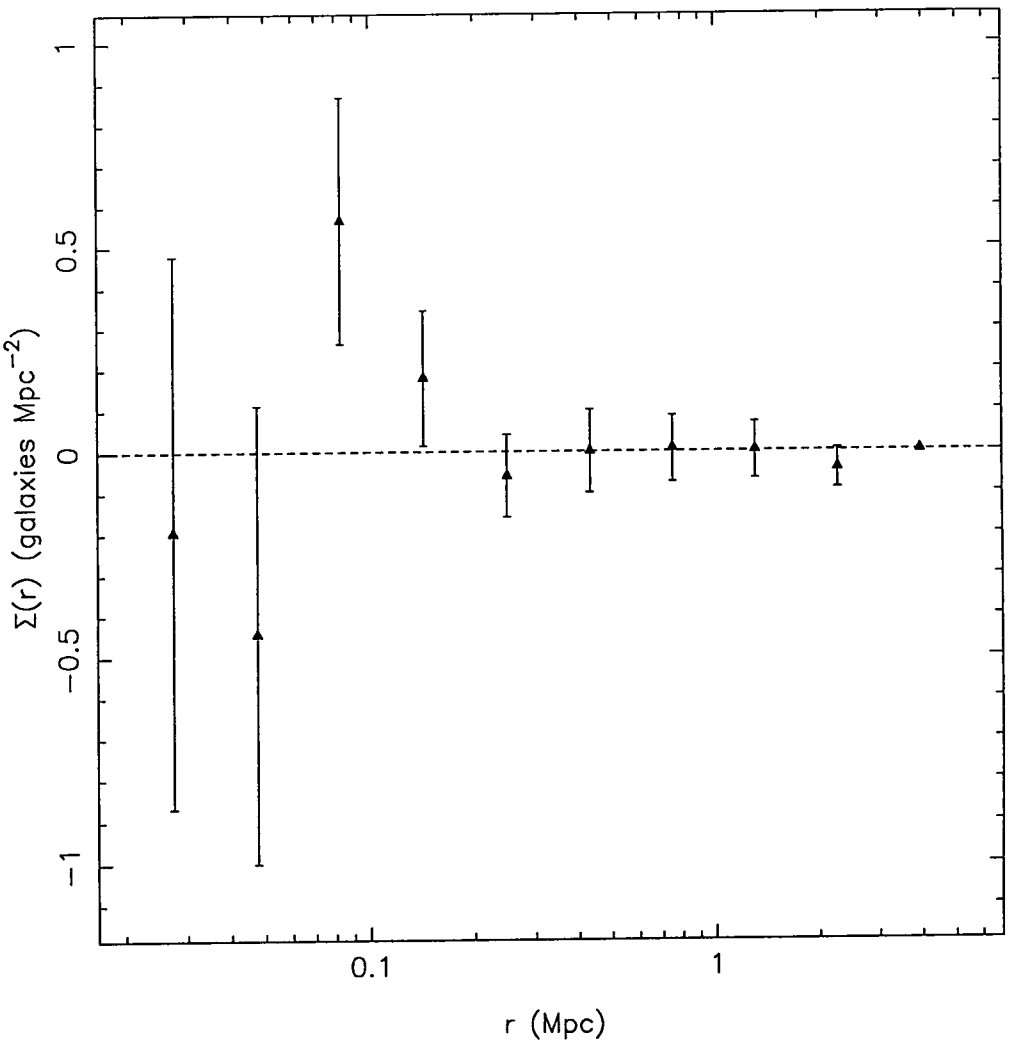

Figure 2.3. The variation in surface density as a function of projected distance using swapped pairs of primaries and faint galaxies. All primaries and satellites brighter than $M_{B_T} = -16.5$ are used. The triangles show the mean of 50 realisations with one sigma error bars derived from the scatter in the realisations. No significant signal is observed.

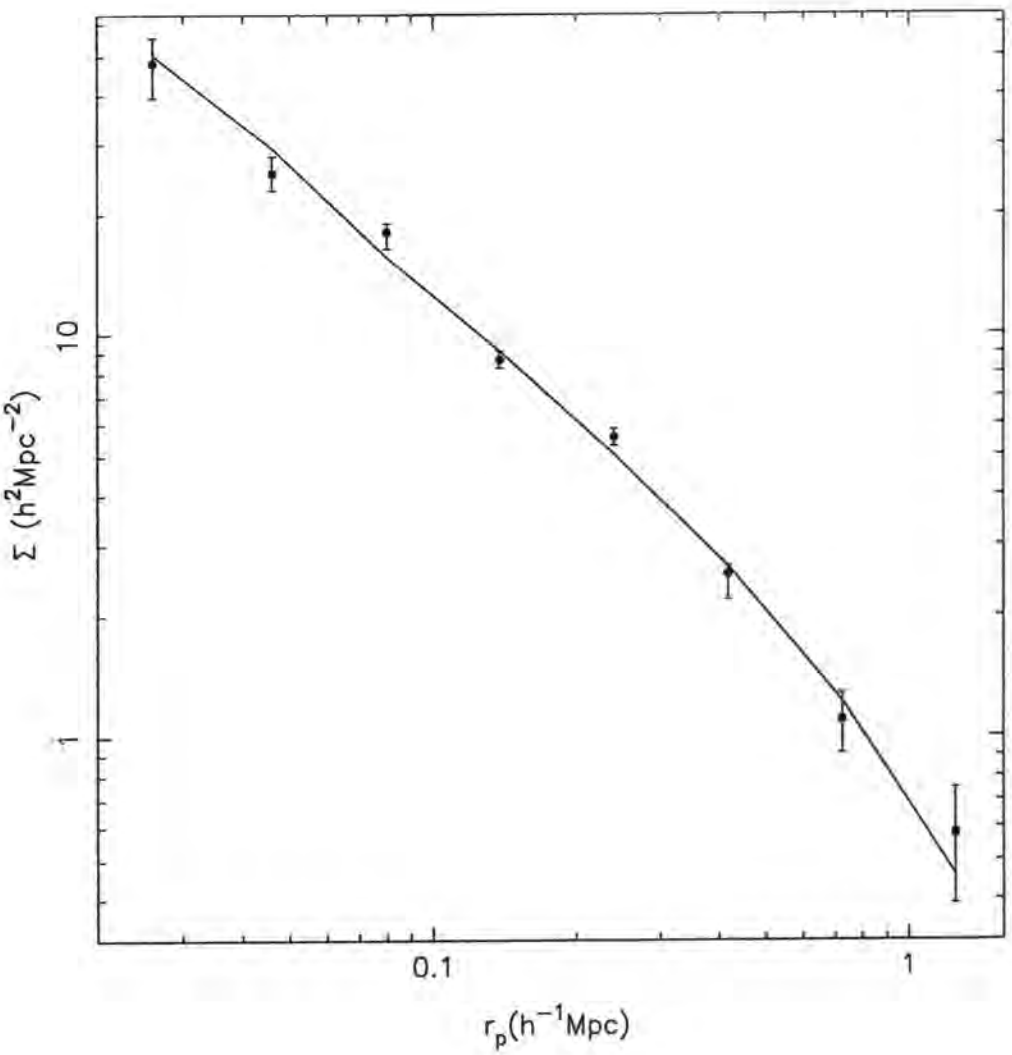

Figure 2.4. The mean of 15 Monte Carlo tests of our analysis. The triangles show the mean using 15 sets of Monte Carlo generated plates, with one CfA galaxy on each plate. The solid line joins the expected results based on the parameters of the satellite population which was originally laid down using equation (2.1) with $\Sigma_0 = 1.4h^2\,\mathrm{Mpc}^{-2}$ and $\epsilon = 1.0$. The two are consistent.

As a second test we verified that our method recovers the correct density of satellites as a function of projected separation. We first created a set of artificial plates by placing the faint galaxies on each plate at randomly chosen (x, y) positions within the boundary of the plate. Each faint galaxy retained its magnitude, so preserving the apparent luminosity function of the plate. This produces an uncorrelated random background. At the position of one primary we added a population of satellites randomly drawn from the distribution of equation (2.1) with $\Sigma_b = 0$, $\Sigma_0 = 1.4\mathrm{h}^2\,\mathrm{Mpc}^{-2}$ and $\epsilon = 1.0$. This gives approximately 9 satellites within $1\mathrm{h}^{-1}\mathrm{Mpc}$ of the primary. The procedure was repeated to generate 15 sets of 45 plates (with one primary each). Each set of 45 plates was analysed separately. The mean density returned by our analysis and the 1σ errors in the mean (derived from the scatter in the realisations) are shown in Figure 2.4. The solid line joins the values predicted by equation (2.14) for the satellite population at the centres of the bins used in our computation. This shows that our method can successfully recover the satellite distribution in the case of one primary per plate.

Our final set of Monte-Carlo simulations was designed to estimate the effects of multiple counting when there is more than one primary per plate. In this case a faint galaxy may be counted as a satellite of more than one primary. Our method is still appropriate for calculating the clustering of the satellites around primaries but will overestimate the number of satellites per primary. To simulate this effect we first generate a random plate with an uncorrelated background as above. We then add a satellite population based on equation (2.1) at the actual position of every CfA galaxy on the plate. These models are then used to estimate the errors in the values found by our method. The clustering of the primaries has a significant influence on the size of the multiple counting effect and so Hubble type will also play an important rôle in the size of this effect. We therefore defer a detailed discussion of these simulations until a later section.

2.4 Results

Our data sets are sufficiently large to allow us to consider the distribution of satellites of different absolute magnitudes and around primaries of different morphological types. We consider three sets of faint galaxies, defined in absolute magnitude – -16 to -18, -16 to -17 and -17 to -18. We found that if we attempted to measure the number of satellites fainter than -16 the background noise began to dominate. The primaries are then subdivided into late (spirals) and early types (ellipticals and S0's). The numbers of primaries and faint-primary pairs used are summarised in Table 2.2. The number of primaries increases slightly as the faint magnitude cut off becomes brighter as a result of condition *(ii)* in §2.2.

Our estimates of the surface density of satellites of different absolute magnitudes and around primaries of different morphological types are shown in Figures 2.5 to 2.7. The errors shown on the plot are 1σ errors found using the Monte-Carlo analysis described in §2.5. A model of the form of equation (2.14) was fitted to the data and this is shown as a solid line. The parameters of these fits and the appropriate value of the reduced χ^2 is given in Table 2.3. The errors shown are 1σ errors obtained using χ^2 boundaries (Avni 1976; Press *et al* 1986). These error estimates were confirmed using Monte-Carlo techniques. In Table 2.4 we show the number of satellites within $1h^{-1}$Mpc, $500h^{-1}$kpc and $250h^{-1}$kpc of the primary. Errors are again based on the Monte-Carlo analysis described below. These numbers were obtained by setting the outer radius of the innermost bin to the separation required and multiplying the resulting surface density by the area of the bin.

Several trends are apparent from our analysis. For late type primaries, the slope of the surface density distribution is approximately independent of the luminosity of the satellites. This appears not to be the case around early type primaries, but for the $-17 \geq M_{B_T} \geq -18$

	All	Late	Early
$-16 \geq M_{B_T} \geq -18$			
Number of primaries	214	139	75
pairs	43247	28619	14628
$-16 \geq M_{B_T} \geq -17$			
Number of primaries	214	139	75
pairs	34730	22906	11824
$-17 \geq M_{B_T} \geq -18$			
Number of primaries	219	143	76
pairs	9802	6816	2986

Table 2.2 The number of primaries and faint galaxy-primary pairs used in each part of our analysis.

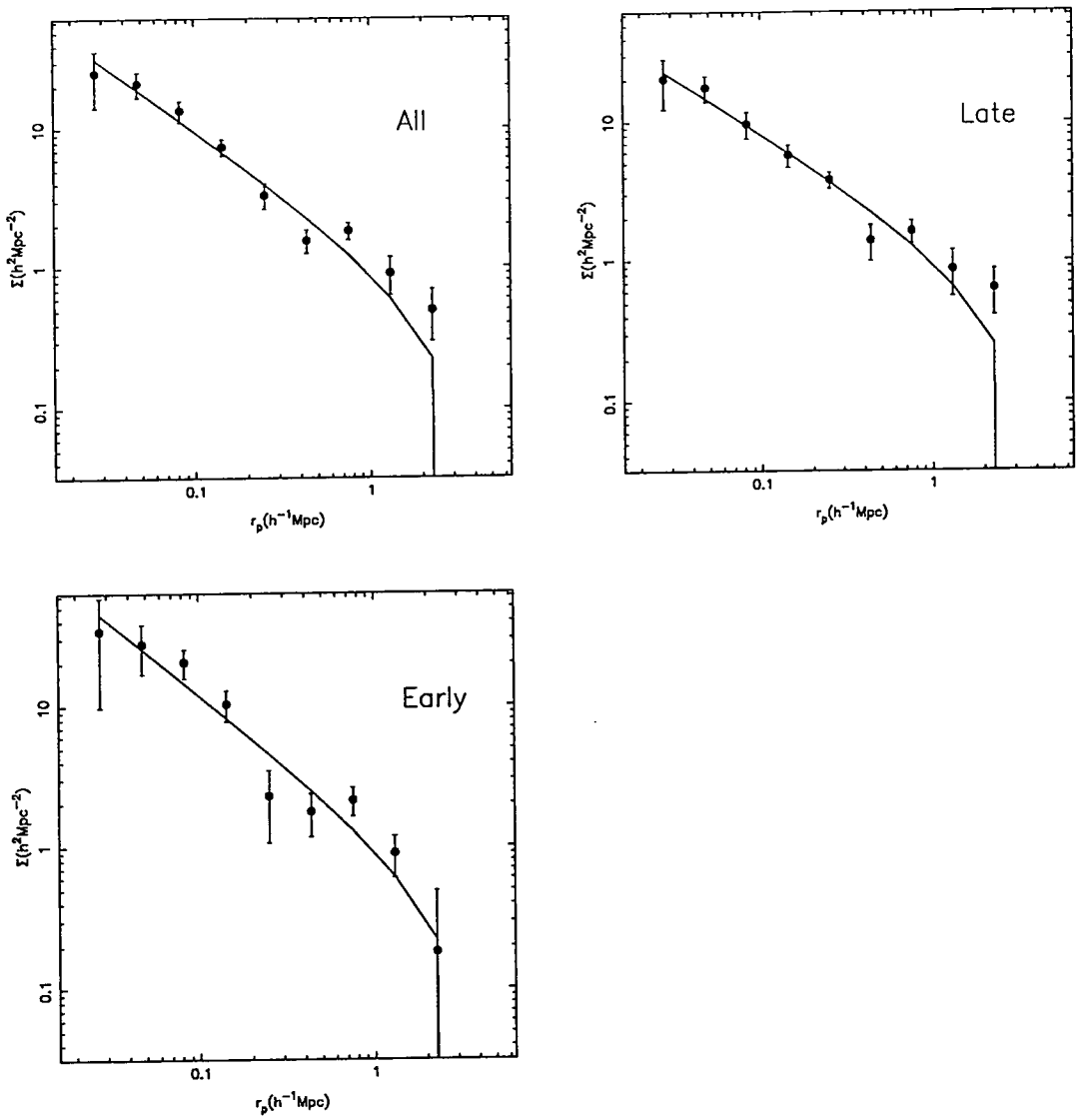

Figure 2.5. Surface density of satellites in the range $-16 \geq M_{B_T} \geq -18$ as a function of projected distance. Each panel shows the result found using all primaries, late type primaries only or early type primaries only as indicated.

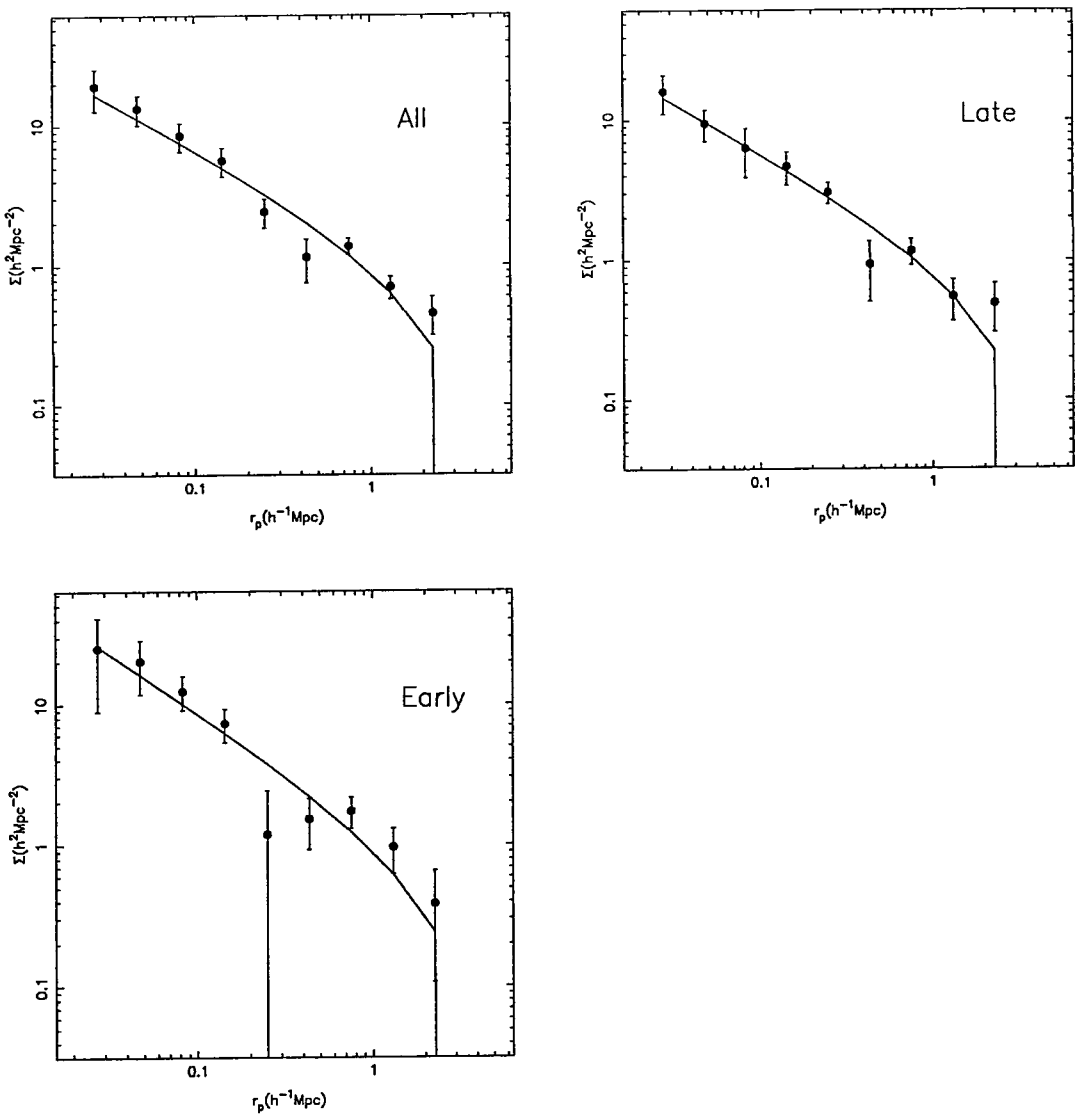

Figure 2.6. Surface density of satellites in the range $-16 \geq M_{B_T} \geq -17$ as a function of projected distance. Each panel shows the result found using all primaries, late type primaries only or early type primaries only as indicated.

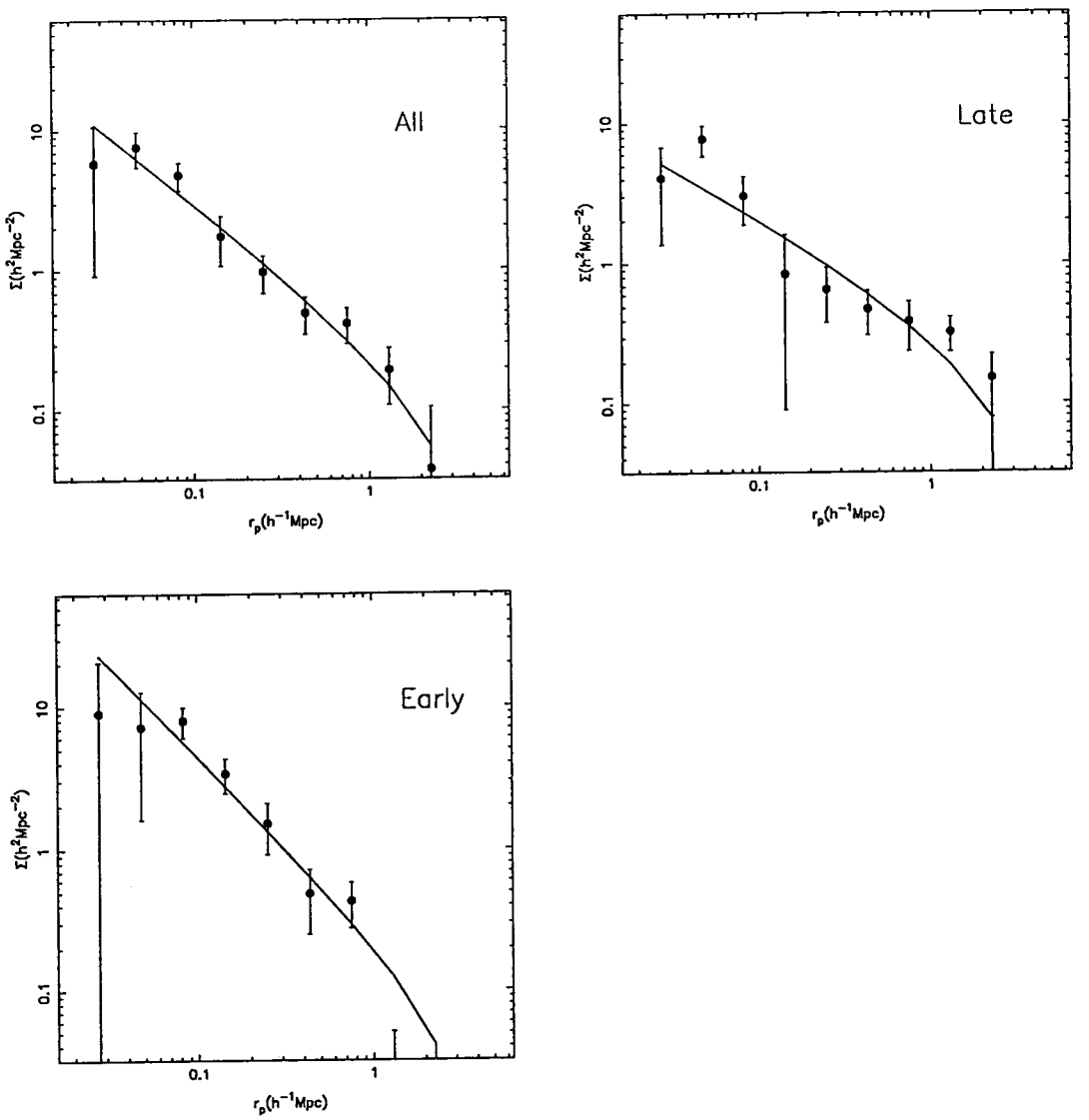

Figure 2.7. Surface density of satellites in the range $-17 \geq M_{B_T} \geq -18$ as a function of projected distance. Each panel shows the result found using all primaries, late type primaries only or early type primaries only as indicated.

Primaries	Σ_0	ϵ	χ^2
	$-16 \geq M_{B_T} \geq -18$		
All	1.21 ± 0.13	0.91 ± 0.05	2.3
Late type	1.41 ± 0.16	0.78 ± 0.05	1.4
Early type	1.19 ± 0.21	1.01 ± 0.10	1.6
	$-16 \geq M_{B_T} \geq -17$		
All	1.44 ± 0.17	0.69 ± 0.06	1.6
Late type	1.25 ± 0.18	0.69 ± 0.06	0.9
Early type	1.29 ± 0.25	0.84 ± 0.10	1.3
	$-17 \geq M_{B_T} \geq -18$		
All	0.29 ± 0.05	1.01 ± 0.09	0.7
Late type	0.43 ± 0.09	0.70 ± 0.11	1.7
Early type	0.23 ± 0.05	1.28 ± 0.11	2.0

Table 2.3 The parameters of the best fit models for each magnitude slice of satellites and division of primaries. All parameters are for a model of the form given by equation (2.14).

Primaries	$1h^{-1}$Mpc	$500h^{-1}$kpc	$250h^{-1}$kpc
	$-16 \geq M_{B_T} \geq -18$		
All	7.8 ± 1.1	2.6 ± 0.4	1.5 ± 0.2
Late type	7.6 ± 1.3	2.5 ± 0.5	1.2 ± 0.2
Early type	7.6 ± 2.3	2.8 ± 0.6	1.9 ± 0.3
	$-16 \geq M_{B_T} \geq -17$		
All	6.4 ± 1.0	1.9 ± 0.4	1.1 ± 0.1
Late type	5.9 ± 1.2	1.8 ± 0.5	0.9 ± 0.1
Early type	6.9 ± 2.5	2.1 ± 1.6	1.4 ± 0.3
	$-17 \geq M_{B_T} \geq -18$		
All	1.6 ± 0.6	0.8 ± 0.1	0.4 ± 0.1
Late type	1.7 ± 0.5	0.7 ± 0.2	0.3 ± 0.1
Early type	1.2 ± 1.2	0.9 ± 0.2	0.7 ± 0.2

Table 2.4 The number of satellites projected within $1h^{-1}$Mpc, $500h^{-1}$kpc and $250h^{-1}$kpc of all, late type and early type primaries. The magnitudes of the satellites is also indicated.

sample the model gives a poor fit ($\chi^2 = 2.0$) and it may be this which is causing the apparent discrepancy. The number of satellites within a given distance decreases monotonically with increasing luminosity of the satellites. The number of satellites within $1h^{-1}$Mpc varies from about 8 brighter than -16 to 1.5 brighter than -17. If the satellite clustering were independent of luminosity this would suggest a very steep luminosity function ($\alpha \sim 2$). The observed number brighter than -16 within $250h^{-1}$kpc is about 1.5.

There is a marked difference between the distributions around early and late type primaries. Within $250h^{-1}$kpc there are in total approximately 60% more satellites around early type primaries than around late type primaries. However, the numbers within $1h^{-1}$Mpc are comparable for both types of primary. The slope of the satellite distribution is also a function of primary morphology. In all cases satellites around early type primaries show a steeper distribution, but with a lower normalisation (Σ_0).

The apparent dependence of the satellite distribution on the primary morphology is particularly intriguing. Our analysis returns the surface density of satellites given the positions of the primaries. It does not take into account the clustering of the primaries, and if a faint galaxy is sufficiently close to more than one primary, it can be counted as a satellite of both. It is therefore possible that the differences in the apparent satellite distributions are reflecting the differences in the primary clustering properties and not an intrinsic difference in the satellite populations. This possibility can be explored in detail using Monte-Carlo methods, as we now discuss.

2.5 Correction for multiple counting

To quantify the effect of multiple counting we generated a set of artificial plates with satellite populations around the positions of all the CfA galaxies on the plate. For each

plate an uncorrelated background was also generated using the method described in §2.3.2. We were then able to alter the parameters of the true satellite population, which, when convolved with the positions of the primaries, give rise to the observed density profiles. We restrict our attention to satellites in the magnitude range $-16 \geq M_{B_T} \geq -18$. We adopted an empirical luminosity function which mimicked the relative numbers given in Table 2.4. Since we wish to investigate the difference in the satellite populations around early and late type primaries we have four free parameters in our models: a slope, ϵ and a normalisation constant, Σ_0 (or equivalently $N(< 1\,\mathrm{h}^{-1}\mathrm{Mpc})$ with $-16 \geq M_{B_T} \geq -18$) for each type of primary galaxy. For each choice of parameter values we generated 20 Monte Carlo realisations, laying down around each primary a satellite population drawn at random from a distribution described by equation (2.1) with $\Sigma_b = 0$. We analyse each realisation in an identical way to the real data and so determine the mean value of $\tilde{\Sigma}_s(r_j)$ and its standard deviation. We obtain a value of χ^2 by comparing these to the estimates for the real data in each bin. The best fit parameters and their uncertainties are then estimated using a minimum χ^2 criterion. We simplified the search for the minimum in the 4-dimensional space by using an iterative approach, allowing the search to be carried out in two 2-dimensional spaces.

As a starting solution, we assumed that there is no difference in the satellite distributions around late and early type primaries. The result of this is shown in Figure 2.8. This search was carried out on a grid with $\Delta\epsilon = 0.1$ and $\Delta N = 1$. The χ^2 values were smoothed using a bivariate gaussian with standard deviations equal to the grid spacing. The minimum for this is given in Table 2.5. The contours show the 1, 2 and 3σ deviations from this minimum using the thresholds given in Avni(1976) and Press *et al* (1986) for 2 degrees of freedom. We now adopt this as our model for the early type primaries and vary the parameters for the late type primaries, until a minimum χ^2 is found. These parameters are kept fixed, whilst the parameters for early type primaries are varied, again searching

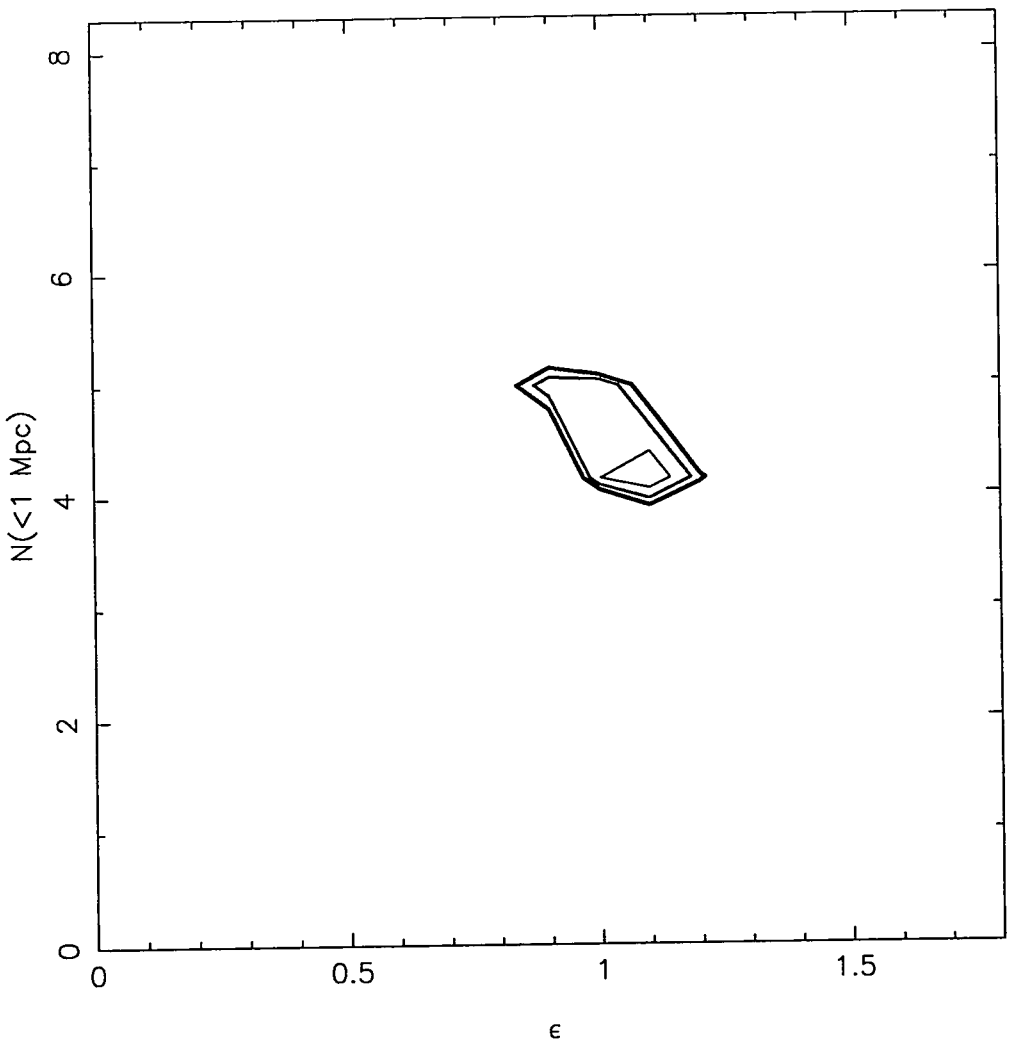

Figure 2.8. Contour of χ^2 values for models assuming that there is no difference in the satellite distributions around late and early type primaries. The contours correspond to 1, 2 and 3σ deviations from the minimum, for which $\chi^2 = 24.4$.

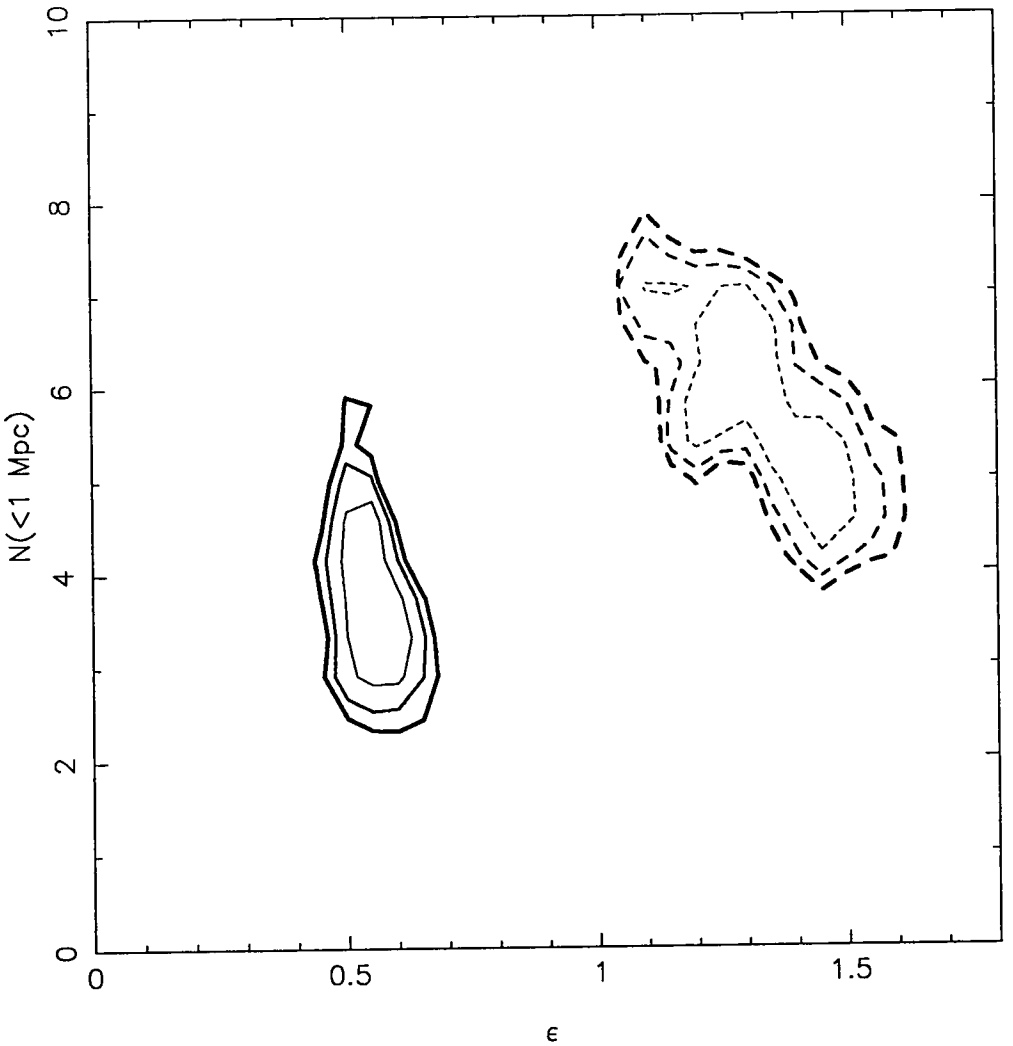

Figure 2.9. Contours in χ^2 values found by allowing the satellite populations around late type and early type primaries to be different. The contours correspond to 1, 2 and 3σ deviations from the minimum. The solid contours are for late type primaries, the minimum being $\chi^2 = 13.7$, and the dashed contours are for early type primaries, the minimum being $\chi^2 = 17.3$.

		$N(< R)$				
	ϵ	$1\,h^{-1}$Mpc	$500\,h^{-1}$kpc	$250\,h^{-1}$kpc	Σ_0	χ^2
All	1.1	4.2	2.1	1.1	0.60	24.4
Late type	0.60	3.3	1.2	0.5	0.74	13.7
Early type	1.25	5.8	3.2	1.8	0.70	17.3

Table 2.5 The best fit models for all primaries, late type primaries and early type primaries. There are five degrees of freedom in the fits.

for a minimum in χ^2. These latter two stages are repeated until the results converge. We required only 2 iterations for this. Having found the minima on this coarse grid, we searched on a finer grid, with $\Delta\epsilon = 0.05$ and $\Delta N = 0.5$. We also fixed the error estimates at those found using the best model on the coarse grid. This allowed us to reduce the number of realisations required at each grid point to 10. The results of this process are also given in Table 2.5 and shown in Figure 2.9. The solid lines are for late type primaries and the dashed lines are for early type primaries.

The χ^2 values at the minima, given in Table 2.5, are a little higher than we might have hoped, given that there are only 5 degrees of freedom. However, comparing the numbers in Tables 2.3 and 2.5, it is clear that the effect of multiple counting is to increase the number of satellites within a given radius and to make the density profile shallower. We characterise the size of this effect by the enhancement factor, $\eta(r_j) = [N_0(r_j) - N_m(r_j)]/N_m(r_j)$, where $N_0(r_j)$ is the number determined from the data and $N_m(r_j)$ is the mean number input into the simulation at the position of the minimum χ^2. The factor η is plotted in Figure 2.10. The shape of η as a function of projected separation is quite similar for late and early type primaries (solid line and dashed line respectively). However, the size for the enhancement is significantly different for the different types of primary. In the case of early type primaries $\eta \sim 0.05$ for the innermost bin. It rises to reach its maximum at $\sim 750\,\mathrm{h^{-1}kpc}$, with $\eta \sim 0.8$. The enhancement then falls. In the case of late type primaries, even in the innermost bin, the enhancement is as high as $\eta \sim 0.7$. The maximum is again reached for $r_p \sim 750\,\mathrm{h^{-1}kpc}$, but in this case $\eta \sim 2.1$ at the maximum. For late type primaries the enhancement in the innermost bin is uncomfortably large. However, crude analytical calculations, based on placing primaries on a regular grid on the sky, suggested that the enhancement in this bin should be $\eta \sim 0.3$. Since this is intermediate between the values for late type and early type primaries alone, we believe that our calculated η is correct. For late type primaries there is also some structure in $\eta(r_p)$ for $r_p \simeq 300\,\mathrm{h^{-1}kpc}$.

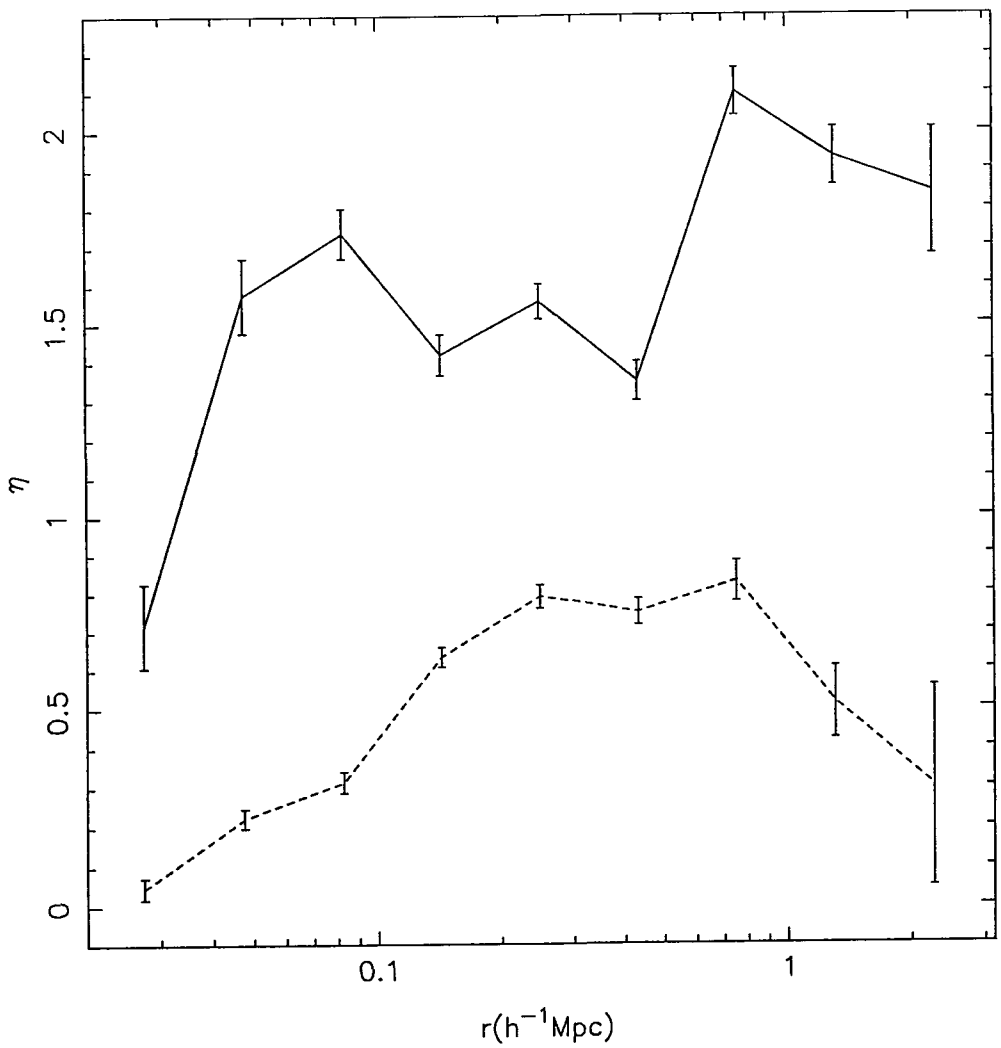

Figure 2.10. The enhancement in the number of satellites due to multiple counting. The solid line connects values for late type primaries and the dashed line those for early type primaries. They are based on 135 Monte-Carlo realisations, and the error bars are 1σ errors in the mean, derived from the scatter in the simulations.

The fluctuations are too large to be attributed to noise. We believe they are probably connected to the detailed distribution of the late type primaries.

Figure 2.9 and Table 2.5 demonstrate that the difference between the satellite populations around late and early type primaries persists even when multiple counting is taken into account. The satellites around late type primaries have a shallower distribution. Within $250h^{-1}$kpc there are typically $\sim$ 4 times as many satellites around early type primaries than around late type primaries. Within $1h^{-1}$Mpc there are about twice as many satellites around early types than around late types. There are about the same number of satellites within $2.4h^{-1}$Mpc. The surface densities are the same around each type of primary at $r \simeq 900\,h^{-1}$kpc. This effect appears to be an intrinsic property of the primary-satellite systems and not an artefact of the way in which the primaries themselves are clustered. The numbers given in Table 2.5 can be interpreted as the mean number of satellites per primary, whilst those given in Table 2.4 are the numbers of satellites actually observed.

We will compare these results with the observational work of Zaritsky *et al* (1993) and our own observational work in Chapter 3.

2.6 The satellite-primary cross-correlation function

Since we have considered the projected distribution of satellites, the spatial correlation function is not simply related to the distribution we have obtained. Phillipps (1985) derived an expression for the satellite-primary cross-correlation function, ξ_{sp}, as a function of true separation, R, between a sample of galaxies of known distance and a satellite population with a surface density profile given by equation (2.1):

$$\Sigma_s(r) = \Phi G r^{-\epsilon} \xi_{sp}(R) R^{\epsilon+1} + \Sigma_b, \tag{2.15}$$

where Φ is the number density of galaxies in the magnitude interval under consideration, found by integrating over the appropriate luminosity function. The geometric factor, G, is given by

$$G = \sqrt{\pi}\frac{\Gamma(\frac{\epsilon}{2})}{\Gamma(\frac{\epsilon+1}{2})}. \tag{2.16}$$

Substituting equation (2.1) into equation (2.15) gives

$$\xi_{sp}(R) = \left(\frac{\Sigma_0}{\Phi G}\right) R^{-(1+\epsilon)}. \tag{2.17}$$

This expression shows explicitly that the amplitude of the cross-correlation function and the luminosity function can not be determined independently using this method. We begin by assuming that the satellite luminosity function is identical to the field luminosity function given by Efstathiou *et al* (1988a): a Schechter luminosity function with $\alpha = -1.07 \pm 0.05$, $M^{\star}_{B_T} = -19.68 \pm 0.10$ and $\phi^{\star} = (1.56 \pm 0.34) \times 10^{-2} \mathrm{h}^3\,\mathrm{Mpc}^{-3}$. This is shown as a solid line in Figure 2.11. These authors do not quote the range of magnitudes over which they believe this to be reliable. However, their sample includes the CfA survey which extends to absolute magnitude $M_{B_T} = -16.5$, not much brighter than our faintest satellites, $M_{B_T} = -16$. However, the error in the luminosity function at $M_{B_T} = -16.5$ is still large. The resulting value of ξ_{sp} at $R = 1\,\mathrm{h}^{-1}\mathrm{Mpc}$ and the slope of the correlation function are given in Table 2.6, in the column headed 'EEP', for our various absolute magnitude cuts and choices of primary morphology. For reference, the bright galaxy autocorrelation function, ξ_{gg}, calculated using the CfA survey for separations of $1\,\mathrm{h}^{-1}\mathrm{Mpc}$, perpendicular to the line-of-sight, is 19.4 ± 2.0 (Davis & Peebles 1983).

The results in Table 2.6 are somewhat puzzling. The slope of ξ_{sp} is similar to the slope found on other scales and for other objects (*eg*, Davis & Peebles 1983a; Lilje & Efstathiou 1988). The satellites are less strongly clustered around the bright galaxies than the bright galaxies are around themselves. However, for the faintest satellites, $-16 \geq M_{B_T} \geq -17$ the amplitude of the correlation function is also consistent with that found for the CfA

Primaries	γ	EEP	SBT	'Hybrid'
		$-16 \geq M_{B_T} \geq -18$		
All	1.91 ± 0.05	11.6 ± 1.3	7.2 ± 0.8	11.1 ± 1.3
Late	1.78 ± 0.05	12.1 ± 1.5	7.5 ± 0.9	11.4 ± 1.4
Early	2.01 ± 0.21	12.3 ± 2.3	7.6 ± 1.4	11.6 ± 2.2
		$-16 \geq M_{B_T} \geq -17$		
All	1.69 ± 0.06	21.1 ± 2.8	12.0 ± 1.6	19.3 ± 2.5
Late	1.69 ± 0.06	22.5 ± 2.8	12.9 ± 1.6	20.6 ± 2.5
Early	1.84 ± 0.10	21.8 ± 4.6	12.5 ± 2.6	20.0 ± 4.2
		$-17 \geq M_{B_T} \geq -18$		
All	2.01 ± 0.09	6.5 ± 1.2	4.5 ± 0.8	6.5 ± 1.2
Late	1.70 ± 0.11	7.3 ± 1.8	5.1 ± 1.2	7.3 ± 1.8
Early	2.28 ± 0.11	6.0 ± 1.3	4.1 ± 0.9	6.0 ± 1.3

Table 2.6 The value of the primary-satellite cross-correlation function, ξ_{sp} at $1h^{-1}$Mpc and its slope, γ, for various choices of luminosity function (see text for details).

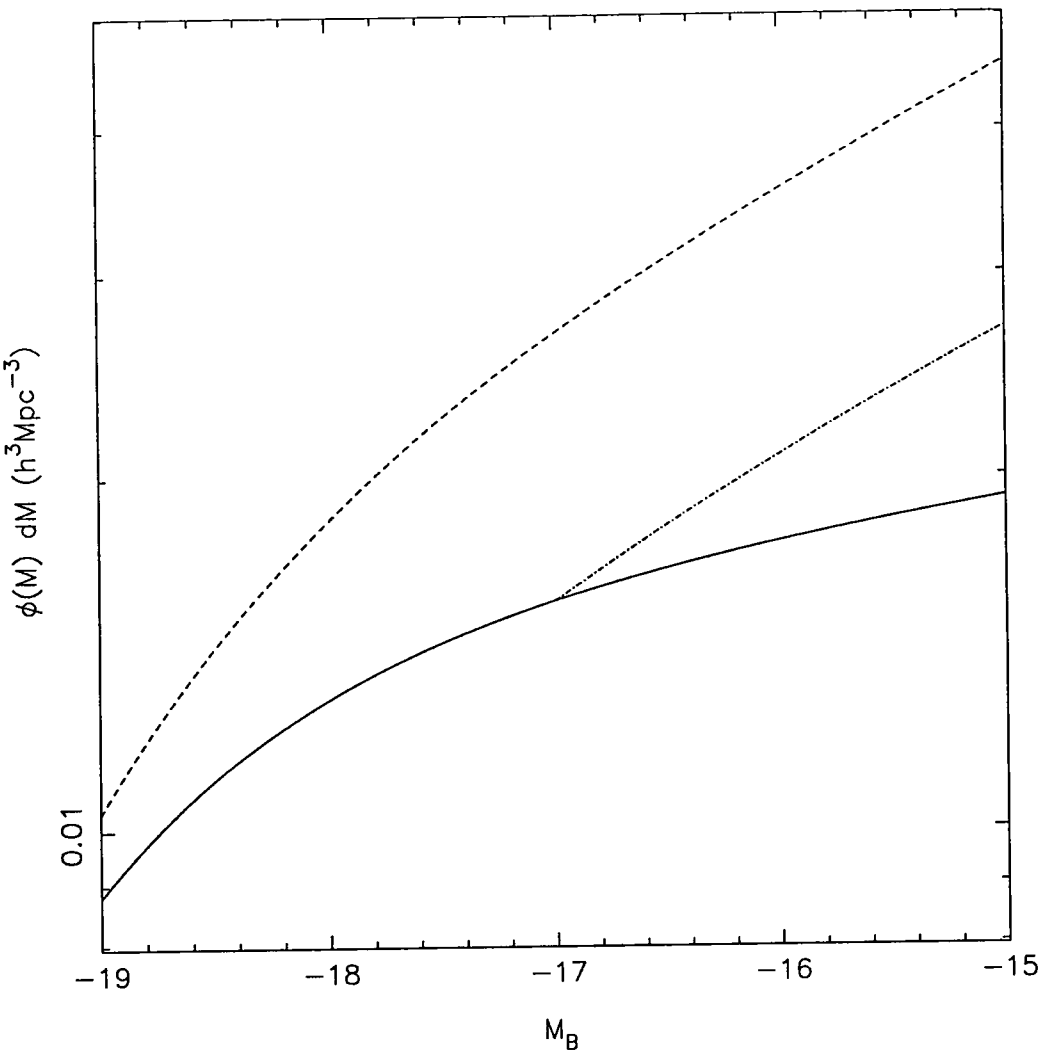

Figure 2.11. The Efstathiou *et al* (1988a) field luminosity function (solid line); the Sandage *et al* (1985) cluster luminosity function (dashed line) and a hybrid of the two.

galaxy autocorrelation function. However, for our subset of brighter satellites, $-17 \geq M_{B_T} \geq -18$, the clustering is weaker by a factor ~ 3. This is puzzling as these satellites are only approximately 1.5 magnitudes fainter than $M^\star$. It has not appeared in previous work (*eg*, Phillipps & Shanks 1987a, 1987b). However, the Phillipps & Shanks study used significantly fewer primaries and faint galaxies. Traditional ideas of biasing (*eg*, Kaiser 1984; White *et al* 1987b) suggest that brighter (and hence more massive) objects should be more strongly clustered (but see Chapter 5 of this Thesis). This appears not to be the case here. Also, the clustering amplitude must rise again rapidly in order to reach the values observed in the CfA catalogue. This strange behaviour suggests that the Efstathiou *et al* (1988a) luminosity function does not describe the satellite luminosity function adequately. As we mentioned earlier, detailed studies of the Virgo and Fornax clusters suggest that the faint end slope may be significantly steeper (Sandage *et al* 1985; Impey *et al* 1988; Irwin *et al* 1990). Adopting a distance modulus for Virgo of 31.7 (Tamman & Sandage 1985) the dwarf luminosity function of Sandage *et al* (1985) is fitted by a Schechter function with $M^\star_{B_T} = -19.6$ and $\alpha = -1.25$. Because they were studying a highly unusual environment they can not estimate the normalisation, $\phi^\star$. However, if we require that this gives the same number of galaxies brighter than $M_{B_T} = -18$ as the Efstathiou *et al* luminosity function we estimate that $\phi^\star = 1.74 \times 10^{-2} \mathrm{h}^3\,\mathrm{Mpc}^{-3}$. This is shown as a dashed line in Figure 2.11. Using this luminosity function gives the results in Table 2.6 under the column headed 'SBT'. The clustering amplitude is significantly lowered, but the brighter satellites are still more weakly clustered than the fainter satellites by a factor ~ 3. Lastly, in the column headed 'Hybrid' we have used the Efstathiou *et al* luminosity function for satellites brighter than $M_{B_T} = -17$ and the Sandage *et al* luminosity function for satellites fainter than this. The normalisation of the Sandage *et al* luminosity function is fixed to match the Efstathiou *et al* luminosity function at $M_{B_T} = -17$. The results are consistent with using the Efstathiou *et al* result for all magnitudes. Thus, whilst it is plausible that the unusual biasing is caused by satellites having a steeper luminosity function than the field,

the satellite luminosity function would have to be very much different from that of the field, even at magnitudes brighter than $M_{B_T} = -17$, in order to fully explain the effect.

We are therefore forced to adopt one of three possible conclusions. Firstly, the biasing we have measured may be correct and bright satellites are more weakly clustered around the primaries than faint satellites are. Secondly, it may not be possible to naively extrapolate the field luminosity function to fainter magnitudes. Lastly, the *satellite* luminosity function may be different from the field luminosity function, perhaps caused by interactions with the primary.

2.7 Discussion and conclusions

We have carried out a statistical analysis of the distribution of satellites around bright galaxies. Our method is based on the approach of Holmberg(1969). We count the number of faint images on the sky around a bright primary galaxy for which a distance estimate is available. Our data set is based on 45 POSS plates (plus a further 8 used for devignetting only) which are typically disjoint. Using plates which are not contiguous poses a particular problem when considering the best way to subtract the background. We developed a bootstrap technique which allowed us to remove the background in a consistent way, whilst making optimal use of our data. We have detected satellites at the 7σ level, even within $1h^{-1}$Mpc. This rises to a 7.5σ detection within $250h^{-1}$kpc. There are typically $\sim$ 8 satellites within $1h^{-1}$Mpc in the magnitude range $-16 \geq M_{B_T} \geq -18$. For the same magnitude range there are typically $\sim$ 1.5 satellites within $250h^{-1}$kpc. The surface density of satellites is fitted well by a power law with index $\sim$ 0.8. This corresponds to a correlation function with a slope similar to that of the bright galaxy autocorrelation function.

As the primaries are themselves clustered, the observed number of satellites does not correspond to the mean number of satellites per primary. Monte-Carlo simulations demonstrate that the observed profile arises from the superposition of individual satellite systems with a similar slope, but with a lower normalisation (4 satellites within $1h^{-1}$Mpc in the range $-16 \geq M_{B_T} \geq -18$).

The satellite systems around late and early type primaries appear to have significantly different spatial distributions. This difference persists even when Monte-Carlo simulations are used to take into account the differences in the clustering properties of the two subsets of primaries. These simulations show that on average early type primaries have approximately twice as many satellites within $1h^{-1}$Mpc. However, in the real distributions this difference in number is only observed within $250h^{-1}$kpc while the number of satellites observed within $1h^{-1}$Mpc is similar for late and early type primaries. Our estimates of the slope required to describe the distribution of satellites is in good agreement with previous studies. Lake & Tremaine (1980), using Holmberg's data, estimated that the satellites around late type primaries had a surface density profile with slope 0.52 ± 0.19. This is in good agreement with our estimates, despite their satellites being typically closer ($< 40\,h^{-1}$kpc) and fainter (~ -11) than ours. For early type primaries Vader & Sandage (1991) carried out a study similar in spirit to our own. They found a slope of 1.22 ± 0.05 for satellites within $200h^{-1}$kpc, again similar to our own estimates. There is thus a considerable body of observational evidence that the abundance and spatial distribution of satellites is a function of primary morphology.

This method offers a number of advantages when trying to determine the bright galaxy-faint galaxy cross-correlation function. In particular this method allows a large dynamic range of luminosities to be included. We can therefore estimate ξ_{sp} in magnitude limited bands. Also, the estimates are not affected by redshift distortions. One major disadvantage is that the estimate of the correlation function is sensitive to the assumed luminosity

function. However, in spite of uncertainties due to an unknown luminosity function the satellites do appear to be more weakly clustered than the bright galaxies.

3 The satellites of spiral galaxies

3.1 Introduction

The discovery of massive halos around galaxies had a major impact on our understanding of galaxy formation and evolution (Rubin & Ford 1970; Freeman 1970; White & Rees 1978). It is often claimed that the dark halos extend far beyond the optically visible part of the galaxy, having a mass $\sim 10^{12} M_{\odot}$. Massive halos of this kind are a generic prediction of hierarchical, $\Omega = 1$ models, in which galactic halos extend to meet the neighbouring halos. Until recently much of this theoretical framework had no observational support. For instance, mass determinations based on HI rotation curves extend out to only a few optical radii (*eg,* Begeman 1987). These small scales give us relatively little information on the mass of the entire halo.

The idea of massive, extended halos was challenged by Little & Tremaine (1980). They suggested that the relatively small radial velocities of 10 nearby satellites of the Milky Way showed that the halo of the Milky Way has a mass $\simeq 2.5 \times 10^{11} M_{\odot}$ and is truncated at $r \lesssim 50\,\mathrm{kpc}$. This is in clear opposition to the ideas outlined above. This conclusion was leant some support by Erickson *et al* (1987) who examined the satellites around 9 spiral galaxies. They concluded that only 4 of these systems could have a massive halo

and one, NGC3992, definitely did not. Although satellites probe further out into the dark galactic halo these studies are limited by the small numbers of satellites in each system. For instance in the Erickson *et al* study the maximum number of satellites in a system is 5 and even in the Little & Tremaine study with 10 satellites large uncertainties remain. This is clearly demonstrated by the Zaritsky *et al* (1989) study (also Zaritsky 1991). This study made use of 16 satellites of the Milky Way, which lead to a mass estimate $\simeq 12.5 \times 10^{11} M_{\odot}$: a factor of 5 greater than the estimate of Little & Tremaine. Most of this change is due to the addition of one system (Leo I). This is both distant (230 kpc) and has a large radial velocity (180 $\mathrm{km\,s^{-1}}$). Thus the data for the Milky Way seems once more to suggest a mass in line with theoretical prejudices. Also, absolute values apart, the uncertainty of this method of estimating the mass of the dark halo is clearly demonstrated. It therefore also casts doubt on the conclusions of Erickson *et al* .

It was these uncertainties which lead Zaritsky *et al* (1993, hereafter ZSFW) to construct their sample of satellites around isolated spiral galaxies similar to the Milky Way. They aimed to probe the dark halos around other bright galaxies using their satellites. However, as we discussed in Chapter 2 satellites are relatively rare: typically only 1 brighter than $M_B = -16.5$ within 250 $\mathrm{h^{-1}kpc}$. They overcome this difficulty by making a statistical analysis of the properties of satellites around a large number of bright primaries. The primaries are carefully selected to ensure that the dynamical properties of each is as similar to the rest of the sample as possible. These selection criteria are based on the optical properties of the primaries. However, as we discussed above, the properties of interest relate to regions well beyond the optically visible part of the galaxy. ZSFW argue that the existence of correlations between disk circular velocity, luminosity and morphological type (Tully & Fisher 1977; Rubin *et al* 1978; Rubin *et al* 1980) demonstrates that a dynamically homogeneous sample is a reasonable goal. They form a sample of 69 satellites within 375 $\mathrm{h^{-1}kpc}$ around 45 central galaxies. The projected density profile of the ensemble falls off

approximately like r_p^{-1}, where r_p is the projected distance. This shows good agreement with the results of Chapter 2. The number of satellites they find is also in good agreement with the results of Chapter 2. At projected separations $< 37.5\,h^{-1}$kpc they find a marginal excess of satellites close to the primary minor axis, relative to the number close to the major axis (the Holmberg effect). The characteristic velocity of the satellites relative to the primary remains approximately constant to the limit of their survey, $\sim 190\,h^{-1}$kpc. Assuming the satellites have isotropic orbits, they find that the typical circular velocity of a halo is $\sim 200\,\mathrm{km\,s^{-1}}$ and that the mass of the dark halo within $150\,h^{-1}$kpc is $2\times10^{12}M_\odot$. This type of dynamical analysis cannot be applied at greater separations, as satellites at such large separations are probably not in dynamical equilibrium. (see White & Zarisky 1992, who demonstrate that for an isothermal sphere model of the halo the halo extends to $r = 0.15V_c/H_0 = 150\,h^{-1}\mathrm{kpc}V_c/100\,\mathrm{km\,s^{-1}}$.) ZSFW thus conclude "spiral galaxies similar to the Milky Way do indeed appear to have very massive extended halos."

ZSFW also find no detectable correlation between the luminosity of the primary and the relative velocity of the satellites. This result is of some consequence, as the Tully-Fisher relationship clearly shows that the luminosity of a spiral is closely connected with its dynamics. The conclusion of ZSFW is, then, that the dynamics of the inner and outer parts of galactic halos may not be well correlated with each other. There are, however, significant uncertainties associated with this result. Firstly, in order to have a dynamically homogeneous sample of primaries, they have strict criteria for the absolute magnitude of the primary – 77% of the primaries in their catalogue lie in the range $-20.4 < M_B < -18.4$. Using the relationship of Pierce & Tully (1992) this corresponds to a range in circular velocities of about $250\,\mathrm{km\,s^{-1}} \gtrsim V_c \gtrsim 130\,\mathrm{km\,s^{-1}}$. This is not a particularly large range over which to pick out a relationship. In Figure 16 of ZSFW the upper envelope of the velocity difference is clearly rising for $V_c < 250\,\mathrm{km\,s^{-1}}$. It is only beyond this that the

envelope flattens and begins to fall. However, at such large V_c's the ZSFW sample is sparse, making it impossible to draw any satisfactory conclusions.

In this chapter we aim to extend the work of ZSFW, using more data and attempting to understand the correlations between $\langle(\Delta v)^2\rangle$ and the luminosity of the primary. Here Δv is the difference in the recessional velocities of the primary and the satellite. Originally it had been hoped to double the size of the sample to a total of around 150. In practice this was not possible. Out of a total of 14 nights which we were allocated on the Anglo-Australian Telescope (AAT) over a period of 3 years, only $\sim$ 2.5 nights were both clear and not affected by instrument failure. This only allowed us to extend the sample by a further 10 satellites. Clearly, this will not make a significant impact on the conclusions of ZSFW. However, we repeat here some of their analysis for comparative purposes.

In addition we make a number of changes to the analysis. Firstly, we employ a different interloper criterion. Rather than rejecting satellites on the basis of their position in the r_p-$|\Delta v|$ plane, we use the V_c-$|\Delta v|$ plane, where V_c is the rotation velocity of the primary. This allows the definition of a much simpler rejection criterion, than that of ZSFW, which is motivated by the results of N-body work (J.F. Navarro, personal communication). We also use our estimates of the mass of the dark halos to find mass-to-light ratios and so place a lower limit on Ω. We present a significant detection of the Holmberg effect: an excess of satellites in the direction of the primary minor axis. This is the first confirmation of this effect since it was originally noticed by Holmberg (1969). We cast some doubt on the evidence for systemic rotation, pointing out some marginal evidence for selection effects in this part of the analysis. However, we are unable to present an explanation or correction for such an effect. We consider the relationship between $|\Delta v|$ and V_c. By using the rms values of $|\Delta v|$ we are able to demonstrate that the data is also consistent with a model in which the halo is an isothermal sphere with rotation velocity equal to that of the primary. However, we cannot rule out ZSFW's result: that there is no correlation between $|\Delta v|$ and

V_c. Finally we consider the satellites of the Milky Way. Using Monte-Carlo simulations we place these on the r_p-$|\Delta v|$ plane as if they were observed by an observer outside the Local Group. This suggests that the Milky Way satellites may be somewhat atypical of the satellite catalogue, but selection effects, H_0 dependence, model dependence and the small number of Milky Way satellites all weaken this comparison.

In §3.2 we describe the ZSFW catalogue and in §3.3 our own sample. Section 3.4 describes our observational procedure and data reduction methods, whilst we describe our detailed analysis in §3.5. Our conclusions are summarised in §3.6.

3.2 The ZSFW satellite catalogue

3.2.1 Selection of primaries

In order to ensure a homogeneous sample of primaries ZSFW adopt the following selection criteria:

(i) A narrow range in absolute magnitude, M_B;

(ii) Hubble type Sb to Sc, unbarred;

(iii) Recession velocity in the range $1000\,\mathrm{km\,s^{-1}} < v_R < 7000\,\mathrm{km\,s^{-1}}$ and;

(iv) Isolated.

ZSFW adopted the first of these criteria because the Tully-Fisher relationship (Tully & Fisher 1977) demonstrates that the absolute magnitude of a galaxy is related to its

dynamics. Thus, in order to obtain a well defined dynamical sample the sample must also be well defined in absolute magnitude. As we noted above 77% of the ZSFW sample lies in the range $-20.4 < M_B < -18.4$. The second criterion is based on the work of Rubin *et al* (1978). They showed that there is evidence that the morphology of a galaxy determines its rotation curve, at least close to the centre of the galaxy. Thus, a small range in morphological types is required to obtain a dynamically homogeneous sample. The third criterion is mainly connected with the field of view of the telescopes used by ZSFW. Recession velocities in this range allow fields with diameters of a few hundred projected kiloparsecs to be surveyed.

ZSFW's isolation criteria are rather more complicated, and for a detailed discussion we refer the reader to their paper. To summarise, two requirements are made of the galaxies around the primary:

(i) If projected within 375 h^{-1}kpc of the primary they should be at least 2.2 magnitudes (a factor of 8) fainter.

(ii) If projected within 750 h^{-1}kpc of the primary they should be at least 0.7 magnitudes (a factor of 2) fainter.

The effect of these isolation criteria can be assessed by considering the Local Group. The Local Group is dominated by the Milky Way and M31, the latter being 0.6 magnitudes fainter than the former (van den Bergh 1980). They are 0.7 Mpc apart. Thus even if we viewed the Milky Way from a direction perpendicular to the vector joining M31 and the Milky Way, ZSFW's isolation criteria would not catagorise either of these galaxies as being isolated. This is despite the dynamics of the Local Group being dominated by the

nearer of the Milky Way and M31 within 200 kpc of each galaxy. On these grounds ZSFW claim that their isolation criteria are conservative.

ZSFW apply these criteria to the Huchra catalogue (Huchra 1987), searching, both internally and in the Huchtmeier-Richter (1989) catalogue, for bright companions. The appropriate POSS or ESO/SERC photographic plates were also checked by eye for companions which were not in the redshift catalogues. ZSFW end up with almost 100 primaries which pass their selection criteria.

3.2.2 Selection of satellites

ZSFW define a satellite as a galaxy which:

(i) Lies within a projected separation, $r_p < 375\,\mathrm{h^{-1}kpc}$ of the primary;

(ii) Is at least 2.2 magnitudes fainter than the primary;

(iii) Has a velocity difference, $|\Delta v| < 500\,\mathrm{km\,s^{-1}}$ relative to the primary.

They impose no morphological restrictions on the satellites. The first of these requirements is based on the expectation that those satellites which are closest to the primary will be influenced less by galaxies external to the system. The second is simply a reiteration of the isolation criteria described above, whilst the third is a compromise between obtaining as many satellites as possible and minimising the number of interlopers in the sample. ZSFW justify this only *a posteriori* by noting that in their sample there are very few satellites in the region $300\,\mathrm{km\,s^{-1}} < |\Delta v| < 500\,\mathrm{km\,s^{-1}}$. The results are therefore reasonably robust to changes in this criterion.

3.3 Construction of our sample

3.3.1 Selection of primaries

We have adopted identical selection criteria to those of ZSFW, except that we have relaxed the magnitude range in which primaries can lie. We have adopted ZSFW's widest range of $-21.4 < M_B < -17.4$. This corresponds to a circular velocity range of $340\,\mathrm{km\,s^{-1}} \gtrsim v_c \gtrsim 100\,\mathrm{km\,s^{-1}}$. This extended range in circular velocity allows a better assessment of the correlations between $|\Delta v|$ and the luminosity of the primary to be made. We applied the selection criteria to the Huchra (1990) catalogue and then made a visual inspection of those which passed the internal tests. We thus constructed a sample of approximately 25 galaxies which we planned to observe during a 5 night run at the AAT in July 1992.

3.3.2 Selection of satellites

We again adopt the same criteria as ZSFW. The objects to be observed were selected from one of two sources: Either the APM faint galaxy survey (Maddox 1988) or from APM scans of the region. The former was preferred as in this case the class of object is more reliable. When working with APM scans, after running the standard software (Irwin, 1985) it was still necessary to make visual inspections of all potential satellites to check that they were truly a galaxy and not a mis-classified star. The objects classified as merged, which are typically binary stars, were also inspected visually to check for any galaxies. Galaxies brighter than $m_B \simeq 19$ were retained for observation. The stellar positions for use as guide stars also came from the same scans.

3.4 Observational procedure and reduction

3.4.1 Observational procedure

The observations were carried out using the AAT on the nights of 26^{th} to 30^{th} June 1992, inclusive. Fibres were placed on as many of the faint galaxies in the field as possible using AUTOFIB (Parry & Gray 1986, Parry & Sharples 1988). This is a robotic fibre positioner which places the end of an optical fibre at the position of the required image in the focal plane. It is used at the Cassegrain focus. The fibres were fed into the RGO spectrograph, and thence to a 1024 square Thomson CCD with 19μm pixels. In good weather we had planned to use the 1200V lines mm^{-1} grating. This gives 33Åmm^{-1}, and so would allow us to cover the wavelength range 4750 Å to 5400 Å. This covers the emission lines: Hβ (4861 Å); [OIII]4959 Å; [OIII]5007 Å; NI (5199 Å) and CaV (5309 Å) and the absorption lines: Hβ (4865 Å); MgI (5167 Å, 5174 Å, 5183 Å) and FeI/CaI (5268 Å). Working in this mode would have required about 8000s of integration on each field.

Sadly, the early part of the June 1992 run (like the whole of the 1990 and 1991 runs) was marred by bad weather. We therefore adopted our alternative setup which concentrates only on emission lines, in particular Hα. Since an accurate continuum level is not required to analyse emission lines this can be done in only 6000s of integration, making maximum use of our remaining time. Clearly, we miss satellites which do not show emission. However, in the ZSFW catalogue only 13 of the 69 satellites show absorption only, suggesting that we would miss at most $\sim$ 20% of the satellites by adopting this strategy. In practice we expect the fraction missed to be significantly lower than this as the ZSFW sample were not examined in the region of Hα. For this set up we used the 600R lines mm^{-1} grating which gives 66 Åmm^{-1}, covering the range 5800 Å to 7000 Å. This allowed us to use up to 5 emission lines: Hα (6563 Å); [NII]6548, 6584 Å; and [SII]6717, 6731 Å. In addition,

Na absorption at 5893Å could in principle be used. However, in practice, we could not make a satisfactory fit to the line and so this was used only to confirm the redshifts based on emission lines.

For each field 3 × 2000s exposures were obtained. After 2000s cosmic ray contamination becomes a significant problem for this CCD. Each set of three exposures was bracketed by a pair of 1s exposures of a neon arc for wavelength calibration purposes. Each of these arcs was taken with AUTOFIB in the same configuration as for the exposure so that any changes in the properties of the system due to flexure of fibres, *etc,* would be accounted for. In addition, observations of a number of B stars were also obtained to use as flat spectrum standards. These produce a relatively featureless intrinsic spectrum, onto which are superimposed the tellurian sky absorption lines. Other stars, particularly white dwarfs, were observed to use as templates to check for absorption lines in the galactic spectra. Twilight sky frames were also obtained to use for tracking the positions of each individual spectrum on the CCD and, finally, bias frames were also taken to allow bias subtraction.

3.4.2 Data reduction

Cosmic rays were removed from the bias frames and these were then coadded to produce a master bias frame. For all other frames this was scaled by the number of counts in the bias strip and subtracted. Cosmic rays were removed from all frames using the FIGARO (Shortridge, 1990) routine BCLEAN. For these purposes a pixel is considered to have been contaminated by a cosmic ray if it is more than 5σ above the value of the surrounding pixels and exceeds the average value by at least a factor of a half or 50 counts, whichever is the greater. Bad pixels are interpolated using a third order polynomial. A visual inspection indicated that using this removed the cosmic rays adequately. The twilight sky

frames were used to generate extraction polynomials. These are sixth order polynomials which describe the location of the centre of each spectrum on the CCD.

All fibres which are not used to observe galaxies are used to observe the sky. There are always at least 5 sky-fibres in each field. For each field the sky-spectra are coadded to generate a master sky-spectrum. The sky contribution to each galactic spectrum is estimated using the three most prominent sky emission lines – 5892 Å, 6300 Åand 6364 Å. To scale the sky spectrum we used a least squares estimator. Suppose that the strength of the i^{th} sky line in the master sky spectrum is given by C_i, and in the galactic spectrum this line has strength D_i. We define the quantity:

$$\Delta^2 = \sum_i (C_i - aD_i)^2. \tag{3.1}$$

We then find the value of a for which this is a minimum, noting that at this point $\frac{d\Delta^2}{da} = 0$. So, we have:

$$a = \frac{\sum_i D_i C_i}{\sum_i D_i^2}. \tag{3.2}$$

The master sky spectrum is then scaled by a factor $\frac{1}{a}$ and subtracted from the galactic spectrum. In order to remove the effects of sky absorption a template was constructed using B star spectra. Neither of these processes entirely removed the sky lines. However, they were sufficiently successful for the true emission and absorption lines to be easily identified.

Some examples of the resulting spectra are shown in Figures 3.1 and 3.2. These show the range in quality of spectra, from those where 5 emission lines (H-α, (6563 Å); [NII]6548, 6584 Å; and [SII]6717, 6731 Å) and one absorption line (Na, 5893 Å) can be seen to those in which only one emission line is present. In the latter case this is take to be H-α. This identification is based on two pieces of information. Firstly, in all of our spectra where more than one emission line is visible H-α is the strongest line. Secondly, either from our own spectra or the Huchra catalogue we already have an estimate of the redshift at

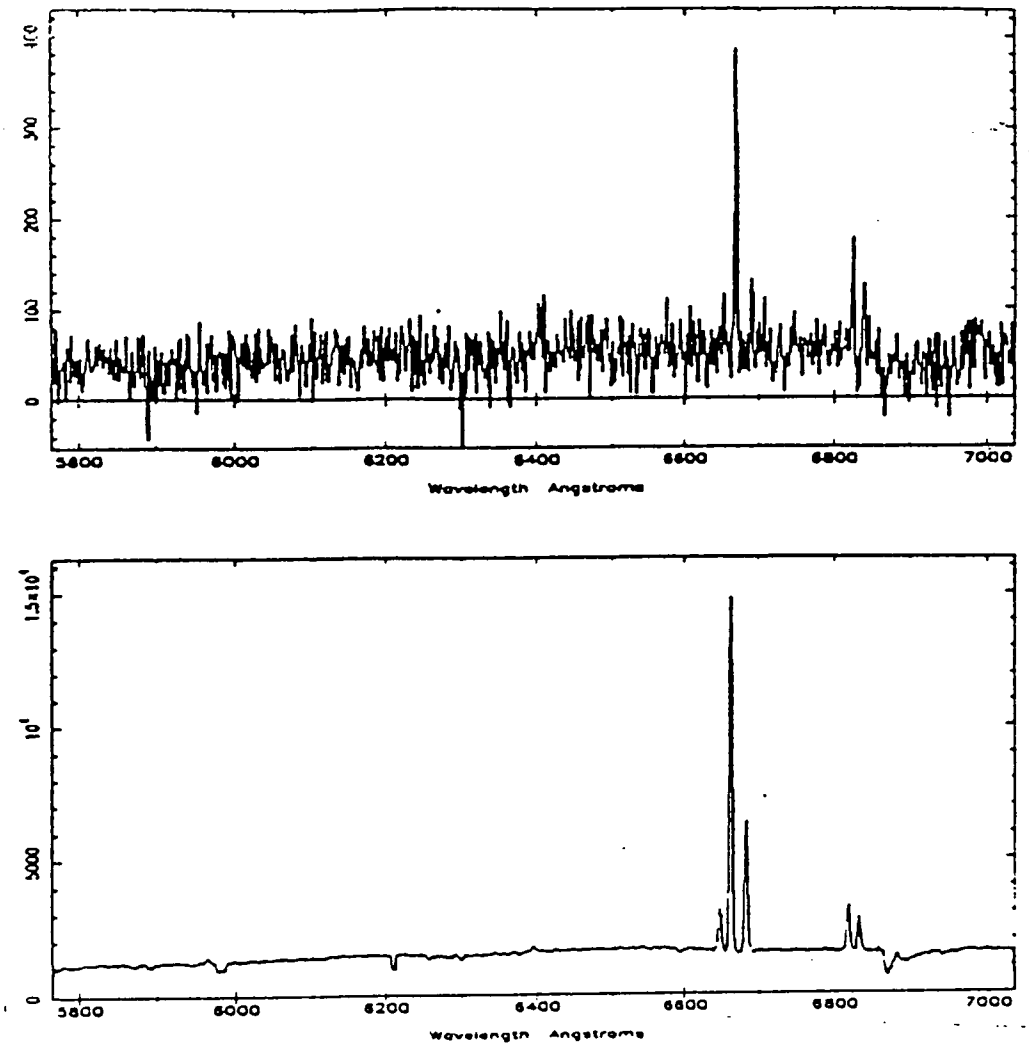

Figure 3.1. The upper panel shows the spectrum of the primary galaxy 2024-52. The H-α, (6563 Å) line is clear at 6668Å. In addition the doublet [SII]6717, 6731 Å is obvious at 6824Å and 6839Å. A more detailed analysis also confirms the presence of [NII]6584 Å at 6689Å. The residual effects of sky subtraction are also evident. This spectrum is fairly typical of those we obtained. In the lower panel is the spectrum of one of its satellites (number 6). This is the best spectrum we obtained. All the emission lines we expected to see are there, as is Na absorption. Some residual sky absorption is also apparent.

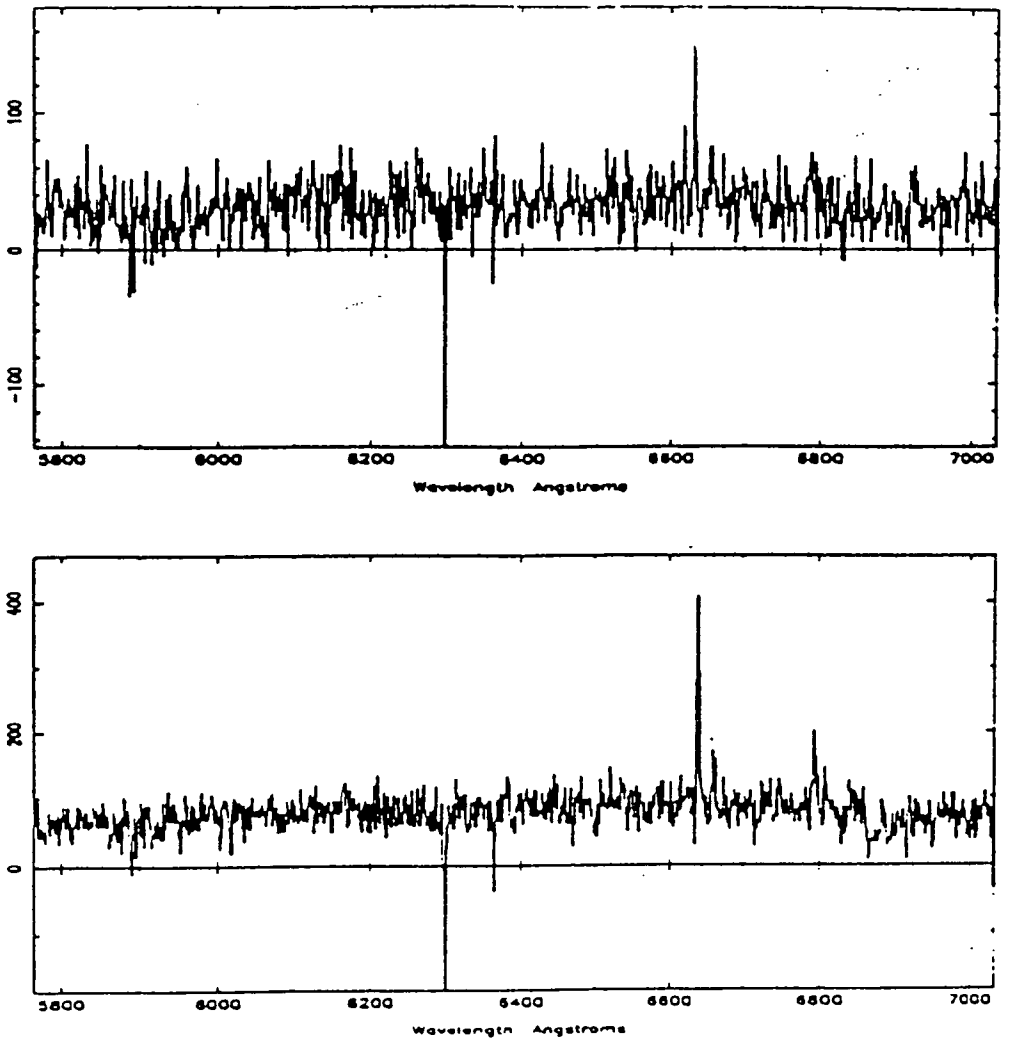

Figure 3.2. The upper panel shows the spectrum of N7329. This is one of the poorest spectra we obtained. It shows only one emission line, which we identified as H-α, at 6630Å. The result of some poor sky subtraction is also evident at around 6300Å. In the lower panel we show the spectrum of its satellite (number 1). This is fairly typical of the spectra we obtained. The H-α, (6563 Å) line, the [SII]6717, 6731 Å and [NII]6584 Å can all be found in this spectrum.

which we expect to see satellites. Hence, if a spectrum contains a single emission line, at approximately the wavelength of interest, it is taken to be H-α and a recession velocity calculated accordingly.

Our final sample consists of 10 satellites, which when combined with the catalogue of ZSFW, gives a sample of 79 in total. The details of these satellites are given in Table 3.1. In this we give the name, position, apparent magnitude, recession velocity, projected separation, morphological type (using the system described in de Vaucouleurs *et al* 1976), major axis, HI line width, inclination and position angle. The names are those of the primaries plus a number for the satellites from 1 to 10. In later sections we will distinguish these satellites from those in ZSFW sample by prefixing the numbers of satellites in the ZSFW sample with a Z. The positions are those given in the APM scans of the appropriate plates. The apparent magnitude is also based on these scans and confirmed by eye. Where more than one emission line is present, the error in the recession velocity can be estimated. This is typically around $30\,\mathrm{km\,s^{-1}}$, which is similar to ZSFW. The morphological types are found, where possible, using existing catalogues. Where this is not possible typing is done by eye. For the first three primaries, the central rotation velocities were taken from Matthewson *et al* (1992). For the other primaries, and all the satellites, the rotation velocity was estimated using the Tully-Fisher relationship:

$$M_B = -7.48(\log V_c - 2.5) - 21.2; \tag{3.3}$$

(Pierce & Tully, 1992).

It is difficult for us to assess how many of the primaries we observed have no satellites, as the observation of many of our fields was interrupted by bad weather. However, for two primaries, 1517-36 and N7184, sufficient integration was obtained to measure the redshift of the primary and no satellites were found. Neither of these objects is on the ZSFW list of primaries with no known satellites.

Name	α (1950)	δ (1950)	m_B	$v_\odot$	r_p	T	a	V_c	i	Θ
(1)	(2)	(3)	(4)	(5)	(6)	(7)	(8)	(9)	(10)	(11)
N7329	$22^h36^m54.0^s$	$-66°44'00''$	12.4	3070	–	3	4.5	235	60	–
1	$22^h35^m17.9^s$	$-66°43'04''$	17.1	3394	86	1	0.2	55	71	5
N6984	$20^h54^m19.0^s$	$-52°03'48''$	13.2	4647	–	5	1.7	154	53	–
2	$20^h54^m33.7^s$	$-51°58'47''$	15.1	4688	74	-2	0.8	128	66	80
3	$20^h53^m43.1^s$	$-52°03'20''$	15.1	4757	75	1	0.6	129	66	5
4	$20^h52^m57.5^s$	$-52°07'43''$	18.4	4715	177	1	0.2	46	76	30
2024-52	$20^h24^m02.0^s$	$-52°33'00''$	14.5	4798	–	3	2.0	162	63	–
5	$20^h24^m31.9^s$	$-52°50'39''$	17.0	4567	254	6	0.7	70	78	15
6	$20^h24^m38.9^s$	$-52°35'31''$	16.5	4527	86	-2	0.4	81	0	45
I4852	$19^h22^m00.0^s$	$-60°28'00''$	13.4	4358	–	5	1.6	205	69	–
7	$19^h23^m07.6^s$	$-60°35'34''$	17.4	4080	143	-2	0.2	57	60	90
8	$19^h20^m25.6^s$	$-60°29'52''$	18.4	4429	211	-1	0.1	45	0	5
9	$19^h20^m44.8^s$	$-60°43'28''$	19.4	4066	229	-2	0.1	31	60	10
N3976	$11^h53^m25.6^s$	$+07°04'37''$	12.3	2690	–	3	3.6	209	72	–
10	$11^h53^m17.8^s$	$+07°00'37''$	18.8	2301	35	3	0.6	25	80	0

Table 3.1 The parameters for the satellites and primaries in our sample. Column (1) gives the name, column(2) the RA, column (3) the declination, column (4) the apparent total blue magnitude, column (5) the heliocentric recession velocity in $\mathrm{km\,s^{-1}}$, column (6) the projected satellite-primary separation in $\mathrm{h^{-1}kpc}$, column (7) the morphological type, column (8) the size of the semi-major axis in arc-minutes, column (9) the central rotation velocity, column (10) the inclination and column(11) the satellite position angle relative to the primary major axis. Details of the other satellites can be found in ZSFW.

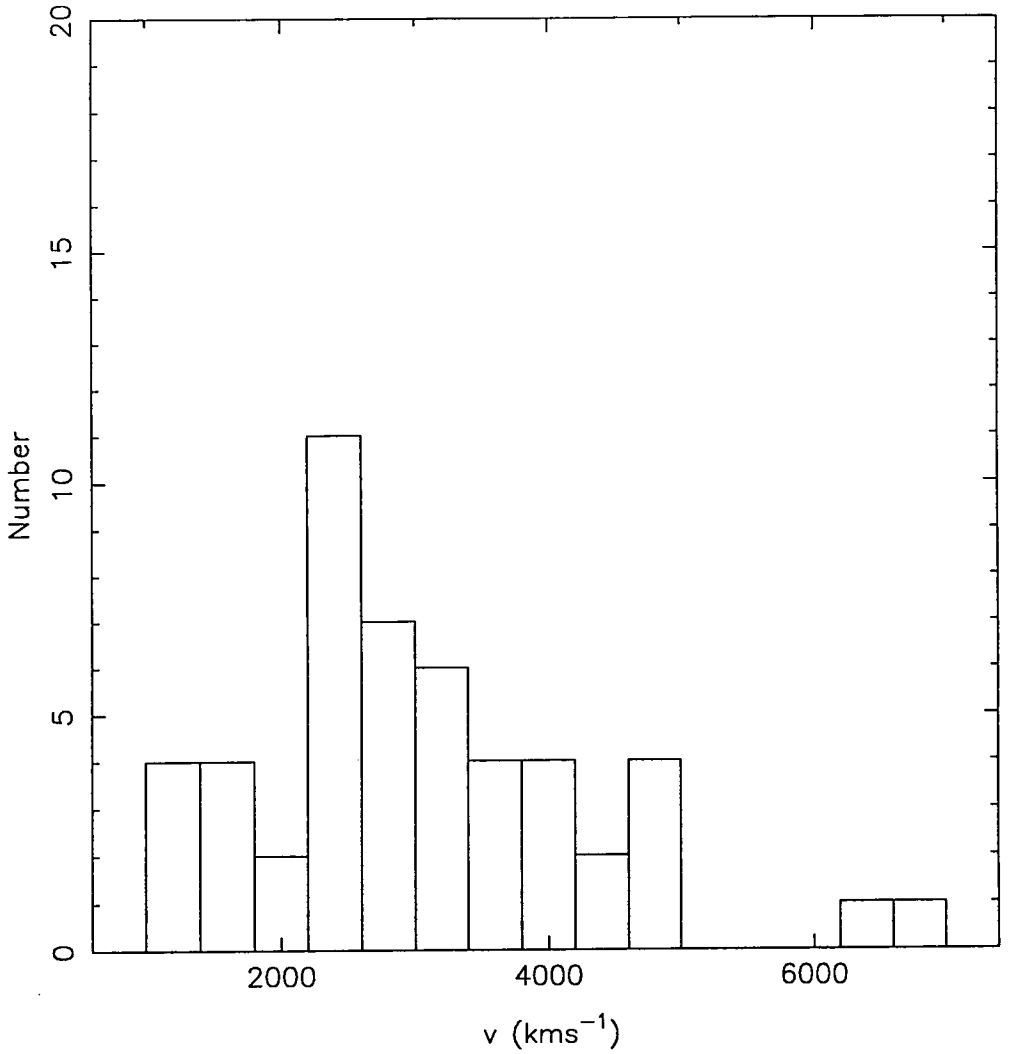

Figure 3.3. The distribution of heliocentric recession velocities of primaries around which satellites have been detected.

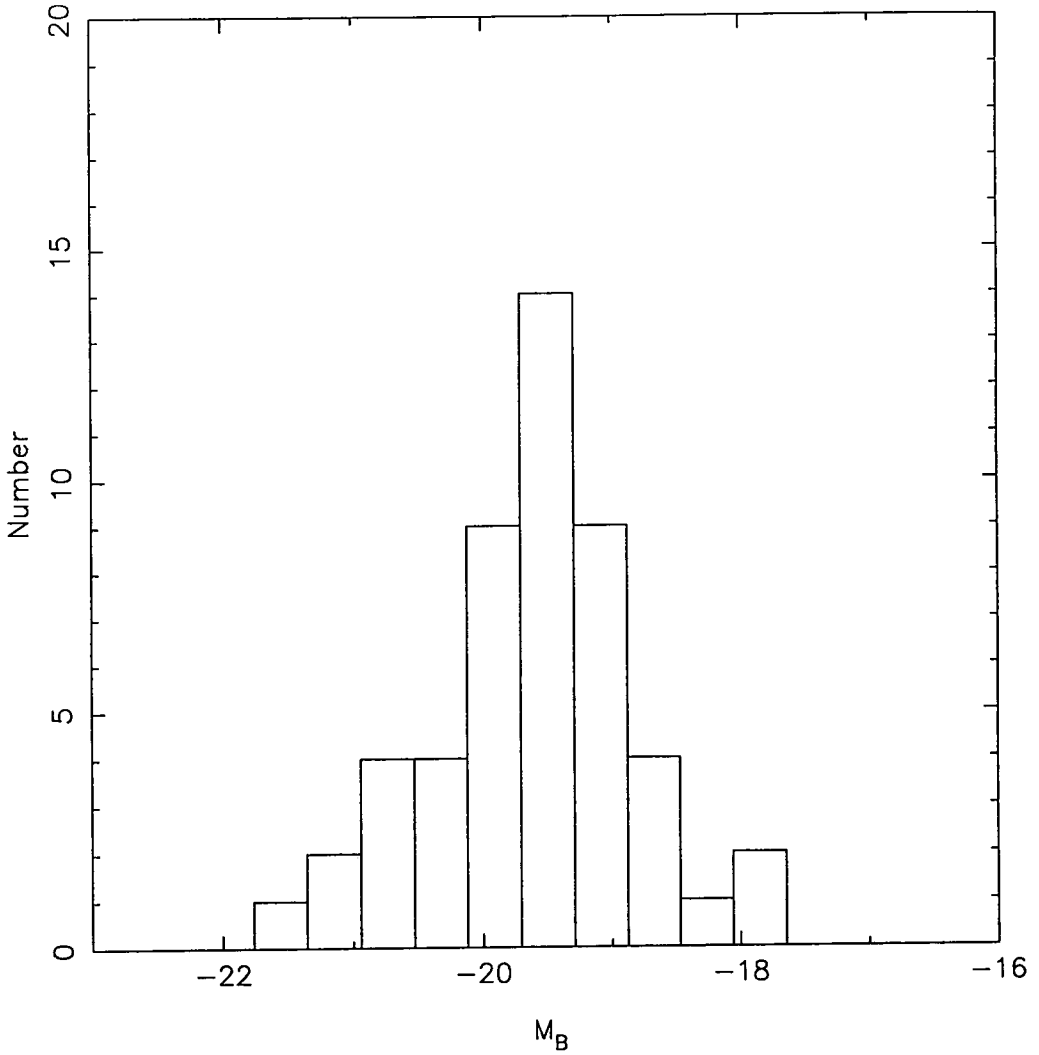

Figure 3.4. The distribution of absolute magnitudes of primaries around which satellites have been detected.

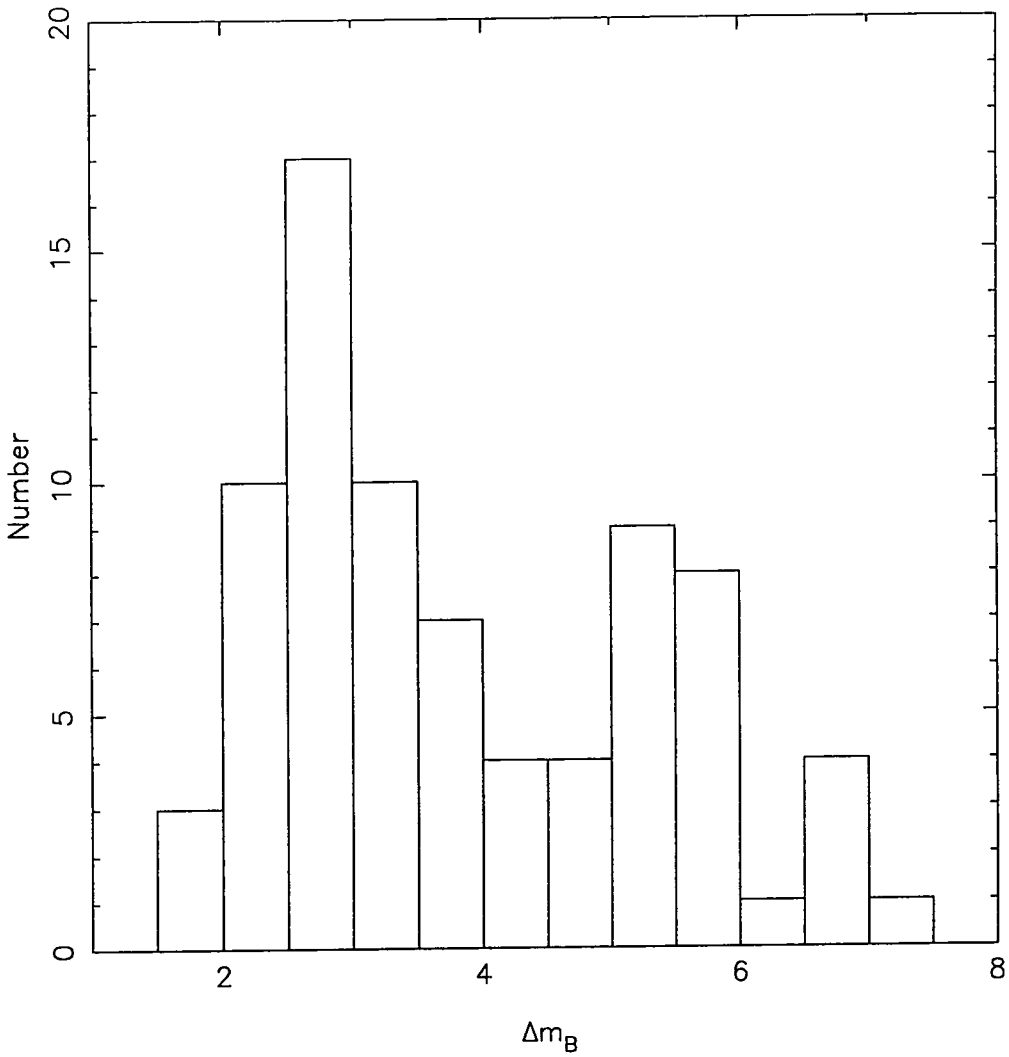

Figure 3.5. The distribution of magnitude differences between primaries and their satellites.

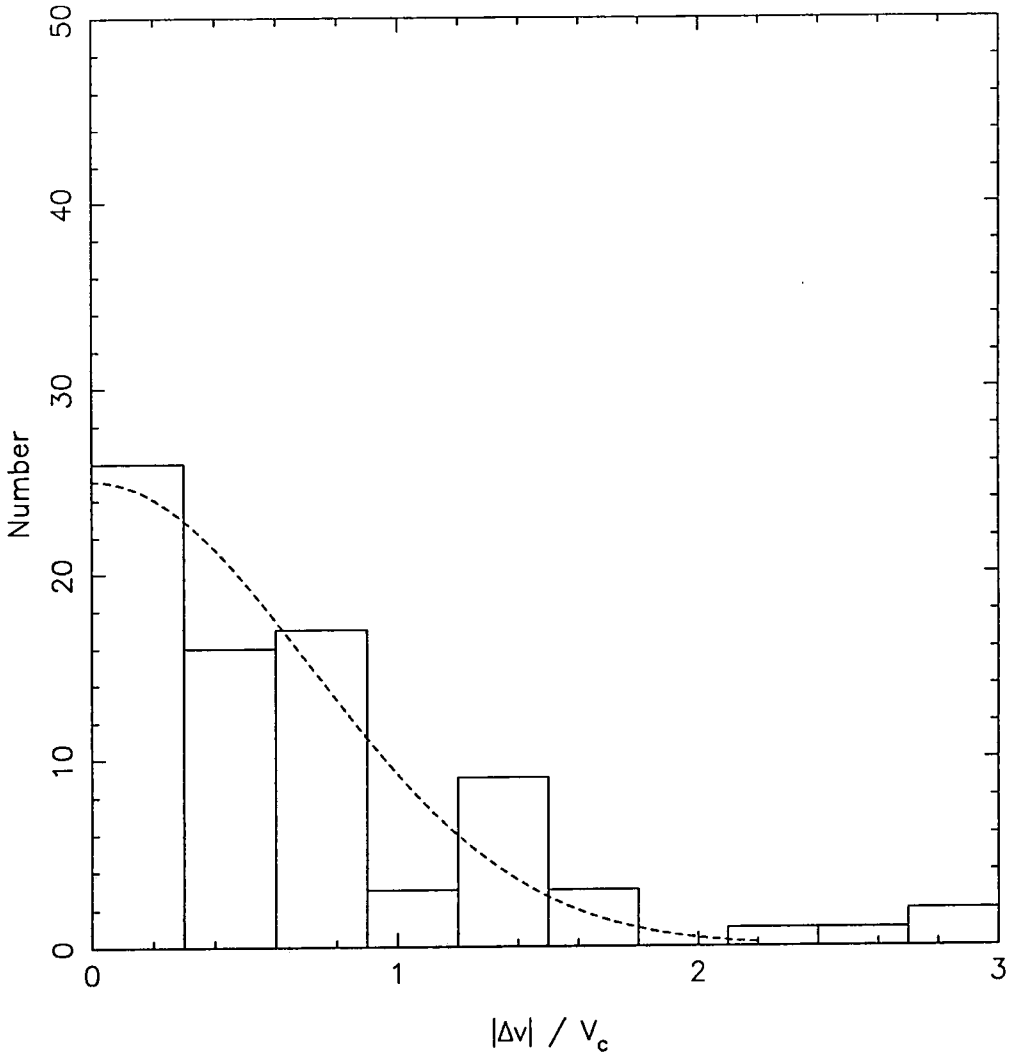

Figure 3.6. The distribution of recession velocity differences between primaries and their satellites relative to the circular velocity of the primary. The dashed line shows a gaussian distribution with $\sigma = 1/\sqrt{2}$. This is the value expected for satellites in an isothermal halo with isotropic orbits.

The properties of the combined sample of 79 satellites and their primaries is summarised in Figures 3.3 to 3.5. Figure 3.3 shows the recession velocities of all those primaries around which satellites have been detected. This peaks at around 2200 $\mathrm{km\,s^{-1}}$, with a long tail to higher velocities. The two primaries at above 6000 $\mathrm{km\,s^{-1}}$are part of the ZSFW sample which were observed at the William Herschel Telescope (WHT), where the AUTOFIB field of view is smaller, forcing them to use more distant primaries. Figure 3.4 shows the absolute magnitude distribution of primaries. The selection criteria discussed above are clearly evident here, with most primaries lying in the range $-20 \leq M_B \leq -19$. In Figure 3.5 we show the distribution of magnitude differences between the satellites and primaries. Despite the initial criterion being that all satellites be 2.2 magnitudes fainter than the primary, subsequent analysis has demonstrated that a small number in the sample have a magnitude difference which is smaller than this, the smallest difference being 1.8 magnitudes. These are from both our own sample and that of ZSFW. However, their number is small and, as ZSFW discuss, the selection criteria are conservative. We will therefore continue to use these satellites in our subsequent analysis. Figure 3.6 shows the distribution of $|\Delta v|/V_c$. Superimposed on this is a half gaussian with $\sigma = 1/\sqrt{2}$, as would be expected for satellites moving in an isothermal halo with isotropic orbits. This describes the distribution of the velocity differences well.

3.5 Analysis of data

3.5.1 Interlopers

The selection criteria require a satellite to have a projected separation $r_p < 375\,\mathrm{h^{-1}kpc}$ and a velocity difference $|\Delta v| < 500\,\mathrm{km\,s^{-1}}$. However, it is inevitable that a few chance

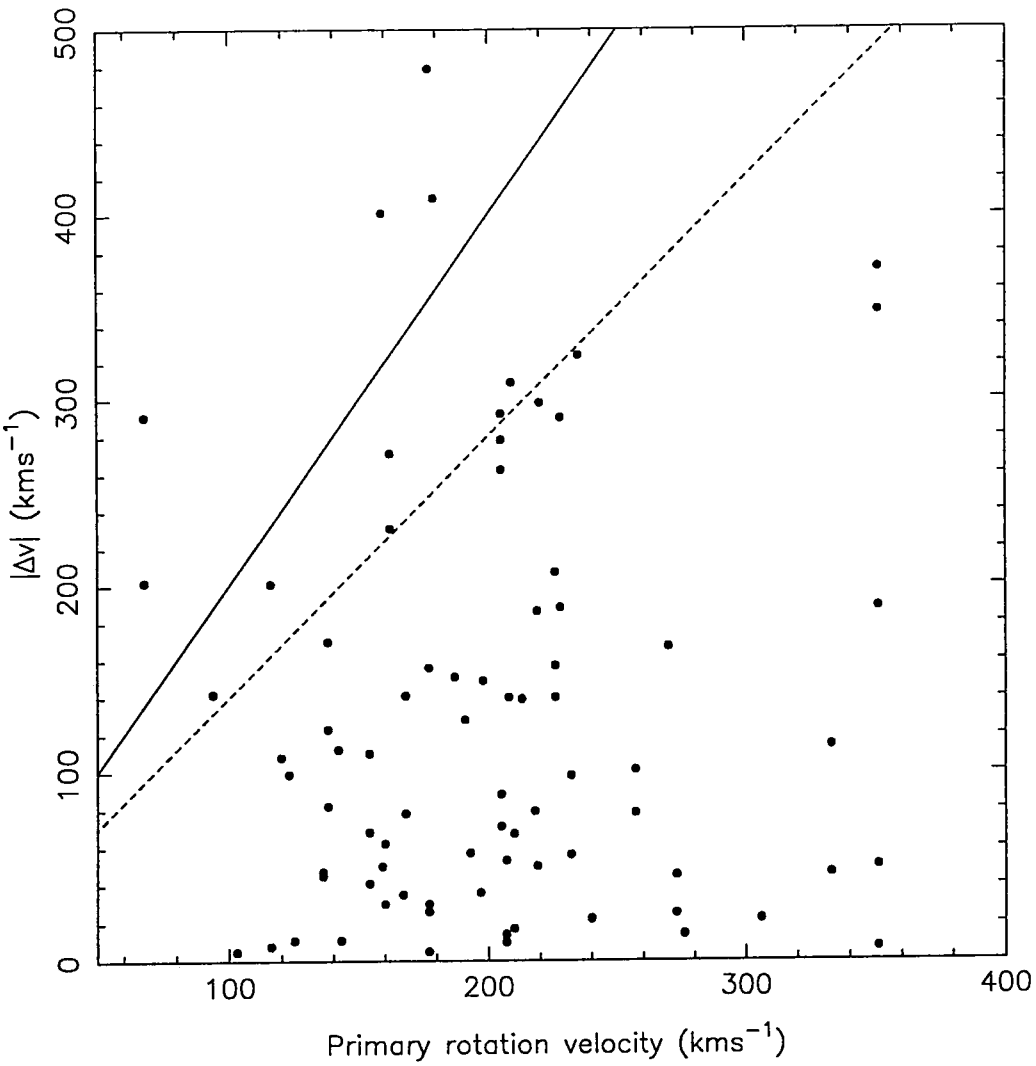

Figure 3.7. Plot of $|\Delta v|$ versus V_c showing the envelopes used to define interlopers: $s = 2.0$ (solid line) and $s = 1.4$ (dashed line).

projections will sneak into the catalogue. By considering the effective volume surveyed around each primary ZSFW estimate that at most 12% of their catalogue (8 satellites) could be interlopers. They suggest that the probable number of interlopers is about half this: 3 or 4. They then exclude Z13, Z14, Z30, Z54 and Z68 on the basis of their position in the $r_p - |\Delta v|$ plane. In our slightly enlarged sample we expect to have about 5 interlopers. We choose to select interlopers on the basis of their position in the $V_c - |\Delta v|$ plane. We believe this is a better method for interloper rejection for two reasons: firstly, it is much simpler than the ZSFW prescription; secondly, it is supported by N-body simulations, in particular those of J.F.Navarro (personal communication). These showed that in this plane the satellites had a well defined upper envelope. We therefore define an envelope:

$$|\Delta v| = sV_c. \tag{3.4}$$

We now adjust s to obtain a set of interlopers of the size expected. For $2.2 \geq s \geq 1.8$ five satellites lie above this line – Z16, Z17, Z30, Z54 and Z68. This agrees well by the N-body simulations, in which $s = 2$. These form our set of most likely interlopers. The latter 3 of these are also in the ZSFW set of most likely interlopers and Z17 is in their set of next most likely interlopers. If $s = 1.4$ we define a set of 11 interlopers, the additional ones being Z42, Z64, 5, 6, 9 and 10. These are our next most likely interlopers. None of these are considered as possible interlopers by ZSFW. So, the minimum set of interlopers is reasonably well defined, both by our technique and that of ZSFW. However, there are still some worrying discrepancies. In principal it would be better to combine both our approach and that of ZSFW and use a surface defined by $\Delta v = \Delta v(r_p, V_c)$. However, the form of such a surface is not clear at present. Those in our set of most likely interlopers will be excluded from the following analysis. The position of these lines on the $V_c - |\Delta v|$ is shown in Figure 3.7. The upper line ($s = 2$) correlates well with an apparent upper envelope in the data.

Zaritsky (1992) discusses the excess in the numbers of satellites with recession velocities greater than that of the primary. This effect, which is also seen in many other samples, can be explained by considering the expected incidence of interlopers. In the extended sample 58% of the satellites have recession velocities greater than that of their primaries ($P/T = 0.58$ in the notation of ZSFW). This is approximately the same size as the effect found in the ZSFW sample alone. Note, however, that this is not, in itself, significant. A binomial distribution in which the underlying distribution has $P/T = 0.5$ would produce a $P/T > 0.58$ approximately 10% of the time.

3.5.2 The $\Delta v - r_p$ plane

The most important analysis of our data is a consideration of the $\Delta v - r_p$ and $|\Delta v| - r_p$ planes. These are shown in Figures 3.8 and 3.9. Both of these are scatter plots with no apparent correlation. The planes are best sampled for $r_p \lesssim 200\,\mathrm{h^{-1}kpc}$. Beyond this separation the fibre sample becomes sparse and we are left with only the literature sample. By definition $|\Delta v| < 500\,\mathrm{km\,s^{-1}}$.

The characteristic velocity difference between the primary and the satellite at a fixed separation is an important quantity as it can be used to estimate the mass of the dark halo in which the primary is embedded. Straightforward energy considerations show that, in order that a satellite be bound, the minimum mass which is within r_p is given by $M_{\mathrm{min}} = (\Delta v)^2 r_p / 2G$. Numerical experiments suggest that the true mass is typically 20-30 times this estimate (White 1981). A more realistic estimate can be found by assuming that the halo is isothermal and the orbits are isotropic. In this case the mass can be estimated using $M = 2f^2 r_p (|\Delta v|_{\mathrm{median}})^2 / G$ where $f = 1.48$ is the ratio of the rms value to the median value of a half-gaussian.

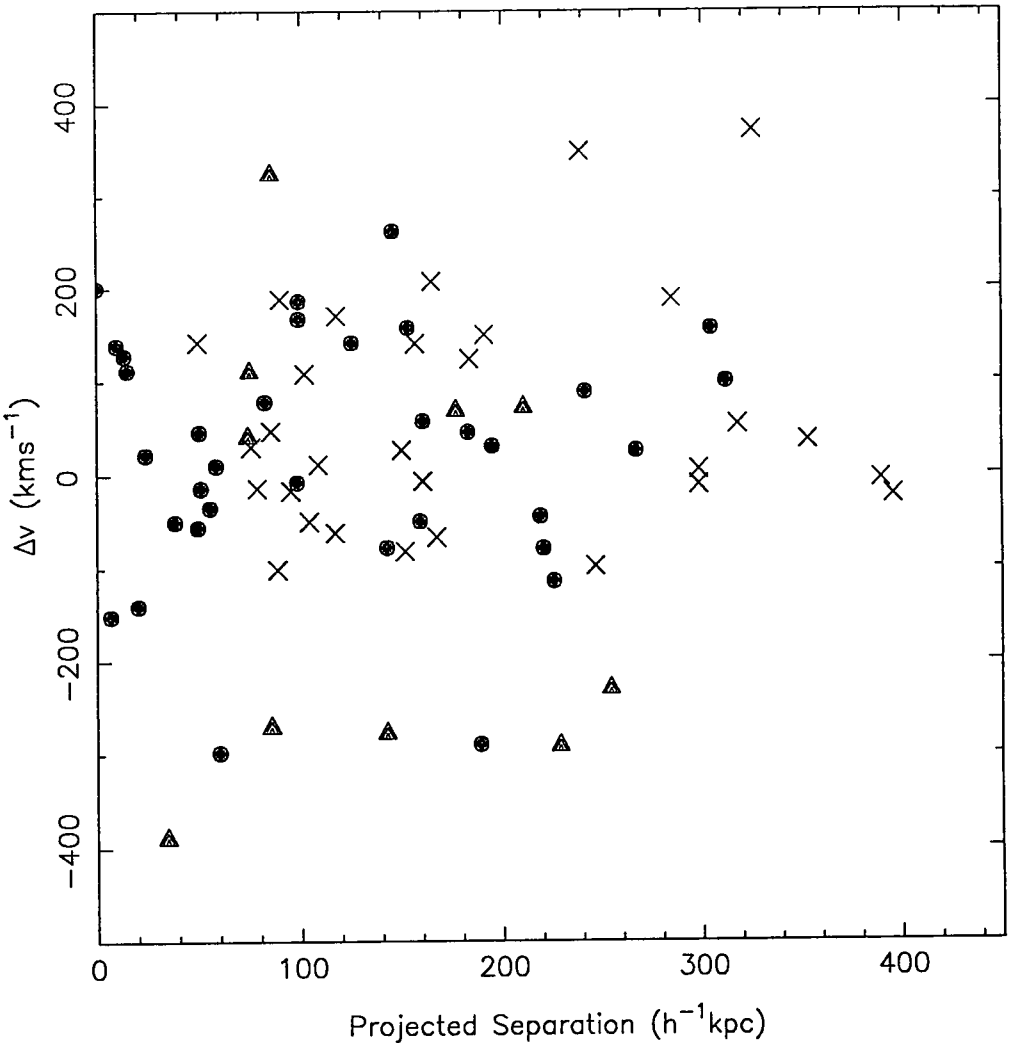

Figure 3.8. Scatter plot of the difference in the recession velocities of satellites and their primaries against the projected separation. Solid circles and crosses are the fibre and literature samples respectively of ZSFW. The solid triangles represent our additional sample.

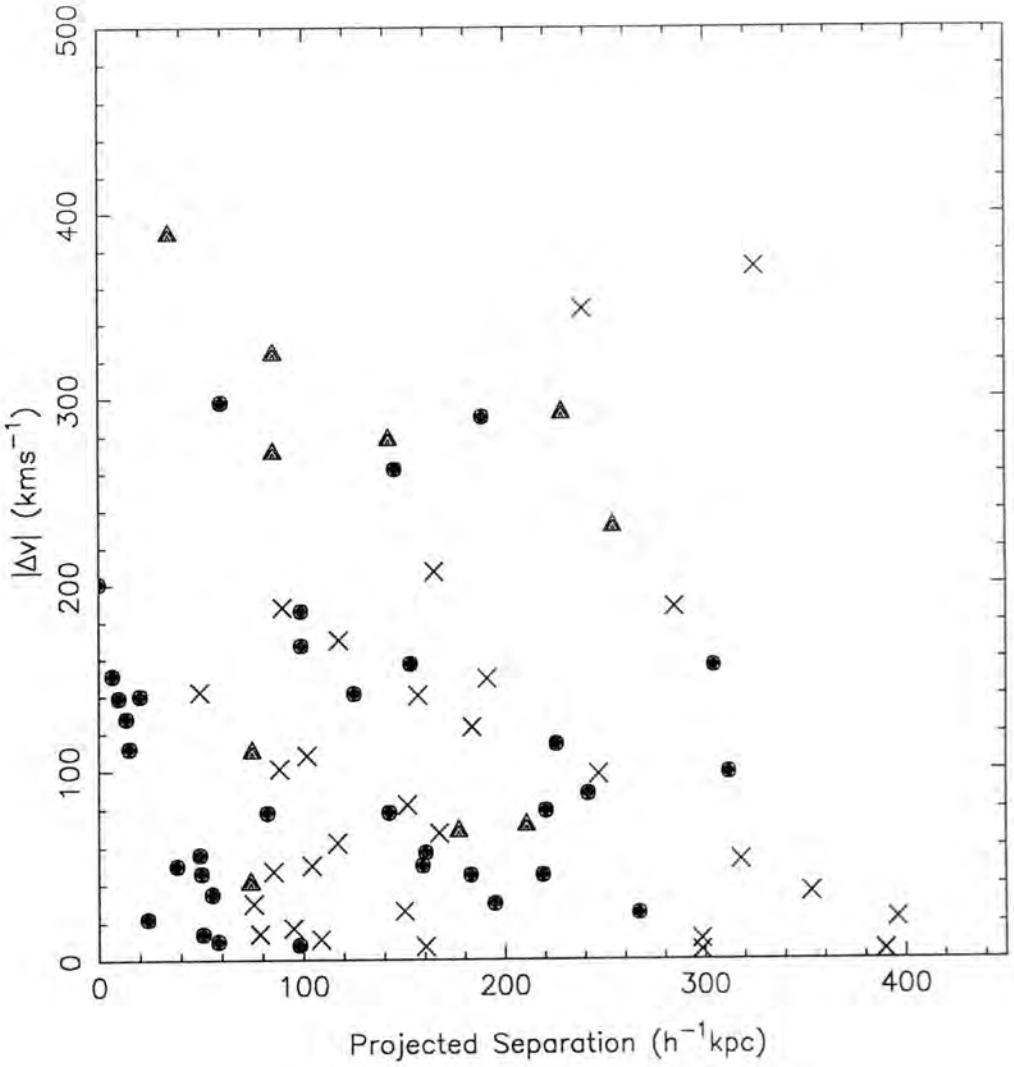

Figure 3.9. Scatter plot of the absolute difference in the recession velocities of satellites and their primaries against the projected separation. Solid circles and crosses are ZSFW's fibre and literature samples respectively. The solid triangles represent our additional sample.

r_p	Number of	$\|\Delta v\|$ (km s^{-1})			$M(h^{-1} \times 10^{11} M_\odot)$			
(h^{-1}kpc)	Satellites	Median	15.9 %	84.2 %	Min	Median	15.9 %	84.2 %
50	11	139	112	142	0.61	8.2	5.4	8.6
100	30	106	56	128	0.31	9.5	2.7	14.0
125	35	101	56	112	0.38	10.9	3.4	13.4
150	40	105	70	125	0.72	14.0	6.3	19.9

Table 3.2 Table showing the typical velocities and mass estimates within various projected radii of the primaries. The columns headed 15.9% and 84.2% indicate the appropriate percentile.

The median velocities and mass estimates are given in Table 3.2. Estimating the errors on these quantities is difficult as they are not normally distributed. The percentiles given in Table 3.2 are found using a bootstrap resampling technique. This method of error estimation involves resampling the data, with replacement, to construct many sets of data of the same size. For each resampled set of data the median $|\Delta v|$ is calculated and so the frequency distribution of the median can be obtained. The percentiles given correspond approximately to $\pm 1\sigma$ errors. There is an apparent anomaly in the error estimates as the $\pm 1\sigma$ range appears to be smaller for the innermost bin, where there are fewest satellites. We believe that this is due to the small number of satellites making the error estimate unreliable. There is no significant change in the median $|\Delta v|$ with projected separation. The minimum mass given in Table 3.2 is based on the 15.9 percentile velocity. These provide a very strong constraint that the mass is $\gtrsim 10^{11} M_{\odot}$. A better estimate of the mass within $150\mathrm{h}^{-1}\mathrm{kpc}$ is $1.4 \times 10^{12} M_{\odot}$ ($1.6 \times 10^{12} M_{\odot}$ if interlopers are included). This estimate is in agreement with recent estimates of the mass of the Milky Way (Zaritsky *et al* 1989; Zaritsky 1991). For our analysis to give a mass as low as that estimated for the Milky Way by Little & Tremaine (1980) we would have to observe a median velocity of only $44\mathrm{km\,s^{-1}}$ within $150\mathrm{h}^{-1}\mathrm{kpc}$. In our bootstrap resampling a velocity as low as this was obtained only 0.1% time. We can thus reject a mass estimate as low as the Little & Tremaine estimate at approximately the 5σ level. Within $150\mathrm{h}^{-1}\mathrm{kpc}$ the rms $|\Delta v|$ is $150\mathrm{km\,s^{-1}}$ ($168\mathrm{km\,s^{-1}}$ if interlopers are included). If the satellite orbits are isotropic this implies a circular velocity of $210\mathrm{km\,s^{-1}}$ (or $240\mathrm{km\,s^{-1}}$). This is similar to the median circular velocity in the optical parts of the primaries, $201.5\mathrm{km\,s^{-1}}$.

We can also use these mass estimates to estimate Ω. The median luminosity of the primaries, weighted by the number of satellites within $150\mathrm{h}^{-1}\mathrm{kpc}$, is $(1.4^{+0.1}_{-0.2}) \times 10^{10}\mathrm{h}^{-2} L_{\odot}$. The errors are again estimated using bootstrap resampling techniques. Using our mass estimate of $1.4\mathrm{h}^{-1} \times 10^{12} M_{\odot}$ within $150\mathrm{h}^{-1}\mathrm{kpc}$, this implies a mass to light ratio of $M/L =$

$100^{+38}_{-49}\mathrm{h}(M_\odot/L_\odot)$. Efstathiou *et al* (1988a) estimate that for closure density ($\Omega = 1$) a mass to light ratio of $M/L = 1500^{+700}_{-400}\mathrm{h}(M_\odot/L_\odot)$ is required. Thus we estimate $\Omega = 0.067^{+0.034}_{-0.037}$. The error estimates here include some contribution from the errors in estimating the critical mass-to-light ratio. As the errors in this are asymmetric, we have assumed that the errors can be modelled by two half gaussians, with $\sigma = 700\mathrm{h}(M_\odot/L_\odot)$ for values greater than the mean and $\sigma = 400\mathrm{h}(M_\odot/L_\odot)$ for values lower than this. However, to make this estimate we have assumed that all the mass in the Universe is within $150\mathrm{h}^{-1}$kpc of bright galaxies. This is clearly not the case, and so our estimates of M/L and Ω are lower limits. We thus conclude that $\Omega \gtrsim 0.07$. We can also calculate a 95% lower limit of $\Omega > 0.02$. This is, in fact, a much stronger limit than 95% as one should also include the probability that all the mass in the Universe is within $150\mathrm{h}^{-1}$kpc of bright galaxies. This result also requires that we assume the Efsthiou *et al* (1988a) luminosity function. However, it is not significantly changed by using the Loveday *et al* (1992a) result. It is interesting to compare this with the density in baryons expected from big bang nucleosynthesis. The best current estimate of this is $\Omega_b = (0.013 \pm 0.003)\mathrm{h}^{-2}$ (Walker *et al* 1991). So, if $H_0 = 100\,\mathrm{km\,s^{-1}\,Mpc^{-1}}$ the dark matter is probably non-baryonic. However, if $H_0 = 50\,\mathrm{km\,s^{-1}\,Mpc^{-1}}$ the result is more marginal. This clearly demonstrates the potential of this kind of technique if it is combined with a larger sample of satellites.

3.5.3 The number of satellites per primary

Holmberg (1969) investigated the possibility that the number of satellites around a primary is correlated with the luminosity of the primary. He found no such effect, but he probed only small separations and had no velocity data, leaving large uncertainties in his analysis. The selection criteria in our survey might lead one to expect such an effect here. A satellite galaxy must be at least 2.2 magnitudes fainter than its primary. Thus, a brighter primary can sample more of the luminosity function and so may have more satellites.

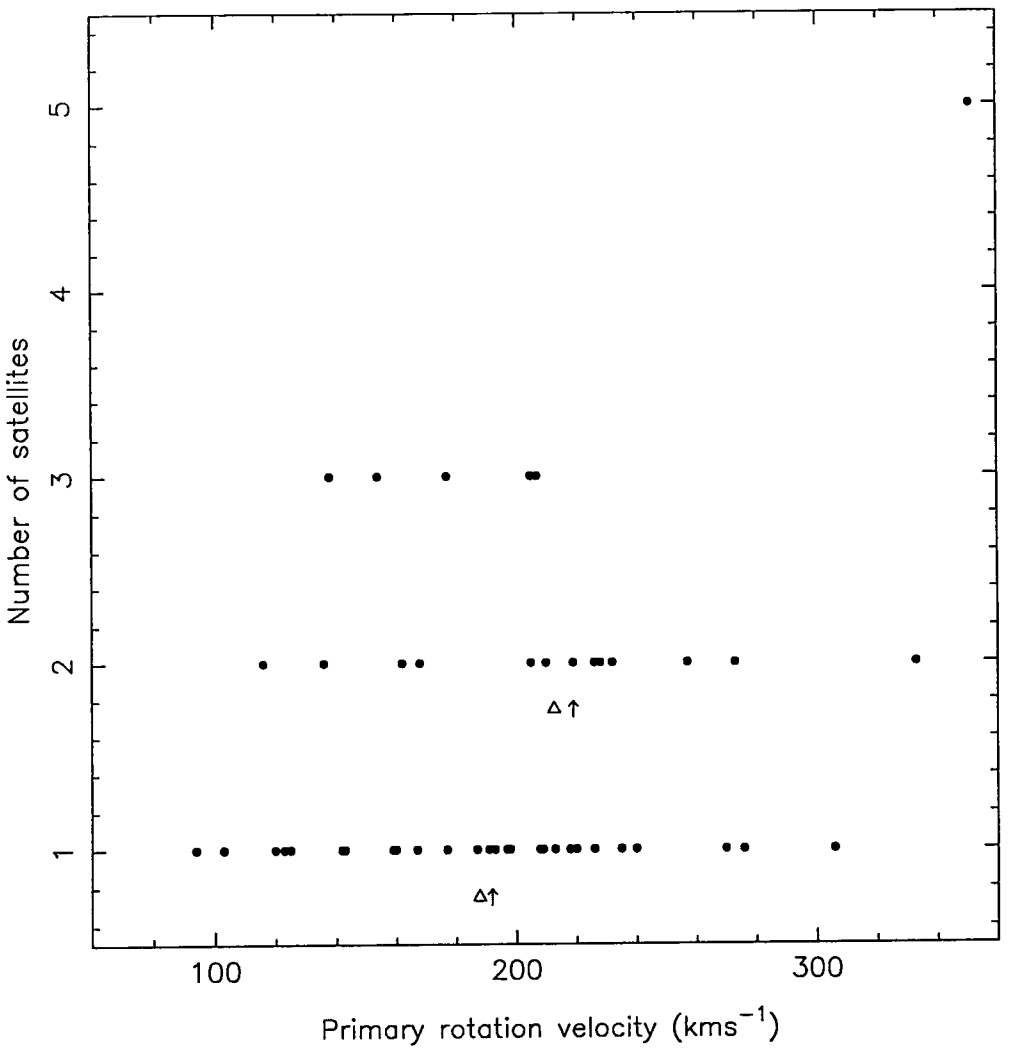

Figure 3.10. The number of satellites around each primary as a function of the primary rotation velocity. For those satellites with 1 or 2 satellites the mean (open triangle) and median (arrow) rotation velocities are also shown.

The number of satellites is plotted against primary rotation velocity in Figure 3.10. The primary rotation velocity is drawn from surveys (*eg*, Matthewson *et al* 1992) where possible. Otherwise it is found using the Tully-Fisher relationship of Pierce & Tully (1992). Also shown is the mean (open triangle) and median (arrow) rotation velocities for primaries with one or two satellites. There is apparently a shift. However, a KS test on the distribution of rotation velocities of primaries with one satellite against that of those with two satellites indicates that there is only a 77% probability that they are different. There is thus no significant effect. We have also split the sample at the median primary rotation velocity (201.5km s^{-1}). A KS test on the two resulting distributions of numbers of satellites indicates that there is only a 1% probability that they are drawn from the same distribution. Thus, there is a significant trend in this sample for the number of satellites to increase as the primary rotation velocity increases. However, whether this is due to the selection effect discussed above or is a genuine physical effect cannot be established from these data.

3.5.4 The radial and azimuthal distribution of satellites

In the upper panel of Figure 3.11 we show the distribution of projected separations found in the extended catalogue. In the lower panel this has been converted into the total projected surface density, *ie*, without taking into account the total number of primaries surveyed. In Chapter 2 we demonstrated that for an isolated late type primary the projected surface density of satellites is given by $\widetilde{\Sigma}_s = 0.74 h^2\,\mathrm{Mpc}^{-2}(r/1\,h^{-1}\mathrm{Mpc})^{-0.6}$. To compare this with the present data we must first estimate the total number of primaries surveyed, *including those with no satellites.* By comparing the number of primaries in the Huchra (1987) catalogue with no satellites with the number with one satellite ZSFW estimate they have surveyed a total of 156 primaries. We found a further 5 primaries with satellites and observed 2 more sufficiently deeply to obtain their redshifts, but found no satellites. We

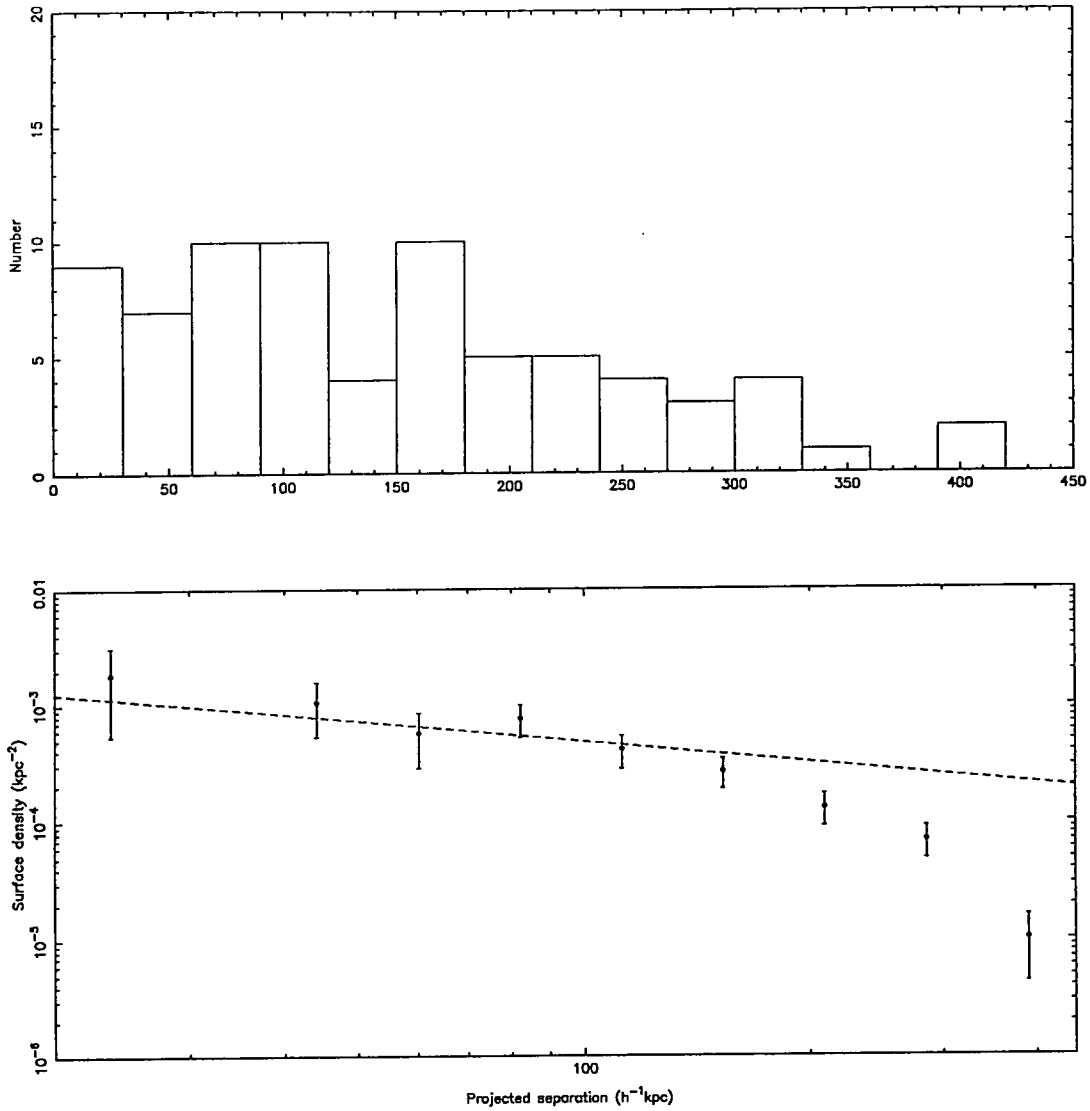

Figure 3.11. The upper panel shows the distribution of projected separations in the extended sample. In the lower panel this is shown as the total surface density as a function of projected separation. The dashed line shows the expected form of this based on the results for isolated late type primaries given in Chapter 2.

have therefore surveyed a further 7 primaries, making the extended catalogue a survey of 163 primaries. Taking this into account we expect the total surface density profile found in this survey to be given by

$$\Sigma_{obs} = 7.6 \times 10^{-3} \mathrm{h}^2\,\mathrm{kpc}^{-2} \left(\frac{r}{1\,\mathrm{h}^{-1}\mathrm{kpc}} \right)^{-0.6} . \tag{3.5}$$

This is shown as a dashed line in the lower panel of Figure 3.11. The agreement between this and the velocity survey data with $r_p \lesssim 100\,\mathrm{h}^{-1}\mathrm{kpc}$ is excellent. At larger separations the survey data trails away. ZSFW suggest this effect may be due to incomplete sampling in their fibre sample. This clearly must have some effect and is supported by the comparison in Figure 3.11. However, it is interesting to note that in the N-body simulations of J.F.Navarro (personal communication) a similar decline is seen.

We also searched for the Holmberg effect in our data: an excess of satellites in the direction of the primary minor axis. ZSFW were unable to find any significant evidence for this effect. In the same way as ZSFW, we measured the position angles of the satellites relative to the major axes of the primaries on the SERC J plates. In Figure 3.12 we show a scatter plot of the position angle of satellites as a function of their projected separation. We use only those primaries which have an inclination, $i > 45^o$ so that the minor and major axes are well defined. The solid points correspond to primaries with $50^o < i \leq 90^o$ and the open points to primaries with $45^o < i \leq 50^o$. There is an apparent deficiency of points in the region with $\Theta < 20^o$ and $r_p < 50\,\mathrm{h}^{-1}\mathrm{kpc}$. To test this we split the sample in two – those with $r_p \leq 50\,\mathrm{h}^{-1}\mathrm{kpc}$ and those with $r_p > 50\,\mathrm{h}^{-1}\mathrm{kpc}$. A KS test comparing the two distributions of position angles showed that there is only a 3% chance that they are drawn from the same distribution. This then corresponds to a 3 to 4σ detection of a difference in the populations. A KS test is also able to rule out an underlying uniform distribution within $50\mathrm{h}^{-1}\mathrm{kpc}$ at the 95% level. Beyond this separation, a uniform distribution cannot be ruled out. There also appears to be a deficiency of satellites with

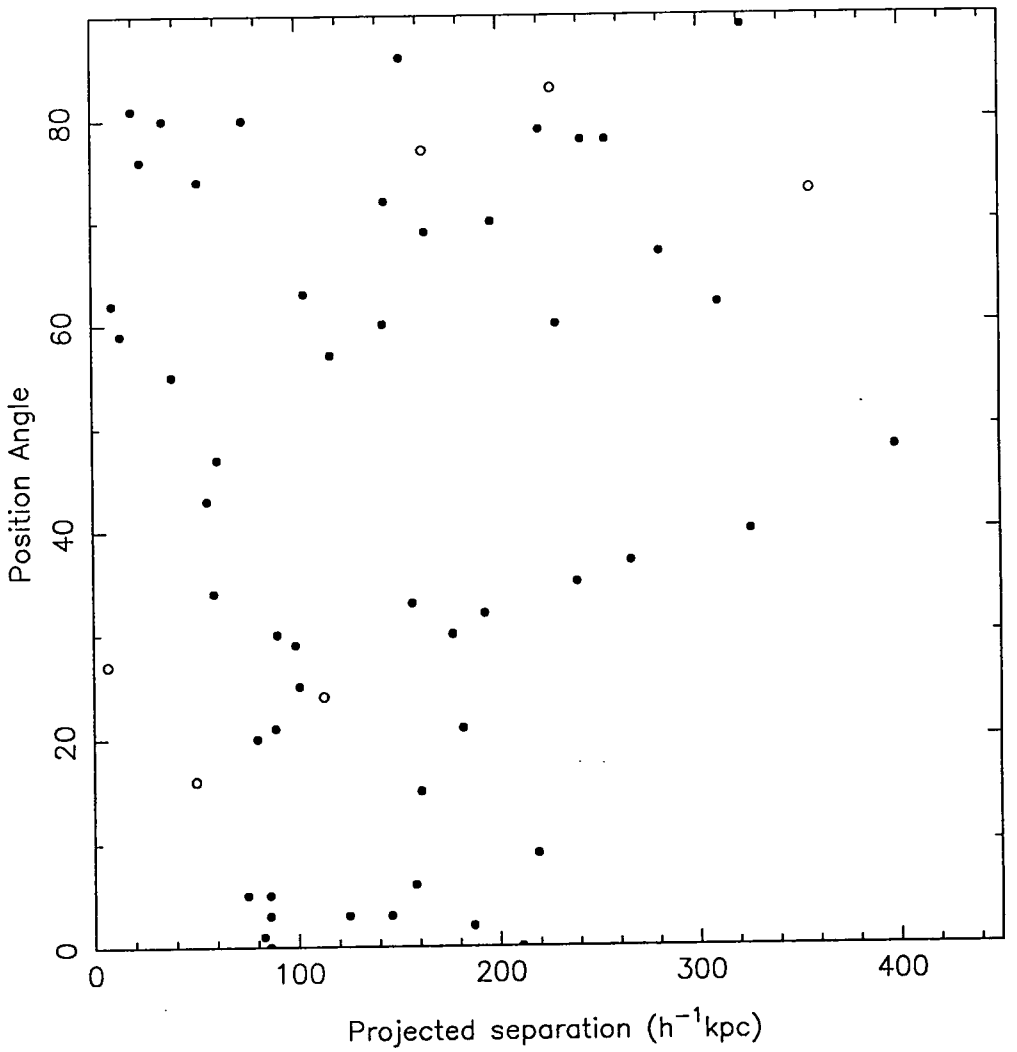

Figure 3.12. The position angle of the satellites as a function of projected separation. The solid points shows those satellites whose primaries have an inclination $50^o < i \leq 90^o$. The open circles shows those satellites whose primaries have inclination $45^o < i \leq 50^o$.

$\Theta < 30^o$ and $r_p > 250\,h^{-1}$kpc. However, a KS test shows that there is a 19% chance that the points with $r_p > 250\,h^{-1}$kpc were drawn from a uniform distribution. We thus conclude that the Holmberg effect is apparent at about the 3σ level for galaxies with $r_p < 50\,h^{-1}$kpc, but there is no detectable effect for satellites beyond this.

3.5.5 Internal properties of the satellites

Einasto *et al*(1974) claimed that as projected separation increased satellites tended to be of a later type. ZSFW also examined this, but found no effect. In the upper panel of Figure 3.13 we plot the morphological type of the satellites as a function of their projected separation. In the lower panel we have plotted the mean projected separation for those morphological types where there are at least 3 satellites There are no obvious trends. If we divide the satellites into late types ($T > 0$) and early types ($T < 0$) we can compare the distributions of projected separations. A KS test does not rule out the hypothesis that the two distributions are drawn from the same underlying distribution. The mean projected separations are $159\,h^{-1}$kpc and $131\,h^{-1}$kpc for late type satellites and early type satellites respectively. A student t-test shows that the means of the two distributions are consistent with one another. Thus we conclude that there is no evidence of any correlation between morphological type and projected separation.

In Figure 3.14 we show the distribution of satellite absolute magnitudes. The luminosity function of the satellites is uncertain for a number of reasons. Firstly, since many of the magnitudes have been estimated by eye, the magnitudes are not particularly accurate. Secondly, the completeness is difficult to estimate; the magnitude limit varies for different parts of the sample and from primary to primary. In addition, our definition of a satellite introduces selection effects at the bright end. Despite this the observed distribution of satellites appears to be in surprisingly good agreement with the luminosity function of

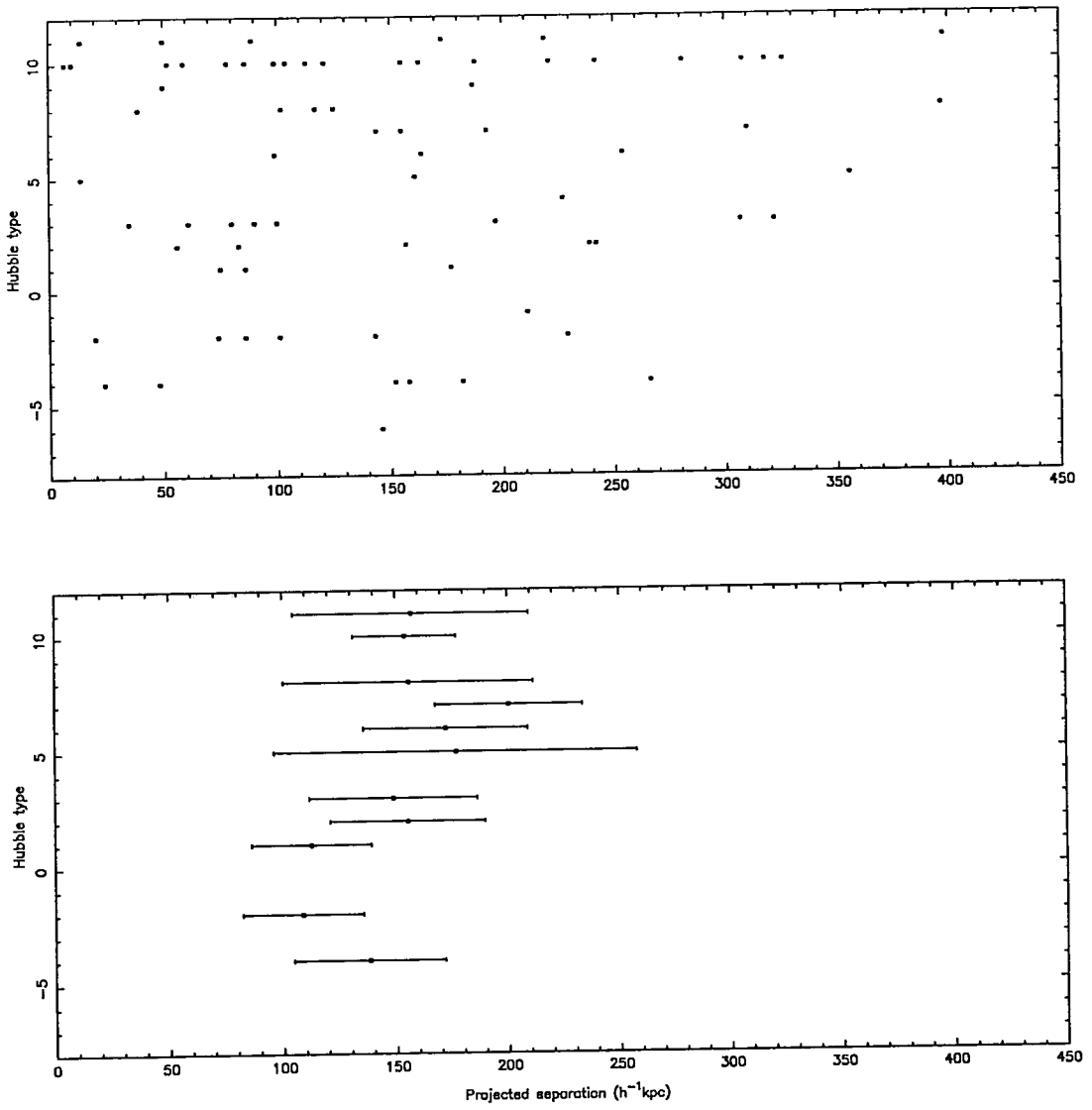

Figure 3.13. In the upper panel we show the morphological types of the satellites as a function of their projected separation. The morphological types are represented using the system in de Vaucouleurs *et al* (1976). In the lower panel we show the mean projected separation for each Hubble type where there are at least 3 satellites.

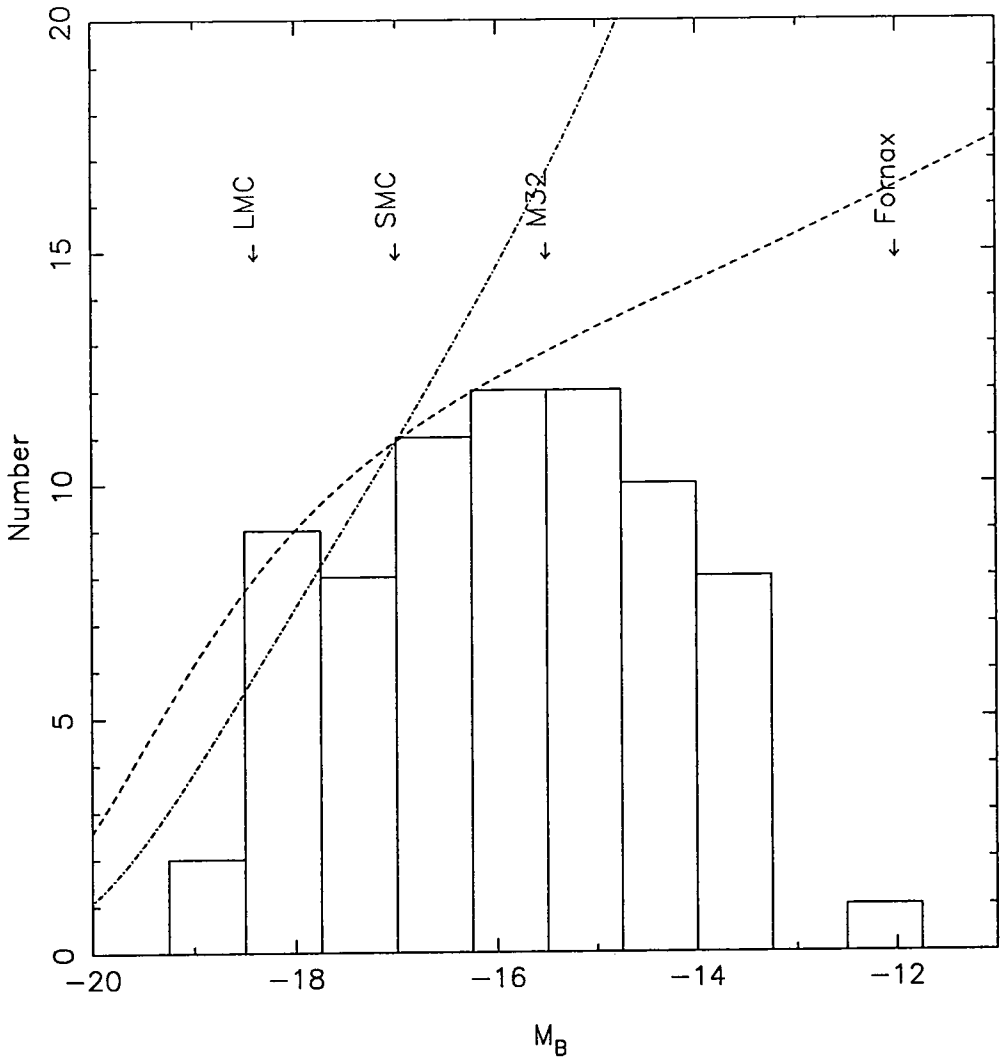

Figure 3.14. Histogram of the absolute magnitude distribution of satellites. Also shown are two luminosity functions with arbitrary normalisation: $\alpha = -1.07, M_\star = -19.68$ (dashed line, Efstathiou *et al* 1988); $\alpha = -1.25, M_\star = -19.6$ (dot-dashed line, Sandage *et al* 1985). For reference the absolute magnitudes of some members of the local group are also shown.

Efstathiou *et al* (1988a) for $-18.5 \lesssim M_B \lesssim -16$. In Figure 3.14 this is shown as a dashed line. Expressed in the usual Schechter form this has $\alpha = -1.07$ and $M_\star = -19.68$. The normalisation is arbitrary. Also shown is the Sandage *et al* (1985) luminosity function for dwarf galaxies in the Virgo cluster (dot-dashed line). This has a somewhat steeper faint end ($\alpha = -1.25$, $M_\star = -19.4$), but is still compatible with our data for $M_B < -17$. For reference the magnitudes of some members of the local group are also indicated. The majority of the sample is fainter than the LMC.

In Figure 3.15 we show the semi-major axis of the the satellites as a function of projected separation. Most of the satellites have semi-major axes of $< 15\,\mathrm{h}^{-1}\mathrm{kpc}$. There are no obvious correlations between the size and projected separation of the satellites. Also shown are the limiting tidal radii for two models (Binney & Tremaine, 1987). The solid line is for a satellite orbiting a mass 10 times its own. The dashed line is for a $10^{10}M_\odot$ satellite moving in an isothermal sphere. The isothermal sphere has a mass of $1.4 \times 10^{12}M_\odot$ within $150\mathrm{h}^{-1}\mathrm{kpc}$. This is the mass we found in §3.5.2. The comparison of both of these limits with the data is acceptable, with only two satellites having semi-major axes greater than the limits described by these models.

3.5.6 The $V_c - |\Delta v|$ plane

In their paper ZSFW claim that there is no strong correlation between V_c and $|\Delta v|$. We show this scatter plot once more in Figure 3.16. ZSFW comment that this lack of correlation, if not caused by selection biases, would have profound consequences for theories of galaxy formation. The Tully-Fisher relationship (see, *eg*, Pierce & Tully 1992) shows that there is a strong correlation between the luminosity of spiral galaxies and their circular velocities. The ZSFW result would then suggest that there is little correlation between the dynamics of the inner and outer parts of the halo. However, as we discussed

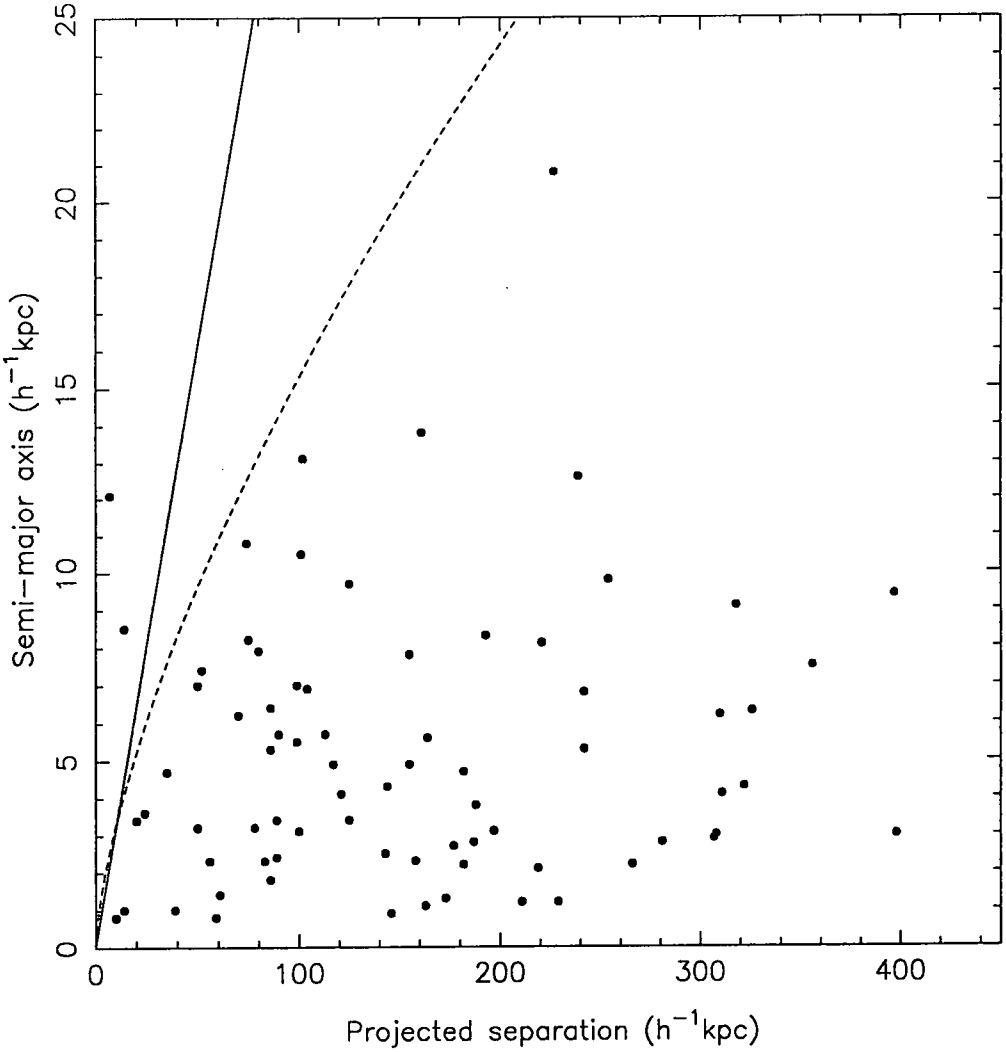

Figure 3.15. The semi-major axis of satellites as a function of projected separation. Also shown is the maximum semi-major axis, assuming that the size of the satellites is tidally limited. The solid line is for a satellite orbiting 10 times its own mass. The dashed line is for a $10^{10}M_{\odot}$ satellite moving in an isothermal sphere. The isothermal sphere has a mass of $1.4 \times 10^{12}M_{\odot}$ within $150h^{-1}$kpc.

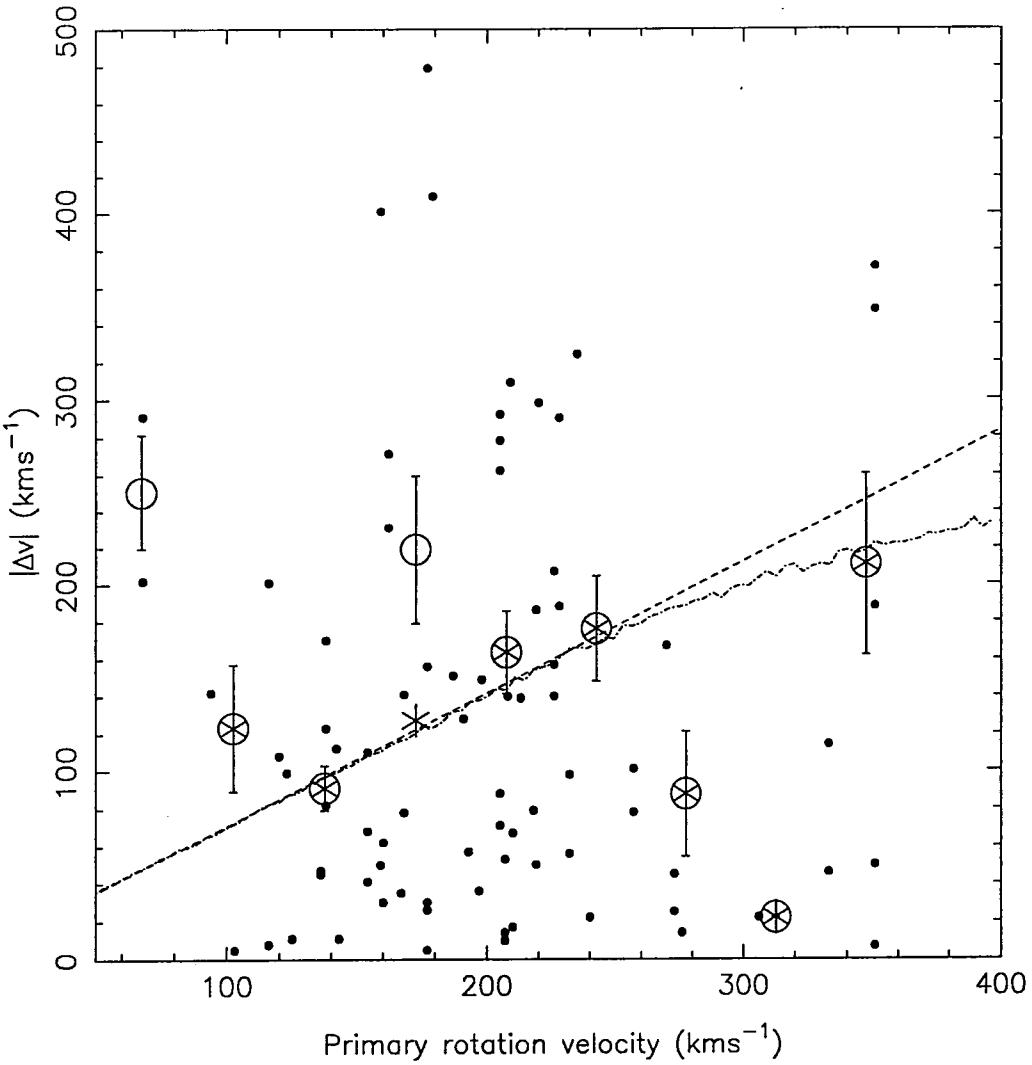

Figure 3.16. Scatter plot showing $|\Delta v|$ as a function of the primary rotation velocity, V_c (solid points). Also shown is the rms $|\Delta v|$ (open circles interlopers included, asterisks interlopers excluded). The dashed line is $V_c = \sqrt{2} \times \mathrm{rms}(|\Delta v|)$. The dot-dashed line shows the same relationship but with selection effects also included.

in §3.5.1 we believe there is an upper envelope corresponding to $|\Delta v| \simeq 2V_c$. To test this further, we calculated the rms $|\Delta v|$ for a number of V_c bins. These are shown as open circles (interlopers included) and asterisks (interlopers excluded) in Figure 3.16. The errors which are shown here are uncertain since to calculate them requires the fourth moment of the data. A better indication of the reliability of the data is the number of data points used. The dashed line is $|\Delta v| = V_c/\sqrt{2}$, corresponding to a halo in which the rotation velocity is equal to that of the primary and the satellites are on isotropic orbits. In the most populous region of the $V_c - |\Delta v|$ plane ($120\,\mathrm{km\,s^{-1}} < V_c < 260\,\mathrm{km\,s^{-1}}$) this is consistent with the rms velocity differences, particularly if interlopers are excluded. The dot-dashed line shows the same relationship, but selection effects have also been included. In particular, satellites with $|\Delta v| > 2V_c$ or $|\Delta v| > 500\,\mathrm{km\,s^{-1}}$ have been excluded. The first condition has virtually no effect on the relationship, as $2V_c$ corresponds to almost 3σ. However, the second selection effect causes a considerable flattening of the relationship for $V_c > 250\,\mathrm{km\,s^{-1}}$. The data are also consistent with no correlation, but we believe that this analysis shows that the conclusions of ZSFW were premature and the hypothesis that the halo rotation velocity is equal to that of the primary cannot be excluded on the basis of this data.

3.5.7 Kinematics & dynamics of the primary-satellite system

In Figure 3.17 we plot Δv as a function of r_p. However, we have also assigned a sign to r_p. If the separation vector lies closer to the receding limb of the primary disc r_p is positive, otherwise it is negative. Only those primaries with inclinations $\geq 45°$ are considered in this analysis, so that the receeding and approaching limbs of the primary could be clearly distinguished. Hence, if in Figure 3.17 a satellite appears in the upper right and lower left quadrants its orbit is prograde relative to the disk of the primary. Otherwise it is retrograde. ZSFW observed the primaries in their catalogue themselves to find rotation

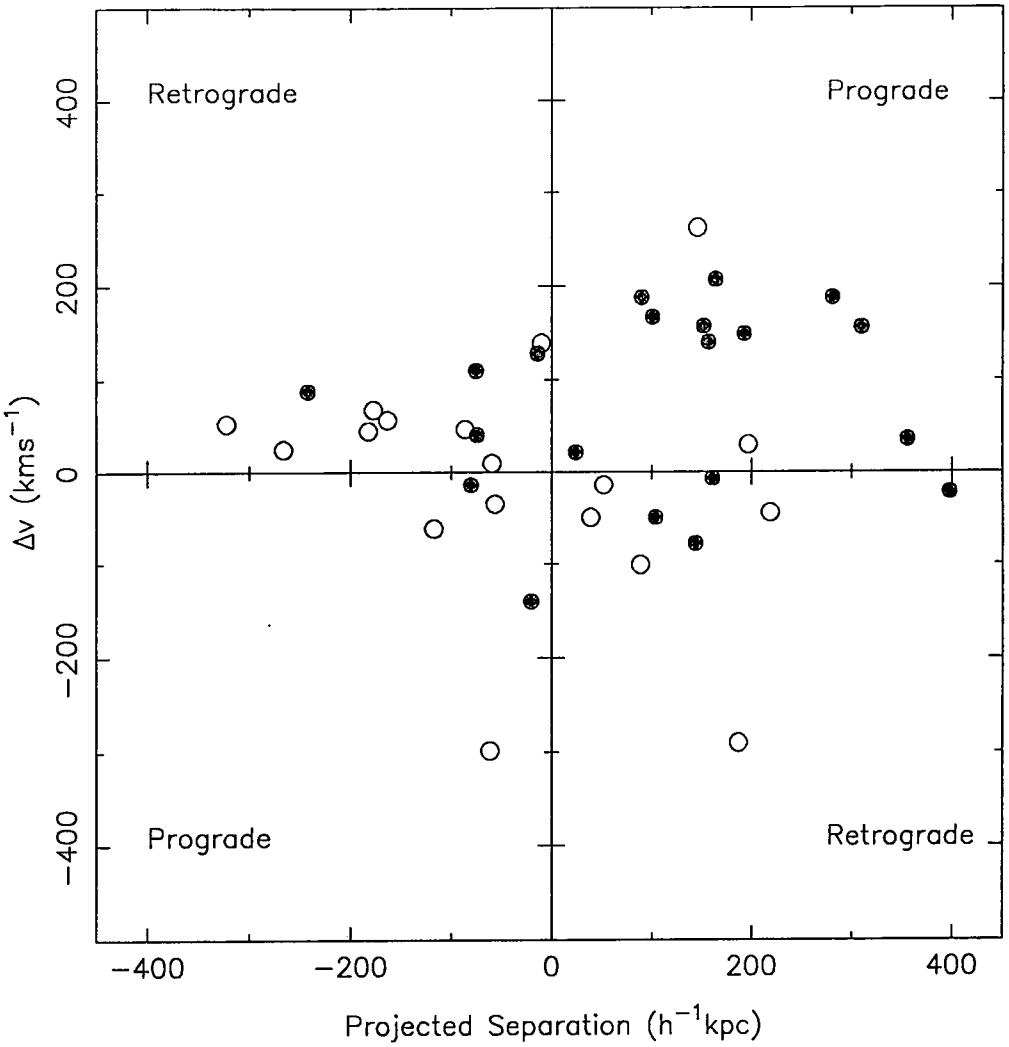

Figure 3.17. The distribution of Δv with projected separation, r_p, for satellites of primaries with inclination angles of 45^o or greater. In this plot we have also assigned a sign to r_p. If the primary-satellite separation vector lies closest to the limb of the primary which appears to be receeding r_p is positive. Otherwise r_p is negative. The indicated quadrants thus represent prograde or retrograde orbits relative to the primary. The solid points are for satellites which are brighter than the median absolute magnitude ($M_B = -15.95$). Open points indicate satellites which are fainter than this.

curves. We were unable to do this, but for one primary (N6984) a rotation curve was available in Matthewson *et al* (1992). All three of its satellites are on retrograde orbits. In Figure 3.17 we have also distinguished between satellites which are brighter than the median absolute magnitude ($M_B = -15.95$) and those which are fainter than this (solid and open points respectively). A number of trends are immediately apparent.

Firstly, satellites on prograde orbits typically have a greater $|\Delta v|$ than those on retrograde orbits. A KS test on the distributions of $|\Delta v|$ rules out that that they are drawn from the same distribution at the 98% level. This is perhaps suggestive of some kind of systemic rotation. However, if we assign a sign to $|\Delta v|$ such that it is positive if the orbit is prograde and negative if it is retrograde, the mean Δv is not significantly different from zero ($20 \pm 20\,\mathrm{km\,s^{-1}}$). It also appears that satellites on prograde orbits are systematically brighter than their retrograde counterparts. Again using a KS test, the probability that the magnitudes were drawn from the same distribution is only 9% . There are no other systematic differences between the prograde and retrograde satellites samples. In particular, there is only a 0.4% probability that the (unsigned) projected separations were drawn from different underlying populations.

There is a further effect apparent within the set of prograde satellites alone. In this set 12 appear in the upper right quadrant, *ie*, they are associated with the receeding limb of the primary disc, but only 5 appear in the lower left quadrant. For a binomial distribution with $P/T = 0.5$ a disparity as extreme as this would only be expected 5% of the time. As Zaritsky (1991,1992) discusses there is a selection effect which operates to make $P/T > 0.5$. However, if this were the case then we might also expect to see more retrograde satellites in the upper left quadrant than in the lower right. The retrograde satellites are much more evenly split (12 in the upper left quadrant, 9 in the lower right quadrant). If we use this to estimate the size of the bias discussed by Zaritsky (1992) we obtain $P/T = 0.57$. Even in this case we only expect to see a split in favour of positive Δv as extreme as 12

to 5 in 8% of cases. The selection effects in this part of the analysis are, then, only poorly understood at present.

3.5.8 The satellites of the Milky Way

The underlying reason for the precise selection process of ZSFW was to probe the halos of galaxies similar to the Milky Way. In this section we discuss the effectiveness of their criteria. In Figure 3.18 we again show the scatter plot of $|\Delta v|$ as a function of r_p. The symbols are as before. In addition the error bars show the likely positions of 9 Milky Way satellites if they were viewed by an external observer and $H_0 = 100\,\mathrm{km\,s^{-1}\,Mpc^{-1}}$. Other values of H_0 would scale the position of the Milky Way galaxies horizontally. The likely positions were found by viewing a primary-satellite pair from random directions. The satellite was taken to have a known separation and line-of-sight velocity as viewed from the primary. Its orbit was assumed to be isotropic. Its velocity perpendicular to the satellite-primary vector was given random direction and noise added to its magnitude. Using approximately 30000 realisations of this kind, we found that a satellite with true separation r and line-of-sight velocity $v_{\rm los}$ would be seen to have $r_p = 0.79r$ and $|\Delta v| = 0.85 v_{\rm los}$. The '$\pm 1\sigma$' range is given by $r_p/r = 0.55 \rightarrow 0.99$ and $|\Delta v|/v_{\rm los} = 0.23 \rightarrow 1.42$. These are, again, not truly 1σ errors, but 68.5% of the realisations lie in this range. These ranges are then applied to the parameters summarised in Moore (1991), to give the ranges shown in Figure 3.18. If the orbits were radial these would move to lower values of $|\Delta v|$

It is clear that the Milky Way system is somewhat atypical relative to the satellite sample. Most of the satellites have $|\Delta v| < 100\,\mathrm{km\,s^{-1}}$. The only exception to this is Leo I (the rightmost point) and since this is observed to be at a projected separation $> 150\,\mathrm{h^{-1}kpc}$ it would not be included in our mass estimates. The majority of the Milky Way satellites are also at small separations ($< 100\,\mathrm{h^{-1}kpc}$). There could be a number of selection effects

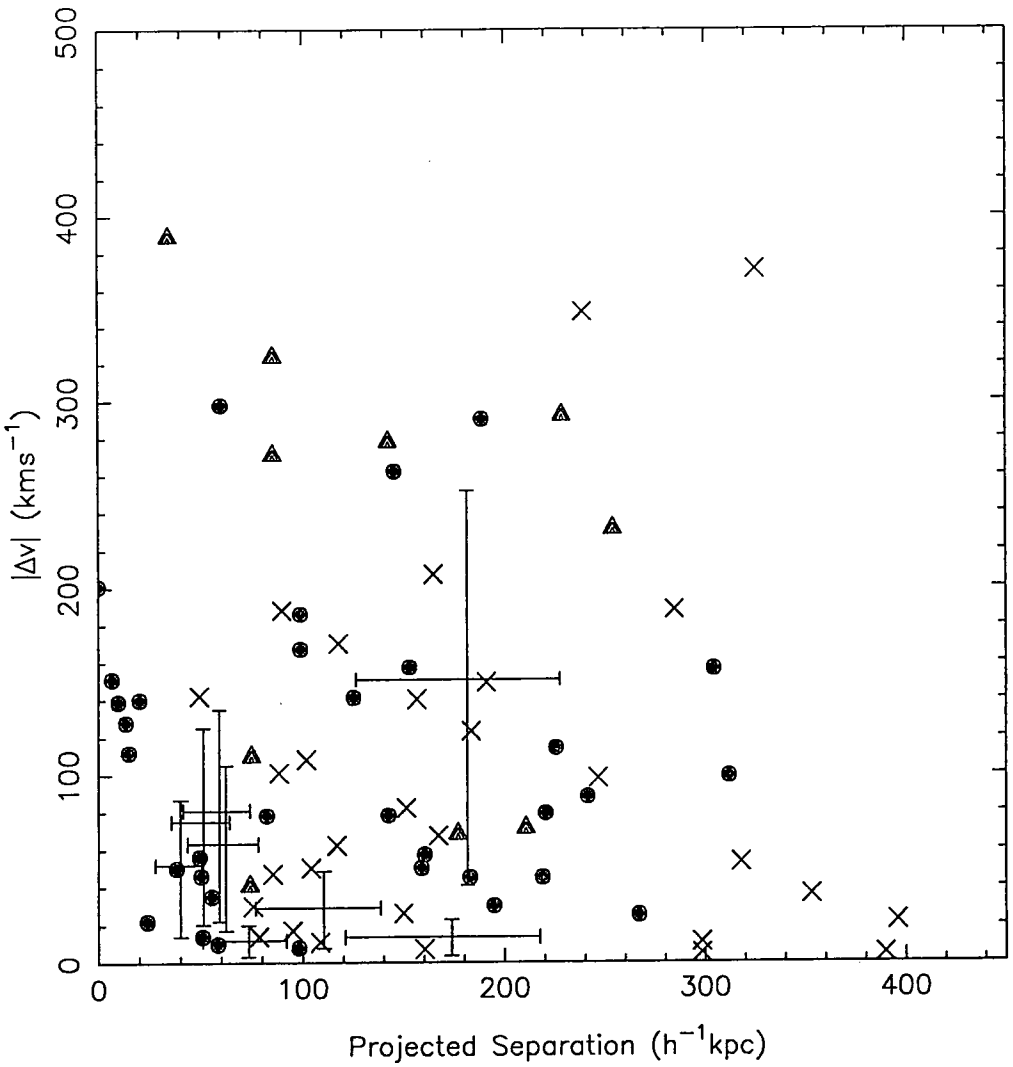

Figure 3.18. The $r_p - |\Delta v|$ plane. The symbols are as in Figure 3.9. The error bars show the likely positions of Milky Way satellites if they were viewed by an external observer and $H_0 = 100\,\mathrm{km\,s^{-1}\,Mpc^{-1}}$.

which cause this apparent dissimilarity. Firstly, the Milky Way would be excluded from the sample anyway as it is not isolated. M31 lies within 1Mpc of the Milky Way and is of a similar magnitude. The close proximity of M31 would also lead to the truncation of the satellite system of the Milky Way. Satellites which are closer to M31 would not be plotted here as they would be catagorised as satellites of M31, not the Milky Way. However, there is no clear reason why the Milky Way satellites should have such low $|\Delta v|$. However, since there are only a small number of Milky Way satellites it is not possible to draw any firm conclusions from this analysis. The H_0 and model dependence of the comparison also further weakens this.

3.6 Summary and conclusions

In this chapter we have presented an extension to the ZSFW survey of satellite galaxies. The extension contains only 10 satellites; poor weather during observing runs prevented it being any larger. For these 10 satellites we have obtained spectra which have allowed us to measure recessional velocities accurate to $\sim 30\,\mathrm{km\,s^{-1}}$. Observations were made using the AAT, and the subsequent data reduction was made using routines in the FIGARO reduction package.

We then followed the work of ZSFW. We excluded interlopers by considering their position in the $|\Delta v| - V_c$ plane, rather than the the $|\Delta v| - r_p$ plane, which is the method used by ZSFW.

By considering the $|\Delta v| - r_p$ plane we have been able to estimate the mass associated with the primaries. Our best estimate of the mass within $150\mathrm{h}^{-1}\mathrm{kpc}$ is $(1.40^{+0.59}_{-0.77}) \times 10^{12}\mathrm{h}^{-1} M_\odot$. We have also placed a very strong lower limit on this of $7.2 \times 10^{10}\mathrm{h}^{-1} M_\odot$. Our best

estimates agree well with the estimate of the Milky Way mass found by Zaritsky *et al* (1989). We are able to exclude a mass as low as the Little & Tremaine(1980) estimate at the 99.9% level. Another new result is that using the median primary luminosity ($L = 1.4^{+0.1}_{-0.2} \times 10^{10} h^{-2} L_{\odot}$) we are able to estimate the mass to light ratio within $150 h^{-1}$kpc as $M/L = 100^{+38}_{-49} h (M_{\odot}/L_{\odot})$. By comparing this with the mass to light ratio required for closure density (Efstathiou *et al* 1988a) we can estimate that $\Omega = 0.067^{+0.034}_{-0.037}$. Since this only considers mass within $150 h^{-1}$kpc of bright galaxies this represents a lower limit on the universal value of Ω. A 95% constraint based on our analysis gives $\Omega > 0.02$. However, since even our best estimate of the mass within $150 h^{-1}$kpc will provide only a lower limit on Ω, this is probably a much stronger constraint than 95%. Comparing this with Ω in baryons expected from big bang nucleosynthesis, favours low values of H_0 if all the dark matter is to be baryonic. The median $|\Delta v|$ is independent of projected separation at $\sim 100\,\mathrm{km\,s^{-1}}$. This is about half the typical circular velocity of the primary galaxies. The inferred halo circular velocity for an isothermal halo model, $\sim 200\,\mathrm{km\,s^{-1}}$, is similar to the median primary rotation velocity.

Most of the satellites in the sample have $\Delta v > 0$. In this sample alone this is not a significant effect, but it is consistent with effects which have been noted in other surveys (see Zaritsky 1991 for a detailed discussion).

We find that low V_c primaries have fewer satellites. This effect is detected at the 99% level. This disagrees with the results of Holmberg (1969) who found no such trend with the luminosity of the primary. However, there were large uncertainties associated with his work, while the effect we have detected may be due to a selection effect. Our definition of a satellite means that brighter primaries (which then also have a higher V_c) can sample more of the luminosity function, perhaps leading to a higher number of satellites.

The radial distribution of satellites is well described by a power law within $100h^{-1}$kpc, and is in excellent agreement with the results of Chapter 2. The decline in the surface density of satellites seen beyond $100h^{-1}$kpc may be due to the limited size of the fields observed using fibres. However, a similar decline is also seen in the N-body simulations of J.F.Navarro. We have also confirmed the Holmberg effect at the 97% level; there is a significant deficiency of satellites within $50h^{-1}$kpc and with position angles $\Theta < 20°$. Satellites within $50h^{-1}$kpc are not uniformly distributed with position angle. This is detected at the 95% level. There is no detectable effect for separations greater than this. This is the first firm confirmation of the effect first noted by Holmberg (1969).

We can find no evidence of any correlation between the morphological type of the satellites and their projected separation. However, such a correlation cannot be firmly excluded either. We are thus unable to comment on the claim of Einasto *et al* (1974) that as projected separation increases satellites tend to be of a later type. The luminosity function of the satellites is ill determined, but shows no obvious peculiarities. Over a limited range of magnitudes it is consistent with both the universal luminosity function of Efstathiou *et al* (1988a) and with the Virgo dwarf luminosity function of Sandage *et al* (1985). There are no obvious correlations between the size of a satellite and its projected distance from the primary. However, the sizes are consistent with the tidal limits found by assuming that the satellites are orbiting a body with 10 times its own mass. They are also consistent with the hypothesis that the primary is an isothermal sphere with a mass of $1.4h^{-1} \times 10^{12} M_{\odot}$ within $150h^{-1}$kpc and that the satellites have a mass of $10^{10}h^{-1} M_{\odot}$.

We agree with ZSFW that there is no significant correlation between $|\Delta v|$ and the rotation velocity of the primary, V_c. However, we believe that there is an upper envelope to the range of allowed values of $|\Delta v|$, corresponding to $|\Delta v| \simeq 2V_c$. Further, if we look at the rms value of $|\Delta v|$ there is a weak correlation with V_c for $V_c < 250\,\mathrm{km\,s^{-1}}$, consistent with the halo having the same circular velocity as the primary.

Considering the kinematics of the primary-satellite system highlights some worrying unexplained systematics. The most worrying of these is that for the prograde satellites alone the ratio of the number of satellites with $\Delta v > 0$ to the total number of satellites is $P/T = 0.71$. If the underlying distribution has $P/T = 0.5$ a value this extreme is expected only 5% of the time. Alternatively, if $P/T = 0.58$ (which is true for the sample as a whole and for the retrograde satellites only) a value this extreme occurs 8% of the time. It seems possible that there are additional selection effects at play when we are considering this aspect of the analysis which are unexplained for the time being.

Using Monte-Carlo realisations we have found the regions in which we might expect to see the Milky Way satellites, if we could observe our own system externally. The Milky Way satellites seem to have atypically small values of $|\Delta v|$. They also lie at relatively smaller separations than typical, although this comparison is sensitive to both the true value of H_0 (we have taken $H_0 = 100\,\mathrm{km\,s^{-1}\,Mpc^{-1}}$) and selection effects.

In conclusion we have demonstrated that isolated spiral galaxies are surrounded by massive halos with masses $\sim 10^{12} M_\odot$. These masses provide constraints on the density of the universe of $\Omega \gtrsim 0.1$. There is no obvious fall off in the median $|\Delta v|$ with separation. This is consistent with the dark halo being an isothermal sphere with a rotation velocity equal to that of the primary. The sizes of the satellites are also consistent with this provided they have masses no larger than about $10^{10} M_\odot$. However, although the systems were picked to have Milky Way-like primaries, the satellites of the Milky Way appear somewhat atypical relative to the rest of satellites in the sample.

4 The Small Scale Environment of Low Surface Brightness Galaxies and Tidally Triggered Star Formation

4.1 Introduction

The physical processes which trigger star formation and determine its rate (and hence a galaxy's surface brightness) remain poorly understood. What is clear is that galaxies have a range of surface brightnesses (*eg,* Schombert *et al* 1990; Peletier & Wilner 1992). This dispels the once popular notion that all disk galaxies have the same central surface brightness (see, *eg,* Freeman 1970). It now seems that the observed central surface brightness of galaxies covers a large range of values. However, the number of galaxies as a function of central surface brightness is poorly known, mainly due to difficulty in interpretting the affect on catalogues of some complex selection effects (Disney & Phillipps 1987). Attempts are now being made to correct for this deficiency, leading to the recognition of new classes of galaxies – low surface brightness (LSB) galaxies and very low surface brightness (VLSB) galaxies (Bothun *et al* 1986; Phillipps *et al* 1987; Davies *et al* 1989).

This class of galaxies is clearly very different from the 'normal' high surface brightness (HSB) galaxies (McGaugh 1992). The star formation rate in LSB galaxies is clearly much lower than in their HSB counterparts, and so they provide an interesting testing ground for studies of star formation. The rôle of environment in star formation is an ambiguous one. The observation that the Universe is made of lone galaxies, loose groups, walls, voids and dense clusters leads one to conclude that a wide range of environments exist. The most

striking examples of the effect of environment on galaxy properties are the morphology density relation (Dressler, 1980; Postman & Geller 1984) and the Butcher-Oemler effect (Butcher & Oemler 1978). The physics of these effects is not clear, but merging has often been suggested as an important mechanism (*eg,* Bower 1991). Merging has also been suggested as a formation mechanism for ultra-luminous infra-red galaxies (Sanders *et al* 1988) and for cD galaxies (Ostriker & Tremaine 1975). Estimates of the merging rate range greatly from those of Schweizer *et al* (1990), who suggest a high merger rate, to that of Zepf (1992), who finds only a modest merger rate in Hickson groups – one of the densest environments.

Recent observations by van der Hulst *et al* (1992) and McGaugh (1992) show that the surface density of HI in LSB disks is lower than that required for star formation (Kennicutt 1989). Without a mechanism for clumping this gas, and so increasing its surface density to trigger star formation, these galaxies undergo only limited star formation. Thus, LSB galaxies may be 'failed' galaxies in which the surface density has never reached a sufficient level for significant star formation. Alternatively LSB galaxies may be 'burnt out' galaxies which have undergone star formation, reducing their surface density of HI, and are now fading. However, this seems unlikely since a substantial earlier period of 'normal' star formation would have left a significant residual red stellar population. With the exception of those with a normal bulge, LSB galaxies do not, in general, show such a stellar population. So, the former suggestion seems more plausible – LSB galaxies have *never* achieved a sufficiently high surface density of HI to form stars.

Lacey & Silk (1991) have suggested that star formation may be triggered by tidal interactions between nearby galaxies. The size and plausibility of this effect can be straightforwardly demonstrated (Zaritsky & Lorrimer 1992). By considering an impulsive encounter we can find the typical velocity impulse produced by an encounter between galaxies in the centre of mass frame. This comes from estimating the acceleration and duration of the

encounter. If v_p is the velocity of the encounter, r the radius of the perturbed body, M_p the mass of the perturber and R the pericentre distance, we can model a tidal interaction as producing a constant acceleration GM/R^2 lasting for a time $2r/v_p$ (Binney & Tremaine 1987, §7.2). The induced velocity perturbation in the centre of mass frame is given by

$$\Delta v \sim \frac{2GM_p r}{R^2 v_p} \tag{4.1}$$

Taking $M_p = 10^{11} M_\odot, R = 100\,\mathrm{kpc}, r = 15\,\mathrm{kpc}$ and $v_p = 300\,\mathrm{km\,s^{-1}}$ gives $\Delta v \sim 5\,\mathrm{km\,s^{-1}}$. So, with reasonable parameters we can obtain a velocity change of order the sound speed in the ISM. It is therefore plausible that such perturbations should have some effect on the star formation rate.

This model would then imply that LSB galaxies lack tidal triggering, presumably because they have few nearby neighbours. The relative isolation of LSB galaxies has been noted by Bothun *et al* (1990) and measured by Bothun *et al* (1992), who compared a sample of 340 LSB disk galaxies with the CfA redshift survey (Huchra *et al* 1990). They find a deficit of companion galaxies within 500 $\mathrm{h^{-1}kpc}$ with velocity differences of less than 500 $\mathrm{km\,s^{-1}}$. Previously only the large scale clustering (5-10$\mathrm{h^{-1}Mpc}$) of LSB galaxies had been investigated (Bothun *et al* 1986; Thuan *et al* 1987; Schneider *et al* 1990).

In this Chapter we aim to test the tidal triggering hypothesis further, again measuring the small scale environment of LSB galaxies, but including companions which are fainter than Bothun *et al* (1992) considered. We make use of the techniques developed in Chapter 2 to estimate the number of companions around LSB galaxies in the redshift survey of D. Sprayberry & C.D. Impey (1992, personal communication). Note that we refer to neighbours as 'companions' rather than 'satellites.' This is because a satellite, by implication, is fainter and less massive than the central object. This will not necessarily be true for the neighbours of LSB galaxies. As a control sample we will use a sample of HSB galaxies drawn from the CfA survey.

4.2 The LSB redshift catalogue and POSS Plate Scans

The LSB galaxy redshift survey supplied by Sprayberry & Impey consists of 256 LSB galaxies with measured redshifts. These are along the declination strip, $|\delta| \leq 3°$, with $|b| \geq 30°$. Not all are true LSB galaxies. Some have medium or high surface brightness knots and a few are small HSB galaxies which were missed in other catalogues. The latter groups form about 30 % of the sample. However, we make use of all the objects in the survey and we shall refer to them all as LSB galaxies hereafter. Any division into high and low surface brightness within the redshift catalogue is made impossible by the small numbers. The survey covers the entire area defined above and does not preferentially select LSB galaxies in particular environments. Incompleteness is not important in our method, provided the sample is fair. The spatial distribution of the LSB galaxies is shown in Figure 4.1, along with the edges of those plates for which we have scans in this region. We have scans for only around half the area covered by the redshift survey, so the strips with $10 \leq \alpha \leq 15$ cannot be utilised. In total we have 19 scanned plates of which 13 have LSB galaxies in their central $5° \times 5°$. The properties of these plates is listed in Table 4.1. As in Chapter 2 only this central region of the plate is used in order to minimize vignetting effects.

The redshift distribution of the sample is shown in Figure 4.2. It peaks at around 7000 $\mathrm{km\,s^{-1}}$. For the central $5° \times 5°$ we can typically count companions out to a distance of around 6 $\mathrm{h^{-1}Mpc}$. It is not essential to, but in order to be able to include low redshift LSB galaxies we will use the bootstrap method of Chapter 2.

Once again we use the Lick map for setting the magnitude zero points of the POSS plates. As in Chapter 2 the region we consider is sufficiently small that we need not worry about systematic effects introduced by possible large scale gradients in the Lick map. Of greater concern is the fact that the APM machine has difficulty detecting LSB galaxies unless

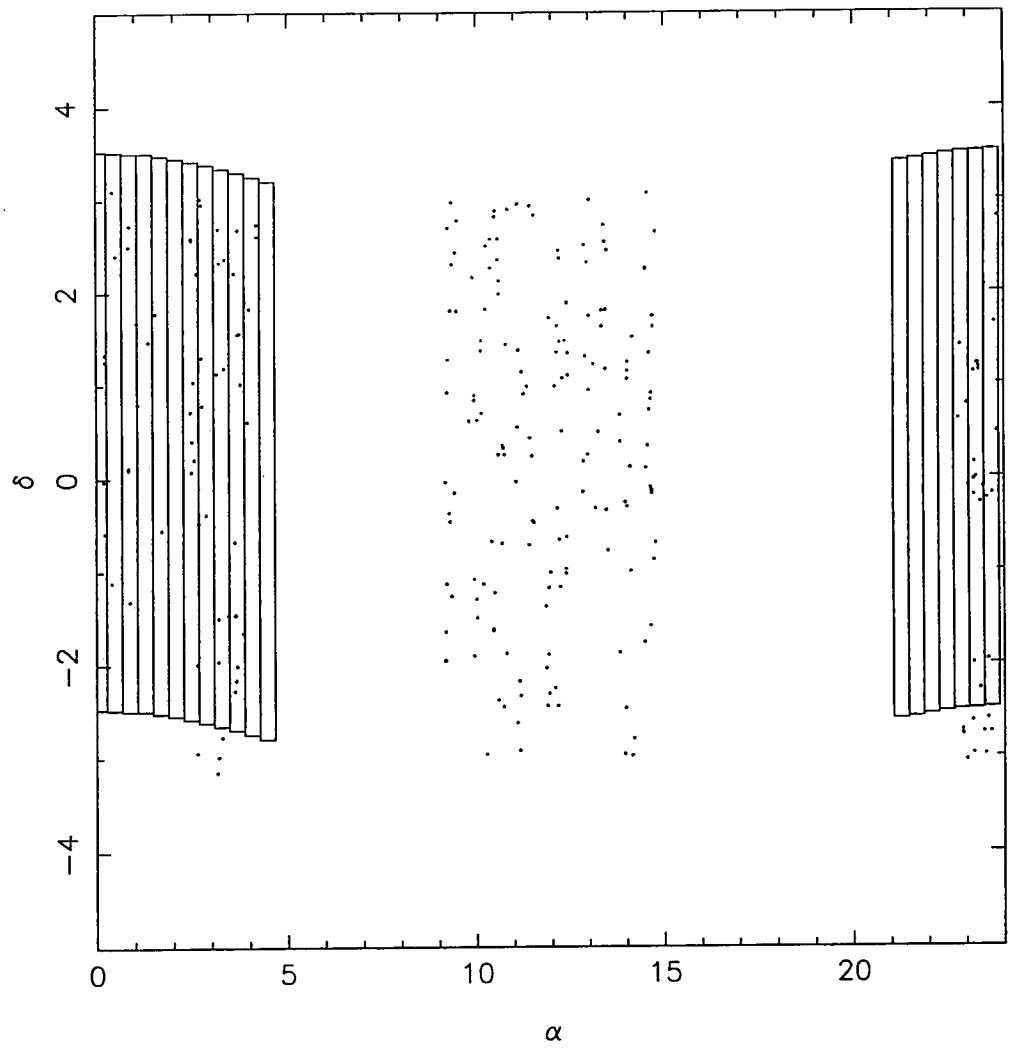

Figure 4.1. The dots show the positions of the LSB galaxies in the redshift survey of Sprayberry & Impey. The solid oblongs show the area covered by our scanned POSS plates. We have 19 scanned plates, covering about half of the LSB galaxy survey region.

POSS plate	RA (1950)	Dec (1950)	N_L	N_c	N_c/N_L	N_{LSB}
1130	$21^h40^m52^s$	00°26′04″	692	689	1.00	0
1146	$22^h04^m32^s$	00°27′47″	961	964	1.00	0
1196	$00^h52^m52^s$	00°30′55″	1863	1871	1.00	5
1259	$01^h16^m22^s$	00°30′22″	1860	1894	1.02	1
1283	$02^h28^m53^s$	00°25′11″	1142	1141	1.00	9
1453	$02^h52^m52^s$	00°23′10″	1162	1183	1.02	3
1524	$04^h28^m52^s$	00°12′25″	642	657	1.02	0
232	$04^h04^m53^s$	00°15′09″	584	584	1.00	4
319	$00^h04^m52^s$	00°31′44″	1592	1601	1.01	4
362	$01^h40^m53^s$	00°28′42″	1328	1341	1.01	2
363	$03^h16^m53^s$	00°20′33″	1064	1070	1.01	7
364	$22^h28^m51^s$	00°29′20″	1039	1052	1.01	0
431	$23^h40^m52^s$	00°31′38″	747	763	1.02	6
575	$21^h16^m51^s$	00°24′55″	794	826	1.04	0
591	$00^h28^m52^s$	00°31′28″	1819	1849	1.02	2
834	$23^h16^m52^s$	00°31′09″	1015	1043	1.03	10
852	$02^h04^m52^s$	00°27′03″	1020	1024	1.00	0
905	$22^h52^m51^s$	00°30′22″	902	910	1.01	3
932	$03^h40^m53^s$	00°18′07″	692	530	0.77	12
Total			20918	20992	1.00	68

Table 4.1 Table showing summary of properties of plates used in this analysis. The columns give the same information as Table 2.1 except column 7 gives the number of LSB galaxies in the plate area, N_{LSB}.

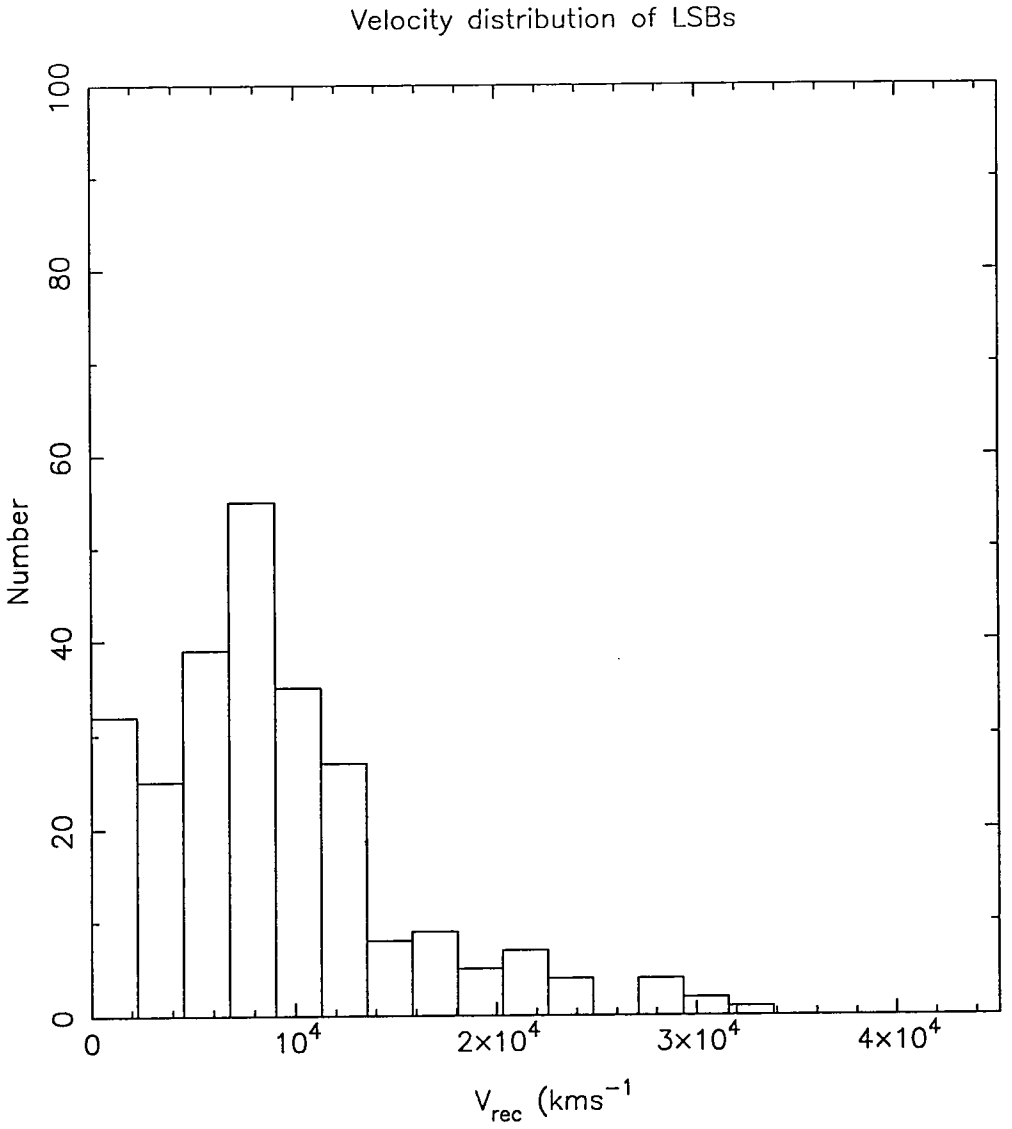

Figure 4.2. The recession velocity distribution of LSB galaxies in the survey of Sprayberry & Impey.

special procedures are followed (Irwin *et al* 1990) or the plates are photographically enhanced or 'Malinised' (Malin, 1978). The scans available to us are not of this type, and so, although we apply a magnitude limit to the companions we count, we also have an unknown surface brightness limit. In practice, we will not be able to detect companions which are themselves LSB galaxies. The number and significance of such missing companions is difficult to estimate. On one hand, Impey *et al* (1988) in a study of LSB galaxies in the Virgo cluster, found a good luminosity-surface brightness relation for galaxies brighter than $M_B = -16$. Since this is our magnitude threshold it suggests that we should be able to detect the majority of companions brighter than this threshold. On the other hand, Davies *et al* (1988) found no evidence for a luminosity-surface brightness relationship in the Fornax cluster and Phillipps *et al* (1988) have argued that any such apparent effect is a selection effect, allowing there to be a large number of LSB companions which we have not detected. However, if this is important, we will also miss LSB companions of our HSB control sample.

4.3 Results

We have used a total of 13 plates, utilising a total of 41 LSB galaxies. Due to the small number of LSB galaxies we use only the faintest absolute magnitude threshold from Chapter 2, $M_{B_T} < -16$. We do not impose any other restriction on the luminosity of companions. We also do not restrict the luminosity of the LSB galaxies or the HSB control sample. The HSB control sample contains galaxies of all morphological types. This gives a total of 19023 faint galaxy-LSB galaxy pairs. This number is too low to yield

the density profile of the companions but it is large enough to allow an estimate of the number of companions within various distances of an LSB galaxy.

In Table 4.2 we present our results for the number of companions within 250, 500 and 1000h^{-1}kpc and compare them with the numbers we found in the control sample. Although the errors are large the number of companions around LSB galaxies is consistent with zero at all separations. In addition the allowed range for the LSB galaxies does not overlap with that for the HSB galaxies, which have significantly more close companions. More specifically, the difference between the number of companions around HSB galaxies and the number around LSB galaxies within 250, 500 and 1000 h^{-1}kpc is 1.44 ± 0.42, 3.8 ± 1.5 and 7.5 ± 4.9 respectively. These differences are significant at the 3.4σ, 2.6σ and 1.5σ levels respectively. Thus the discrepancy between the number of companions around LSB and HSB galaxies is reduced as the radius considered becomes larger. This trend is to be expected since the number of companions must eventually become small at a sufficiently large radius.

4.3.1 Systematic errors

As in Chapter 2 care must be taken to ensure that our results are free of systematic errors. These are potentially more important in this Chapter since the signal we are trying to detect is smaller. To test this we again used the 'plate swapping' process described in §2.3.2. This was done using all the available plates and not just the 13 used in the data analysis. Unfortunately 13 plates are not sufficient to ensure that real structure on the plates does not lead to apparent systematic effects. The results of 66 realisations of this kind are shown in Table 4.2 under the heading 'Null Test'. These realisations were also used to estimate the errors in this Table. The quoted errors are 1-σ errors. The test results

Radius	HSB Galaxies	LSB Galaxies	Null Test
250 h^{-1}kpc	1.66 ± 0.17	0.22 ± 0.38	-0.01 ± 0.05
500 h^{-1}kpc	3.67 ± 0.41	-0.1 ± 1.4	0.01 ± 0.17
1000 h^{-1}kpc	9.91 ± 0.77	2.4 ± 4.8	-0.14 ± 0.59

Table 4.2 Table showing the number of companions found around HSB galaxies, LSB galaxies and in a null test of our method within various separations.

are consistent with zero indicating that our results are not contaminated by systematic effects.

4.4 Discussion & Summary

In this Chapter we have tested the possibility that gravitational interactions with nearby neighbours may trigger star formation in galaxies. Having identified LSB galaxies as sites of particularly low star formation rates we tested the hypothesis that these galaxies lack nearby companions, and thus a tidal trigger, by counting the number of close companions around the LSB galaxies in the Sprayberry & Impey redshift survey. We used a sample of galaxies from the CfA survey as a HSB control sample. The results clearly demonstrate that the number of companions around LSB galaxies is significantly lower than the number around HSB galaxies, particularly within $250h^{-1}$kpc. The difference appears to diminish as the distance from the LSB galaxy is increased.

We have attempted to quantify possible systematic effects in our analysis. Our most powerful test, comparing LSB galaxies with the 'wrong' Palomar plate is only useful if we use a large number of plates, including those from Chapter 2. Our test shows that systematic effects are of a negligible size and do not affect our conclusion that LSB galaxies have fewer neighbours than their HSB counterparts. A more worrying possibility is that we have missed LSB companions which are not detected on our APM scans of Palomar plates. If LSB galaxies are themselves clustered, as might be expected if star formation is triggered by some other environmental effect, they would produce tidal effects on each other. If these are present they clearly do not trigger star formation.

We have therefore demonstrated that LSB galaxies, which have a low star formation rate, have significantly fewer close companions than HSB galaxies. This could be caused by many effects, but is compatible with models in which star formation is triggered by tidal interactions with nearby companions.

5 Clustering in the Press-Schechter formalism

5.1 Introduction

The gravitationally bound structures seen in the Universe are often thought to have grown out of small perturbations in the early Universe (*eg,* Peebles, 1980). The fluctuations may grow from quantum mechanical effects at very early times. In most models (*eg,* Cold Dark Matter, Davis *et al* 1985) a large fraction of the power in such fluctuations is on small scales. Larger structures then grow by the agglomeration of small units. Throughout this Chapter we will refer to clumps which have undergone gravitational collapse and so condensed out of the field as condensates. The power on larger scales then determines the large scale clustering of these condensates.

The amount of power in fluctuations on different scales is described by the power spectrum, $P(k)$. In practice this can only be measured from the clustering of, or the velocities induced in, the luminous objects which condense out of the field. To relate the former to $P(k)$ we require some prescription for galaxy formation. Previous studies have simply identified galaxies with high peaks in the field (*eg,* Kaiser 1984; Davis *et al* 1985; Bardeen *et al* 1986). In this Chapter we present a method for specifically calculating the clustering of *condensates,* by more closely approximating the complex physics of gravitational collapse.

In principle the condensates are more directly related to the luminous objects that are observed than the density field is. The calculation of their clustering properties is achieved using an extension of the Press-Schechter formalism (Press & Schechter, 1974, hereafter PS). This is reviewed in §5.2 and §5.3. This method allows us, given the complementary cumulative probability distribution, $\mathcal{P}$, for the field, to find the autocorrelation or cross-correlation of condensates of a single mass or in a range of masses.

Peebles (1980) shows that for a Gaussian field with a power spectrum, $P(k) = (\frac{A_0}{1+z})^2 k^n$, the mass autocorrelation function at large separations is $\propto r^{-(n+3)}$. Models described by such a power law spectrum are termed *scale free hierarchical models.* He also demonstrated that for $-3 \leq n < 0$, ξ is positive and for $0 < n \leq 2$, ξ is negative at large separations. As expected, it vanishes for $n = 0$, as this is the white noise case. At large separations then, assuming galaxies act as fair tracers of the mass (but see Bower *et al* 1993) we expect the correlation function to be $\propto r^{-(n+3)}$. At small separations non-linear effects become important. There have been other attempts to find correlation functions using semi-analytical techniques. Kaiser (1984) used the high peak model to find correlation functions in the highly linear regime, $\xi \ll 1$. Kashlinsky (1986, 1991) adopted the same approach as ourselves, using the PS formalism to calculate correlation functions. However, this paper has been misinterpreted as showing that the field correlation function, ξ_N, is independent of the scale on which the density field is smoothed (*eg*, Henry 1991). Kashlinsky (1991) clearly states this dependence and we also include this explicitly. In both Kashlinsky (1986) and Kashlinsky (1991) only the correlations of objects of a single mass are considered. We consider this case in §5.4. In §5.5 we also consider the correlations of condensates with a range of masses. Since redshift surveys are seldom confined to objects of a single luminosity we believe that allowing this freedom is a significant advantage. The work of Bower (1991, hereafter B91) and Bond *et al* (1991) has already shown that the PS formalism can be effectively used to calculate halo merger rates. In this Chapter we shall follow many of

the ideas used in B91 to make the natural progression into calculating the correlation function.

The study of clustering in scale free models was extended into the non-linear regime by Efstathiou *et al* (1988b, hereafter EFWD). They predicted correlation functions by simulating the Universe using an N-body code. They also derived multiplicity functions and found them to be in good agreement with the PS formalism. It is important to test our method against the results of EFWD and this comparison is made in §5.8.1. For the majority of specific problems the N-body approach is superior, extending into the non-linear regime and avoiding the simplifications of the PS approach. However, without an underlying analytical framework it is difficult to extrapolate the results to other cosmological parameters or to understand the physical processes which are involved. Also, N-body codes have only a limited resolution and a finite volume. This makes them unreliable when considering rare or small condensates or on the largest scales. Using the PS formalism avoids these difficulties, although poor agreement between the observed multiplicity function and that predicted by the PS formalism, and other models, forces us to regard work with condensates of the smallest masses with some suspicion (*eg*, Cole 1990). Finally, N-body codes require a large investment in CPU time, while our method requires only minimal CPU time, making the testing of non-standard power spectra feasible.

In §5.8.2 we also compare our results with those of standard CDM, using the simulations of Frenk *et al* (1990). These simulations are larger and have a much better resolution than those of EFWD, making a more rigorous comparison possible. The method shows an excellent agreement with the N-body results, clearly demonstrating its usefulness. This comparison also demonstrates the versatility of the technique, which allows many different power spectra to be considered with only minor changes.

In sections 5.9 and 5.10 we consider some applications of the method. For instance the ROSAT satellite (Trümper, 1983) promises to provide large, cleanly selected cluster catalogues. These catalogues will be a major advance, since X-ray selected catalogues will suffer from none of the projection effects which hinder their optical counterparts (Lucey 1983, Frenk *et al* 1990). However, they will be on scales which are typically too large for N-body codes to cope with easily and so semi-analytical techniques such as our own will be required to make a comparison between the observed clustering and that predicted by theoretical models. These data are not yet available. However, good quality correlation functions are available on smaller scales. Here we compare our calculations with the work of Moore *et al* (1993), who found the correlation function of groups in the Center for Astrophysics (CfA) redshift survey (Huchra *et al* 1990).

The ease with which we can predict the variation of the correlation function with redshift means that by using Limber's equation we can also make predictions for the relationship between the amplitude of $\omega(\theta)$ and the limit of magnitude limited surveys (Roche *et al*, 1992). As increasingly faint limits are reached, simple scaling relations no longer apply to the evolution of $\omega(\theta)$ and the evolution of both galaxian properties and the correlation function, with redshift, must be accounted for. We show here that the latter cannot be straightforwardly modelled and is strongly dependent on the luminosity of the objects and the assumed power spectrum. Our technique allows the evolution in the correlation function to be easily calculated.

We commented previously that the method allows unusual power spectra to be tested quickly and with little investment of CPU time. This makes it ideal for initial studies into non-standard power spectra for which large N-body simulations do not already exist. This is particularly useful as the standard CDM power spectrum is now being placed in some doubt by a number of results which apparently show a large amount of power on large scales (see, *eg*, Maddox *et al*, 1990). A possible solution to these difficulties is to allow

more power on large scales (*eg,* Sutherland 1991). Although this approach is somewhat arbitrary at present, the measurement of the power spectrum amplitude using the COBE satellite is the first step in producing a directly measured power spectrum.

5.2 The principles of the PS formalism

We present here a derivation of the PS ansatz and a discussion of the assumptions and ideas involved. This is presented in the hope of providing background and context. It also introduces and helps to motivate our notation. For alternative derivations see PS, EFWD or Lacey & Cole (1993).

At some early epoch we imagine the Universe to be well described by an isotropic field of small random perturbations. The phases of the fluctuations are also assumed random and so the field is completely defined by its power spectrum, $P(k)$, *ie,* the amplitude of its Fourier components. The initial density perturbations are small ($\Delta\rho \ll \rho_0$) and so their evolution can be described by Vlasov's linearised equation in comoving coordinates:

$$\begin{aligned} \frac{\partial^2\delta}{\partial t^2} + 2\frac{\dot{a}}{a}\frac{\partial\delta}{\partial t} &= \frac{\nabla^2 p}{\rho_0 a^2} + 4\pi G\rho_0\delta; \\ \frac{\partial\delta}{\partial t} + \frac{1}{a}\nabla.\mathbf{v} &= 0; \end{aligned} \tag{5.1}$$

where a is the expansion factor of the Universe, t is time and δ is a density parameter, $\delta(x) \equiv (\rho(x) - \rho_0)/\rho_0$. To simplify the solution we assume that pressure effects are negligible and that the Universe is flat (in particular $\Omega = 1, \Lambda = 0$). Then, noting that $a \propto (1+z)^{-1} \propto t^{2/3}$ and that $\rho_0 \propto (1+z)^3 \propto t^{-2}$, we then obtain the solution,

$$\delta = A(x)t^{2/3} + B(x)t^{-1}, \tag{5.2}$$

where the first term describes perturbations which are growing in density contrast and the second those which are decaying. So the fluctuations grow linearly with the expansion

factor, the field growing but its shape unchanging, until $\delta \sim 1$, when the field becomes non-linear. At this point these linear equations no longer hold, the growth of the peaks speeds up and collapse occurs. PS avoids having to consider the non-linear evolution by making two further simplifying assumptions.

(i) The evolution of the field can be followed using linear theory until the clumps "turn around" and become non-linear, condensing out of the universal expansion. They assume that a perturbation can be treated like a spherically symmetric overdense region. For such a spherically symmetric overdense region this occurs for $\delta \sim \delta_c = 1.68$. A condensate which achieves this overdensity at time τ will have turned around at time $\tau/2$.

(ii) When this density contrast is achieved the perturbations collapse rapidly and independently of their surroundings. All internal structure is lost by processes such as violent relaxation (Lynden-Bell, 1967). The rest of the field sees this condensate as a point mass. The PS formalism cannot, therefore, address issues relating to substructure.

By sacrificing our knowledge of the internal structure of condensates in this way we can continue to use linear theory to evaluate the evolution of the density field. This allows a considerable simplification of the description of the evolving field, but still leaves us with the problem of counting the condensates as a function of mass. In order that a point in the field, $\mathbf{a}$, corresponds to a condensate of mass M it must fulfill two conditions. Firstly, when smoothed on a scale R, where $M \propto \rho_0 R^3$, the field at $\mathbf{a}$ must be above the threshold for collapse, $\delta(\mathbf{a}) > \delta_c$. Secondly, when smoothed on *all* larger scales the field must be below threshold, $\delta(\mathbf{a}) < \delta_c$. These two conditions are designed to ensure that at $\mathbf{a}$ a condensate of mass M will form whilst not one of greater mass. This was not the approach taken by PS. They made the assumption that if a point in the field is below threshold when smoothed on some scale, it is also below threshold when smoothed on all larger scales. So,

to form a condensate of scale R, a point must be above threshold on scale R and below threshold on scale $R + dR$. The error in this is easily demonstrated.

Following B91 we define the following notation. Suppose that when the field is smoothed on a scale R, $\delta(\mathbf{a}) > \delta_c$. We will describe this condition as $\Delta_{\mathbf{a}}(R)$. The field being below threshold we describe as $\overline{\Delta_{\mathbf{a}}}(R)$. So, according to the PS prescription the probability of forming a condensate at $\mathbf{a}$ can be expressed as $P(\Delta_{\mathbf{a}}(R), \overline{\Delta_{\mathbf{a}}(R+dR)})$. Now using Bayes theorem we have,

$$\begin{aligned} P(\Delta_{\mathbf{a}}(R), \overline{\Delta_{\mathbf{a}}(R+dR)}) &= P(\Delta_{\mathbf{a}}(R)) P(\overline{\Delta_{\mathbf{a}}(R+dR)} | \Delta_{\mathbf{a}}(R)) \\ &= P(\Delta_{\mathbf{a}}(R))(1 - P(\Delta_{\mathbf{a}}(R+dR) | \Delta_{\mathbf{a}}(R))) \\ &= P(\Delta_{\mathbf{a}}(R))\left(1 - \frac{P(\Delta_{\mathbf{a}}(R+dR), \Delta_{\mathbf{a}}(R))}{P(\Delta_{\mathbf{a}}(R))}\right). \end{aligned} \tag{5.3}$$

The assumption of PS that if a point is at threshold when the field is smoothed on some scale R, it is below threshold when the field is smoothed on all larger scales also implies that if the field is above threshold when smoothed on scale R it is also above threshold when smoothed on all *smaller* scales. We can express this assumption in our notation as the approximation $P(\Delta_{\mathbf{a}}(R), \Delta_{\mathbf{a}}(R+dR)) \simeq P(\Delta_{\mathbf{a}}(R+dR))$. So, equation (5.3) becomes

$$\begin{aligned} P(\Delta_{\mathbf{a}}(R), \overline{\Delta_{\mathbf{a}}(R+dR)}) &\simeq P(\Delta_{\mathbf{a}}(R)) - P(\Delta_{\mathbf{a}}(R+dR)) \\ &= -\frac{\partial}{\partial R} P(\Delta_{\mathbf{a}}(R))\, dR \end{aligned} \tag{5.4}$$

We aim to obtain an expression for the multiplicity of condensates of a particular scale, *ie*, the density, $\rho(R)dR$, contained in condensates of size $R \to R + dR$. This is proportional to the probability of forming an object of size R. So, we have,

$$\rho(R)\, dR = K \times -\frac{\partial}{\partial R} P(\Delta_{\mathbf{a}}(R))\, dR \tag{5.5}$$

To find K we note that if we integrate the multiplicity function over condensates of all sizes we must obtain the mean density of the field, ρ_0. Hence,

$$\begin{aligned} \int_0^\infty \rho(R)\, dR &= \rho_0 \\ \Rightarrow \rho_0 &= -K \int_0^\infty \frac{\partial}{\partial R} P(\Delta_{\mathbf{a}}(R))\, dR \\ &= K[P(\Delta_{\mathbf{a}}(R))]_\infty^0 \end{aligned} \tag{5.6}$$

Now, as the smoothing length becomes larger the field becomes flatter and so less likely to cross the threshold, *ie*, $\lim_{R\to\infty} P(\Delta_{\mathbf{a}}(R)) = 0$. Similarly, as the smoothing length becomes shorter the field oscillates wildly. The amplitude of these oscillations is much greater than the threshold value and so we can take $\delta_c \to 0$. Since $\overline{\delta} = 0$ by construction, we have $\lim_{R\to 0} P(\Delta_{\mathbf{a}}(R)) = \frac{1}{2}$. Substituting these into equation (5.6) we have $K = 2\rho_0$. Using equation (5.5) we arrive at the Press-Schechter ansatz,

$$\rho(R)\, dR = -2\rho_0 \frac{\partial}{\partial R} P(\Delta_{\mathbf{a}}(R))\, dR. \tag{5.7}$$

The derivation has been frequently criticized for the *ad hoc* nature in which the factor of 2 is justified (*eg*, Peacock & Heavens 1990). Bond *et al* (1991) clearly demonstrated that this derivation is fundamentally incorrect. They considered the value of the field at some point as a function of smoothing scale and considered when the paths in the R-δ plane cross a boundary. In this application the boundary is $\delta = \delta_c$. The most straightforward case is when sharp k-space smoothing is used (see below). In this case the path is a random walk. So, at a point in the path where $\delta = \delta_c$ the path is as likely to move above the boundary as to fall below it. At a fixed smoothing scale the distribution of δ's can be examined, and in particular the distribution of δ's for those paths which are *or have been* above the threshold. This distribution is symmetric about the boundary and can be shown to lead to equation (5.7). It is the symmetry about the boundary which leads to the factor of 2. In the case of other smoothings a knowledge of the whole of the previous path is required to assess its further progress. This prevents the distribution of δ's being cast in the form of a differential equation. So, except in the case of sharp k-space smoothing, the PS ansatz is wrong. A possible physical motivation for the factor is presented by Bower (1993), who points out that this factor must take into account the infall of mass into the condensate from below threshold areas. Using the contact probability he demonstrates that this factor is correct for top hat smoothings, but why it should be exactly a factor of 2 remains unresolved.

So, it seems that the PS formalism is fundamentally flawed. Despite this, it compares well with numerical experiments (see the following section). This has lead some to suggest that the PS formalism is little more than a fortunate accident. Nonetheless, it does appear to be useful in practice and is at least physically motivated. We will therefore simply accept the PS ansatz from here onwards.

5.3 The multiplicity function

The most straightforward application of the PS ansatz is the multiplicity function (PS, EFWD). To derive this we must first assume a form for $P(\Delta_{\mathbf{a}}(R))$. We will assume a random phase Gaussian field. There are a number of reasons for this. Firstly, this case is analytically tractable and well studied (Adler, 1981). Secondly, Gaussian fluctuations arise naturally in inflationary theories (Guth, 1981). Finally, and perhaps most fundamentally, the fluctuations are observed to be Gaussian. This was measured most recently by COBE (Smoot *et al* 1992) and perhaps more convincingly by an analysis of the observed peculiar velocities in the IRAS survey (Nusser 1993). For such a field the probability that some point, **a**, is above threshold is given by:

$$P(\Delta_{\mathbf{a}}(R_0)) = \int_{\delta_c}^{\infty} \frac{1}{\sqrt{2\pi}\sigma} \exp\left(-\frac{\delta^2}{2\sigma^2}\right) d\delta; \tag{5.8}$$

where σ^2 is the variance of the field, given by:

$$\sigma^2(R_0) = \int_0^{\infty} P(k)\widetilde{W_k}(kR_0)^2 \, d^3\mathbf{k}; \tag{5.9}$$

where $\widetilde{W_k}(kR_0)$ is the fourier transform of the smoothing or window function, $W(r/R_0)$. The precise form of the window function is ill defined, but there are three commonly used functions, each of which has advantages and disadvantages. They are the two extremes

of the 'reasonable' range of window functions (the sharp k-space and the top hat) and a more conservative mid-range choice (the Gaussian).

- **Spherical top hat** This is a Heaviside step function, ϑ, in real space. As such it is easy to interpret as picking out mass which collapses into the condensate. However, it has an oscillating form in k-space and so is difficult to understand in terms of the power it picks out on different scales.

$$\begin{aligned} W_{TH}(r/R_0) &= \frac{3}{4\pi R_0^3}\vartheta\left(1-\frac{ry_\star}{R_0}\right) \\ \widetilde{W_{TH}}(kR_0) &= \frac{3}{x^3}(\sin x - x\cos x), \qquad x \equiv \frac{kR_0}{y_\star} \end{aligned} \tag{5.10}$$

- **Sharp k-space** This is the opposite extreme, a Heaviside step function in fourier space. It picks out power on scales larger than the condensate size, but has an oscillating form in real space, which is difficult to interpret as picking out the matter which goes to form a particular condensate.

$$\begin{aligned} W_K(r/R_0) &= \frac{3y_\star^3}{4\pi R_0^3}\frac{3(\sin x - x\cos x)}{x^3}, \qquad x \equiv \frac{ry_\star}{R_0} \\ \widetilde{W_K}(kR_0) &= \vartheta\left(1-\frac{kR_0}{y_\star}\right) \end{aligned} \tag{5.11}$$

- **Gaussian** This is intermediate between the previous two because it is continuous and differentiable at all points, as is its fourier transform. This makes it physically appealing, although it is no more physically motivated than either of the previous two possibilities.

$$\begin{aligned} W_G(r/R_0) &= \frac{y_\star^3}{(2\pi R_0^2)^{3/2}}\exp\left(-\frac{r^2y_\star^2}{2R_0^2}\right) \\ \widetilde{W_G}(kR_0) &= \exp\left(-\frac{R_0^2k^2}{2y_\star^2}\right) \end{aligned} \tag{5.12}$$

We have deviated slightly from the form typically taken by other authors (*eg,* Bond *et al,* 1991) by including the constant $y_\star$. This is chosen such that $\sigma^2(R)$ is independent of the choice of window function. We choose it such that the variance is the same as that given by a top hat filter function, radius R_0. The choices of $y_\star$ this requires are given in Table 5.1 for a variety of power spectra, including the CDM-like power spectra discussed in §5.9.1. For these spectra $y_\star$ is actually a function of scale. However, over the range of sizes of condensates we are interested in this is only a weak dependence and so we adopt the values shown in Table 5.1 as constants.

So, we can now substitute equation (5.8) into the PS ansatz, giving,

$$\rho(R_0)\,dR_0 = \frac{-2\rho_0}{\sqrt{2\pi}}\exp\left(-\frac{\delta_c^2}{2\sigma^2}\right)\frac{\delta_c}{\sigma^2}\frac{\partial\sigma}{\partial R_0}\,dR_0 \tag{5.13}$$

Now, if we define a typical length scale, $R_\star$, such that $\delta_c = \sigma(R_\star)$ we have

$$\rho(R_0)\,dR_0 = \frac{-2\rho_0}{\sqrt{2\pi}}\exp\left(-\frac{1}{2}\frac{\sigma^2(R_\star)}{\sigma^2(R_0)}\right)\frac{\sigma(R_\star)}{\sigma^2(R_0)}\frac{\partial\sigma(R_0)}{\partial R_0}\,dR_0. \tag{5.14}$$

and so defining $Q = \sigma(R_\star)/\sigma(R_0)$ we have:

$$\rho(Q)\,dQ = \frac{2\rho_0}{\sqrt{2\pi}}\exp\left(-\frac{1}{2}Q^2\right)\,dQ. \tag{5.15}$$

For instance, if we once again consider a scale free hierarchical model with $P(k) = (A_0/(1+z))^2 k^n$ then the variance is given by

$$\sigma^2(R_0) = \left(\frac{A_0}{1+z}\right)^2 \frac{y_{\star,\mathrm{SK}}^{n+3}}{n+3} R_0^{-(n+3)}; \tag{5.16}$$

where $y_{\star,\mathrm{SK}}$ is the value of $y_\star$ appropriate for a sharp k-space window function. Hence, $Q = (R/R_\star)^{(n+3)/2}$ and so, substituting this into equation (5.15) we have

$$\rho(R_0)\,dR_0 = \frac{\rho_0(n+3)}{\sqrt{2\pi}}\left(\frac{R_0}{R_\star}\right)^{(n+3)/2}\exp\left(-\frac{1}{2}\left\{\frac{R_0}{R_\star}\right\}^{n+3}\right)\,d\left(\ln\left\{\frac{R_0}{R_\star}\right\}\right). \tag{5.17}$$

Power Spectrum	Top Hat	Gaussian	Sharp k-space
$n = -2$	1.00	2.11	1.87
$n = -1$	1.00	2.07	2.07
$n = 0$	1.00	2.04	2.24
$n = +1$	1.00	2.00	2.38
'CDM,' $\Gamma = 1.0$	1.00	2.11	1.90
'CDM,' $\Gamma = 0.9$	1.00	2.11	1.89
'CDM,' $\Gamma = 0.8$	1.00	2.11	1.88
'CDM,' $\Gamma = 0.7$	1.00	2.11	1.87
'CDM,' $\Gamma = 0.6$	1.00	2.12	1.86
'CDM,' $\Gamma = 0.5$	1.00	2.12	1.85
'CDM,' $\Gamma = 0.4$	1.00	2.12	1.83
'CDM,' $\Gamma = 0.3$	1.00	2.12	1.81
'CDM,' $\Gamma = 0.2$	1.00	2.13	1.79
'CDM,' $\Gamma = 0.1$	1.00	2.13	1.75

Table 5.1 The values of $y_\star$ (see text for definition) for a variety of choices of window function and power spectrum.

EFWD showed that this agreed well with the results of their scale free N-body simulations. A comparison with the more complex standard CDM spectrum is shown in Figure 5.1. This shows a comparison of the multiplicity per unit Q for the simulations of Frenk *et al* (1990). The heavy, solid line shows the PS calculation, based on equation (5.15). The data is for simulations with output times corresponding to biasing parameters of $b = 1$ (dash-double dotted line), $b = 1.3$ (dotted line), $b = 1.6$ (dot-dashed line) and $b = 2$ (dashed line). In order to calculate each line the value of $M*$ has been calculated, according to our definition, $\sigma(M_\star) = \delta_c$, taking $\delta_c = 1.68$. The derived values are given in Table 5.2. There are thus no free parameters in this comparison. The comparison is generally of a similar standard to that in EFWD. The multiplicity of the largest condensates (high Q) is generally underestimated, whilst around $M_\star$ ($Q = 1$) the multiplicity is overestimated by the PS formalism. When the N-body mass resolution becomes significant (low mass or low Q) the N-body results deviate wildly from the PS formalism. This is largely due to the friends-of-friends group finder (described in EFWD) becoming unreliable for small masses.

5.4 The cross-correlation of single mass condensates

In the following section we will derive an expression for the cross-correlation of condensates of size R_1 with those of size R_2 as a function of their separation, $\mathbf{R}$, $\xi(\mathbf{R})$. We will do this by using conditional probabilities, as suggested by B91. Consider two points in a field, $\mathbf{a}$ and $\mathbf{b}$, such that $\mathbf{a} - \mathbf{b} = \mathbf{R}$. To find the cross-correlation function we require the probability that a condensate exists at $\mathbf{a}$ given that a condensate exists at $\mathbf{b}$. Expressing this using the notation defined above, we require the probability $P(\Delta_{\mathbf{a}}(R_1), \overline{\Delta_{\mathbf{a}}(R_1 + dR_1)} | \Delta_{\mathbf{b}}(R_2), \overline{\Delta_{\mathbf{b}}(R_2 + dR_2)})$. Using Bayes theorem we simply

Biasing, b	$M_\star$ / particle mass	$R_\star$ / h^{-2}Mpc
2.0	11	1.94
1.6	28	2.64
1.3	62	3.44
1.0	156	4.68

Table 5.2 The calculated values of $M_\star$ for a standard CDM power spectrum assuming a top-hat window function (the N-body simulation is in a box of size $90h^{-2}$Mpc).

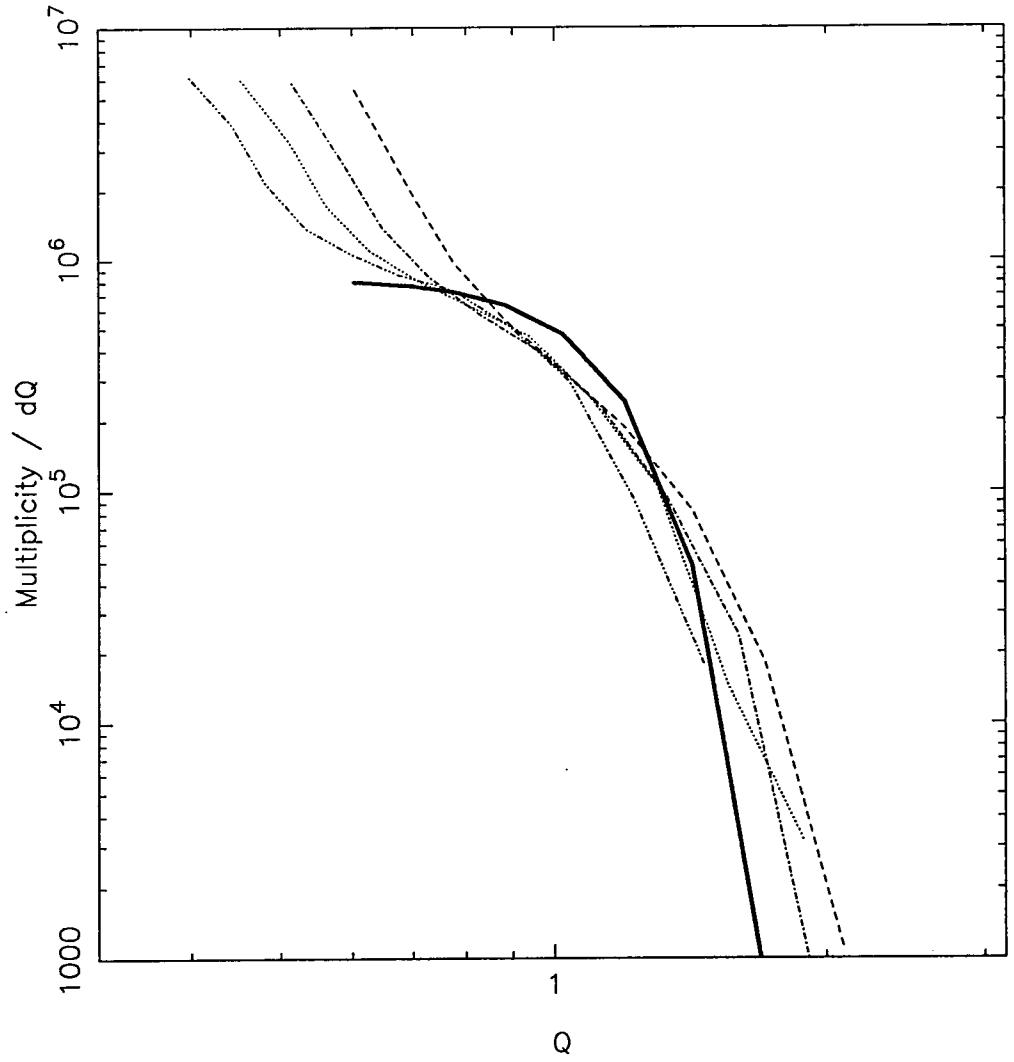

Figure 5.1. The multiplicity of condensates per unit interval in Q. The heavy, solid line is the PS formalism prediction and the broken lines are the results of the N-body simulations of Frenk *et al* (1990). Specifically, the double dot-dashed line is for $b = 1$, the dotted line for $b = 1.3$, the dot-dashed line for $b = 1.6$ and the dashed line for $b = 2$.

obtain,

$$P(\Delta_{\mathbf{a}}(R_1), \overline{\Delta_{\mathbf{a}}(R_1+dR_1)}|\Delta_{\mathbf{b}}(R_2), \overline{\Delta_{\mathbf{b}}(R_2+dR_2)}) = \frac{P(\Delta_{\mathbf{a}}(R_1), \overline{\Delta_{\mathbf{a}}(R_1+dR_1)}, \Delta_{\mathbf{b}}(R_2), \overline{\Delta_{\mathbf{b}}(R_2+dR_2)})}{P(\Delta_{\mathbf{b}}(R_2), \overline{\Delta_{\mathbf{b}}(R_2+dR_2)})}. \tag{5.18}$$

Making the assumption that $P(\Delta_{\mathbf{b}}(R_2), \Delta_{\mathbf{b}}(R_2+dR_2)) \simeq P(\Delta_{\mathbf{b}}(R_2+dR_2))$, we find:

$$\begin{aligned} P(\Delta_{\mathbf{b}}(R_2), \overline{\Delta_{\mathbf{b}}(R_2+dR_2)}) &\simeq -\frac{\partial}{\partial R_2} P(\Delta_{\mathbf{b}}(R_2))\, dR; \\ P(\Delta_{\mathbf{a}}(R_1), \overline{\Delta_{\mathbf{a}}(R_1+dR_1)}, \Delta_{\mathbf{b}}(R_2), \overline{\Delta_{\mathbf{b}}(R_2+dR_2)}) &\simeq -\frac{\partial^2}{\partial R_1 \partial R_2} P(\Delta_{\mathbf{a}}(R_1), \Delta_{\mathbf{b}}(R_2))\, dR; \end{aligned} \tag{5.19}$$

in a similar fashion to §5.3. Substituting this into (5.18) we have

$$P(\Delta_{\mathbf{a}}(R_1), \overline{\Delta_{\mathbf{a}}(R_1+dR_1)}|\Delta_{\mathbf{b}}(R_2), \overline{\Delta_{\mathbf{b}}(R_2+dR_2)}) = \frac{\partial^2 P(\Delta_{\mathbf{a}}(R_1), \Delta_{\mathbf{b}}(R_2))}{\partial R_1 \partial R_2} \Big/ \frac{\partial P(\Delta_{\mathbf{b}}(R_2))}{\partial R_2}. \tag{5.20}$$

Substituting this into the PS ansatz we have the following for the multiplicity of $R_1 - R_2$ pairs with separation $\mathbf{R}$.

$$\rho(\mathbf{R}; R_1, R_2)\, dR_1\, dR_2 = -2\rho_0 \frac{\partial^2 P(\Delta_{\mathbf{a}}(R_1), \Delta_{\mathbf{b}}(R_2))}{\partial R_1 \partial R_2} \Big/ \frac{\partial P(\Delta_{\mathbf{b}}(R_2))}{\partial R_2}\, dR_1\, dR_2 \tag{5.21}$$

Now, the correlation function is given by,

$$\begin{aligned} \xi(\mathbf{R}; R_1, R_2) &= \frac{\langle \rho(\mathbf{x})\rho(\mathbf{x}+\mathbf{R})\rangle_{\mathbf{x}}}{\langle \rho(\mathbf{x})\rangle^2_{\mathbf{x}}} - 1 \\ &= \frac{\langle \rho(\mathbf{a})\rho(\mathbf{R}; R_1, R_2)\rangle_{\mathbf{a}}}{\langle \rho(\mathbf{a})\rangle^2_{\mathbf{a}}} - 1 \end{aligned} \tag{5.22}$$

Equation (5.21) has no dependence on any particular point in the field. So, it can be taken outside the average in equation (5.22). This gives:

$$\xi(\mathbf{R}; R_1, R_2) = \frac{\rho(\mathbf{R}; R_1, R_2)}{\overline{\rho}} - 1; \tag{5.23}$$

and so the correlation function is given by

$$\xi(\mathbf{R}; R_1, R_2) = \frac{\partial^2 P(\Delta_{\mathbf{a}}(R_1), \Delta_{\mathbf{b}}(R_2))}{\partial R_1 \partial R_2} \Big/ \frac{\partial P(\Delta_{\mathbf{a}}(R_1))}{\partial R_1} \frac{\partial P(\Delta_{\mathbf{b}}(R_2))}{\partial R_2} - 1. \tag{5.24}$$

5.4.1 Correlations in a scale free Gaussian field

As an example we will now again assume that the perturbation field is a scale free Gaussian field and that the power spectrum has the form $P(k) = (A_0/(1+z))^2 k^n$. The probability of the field having value δ_1 at **a** whilst having value δ_2 at **b** is then given by the bivariate Gaussian (Adler, 1981):

$$P(\delta_1,\delta_2)\,d\delta_1 d\delta_2 = \frac{1}{\sqrt{2\pi}}\frac{1}{(\sigma_1^2\sigma_2^2-\sigma_{12}^4)^{1/2}}\exp\left(-\frac{1}{2}\frac{\sigma_1^2\sigma_2^2}{\sigma_1^2\sigma_2^2-\sigma_{12}^4}\left\{\frac{\delta_1^2}{\sigma_1^2}-2\delta_1\delta_2\frac{\sigma_{12}^2}{\sigma_1^2\sigma_2^2}+\frac{\delta_2^2}{\sigma_2^2}\right\}\right)d\delta_1 d\delta_2. \tag{5.25}$$

Here σ_i^2 is the variance of the field when smoothed on scale R_i and σ_{12} is the cross-correlation of the two fields, which is given by:

$$\sigma_{12}^2 = \int_0^\infty |\delta_k|^2 \widetilde{W_k}(kR_1)\widetilde{W_k}(kR_2)\mathrm{e}^{-\mathbf{ik}\cdot(\mathbf{a}-\mathbf{b})}\,d^3\mathbf{k}. \tag{5.26}$$

So, if we define the correlation coefficient $r_{cc} = \sigma_{12}^2/\sigma_1\sigma_2$, $Q = (R/R_*)^{(n+3)/2} = \delta_c/\sigma(R)$ and $\Delta_i = \frac{\delta_i}{\delta_c}$ the probability we require is:

$$P(\Delta_{\mathbf{a}}(R_1),\Delta_{\mathbf{b}}(R_2)) = \int_1^\infty\int_1^\infty d\Delta_1 d\Delta_2 \frac{Q_1Q_2}{\sqrt{1-r_{cc}^2}} \times \exp\left(\frac{-1}{2(1-r_{cc}^2)}\left\{\Delta_1^2Q_1^2 - 2r_{cc}Q_1Q_2\Delta_1\Delta_2 + \Delta_2^2Q_2^2\right\}\right) \tag{5.27}$$

It is an apparently straightforward task to use this in equation (5.24) to obtain the correlation function. However, there is a computational problem. Equation (5.27) is symmetrical in Q_1 and Q_2, and this leads to a cusp along the line $Q_1 = Q_2$. So, the first derivative is not defined along this line. This line is particularly important as it is along this line that the derivative of the function is required to calculate the autocorrelation function. So, it is not possible to calculate the autocorrelation function using the numerical prescription

$$\frac{\partial^2 f(x',y')}{\partial x\partial y} \simeq \frac{f(x'+h,y'+h)-f(x'+h,y'-h)-f(x'-h,y'+h)+f(x'-h,y'-h)}{4h^2} \tag{5.28}$$

for h sufficiently small. This is because the first derivative is not uniquely defined at the cusp. In our case it changes sign depending upon which side of the cusp is considered. This difference is negated by taking the second derivative. So, the second derivative is defined, but we must take the limit from one side of the cusp only. Hence, we calculate the second derivative using the alternative approximation

$$\frac{\partial^2 f(x',y')}{\partial x \partial y} \simeq \frac{f(x'+h,y'+h) - f(x'+h,y') - f(x',y'+h) + f(x',y')}{h^2}. \tag{5.29}$$

This does converge sensibly and so we are able to calculate the autocorrelation function. For ease of programming this approximation is then used for all choices of Q_1 and Q_2.

In Figure 5.2 we show some correlation functions calculated using this technique for $n = -1$. We plot here the autocorrelation functions of 5, 4, 3, 2, 1 and $\frac{1}{2}R_\star$ condensates. The work of Kaiser (1984) suggests that we should expect more massive (and hence larger) condensates to be more strongly clustered. This is in general true, if we neglect the $R_\star$ correlation function. We also commented above that we would expect the correlation functions to tend, for large R, to the slope of the field correlation function, in this case $\gamma = 2$. Again all except the $R_\star$ correlation function shows the expected behaviour. The $R_\star$ correlation function shows weaker clustering than the $\frac{1}{2}R_\star$ correlation function and falls off with a much steeper slope than the expected $\gamma = 2$. We will return the anomalous behaviour of the $R_\star$ correlation function in a later section.

5.5 The correlations of condensates with a range of masses

The above result, whilst useful, is atypical of astronomical problems. It is more typical to have condensates which cover a range of masses, and so the following extension will be

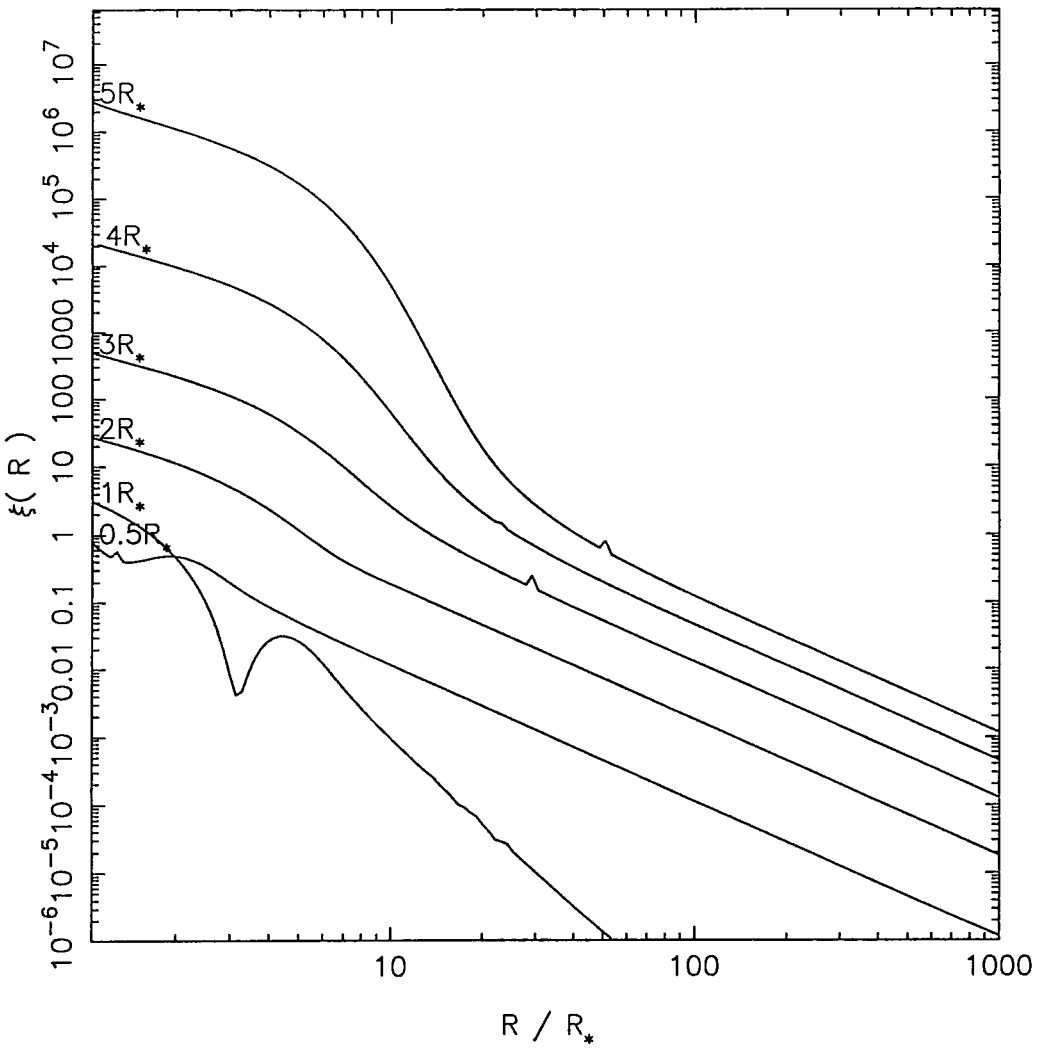

Figure 5.2. The autocorrelation functions of condensates of 5, 4, 3, 2, 1 and $\frac{1}{2}R_\star$ for a scale free power spectrum with $n = -1$. Larger condensates are generally more strongly clustered, but note that $\frac{1}{2}R_\star$ are more strongly clustered than $R_\star$ objects.

more useful in practice. Also, since the calculation of a differential is not required it is in most cases significantly faster than the method described above.

For this we must first extend the usual form of Bayes' theorem:

$$P(A|B) = \frac{P(A,B)}{P(B)}. \tag{5.30}$$

Now, consider three events A, B and C of which B and C are mutually exclusive. Given this exclusivity we can use the notation $B \cup C$ to indicate C or B *but not both.* So, we can extend Bayes' theorem to give:

$$\begin{aligned} P(A|B \cup C) &= \frac{P(A, B \cup C)}{P(B \cup C)} \\ &= \frac{P(A,B) + P(A,C)}{P(B) + P(C)} \end{aligned} \tag{5.31}$$

Now, suppose that rather than A we have N mutually exclusive events, $A_1, A_2, \ldots, A_N$ and that rather than B and C we have M similarly exclusive events $B_1, B_2, \ldots, B_M$. It is then an obvious extension of equation (5.31) to give

$$P(A_1 \cup A_2 \cup \ldots \cup A_N | B_1 \cup B_2 \cup \ldots \cup B_M) = \frac{\sum_{j=1}^{N} \sum_{i=1}^{M} P(A_j, B_i)}{\sum_{i=1}^{M} P(B_i)}. \tag{5.32}$$

Finally, we suppose that each of the sets, A_j and B_i, is infinitesimal and can be described by two continuous variables, x_1 and x_2 respectively. We then have:

$$P(x_1 \in [x_1', x_1'']|x_2 \in [x_2', x_2'']) = \frac{\int_{x_1'}^{x_1''} \int_{x_2'}^{x_2''} P(x_1, x_2)\, dx_2\, dx_1}{\int_{x_2'}^{x_2''} P(x_2)\, dx_2}. \tag{5.33}$$

Now, we identify the continuous variable with the smoothing length applied to the primordial density field, R_i. However, the condition $\Delta_{\mathbf{a}}(R_1 \in [R_1', R_1''])$ does not satisfy our requirement for mutual exclusivity. This requirement is satisfied by the joint condition $\Delta_{\mathbf{a}}(R_1), \overline{\Delta_{\mathbf{a}}(R_1 + dR_1)}$ for $R_1 \in [R_1', R_1'']$. We will define this joint event as $\Delta_{\mathbf{a}}'(R_1 \in [R_1', R_1''])$. So, we have

$$P(\Delta_{\mathbf{a}}'(R_1 \in [R_1', R_1'']) | \Delta_{\mathbf{b}}'(R_2 \in [R_2', R_2'']) = \frac{\int_{R_1'}^{R_1''} \int_{R_2'}^{R_2''} P(\Delta_{\mathbf{a}}'(R_1), \Delta_{\mathbf{b}}'(R_2))\, dR_1\, dR_2}{\int_{R_2'}^{R_2''} P(\Delta_{\mathbf{b}}'(R_2))\, dR_2} \tag{5.34}$$

This is analogous to equation (5.18), and derivation which follows is similar, except the differentials are replaced with finite differences. So, we have the correlation function,

$$\xi(\mathbf{R}) = -1+ \frac{P(\Delta_{\mathbf{a}}(R_1'),\Delta_{\mathbf{b}}(R_2')) - P(\Delta_{\mathbf{a}}(R_1'),\Delta_{\mathbf{b}}(R_2'')) - P(\Delta_{\mathbf{a}}(R_1''),\Delta_{\mathbf{b}}(R_2')) + P(\Delta_{\mathbf{a}}(R_1''),\Delta_{\mathbf{b}}(R_2''))}{P(\Delta(R_1'))P(\Delta(R_2')) - P(\Delta(R_1'))P(\Delta(R_2'')) - P(\Delta(R_1''))P(\Delta(R_2')) + P(\Delta(R_1''))P(\Delta(R_2''))}. \tag{5.35}$$

In this equation we have suppressed the suffixes in the denominator for conciseness and because the point at which the denominator is calculated is of no consequence. Note that if $R_i'' = R_i' + dR_i$ we return to the case of single mass condensate correlation functions (equation (5.24)).

5.6 Changes in the window function

Bond *et al* (1991) showed that the precise form of the window function does have a small effect on the form of the multiplicity function. What is not clear, however, is what the window function should be. So, we require our expression to be reasonably robust to changes in the form of the window function.

In Figure 5.3 we show the correlation function of condensates in the range $3 \leq R/R_\star \leq 30$ calculated using each of the window functions listed previously (Gaussian (solid), top hat (dashed) and sharp k-space (dot-dashed)). There is some ringing seen, particularly for the sharp k-space window function and for $n = 0$ and $n = +1$. However, if this ringing is neglected (it could be smoothed over in practice) there is good agreement for $R/R_\star > 0.1$.

The ringing has a physical interpretation. Consider objects which are solid spheres of radius r. Now, consider their autocorrelation function, separations being measured as the

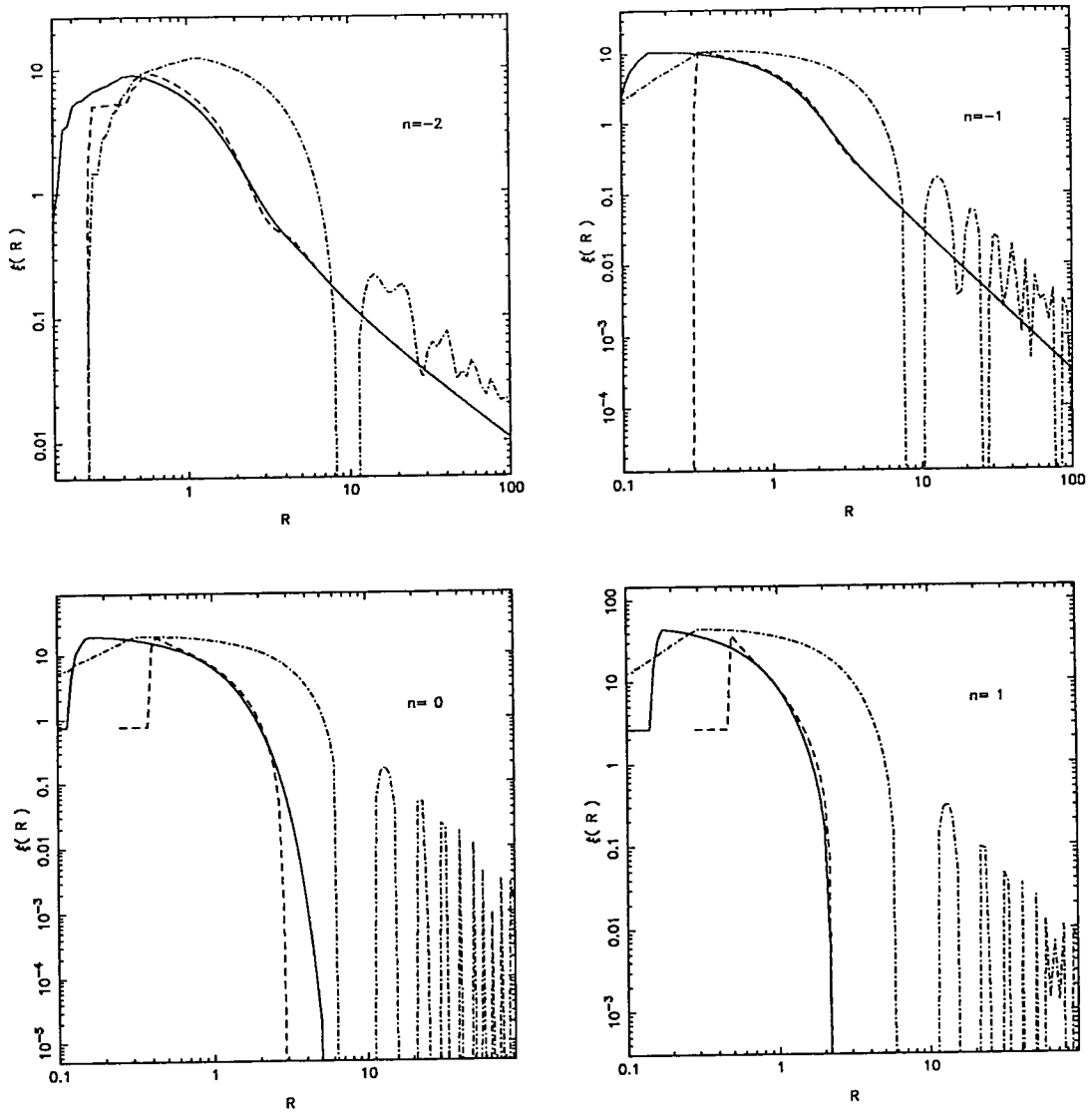

Figure 5.3. A comparison of the autocorrelation functions of objects in the range $3 \leq R/R_\star \leq 30$ found using different window functions and values of n as a function of $R/R_\star$. In each panel the solid line shows the correlation function found using a Gaussian window function, the dashed line that using a top hat window function and the dot-dashed line that using a sharp k-space window function. The value of n used is indicated in the panel. The correlations found using different window functions, although showing different degrees of ringing, are in good agreement to within $R/R_\star \ll 0.1$.

distance between their centres. Clearly $\xi(R) = -1$ for $0 < R < 2r$. It can then become positive. Now suppose that the clustering of these spheres is such that it is highly likely that each sphere has at least one close companion (nearly touching). We would then expect the correlation function to rise briefly around $2r$ and then fall, peaking again at around $4r$. This oscillation would then continue, becoming weaker with increased separation because of the greater volume available. Now, if we consider spheres with a range of sizes such oscillations would occur with a range of frequencies and interference would follow. Thus, the ringing would be diminished. The case of single sized solid spheres is analogous to using single mass condensates and the second case is analogous to considering condensates with a range of masses. In Figure 5.3 we also see a dip in the correlation function at the smallest separations, corresponding to the drop to -1 between 0 and $2r$ mentioned above. Thus the position of this dip may give some indication of the size of the condensates considered. This effect is also seen in observed correlation functions, for instance the brightest 100 AGS correlation function of Moore et al (1993) (see Figure 5.7). In practice we also see a reduction in ringing when we use a Gaussian window function. Using a window function of this kind makes the edges of the spheres in our analogy 'soft,' so the oscillation is smoothed.

5.7 Large separations and other models

5.7.1 The large separation limit

In the case of scale free power spectra, $P(k) \propto k^n$, there have previously been a number of attempts to model the correlation function in an analytical fashion. So we will here show that in the limit of large separations we agree with the work of previous authors

and develop an analytical approximation which provides more insight into the clustering of condensates than equation (5.24) does in itself.

Peebles (1980) showed that the mass correlation function for the field goes like $\xi(r) \propto r^{-(n+3)}$ for large separations. For large separations we expect the condensates to simply act as tracers of the field, and so they should also obey this proportionality. To obtain the large separation limit of equation (5.24) we must first find the large separation limit of σ_{12}^2. Integrating over angles and changing variables we have:

$$\sigma_{12}^2 = \left(\frac{A_0}{1+z}\right)^2 4\pi R^{-(n+3)} \int_0^\infty x^{n+1} \sin(x) \widetilde{W}(xR_1/R) \widetilde{W}(xR_2/R)\, dx. \tag{5.36}$$

The window function varies much more slowly than $\sin x$ and so we can use the approximation that as $R \to \infty$ the arguments of $\widetilde{W}$ go to zero and $\widetilde{W}(xR_i/R) \to 1$. So, the large separation limit of the variance is given by

$$\sigma_{12}^2 = \left(\frac{A_0}{1+z}\right)^2 4\pi R^{-(n+3)} \int_0^\infty x^{n+1} \sin(x)\, dx. \tag{5.37}$$

We evaluate this integral by evaluating $\oint z^{n+1} \mathrm{e}^{-z}\, dz$ around the two complex paths (one in each quadrant) shown in Figure 5.4. This gives

$$\sigma_{12}^2 = \left(\frac{A_0}{1+z}\right)^2 4\pi \tilde{\Gamma}(n+2) R^{-(n+3)}, \tag{5.38}$$

where $\tilde{\Gamma}(n) = \Gamma(n+1)\frac{\sin(n\pi/2)}{n}$. The variance is given by equation (5.16), so the large separation approximation to the correlation coefficient is

$$r_{cc} = (n+3)\tilde{\Gamma}(n+2) y_{\star,\mathrm{SK}}^{-(n+3)} Q^{-2} Q_1 Q_2. \tag{5.39}$$

Using the Gaussian probability function the large separation limit of equation (5.24) is

$$\xi(Q) = \frac{\frac{\partial^2}{\partial Q_1 \partial Q_2} r_{cc} \int_1^\infty \int_1^\infty Q_1^2 Q_2^2 \Delta_1 \Delta_2 \exp(-\frac{1}{2}(\Delta_1^2 Q_1^2 + \Delta_2^2 Q_2^2))\, d\Delta_1 d\Delta_2}{\frac{\partial^2}{\partial Q_1 \partial Q_2} \int_1^\infty \int_1^\infty Q_1 Q_2 \exp(-\frac{1}{2}(\Delta_1^2 Q_1^2 + \Delta_2^2 Q_2^2))\, d\Delta_1 d\Delta_2}. \tag{5.40}$$

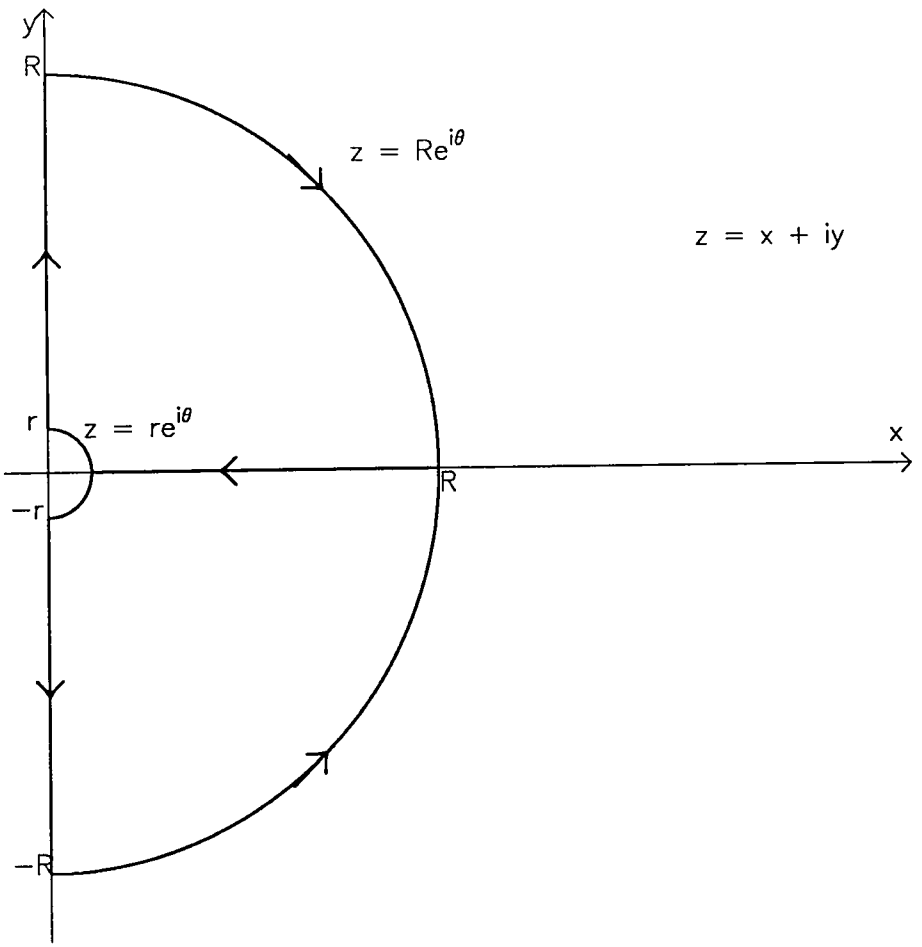

Figure 5.4. The two paths (one in the upper quadrant, one in the lower) around which the integral $\oint z^{n+1}\mathrm{e}^{-z}\,dz$ is evaluated in order to evaluate $\int_0^\infty x^{n+1}\sin(x)\,dx$.

The denominator in this expression becomes $\exp(-\frac{1}{2}(Q_1^2+Q_2^2))$, whilst the numerator reduces to $(n+3)\tilde{\Gamma}(n+2)y_{\star,\mathrm{SK}}^{-(n+3)}Q^{-2}(1-Q_1^2)(1-Q_2^2)\exp(-\frac{1}{2}(Q_1^2+Q_2^2))$. Combining these the large separation limit of the condensate correlation function is

$$\xi(R) = (n+3)\tilde{\Gamma}(n+2)\left(\frac{Ry_{\star,\mathrm{SK}}}{R_\star}\right)^{-(n+3)}\left(\left(\frac{R_1}{R_\star}\right)^{n+3}-1\right)\left(\left(\frac{R_2}{R_\star}\right)^{n+3}-1\right) \qquad (5.41)$$

From Peebles (1980) the underlying mass field has a correlation function given by $\xi_\rho(R) = (A_0/(1+z))^2\tilde{\Gamma}(n+2)R^{-(n+3)}$. Noting that $\delta_c^2 = (A_0/(1+z))^2(n+3)^{-1}(y_{\star\mathrm{SK}}/R_\star)^{n+3}$ we have

$$\xi(R) = \frac{\xi_\rho}{\delta_c^2}\left(\left(\frac{R_1}{R_\star}\right)^{n+3}-1\right)\left(\left(\frac{R_2}{R_\star}\right)^{n+3}-1\right). \qquad (5.42)$$

Equations (5.41) and (5.42) give considerable insight into the relationship between the sizes of objects and their clustering properties. For $R_i \gg R_\star$ the term $(R_i/R_\star)^{n+3}-1 \simeq (R_i/R_\star)^{n+3}$, and thus (at large separations) the amplitude of the correlation function increases strongly as the size of the condensates is increased. This is the same effect as noted by Rice (1954) (also Kaiser, 1984, and Kashlinsky, 1986): rarer peaks are more strongly clustered than peaks of average height. This is demonstrated in Figure 5.2. For $R_i \ll R_\star$, $(R_i/R_\star)^{n+3}-1 \simeq -1$, so that in this regime the clustering amplitude has a constant value. This is due to the integral in the numerator of equation (5.41) tending towards a constant value. This integral, combined with that in the denominator, yields the average peak height corresponding to objects of size R_i. For rare objects this is strongly dependent on the dimensionless threshold $\delta_c/\sigma_i = Q_i$. However, for small objects the integral approaches a constant value, and the correlation of the objects is driven by the dependence of r_{cc} on Q_i. Specifically, r_{cc} increases linearly with Q_i, but this means that the *condensates* of size R_i (and no larger) that are "left behind" are anti-clustered with respect to larger masses (see below), and positively correlated with themselves. In the intermediate regime, $R_i \simeq R_\star$, $(R_i/R_\star)^{n+3}-1 \simeq 0$. The two effects discussed above cancel, and no correlation is observed. These effects are clearly demonstrated in Figure 5.2.

We see there that the amplitude of the correlation function drops as $R/R_\star$ falls, reaching a minimum for $R/R_\star = 1$ and then rising again as $R/R_\star$ falls below 1. In addition the autocorrelation function of $R_\star$ objects falls much more rapidly than the field correlation function. Thus, at large separations it becomes consistent with zero. In the regime where $R_1 \gg R_\star$ and $R_2 \ll R_\star$, $((R_1/R_\star)^{n+3} - 1)((R_2/R_\star)^{n+3} - 1) < 0$ and an anticorrelation is indeed observed. These effects were first noted by Kashlinsky (1991). It also worth noting that as the condensates become smaller ($R_i/R_\star \to 0$) the correlation function does not approach the field correlation function, as might be naively expected, but tends towards ξ_ρ/δ_c^2.

A physical interpretation of these effects is demonstrated schematically in Figure 5.5. This Figure is a simplified view of a slice through the universe. The circles represent the pre-collapse sizes and positions of condensates. Firstly, consider a population of condensates with $R_i \gg R_\star$ (the largest circles in Figure 5.5). These are strongly clustered, populating the regions where the underlying field is more dense than average. A second population of condensates with $R_i \ll R_\star$ (the smallest circles in Figure 5.5) are unlikely to be found in these regions as they would tend to be merged into the larger condensates. So, these are found in regions where the field is less dense than average. Hence, each of these two populations are themselves clustered in distinct regions of the universe (a positive autocorrelation), but are anti-correlated with respect to the other population. The $R_\star$ objects (intermediate sized circles in Figure 5.5) then tend to lie along the boundaries between these regions and so have a low clustering amplitude. To summarise, our work predicts 'scale segregation,' where super-$R_\star$ and sub-$R_\star$ condensates occupy physically distinct regions of the Universe. This segregation was also first suggested by Kashlinsky (1991). It is currently very difficult to test this interpretation using N-body codes as when $M_\star$ is small it is difficult to construct a sufficiently large sample of sub-$R_\star$ condensates, and conversely for realisations with a large $M_\star$. Those with intermediate $M_\star$ tend to leave

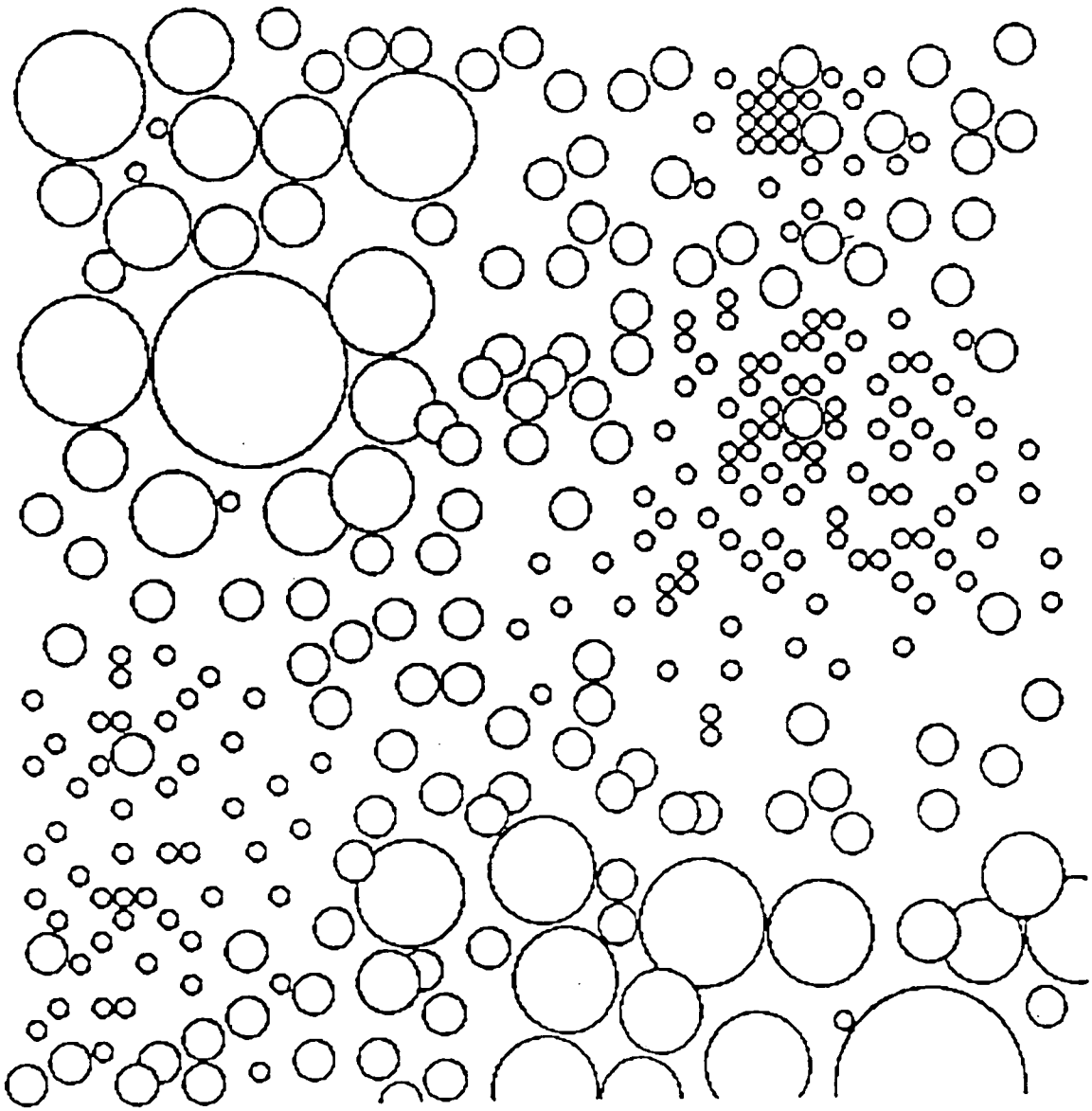

Figure 5.5. A slice through a schematic universe demonstrating 'scale segregation.' (See text for discussion).

two sub-samples which are both too small for this comparison. Simulations with a large number of particles and an intermediate $M_\star$ are required before a confident comparison can be made. However, this picture is supported by the findings of Lacey & Cole (1993) who found that condensates with masses greater than $M_\star$ tended to merge with others which are more massive than $M_\star$. This would lead naturally to the formation of large voids containing only a few small condensates.

5.7.2 Comparison with previous analytical work

The first comparison that can be made is with the slope of the field correlation function (Peebles, 1980). As can be seen from equation (5.41), the expected slope is preserved by the non-linear transformation that we have applied. This is also demonstrated in Figure 5.6 in which we show the autocorrelation function of $2R_\star$ condensates and the results of equation (5.41). At large separations the two are clearly consistent. Note that for $n = 0$ the scales in Figure 5.6 are linear and for $n = +1$ we have plotted the logarithm of $-\xi$ against the logarithm of the separation.

Kaiser (1984) studied the clustering of Abell clusters by equating rare objects with high peaks in the density field. We show agreement with this work in the limit of large smoothing scales. However, it should be noted that the amplification in the clustering amplitude is not simply proportional to the square of the dimensionless threshold (*ie*, δ_c^2/σ^2), but also depends on the effect of varying the smoothing scale on the field correlation function. Indeed, in Table 1 of Kaiser (1984) the amplification factor increases with increasing smoothing scale, despite the dimensionless threshold level falling. In addition, we agree with his comment that the cross correlation is the geometric mean of the autocorrelation functions of the two sets, although our work also shows that in the case where $R_1 > R_\star$ and $R_2 < R_\star$ (or *vice versa*) the negative value of the square root is the appropriate choice.

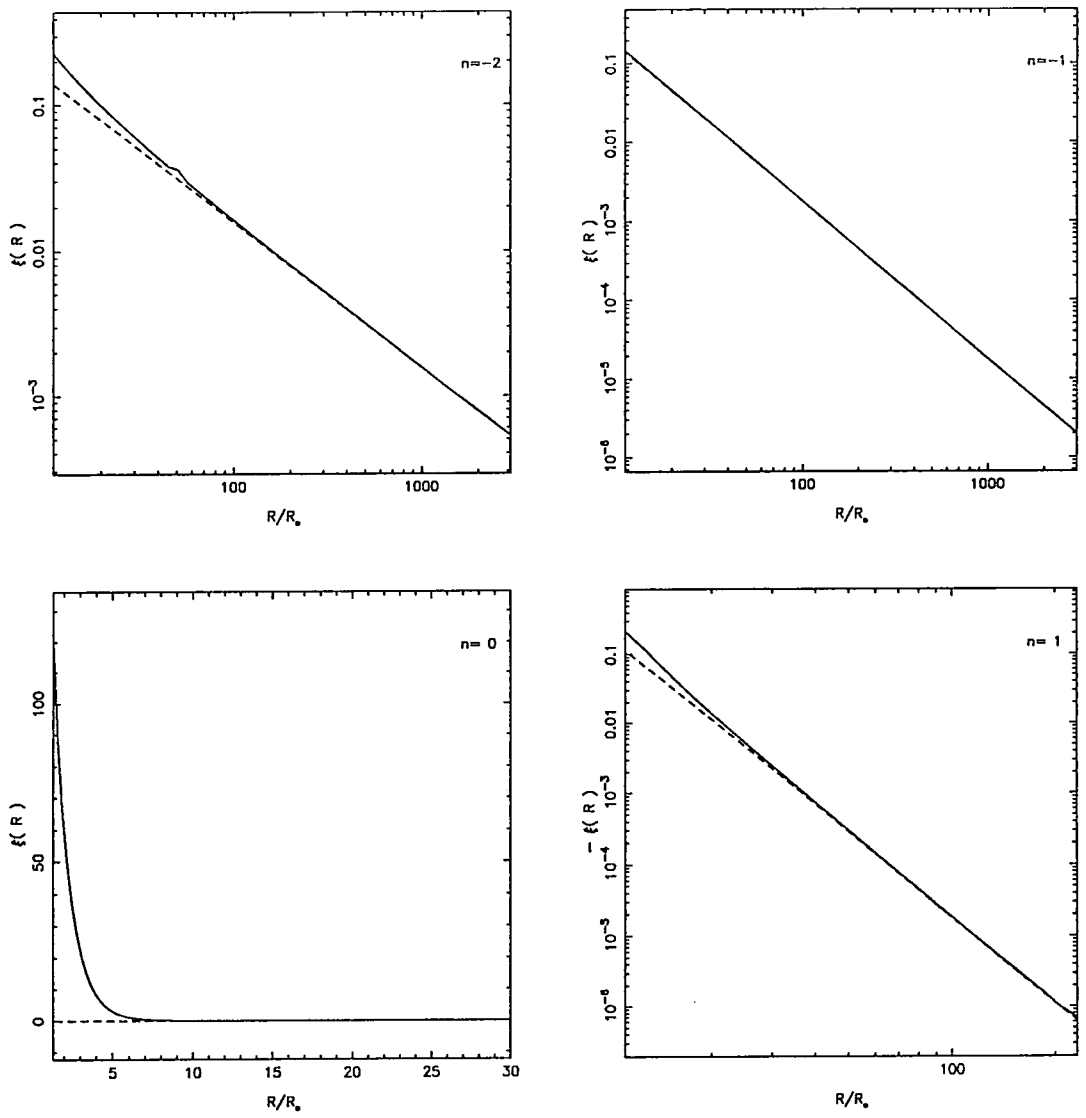

Figure 5.6. A comparison of our predictions for the autocorrelation function of 2 R_* condensates with the correlation function given by Equation (5.41). Our numerical calculations are shown as a solid line. The large separation approximation, shown dashed, is a power-law of slope $-(n+3)$. Note that the lower two panels are plotted on different scales. For $n = 0$ we have used a linear scale, whilst for $n = +1$ we have plotted $-\xi$ against R/R_*.

Two studies more similar to, and entirely consistent with our own are those of Kashlinsky (1986, 1991). In Kashlinsky (1986) he derives an expression for the two point correlation function which is identical to equation (5.24). However this work has been misinterpreted (*eg,* Henry 1990) as indicating that the field correlation function (Kashlinsky's ξ_N) is independent of smoothing scale. In our work we have made this dependence clear. In Kashlinsky (1991) he derives a general expression for the N-point correlation function, and makes the dependence of ξ_N on smoothing clear. Although this work does not explicitly use the PS formalism, it is based on broadly similar principles. Our equation (5.41) is consistent with his expression for the large separation limit of the two point correlation function. As we commented above this paper also notes the 'scale segregation' effect.

5.7.3 An alternative interpretation

For regions in which locally $\Omega \neq 1$ the solution of Vlasov's equations which we have used (equation 5.2) is no longer applicable. There is also some further expansion or contraction when $\Omega < 1$ and $\Omega > 1$ respectively. However, in general this extra evolution can be included in a single factor of $1 + \overline{\delta}$, where $\overline{\delta}$ is the mean overdensity of the region being considered. This mapping takes the positions of the condensates from Lagrangian to Eulerian coordinates. If this extra factor is also required in our work then the correct interpretation of equations (5.24), (5.35) and (5.41) would be that they give the biasing of the condensates. Thus $M_\star$ condensates would be unbiased, rather than unclustered. Unfortunately there is no clear test to differentiate between these two possible interpretations. However, we feel that our interpretation is correct for a number of reasons. The principal reason is that in regions where Ω deviates significantly from 1 the field is non-linear. As we have already discussed, we do not expect our technique to hold in these regimes. In the regions where we expect our technique to be effective the field is in the linear regime and $\Omega \sim 1$. As well as defining the region where our technique should work,

this also defines those regions for which any Eulerian correction is unimportant. Hence, we believe that in the regimes where the PS formalism is effective an Eulerian correction is not necessary. In those regions where an Eulerian correction is necessary, non-linear effects become important and invalidate the Press-Schechter approach.

5.8 Comparison with N-body codes

5.8.1 Scale free power-spectra

We compare our calculations with the scale free N-body simulations of EFWD. Using the friends-of-friends groups finding algorithm described in their paper, we derive mass weighted correlation functions for groups containing 3 or more particles. The derived correlations are expected to be reliable only for separations less than one-tenth of the box-size used for the simulation. Also, the reliability of the group finding algorithm is uncertain for groups of masses as small as 3 particles. However, it is not possible to use a larger lower mass limit (say groups of 8 particles) as this would reduce the number of groups to such an extent that the errors would make the comparison almost meaningless. This test is, then, far from satisfactory.

In order to make a comparison with our calculations, we must determine a strategy for converting the measured group mass into a filter function size. Since EFWD show that the mass distribution is reasonably well reproduced by the basic PS formalism, we may reduce this problem to that of relating the observed characteristic mass, $M_\star$, to an appropriate characteristic filtering scale, $R_\star$. In previous comparisons, this complication can be avoided because $R_\star$ does not explicitly enter the PS multiplicity function. However,

in our expression for the correlation function, $R_\star$ is explicitly required to set the physical scale of object separations. By including $y_\star$ in the window functions we have ensured that, irrespective of window function, an object of a certain relative scale, $R/R_\star$, corresponds to an object of a specific rarity, and, thus, to an object of a specific mass. Hence, there is a unique relationship between the mass and radius of condensates, independent of window function. We choose to use the relationship

$$R_\star = \sqrt[3]{\frac{3}{4\pi}\frac{M_\star}{(1+\delta_c)\rho_0}}, \tag{5.43}$$

This is based on smoothing the field with a spherical top hat, where the included mass is easily visualised. Bower (1993) presents a more detailed discussion of the reasons for choosing this interpretation.

Our definition of $M_\star$ (*cf*, B91) differs from that of EFWD and so using equation (15) of EFWD and taking this difference into account we have:

$$M_\star = 2^{-3/(3+n)} C_n a^{6/(3+n)}; \tag{5.44}$$

where a is the expansion factor of the simulation and $C_n = 0.80$, 0.71, 0.53 and 1.23 for $n = +1, 0, -1$ and -2 respectively. Direct fitting of the measured multiplicity function does not significantly change these results. For each value of n we have 3 realisations at 2 expansion factors. The comparisons with these are shown in Figure 5.7.

In all cases we see acceptable agreement at separations where $\xi \lesssim 1$ and R is less than one-tenth of the box size, although we show a systematic trend to underestimate the correlation function. However, considering that there are no free parameters in this comparison and that there is considerable uncertainty in the 'correct' form of equation (5.43) the comparison seems reasonable. To demonstrate the effect of this uncertainty we also show

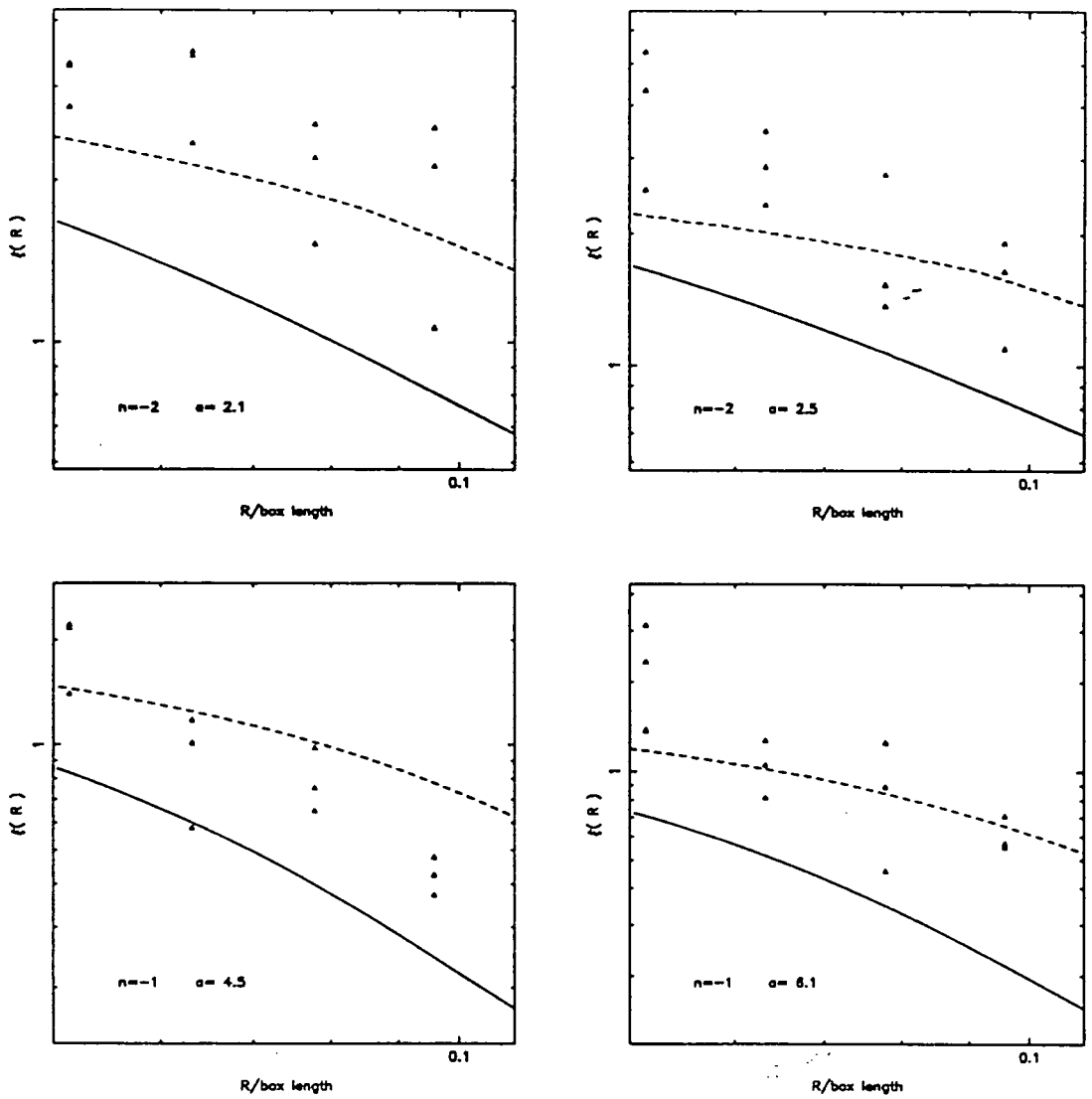

Figure 5.7. A comparison of mass weighted correlation functions calculated using the Press-Schechter formalism (the solid line) and the same calculated using the N-body simulations of EFWD (triangles) for groups of 3 or more particles. We also show the results found when some freedom is allowed in the determination of the $R_\star \rightarrow M_\star$ conversion. These results are for $C_V = 1.1$ (see text).The appropriate slope of the power spectrum, n, and expansion factor, a, is indicated in each panel.

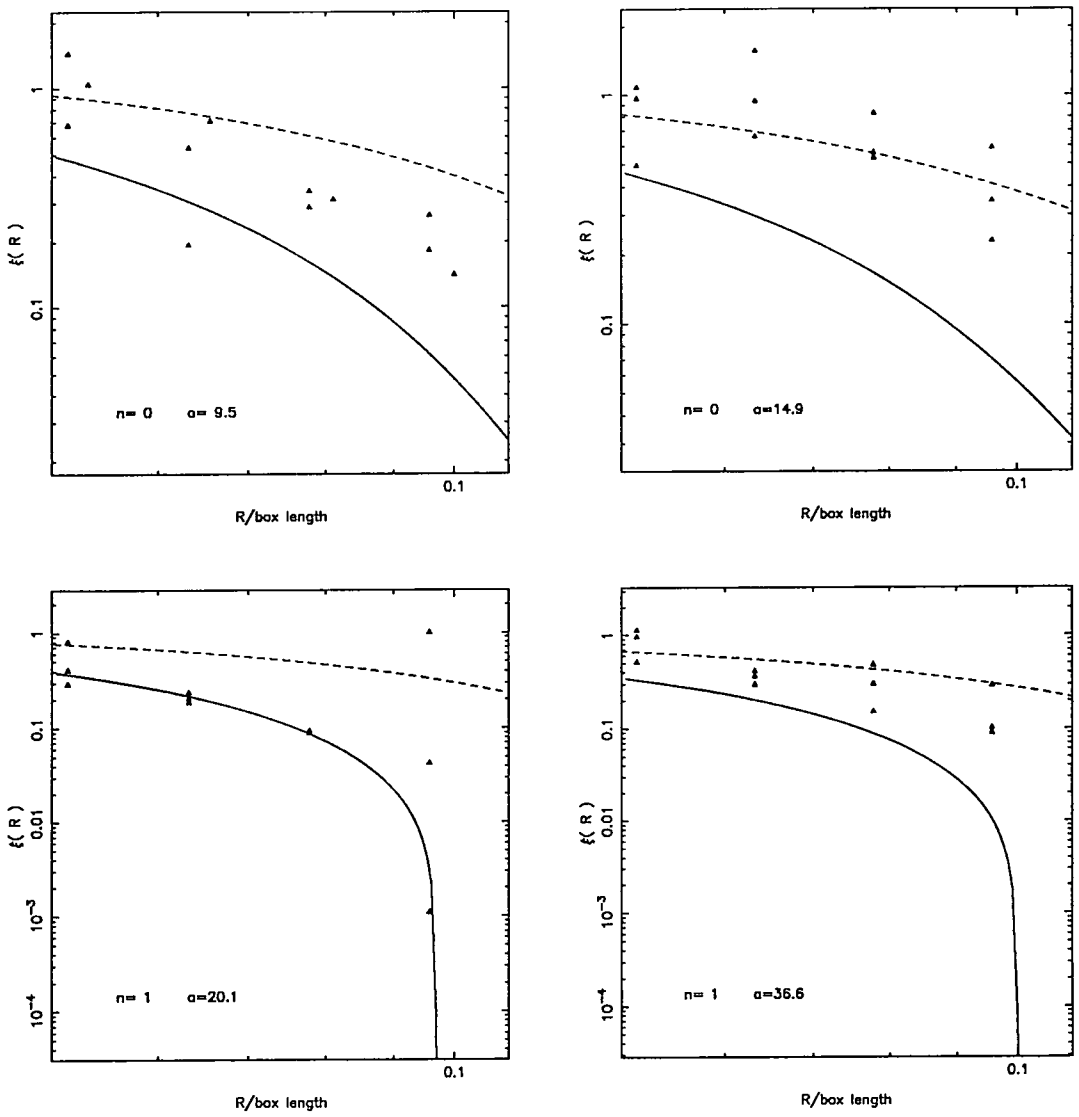

Figure 5.7. continued.

in Figure 5.7 the results found using an alternative relationship for the conversion from $M_\star$ to $R_\star$ (the dashed line). In this case we have used the relationship

$$R_\star = C_V \sqrt[3]{\frac{M_\star}{(1+\delta_c)\rho_0}}. \tag{5.45}$$

Here C_V is a free parameter. In the case of equation (5.43) we have effectively taken $C_V = 0.62$. Using the results of EFWD for $n = -1$ and $a = 6.1$ we have fixed this parameter to be $C_V = 1.1$. So we have changed it by only a factor of 2 (although this corresponds to adjusting the mass by a factor of 8). In some cases we now tend to overestimate the correlation, but in general the comparison is much improved.

At separations where $\xi \gtrsim 1$ the N-body groups are found to be significantly more clustered due to non-linear evolution which can not be addressed within the PS formalism. In particular, our approach does not model the peculiar motions of groups and the consequent amplification of correlations. This may also be responsible for some of our more general underestimation. However, it is interesting to note that both the N-body experiments and our calculation show a dip in the correlation function at the smallest separations. At these separations it is not possible for two distinct condensates to exist as they would be merged into a single, more massive, condensate. Thus, we see a fall in the correlation function. Overall, we believe that this comparison is satisfactory, especially if we take into account the uncertainty in the relationship between the mass and size of condensates and that the groups found in the N-body simulations may not be entirely reliable.

5.8.2 Standard CDM

We have also compared our technique with the standard CDM models of Frenk *et al* (1990). This has a number of advantages. Firstly the simulations contain significantly more particles – 2^{18} compared with 2^{15} in scale free simulations described above. This allows us to use larger groups – those containing 5 or more particles – where the group

finding algorithm is more reliable. Secondly, and in some ways more significantly, it is of more practical interest. Although standard CDM has been placed under pressure in recent years for its apparent lack of power on the largest scales, it is still the canonical model against which most observations are first compared and so agreement with these codes is essential. To make the comparison we have used the calculated $M_\star$ and $R_\star$ values given in Table 5.2. The conversion between these two assumes the top hat window function, equation (5.43). The values of $y_\star$ are those given in Table 5.1 for CDM with $\Gamma = 0.5$ (see §5.9.1 below). There are thus, once again, no free parameters available when making this comparison. In Figure 5.8 we show the results for four output times, corresponding to $b = 1$, 1.3, 1.6 and 2. In each case we have four realisations and these data are shown by the triangles. The result found using the PS formalism and a Gaussian window function is shown using the solid line. The agreement is generally very good, especially for the higher biasing models.

However, there is clearly a 'glitch' in all the curves. As the biasing decreases this glitch moves outwards and appears to deepen. Its position corresponds very closely to the size of the largest condensate in the simulation. The apparent deepening of the 'glitch' is mainly due to the logarithmic coordinates. Its depth is in fact roughly constant at around $\Delta\xi \sim 0.2$. The glitch is caused by the breakdown of the assumptions of the PS formalism as non-linear effects become important. To calculate the correlation function we have used equation (5.35). For the separations at which the glitch occurs this is dominated by the fourth term in the numerator, relating to the autocorrelation of the largest condensates in the sample. As the separations become smaller and approach the size of the largest condensates, the correlation coefficient, r_{cc}, for this term rapidly approaches 1. It can not go above 1 and so at this point it must stay at 1. There is thus a discontinuity at this point, leading to a sudden change in the value of $P(\Delta_{\mathbf{a}}(R_1''), \Delta_{\mathbf{b}}(R_2''))$. This leads to the

'glitch' we observe. As other terms in the numerator of equation 5.35 become important, a smoother behaviour is once again observed.

It would be interesting to test if our prediction that sub-$M_\star$ and super-$M_\star$ condensates are anti-correlated is borne out by N-body simulations. Unfortunately this is not yet practical, and this fundamental test of our work must await larger simulations. These simulations must have sufficient particles to have a large number of reliably found groups which are more or less massive than $M_\star$.

5.9 Applications of PS calculated clustering

5.9.1 Comparison with the All Galactic Systems Correlation Function

The condensates to which we have referred throughout this paper can not necessarily be associated with individual galaxies. It is more consistent to identify them with halos, which may contain more than one galaxy. So, our technique is particularly suited to a comparison with the All Galactic Systems (AGS) correlation function (Moore *et al* 1993). The AGS correlation function treats lone galaxies, binaries, poor groups and clusters as separate, but equal, units. So, it is probably closer to the halo correlation function, which we seek, than the more traditional galaxy correlation function. Moore *et al* (1993) assign the galaxies in the Center for Astrophysics (CfA) redshift survey (Huchra *et al* 1990) to groups and so are able to calculate an AGS correlation function. Each 'group' (which may be a single galaxy) is weighted by the reciprocal of the volume in which it would have been detected. This effectively leads to a volume limited sample. Moore *et al* present two correlation functions. One is for the brightest 100 'groups' (ξ_{100})and the other for the brightest 400

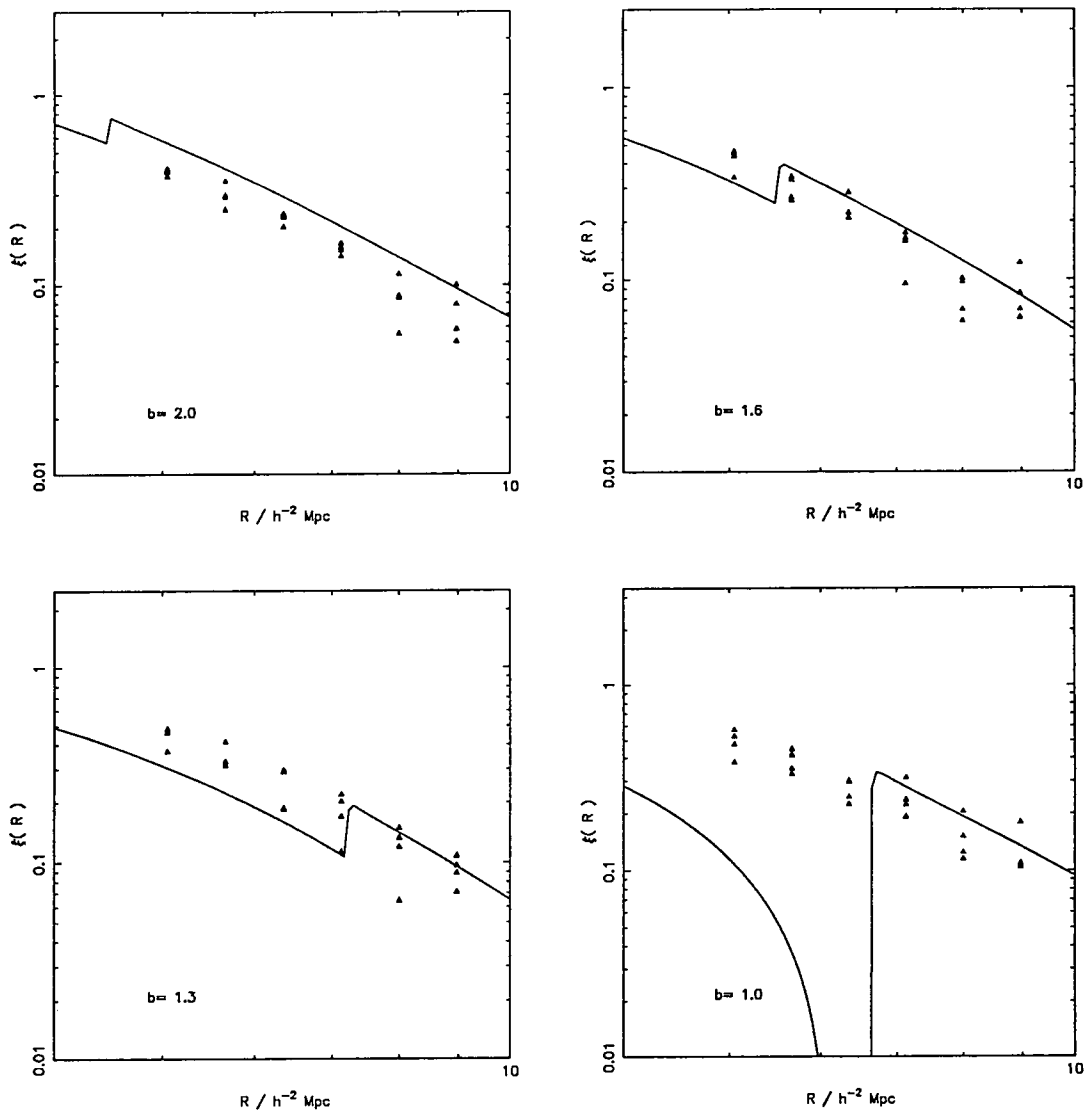

Figure 5.8. A comparison between the the correlation function of groups of 5 or more particles found in the standard CDM simulations of Frenk *et al* (1990) (points) with the correlation function calculated using the PS formalism. The comparison is broadly very good, with the exception of a 'glitch' which occurs at the scale of the largest group in the simulations. It is, thus, clearly the signature of the onset of non-linear conditions.

'groups' (ξ_{400}). These have magnitude ranges of $-24.26 \leq M \leq -20.53$ and $-24.26 \leq M \leq -19.1$ respectively, the brightest object being the Coma cluster (B. Moore, personal communication). The correlation functions are fitted by $\xi_{100} = (R/3.5\,\mathrm{h^{-1}Mpc})^{-1.3}$ and $\xi_{400} = (R/2.5\,\mathrm{h^{-1}Mpc})^{-1.3}$. Using a Marshall (1987) double power law, Moore *et al* find $M_\star = -22.2 \pm 0.2$. Using this and a constant mass to light ratio this converts into size ranges of $1.20 \leq R/R_\star \leq 3.60$ for ξ_{100} and $0.74 \leq R/R_\star \leq 3.60$ for ξ_{400}. This is sufficient to find ξ as a function of $R/R_\star$. In order to calculate the separation in physical units we must also derive a value for $R_\star$. To determine this we consider the Coma cluster, which corresponds to $3.60R_\star$. Dynamical arguments (Kaiser 1991) suggest that the Coma cluster had a pre-collapse radius of $10\,\mathrm{h^{-1}Mpc}$. Taking this we arrive at $R_\star \simeq 2.8\,\mathrm{h^{-1}Mpc}$. So we can obtain a prediction for correlation functions with only one free parameter, the shape of the power spectrum, $P(k)$.

The standard CDM power spectrum has a form (classically) given by the fitting function:

$$P(k) \propto \frac{k}{(1 + dk + ek^{3/2} + fk^2)^2}; \tag{5.46}$$

(see *eg,* White & Frenk 1992) where $d = 3.4\mathrm{h^{-1}\,Mpc}$, $e = 25\mathrm{h^{-3/2}\,Mpc^{3/2}}$ and $f = 4\mathrm{h^{-2}\,Mpc^2}$. The pressure which has been recently placed on CDM has lead to the evolution of an alternative fitting function. This is given by:

$$P(k) \propto \frac{k}{(1 + (ak + (bk)^{3/2} + (ck)^2)^{1.13})^{2/1.13}} \tag{5.47}$$

where $a = (6.4/\Gamma)\mathrm{h^{-1}\,Mpc}$, $b = (3.0/\Gamma)\mathrm{h^{-1}\,Mpc}$ and $c = (1.7/\Gamma)\mathrm{h^{-1}\,Mpc}$ (Efstathiou *et al* 1992) . This fits the standard CDM, $\Omega_0 = 1$ power spectrum with $\Gamma = \mathrm{h}$ for a small baryon density (Bond & Efstathiou 1984). However, by varying Γ, many other models can also be fitted, such as low density, spatially flat CDM models, CDM with decaying neutrinos and mixed dark matter (MDM) models.* Using the PS formalism we can now

* For a summary of how to calculate Γ in these cases see Efstathiou *et al* (1991).

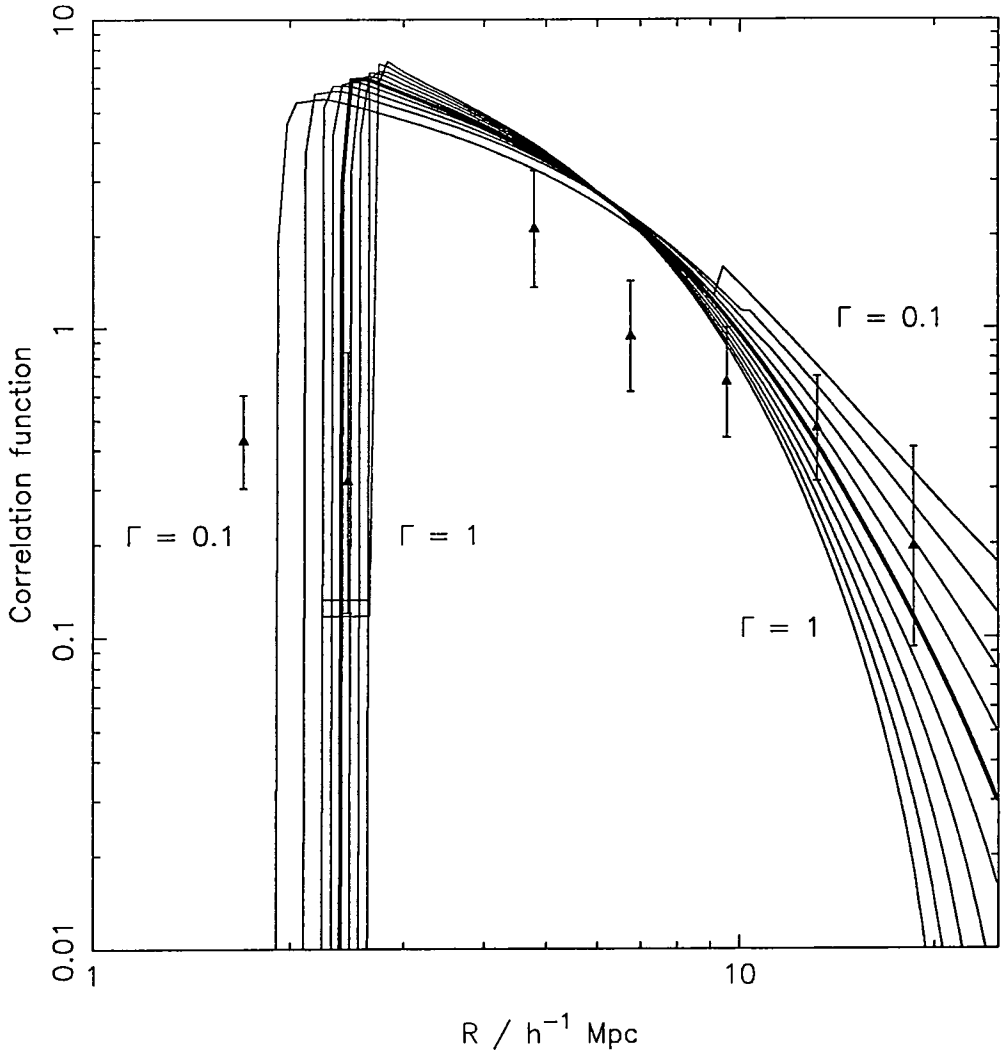

Figure 5.9. A comparison of the Moore *et al* (1993) AGS correlation function for the brightest 100 groups in the CfA survey with the calculated correlation functions using a CDM-like power spectrum for $\Gamma = 0.1$ to $\Gamma = 1$. There are no free parameters in the comparison.

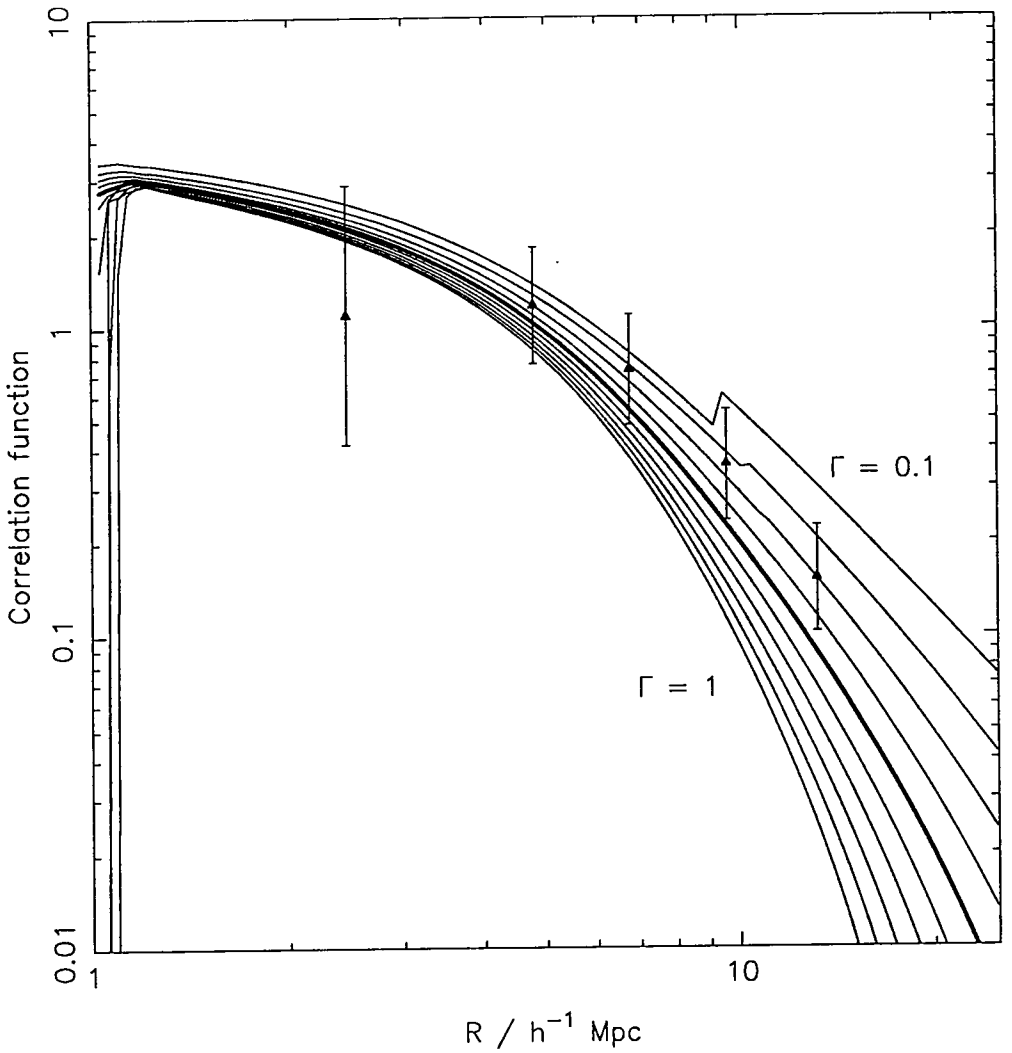

Figure 5.10. A comparison of the Moore *et al* (1993) AGS correlation function for the brightest 400 groups in the CfA survey with the calculated correlation functions using a CDM-like power spectrum for $\Gamma = 0.1$ to $\Gamma = 1$. There are no free parameters in the comparison.

calculate the AGS correlation function for a range of choices of Γ. These are calculated using the Gaussian window function and the size ranges calculated above. In Figure 5.9 we show the correlation function of the brightest 100 objects in the survey and in Figure 5.10 that for the brightest 400. The solid lines show the PS calculation for $\Gamma = 0.1$ to $\Gamma = 1.0$ in steps of 0.1. Standard CDM, $\Gamma = 0.5$ is shown in bold. For a classical CDM scenario this would correspond to $H_0 = 10\,\mathrm{km\,s^{-1}\,Mpc^{-1}}$ to $100\,\mathrm{km\,s^{-1}\,Mpc^{-1}}$. For all the choices of Γ presented here the correlation functions are of broadly the correct amplitude at around 5 Mpc. For ξ_{100} they all show a steep fall in the correlation function at around the point where the data also falls. However, even taking into account that there may be some scope to renormalise the separation axis, it is clear that low values of Γ are favoured. For instance, even if rescaling of the separation axis is allowed, the $\Gamma = 1$ line is far too steep to fit the data. On the basis of these calculations $\Gamma \sim 0.3 \pm 0.2$ is probably the preferred range.

5.9.2 The redshift evolution of clustering

The redshift evolution of the correlation function is an important parameter in studies of the evolution of the amplitude of $\omega(\theta)$ as a function of limiting magnitude (Roche *et al* 1992). At bright magnitudes estimates of $\omega(\theta)$ at different limiting magnitudes are related by a simple scaling relation. However, when faint magnitudes are reached greater depth is achieved and the redshift evolution of the galaxies and the clustering becomes important. Previously one of two models have been assumed for the redshift evolution of the clustering. Either the clustering length is assumed to vary only with the cosmological expansion, *ie,* to be fixed in comoving coordinates, or it is assumed that the clusters drop out of the expansion and so the clustering length is fixed in physical coordinates. In neither case is any evolution in the shape of the correlation function considered. Our technique allows a detailed modelling of the redshift evolution of the correlation function. Here we

confine our discussion to the qualitative features of the evolution of $\xi(r)$: a more detailed comparison with the observational work requires us to introduce an understanding of the faint galaxy number counts and projection effects — these are outside of the scope of this initial study. In addition, since most of the effect is from regions where $\xi > 1$ it would be necessary to extrapolate the PS correlation functions into the non-linear regime.

Hamilton *et al* (1991) have also addressed this problem. However, it is difficult for us to express our evolution in the same terms as they use $\overline{\xi}$, the mean correlation function within some separation. To calculate this a knowledge of the correlation function in the non-linear regime is essential and so this approach is not available to us. However, their technique gives good agreement with and is normalised using the simulations of EFWD and so we expect reasonable agreement in the appropriate regimes.

It is conventional to parameterise the clustering strength in terms of the clustering length, defined as the separation at which $\xi(R) = 1$. At this point the correlation function is on the boundary of the linear and the non-linear regimes, and so we should regard our results here as unsafe. Hence, we must define the clustering strength at larger separations. We choose to define the clustering length as the separation at which $\xi(R) = 0.1$. This is a compromise between being close to $\xi(R) = 1$ (and thus observable) and being as well into the linear regime as possible.

At each redshift we want to calculate the correlation function for objects of the same mass. To achieve this for a scale free power spectrum we calculate the $R/R_\star$ corresponding to this mass using $\frac{R}{R_\star}(z) = \frac{R}{R_\star}(z = 0)\ (1 + z)^{2/(n+3)}$ (White & Rees, 1978). We also use this relationship to convert our results from $\xi(\frac{R}{R_\star}(z))$ to $\xi(\frac{R}{R_\star}(z = 0))$ (*ie*, comoving

coordinates). Using equation (5.41) we find

$$\frac{R}{R_\star}(z=0;\xi_0) = \frac{1}{y_{\star,\mathrm{SK}}}\left(\frac{(n+3)}{\xi_0}\widetilde{\Gamma}(n+2)(1+z)^{-2}\right. \\ \left.\left\{\left[\frac{R_1}{R_\star}(z=0)\right]^{n+3}(1+z)^2-1\right\}\left\{\left[\frac{R_2}{R_\star}(z=0)\right]^{n+3}(1+z)^2-1\right\}\right)^{1/(n+3)} \tag{5.48}$$

for the evolution of the scale at which $\xi = \xi_0$.

Figure 5.11 shows the evolution in clustering strength for objects which are always much larger than the typical size, $R_\star$, measured in comoving coordinates. At $z = 0$ these condensates are 3 - 3.3 $R_\star$. We only show the results for $n = -2$ (upper set of lines) and $n = -1$ (lower set of lines). The dashed lines are the results of equation (5.48) for $R_1 = R_2 = 3R_\star$ and $R_1 = R_2 = 3.3R_\star$. A good agreement is seen. The analytical approximation never crosses $\xi = 0.1$ for $n = 0$ and $n = +1$ and so these are not shown.

Figure 5.12 shows the more complex evolution which can occur when at $z = 0$ the condensates are smaller than $R_\star$ and become rarer and thus larger than $R_\star$ as redshift increases. This more complicated evolution is caused by evolution in the shape of the correlation function. In practice, magnitude limited surveys pick out galaxies which are typically close to $L_\star$ and so this regime is likely to be more appropriate for comparison with observations. This suggests that studies of this kind may be a good way to distinguish between different power spectra. Note, however, that for all values of n there is relatively little evolution for $z < 0.3$. So determining the power spectrum for this kind of study would require relatively deep catalogues. Also, the effects of clustering evolution could be confused with luminosity evolution and so the latter would have to be carefully modelled and accounted for. It is interesting to note that for relatively low redshifts it is reasonable to assume that the clustering length is fixed in comoving coordinates. For $n = +1$ and $n = 0$ this assumption appears to be safe at still higher redshifts. However, these properties may be functions of the magnitude range (and hence the size range) present in the catalogue

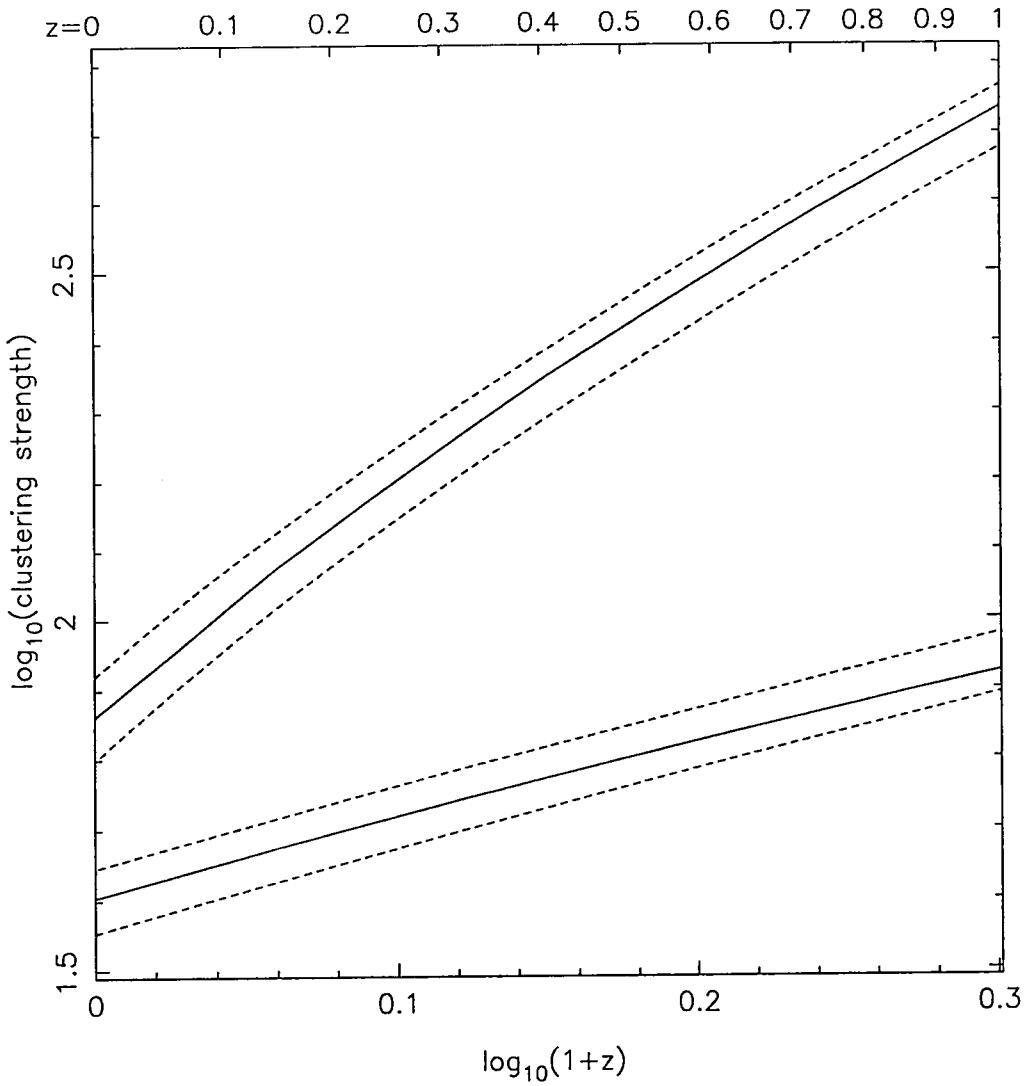

Figure 5.11. The redshift evolution of the clustering of $3 - 3.3\ \frac{R}{R_\star}(z=0)$ condensates for $n=-2$ (upper solid line) and $n=-1$ (lower solid line). Each solid line is surrounded by two dashed lines showing the analytical model (equation (5.48)) for $3R_\star$ and $3.3R_\star$. Good agreement with these is seen.

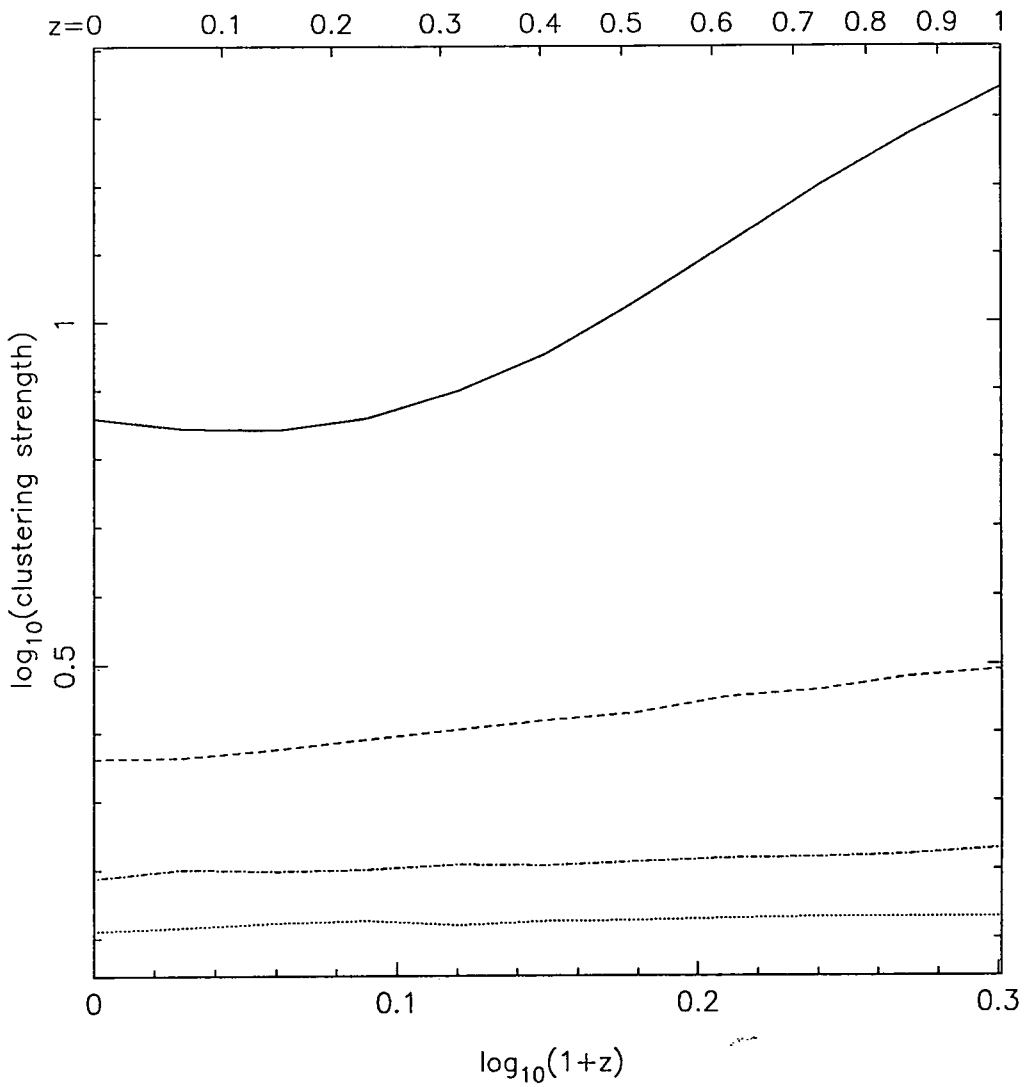

Figure 5.12. The redshift evolution of the clustering of $0.1 - 10\ \frac{M}{M_*}(z = 0)$ condensates. The solid line shows the results for $n = -2$, the dashed line for $n = -1$, the dot-dashed line for $n = 0$ and the dashed line for $n = +1$.

being modelled. So, these calculations should be made individually for each catalogue considered.

5.10 Summary

In this Chapter we have described a new technique for estimating correlation functions based on the PS formalism. This formalism has a chequered history and despite the recent work of Bond *et al* (1991) shwoing it as little more than a fluke, it has proved surprisingly useful. Its usefulness has been confirmed by the comparisons with the multiplicity functions found in scale free simulations by EFWD. We have also demonstrated that it compares well with multiplicity functions found in the CDM simulations of Frenk *et al* (1990). Other authors (B91; Bond *et al* 1991) have demonstrated that it can be effectively used to estimate the rate at which collapsed objects (condensates) merge. B91 demonstrated that this then provides a possible explanation for the Butcher-Oemler effect (Butcher & Oemler 1978). Following these successes we have extended the use of the formalism to allow the calculation of two point correlation functions. (For higher order correlation functions see Kashlinsky 1991.) We have confined our attention to scale free and CDM like fluctuation spectra, although it could in principal be applied to any spectrum.

We have demonstrated that the cross correlation of condensates of single masses can be described by a simple differential equation. Since we have adopted the same starting point as Kashlinsky (1986) we reproduce his formula for the 'cluster' correlation. Our expressions also agree with those in Kashlinsky (1991). This is of only limited astronomical use as galaxy catalogues contain galaxies and clusters of a range of masses, not a single mass. We therefore developed this further to show that if a range of masses is considered the

expression simplifies considerably to simply the sum of four terms. Numerical experiments show that the results of these expressions are relatively robust to changes in the window function. The detailed shape of the correlation function does show some dependence on the window function (ringing) – particularly if the window function is sharply truncated in k-space.

Using the differential version of our expression we have shown that in the limit of large separations the correlation function can be straightforwardly expressed. This allows a comparison with previous analytical work. It is proportional to the field correlation function ($\xi \propto r^{-(n+3)}$ for scale free spectra) and in the limit of large condensates it is equivalent to the expression of Kaiser (1984). However, our expression is also valid for smaller condensates. It agrees with the work of Kashlinsky (1986, 1991) and Mo *et al* (1993). A consideration of our expression for the large separation limit of the correlation function leads to considerable insight into the way that clustering changes as a function of the size of the condensates. The largest and rarest condensates are the most strongly clustered. As the condensates become smaller, the clustering strength decreases until the $R_\star$ condensates are reached. These are the most common condensates and only weakly clustered. As the condensates become still smaller (and rarer) the clustering strength increases again. As the size of the condensates tends towards $R/R_\star = 0$ the correlation function approaches ξ_ρ/δ_c^2. The cross correlation of condensates also shows some interesting behaviour. We agree with Kaiser (1984) that the cross correlation of two populations is the geometrical mean of the autocorrelation functions. In addition, the cross correlation of sub-$R_\star$ and super-$R_\star$ condensates is negative. This behaviour has lead us to propose that the Universe must display 'scale segregation.' Condensates which are sub-$R_\star$ are found in some parts of the Universe, whilst super-$R_\star$ condensates are found in others. Only a small number of condensates of one type are found in regions dominated by the other type. Condensates with $R = R_\star$ are found in the intermediate regions. This may provide some insight into

the puzzling behaviour of the faint-bright galaxy correaltion functions found in Chapter 2. All of the satellites in Chapter 2 are fainter than $M_\star$. So, this expression would predict that the bright-faint autocorrelation function would be stronger for fainter satellites, as is observed.

Although our expression for the large separation limit has provided considerable insight, it can not replace a proper numerical calculation. It fails in two areas. Firstly, it can not deal with a range of condensate masses. Secondly, it can not deal with intermediate scales between the linear and non-linear regimes.

We have compared our results with those of N-body simulations. A comparison with the scale free simulations of EFWD is difficult as there are relatively few particles. Thus, to calculate a reliable correlation function we are forced to use groups of a size at which the friends-of-friends group finding algorithm is unreliable. Despite this we are able to make an acceptable comparison if we allow the proportionality between the size and mass of condensates to be freely determined. A comparison with the standard CDM simulations of Frenk *et al* (1990) is more encouraging. Here the comparison is excellent except for a glitch at a separation equal to the size of the largest condensates in the sample. This marks the onset of non-linear behaviour.

As an example of the potential applications of this method we have studied the AGS correlation functions found by Moore *et al* (1993) (also Moore 1991). We compared these with correlation functions found using CDM-like power spectra. These were parameterised by the Γ factor (Efstathiou *et al* 1992). The data of Moore *et al* is best fitted by power spectra with $0.1 \lesssim \Gamma \lesssim 0.5$. This corresponds to 'standard' CDM with $10\,\mathrm{km\,s^{-1}\,Mpc^{-1}} \lesssim H_0 \lesssim 50\,\mathrm{km\,s^{-1}\,Mpc^{-1}}$ among many other alternatives. This is similar to the range of Γ required to fit the APM survey estimate of $\omega(\theta)$ (Maddox *et al* 1990). We have also taken a brief look at the evolution of clustering with redshift for use with deep surveys.

The detailed behaviour of this evolution is a strong function of both the assumed power spectrum and the dynamic range of the survey. In the case considered the assumption that the clustering strength is fixed in comoving coordinates appears good for $z < 0.3$. The work has many other applications. For instance Mo *et al* (1993) have used a formalism identical to our own to investigate the clustering of Lyman-α clouds. Their work would not be possible using an N-body code as they currently do not have sufficient mass resolution. Future work should include the prediction of cluster-cluster correlation functions based on the ROSAT (Trümper 1983) X-ray selected clusters (*eg*, Romer & Collins 1993). These simulations can not be carried out using N-body simulations as the available volume is not sufficient to generate a significant number of clusters.

In conclusion, we believe that in this Chapter we have described a reliable, fast method for estimating correlation functions from the linear to the mildly non-linear regime. It provides a complementary approach to N-body codes, allowing the consideration of very large or very small separations and very high or very low mass condensates. Overall, we feel that this technique provides an important new tool for the comparison of observational data with proposed models.

6 Discussion & Summary

In this Thesis we have looked at a number of aspects of the clustering of galaxies and groups of galaxies. In this Chapter we will summarise our main results and consider some possible routes for this work in the future.

In Chapter 2 we considered the clustering of faint galaxies around bright galaxies. The small scales considered means the faint galaxies are effectively satellites of the primaries. However, if faint galaxies simply trace the same structures as bright galaxies, without being physically associated with them, we would still, apparently, detect satellites. It seems unlikely, however, that a faint galaxy could lie close to a bright galaxy without the gravitational field of the bright galaxy being the dominant influence on the faint one. Our method is based on the work of Holmberg (1969), although we have developed it further to allow non-contiguous POSS plates to be used in an efficient manner. We count the number of faint images on the POSS plates around the positions of bright galaxies drawn from the CfA survey. Using this method we detected satellites within $1h^{-1}$Mpc at the 7σ level. There are typically ~ 8 satellites within $1h^{-1}$Mpc in the magnitude range $-16 \geq M_{B_T} \geq -18$. The surface density of satellites is well fit by a power law with index ~ 0.8. This corresponds to a correlation function with a similar slope to the bright galaxy autocorrelation function.

To take the clustering of the primaries into account we carried out a number of Monte-Carlo simulations. These show that the observed satellite distribution could arise from

the superposition of satellite systems with a slightly steeper slope ($\sim$ 1.1) and a lower normalisation (4 satellites within $1h^{-1}$Mpc in the range $-16 \geq M_{B_T} \geq -18$).

The satellite systems around late and early type primaries appear to have significantly different spatial distributions. This difference cannot be accounted for simply by the differences in the clustering of early and late type primaries. The simulations show that the early type primaries have about twice as many satellites within $1h^{-1}$Mpc. However, this is only observed within $250h^{-1}$kpc. Our estimates of the slope of the satellite distributions are in good agreement with Lake & Tremaine (1980) for late type primaries and Vader & Sandage (1991) for early type primaries. However, our work is the first to study late and early type primaries separately whilst drawing them from the same redshift survey.

It is not clear from our data if the difference in the satellite distributions is due to the different environments in which late and early type primaries are typically found or if it is due to the morphology of the primary. This is an alternative version of the 'nature versus nurture' debate. It might be possible to address this question using the techniques developed by Moore (1991). Moore places galaxies in groups of different sizes, effectively a measurement of their environment. If the sample of primaries could be extended it would then be possible to further subdivide each sample of primaries on the basis of environment. This would provide a particulalrly clean test.

Using the result of Phillipps (1985), and assuming a luminosity function, we were able to estimate the bright-faint cross-correlation function, ξ_{bf}. The results of this process are somewhat puzzling. For the faintest satellites, $-16 \geq M_{B_T} \geq -17$, the result is consistent with the bright-bright autocorrelation function, ξ_{bb}. However, for brighter satellites, $-17 \geq M_{B_T} \geq -18$ the clustering strength is reduced by a factor ~ 3. This is particularly curious as the satellites are only 1.5 magnitudes fainter than M_*. It also poses problems for traditional ideas of biasing (*eg*, Kaiser 1984) which suggest that more

massive (and presumably brighter) objects are more strongly clustered than their less massive, fainter counterparts. This result is dependent on the shape of the faint end of the luminosity function, although none of the luminosity functions we tried proved to be satisfactory. A luminosity function with a faint end slope as steep as $\alpha \sim 2$ would be required for the faint and bright satellites to have equal clustering strengths. It is known that the APM machine sometimes misses or misclassifies bright galaxies. If this is important in our brighter satellite bin, it would lead to an apparent reduction in the clustering strength of the brighter satellites. However, it is likely that at most only 10% of bright galaxies are missed in this way (N.Metcalfe, personal communication) and so it seems unlikely that this can account for the whole effect. The misclassification of stars as galaxies would lead to an error in the satellite magnitudes, and so the amplitude of the correlation functions. However, since the stars are not correlated with the positions of the primaries this would have no effect on the relative strength of the correlation functions. It seems, therefore, that no systematic effect can adequately explain this trend in clustering strength and it must, therefore, be accepted at face value.

This work has a number of advantages over previous studies of a similar nature. In particular, we have used a significantly larger data set than Phillipps & Shanks (1987a, 1987b) and our bootstrap method allows primaries to be used which have much lower recession velocities. We are able to use primaries which are 10 times closer than those used by Phillipps & Shanks. We have considered much larger projected separations than either Lake & Tremaine (1980) or Vader & Sandage (1991). Our results are, thus, significantly better determined. Our bootstrap technique may also prove to have wider applications. As large format CCD's become more common it may be possible to use CCD images to provide a deep, extensive positional survey. However, large format CCD's are still significantly smaller than photographic Schmidt plates, making it more difficult to make

an accurate background correction. We believe that our bootstrap technique would allow this to be done in an efficient and effective manner.

In Chapter 3 we complemented the statistical study of satellites of Chapter 2 with a direct observational survey. It was intended that this work should extend the catalogue of ZSFW. Bad weather at the AAT prevented us from adding more than 10 satellites to the sample. However, our subsequent analysis of the total sample, now consisting of 79 satellites, differed in a number of ways. Firstly we used an alternative criterion for interloper rejection. Inspired by the N-body simulations of J.F.Navarro (personal communication) we reject any satellite for which $|\Delta v| > 2V_c$. Five satellites are rejected on this basis, in agreement with the number we would have expected. This alternative criterion picks out a set interlopers which agrees with 60% of the ZSFW sample. However, their interloper rejection criterion is somewhat arbitrary and we believe our's is significantly better motivated.

We estimate that the mass within $150\mathrm{h}^{-1}$kpc of the primary is $(1.40^{+0.59}_{-0.77}) \times 10^{12}\mathrm{h}^{-1}M_{\odot}$. This agrees well with the Milky Way mass found by Zaritsky *et al* (1989) and we are able to exclude a mass as low as the Little & Tremaine (1980) estimate at the 99.9% level. The size of the satellites is also consistent with an isothermal sphere of this mass. If we assume that all the mass in the universe is within $150\mathrm{h}^{-1}$kpc of bright galaxies we are able to estimate that $\Omega = 0.067^{+0.034}_{-0.037}$, with a 95% lower limit of $\Omega > 0.02$. It is interesting to compare this with the density in baryons, $\Omega_b = (0.013 \pm 0.003)\mathrm{h}^{-2}$ (Walker *et al* 1991). If the Universe were to be entirely baryonic, then low values of H_0 would be favoured.

The radial distribution of satellites is well described by a power law, in agreement with the results of Chapter 2. We have also confirmed the Holmberg effect at the 97% level; there is a significant deficiency of satellites within $50\mathrm{h}^{-1}$kpc and with position angles

$\Theta < 20^{o}$. There is no detectable effect for separations greater than this. This is the first firm confirmation of the effect first noted by Holmberg (1969).

We agree with the ZSFW result that there is no significant correlation between $|\Delta v|$ and V_c. However, we have demonstrated that there is a weak correlation between V_c and the rms $|\Delta v|$. This correlation is consistent with the dark halo having the same circular velocity as the inner parts of the primary.

To investigate this correlation, and the many other marginal effects in this data set, more data is needed. Further satellite redshifts have been recently been obtained by R.M.Smith at the AAT and D.Zaritsky at CTIO. We await the result of adding these additional data with interest.

Using Monte-Carlo simulations we have been able to find the values of r_p and $|\Delta v|$ at which the Milky Way satellites would be likely to be observed by an external observer. These are at separations and velocity differences which are somewhat smaller than is typical of the satellite sample. The difference in projected separations may be due to H_0 dependance and selection effects. However, the only possible explanation for the small velocity differences is that the small number of Milky Way satellites do not provide a large enough sample.

Overall, the results of Chapter 3 provide significant evidence that galactic halos are well described by an isothermal sphere with a mass of $\sim 10^{12}\mathrm{h}^{-1}M_{\odot}$, the isothermal sphere having a circular velocity similar to that of the primary. The isothermal sphere extends to at least $150\mathrm{h}^{-1}$kpc.

In Chapter 4 we investigated the small scale environment of LSB galaxies and demonstrated that they have significantly fewer close companions than 'normal' HSB galaxies drawn from the CfA survey. We also discussed that these galaxies are probably sites of abnormally low star formation. The combination of an abnormal environment and an

abnormally low star formation rate provides support for theories of environmentally triggered star formation. In particular, our results support the theory of tidally triggered star formation (Lacey & Silk 1991). Our work supports the earlier conclusions of Bothun *et al* (1990, 1992). However, we have searched for companions which are significantly fainter than those considered previously. We have been able to do this by using the mixed statistic developed in Chapter 2; Bothun *et al* (1992) cross-correlated two redshift surveys. We have thus been able to test the effect of environment on LSB galaxies much more rigorously. However, both our result and that of Bothun *et al* (1992) is difficult to reconcile with the large numbers of LSB galaxies which are found in clusters (*eg*, Irwin *et al* 1990), showing that LSB galaxies are found in dense environments. However, these are special environments. The Sprayberry & Impey redshift survey is designed to avoid these unusual environments and so be a fair sample of LSB galaxies. We would therefore expect that our result is more typical of an average LSB galaxy. In addition, previous work has concentrated on the clustering of LSB galaxies at significantly larger scales (5-10h^{-1}Mpc). Our result suggests then that the star formation rate is affected only by the environment within 5h^{-1}Mpc, perhaps even as locally as 1h^{-1}Mpc. However, these scales are comparable to size of rich clusters (Coma is about 10h^{-1}Mpc across) and so in such dense environments we would still expect many companions within 1h^{-1}Mpc, leading to frequent tidal interactions. The resolution of this contradiction is not clear. There are no obvious systematic effects in our analysis. However, it does not, as yet, cover a particularly large area. Increasing the size of the survey area may lead to the resolution of this contradiction. However, if it did not we would be forced to conclude that either, environment has no significant effect on star formation rate, or, that the star formation rate in cluster LSB galaxies is suppressed by another mechanism.

In Chapter 5 we developed an analytical method for calculating correlation functions based on the Press-Schechter formalism (PS). Despite the formal derivation of this formalism

having been discredited, it still compares well with the results of N-body simulations. We have demonstrated that correlation functions calculated using this formalism also compare well with the results of N-body codes. Given the poor justification of the PS formalism this was essential before any serious conclusions could be drawn. This comparison has been lacking from previous work in this area, such as Kashlinsky (1986, 1991). The results are also relatively independent of the choice of window function, although if a window function with sharp edges, particularly in k-space, is used some ringing results.

Having demonstrated that the results of our method both agree with N-body codes and are robust to changes in the window function we demonstrated the possible uses of this method. In the limit of large separations and large masses the correlation function behaves as expected, more massive objects being more strongly clustered. However, as $M_\star$ objects are approached the clustering strength drops rapidly. The $M_\star$ objects are in principle unclustered. If masses which are lower than $M_\star$ are considered then clustering becomes stronger as the masses become smaller. This leads to a cosmological model in which the super-$M_\star$ and sub-$M_\star$ objects are spatially segregated ('scale segregation'). It is necessary that this effect be verified using N-body codes. However, current codes do not combine sufficient dynmaic range with a large enough box.

We have also compared our models with the AGS correlation functions of Moore *et al* (1993). These are consistent with a CDM-like power spectrum but with more power on large scales. We considered the redshift evolution of clustering, demonstrating that it has a complex form which depends critically on the mass of the objects considered. However, the assumption that the clustering strength is fixed in comoving coordinates appears good for $z < 0.3$.

At first sight the results of Chapter 5, that massive and small condensates are anti-correlated, appears to contradict the results of Chapter 2, that bright and faint galax-

ies are strongly clustered. However, we have only measured the bright-faint correlation function on scales where it is highly non-linear, whilst the PS formalism only predicts an anti-correlation at much larger separations. There is thus no contradiction. In fact the PS formalism may be helpful in understanding the trends we have found. We have shown that for condensates that are less massive than $M_\star$ the less massive condensates are more strongly clustered. This is just the kind of behaviour we have observed in Chapter 2, although in the non-linear regime. Thus, the biasing we observe here may be consistent with statistical biasing.

Overall, we have demonstrated that the clustering of faint galaxies can be effectively studied. However, this work suffers from two severe problems. Firstly, the luminosity function is only poorly determined at faint magnitudes. This makes any assessement of the clustering strength uncertain. Also, cosmological models are unable to make reliable predictions about the properties of faint galaxies. Our work on the PS formalism has gone some way towards correcting this, but before an accurate comparison with theoretical models can be made it is necessary to either, make predictions for separations $\xi > 1$, or, extend the scope of the observations to separations where $\xi < 1$.

BIBLIOGRAPHY

Adler, R.J., 1981. *The Geometry of Random Fields* (Wiley, Chichester).

Alimi, J.M., Valls-Gabaud, D. & Blanchard, A., 1988. *Astr. Astrophys.*, **206**, L11.

Avni, Y., 1976. *Astrophys. J.*, **210**, 642.

Bahcall, N.A. & Soneira, R.M., 1983. *Astrophys. J.*, **270**, 20.

Barrow, J.D., Bhavasar. S.P. & Sonoda, D.H., 1985. *Mon. Not. R. astr. Soc.*, **216**, 17.

Bardeen, J.M., Bond, J.R., Kaiser, N. & Szalay, A.S., 1986. *Astrophys. J.*, **304**, 15.

Bean, A.J., Efstathiou, G., Ellis, R.S., Peterson, B.A. & Shanks, T., 1983. *Mon. Not. R. astr. Soc.*, **205**, 605.

Begeman, K., 1987. *PhD Thesis*, Groningen University.

Bertschinger, E. & Gelb, J.M., 1991. *Computers in Physics*, **5**, 164.

Binggeli, B., Sandage, A. & Tammann, G.A., 1985. *Astr. J.*, **90**, 1681.

Binggeli, B., Sandage, A. & Tammann, G.A., 1988. *Ann. Rev. Astr. Astrophys.*, **26**, 509.

Binggeli, B., Sandage, A. & Tarenghi, M., 1984. *Astr. J.*, **89**, 64.

Binggeli, B., Tammann, G.A. & Sandage, A., 1988. *Astr. J.*, **94**, 251.

Binney, J. & Tremaine, S., 1987. *Galactic Dynamics* (Princeton: Princeton University Press).

Bond, J.R. & Efstathiou, G., 1984. *Astrophys. J.*, **285**, L45.

Bond, J.R., Cole, S.M., Efstathiou, G. & Kaiser, N., 1991. *Astrophys. J.*, **379**, 440.

Bothun, G.D., Beers, T., Mould, J. & Huchra, J.P., 1986. *Astrophys. J.*, **308**, 510.

Bothun, G.D., Impey, C., Malin, D. & Mould, J., 1987. *Astr. J.*, **94**, 23.

Bothun, G.D., Schombert, J.M., Impey, C. & Schneider, S., 1990. *Astrophys. J.*, **360**, 427.

Bothun, G.D., Schombert, J.M., Impey, C.D., Sprayberry, D. & McGaugh, S.S., 1992. *Preprint.*

Bower, R.G., 1991. *Mon. Not. R. astr. Soc.*, **248**, 332(B91).

Bower, R.G., 1993. *In preparation.*

Bower, R.G., Coles, P., Frenk, C.S. & White, S.D.M., 1993. *Astrophys. J.*, **405**, 403.

Burstein, D & Heiles, C, 1984. *Astrophys. J. Suppl.*, **54**, 33.

Butcher H. & Oemler, A., 1978. *Astrophys. J.*, **219**, 18.

Cole, S., 1990. *Astrophys. J.*, **367**, 45.

Cole, S., Aragon-Salamanca, A., Frenk, C.S., Navarro, J.F. & Zepf, S., 1993. *In preparation.*

Colless, M.M. & Hewett, P., 1987. *Mon. Not. R. astr. Soc.*, **224**, 453.

Davies, J.I., Phillipps, S., Cawson, M.G.M, Disney, M.J. & Kibblewhite, E.J., 1988. *Mon. Not. R. astr. Soc.*, **232**, 239.

Davies, J.I., Phillipps, S. & Disney, M.J., 1989. *Mon. Not. R. astr. Soc.*, **239**, 703.

Davis, M., Efstathiou, G., Frenk, C.S. & White, S.D.M., 1985. *Astrophys. J.*, **292**, 371.

Davis, M., Efstathiou, G., Frenk, C.S. & White, S.D.M., 1992. *Nature*, **356**, 489.

Davis, M. & Geller, M.J., 1976. *Astrophys. J.*, **208**, 13.

Davis, M., Huchra, J., Latham, D.W. & Tonry J., 1982. *Astrophys. J.*, **253**, 423.

Davis, M. & Peebles, P.J.E., 1983a. *Astrophys. J.*, **267**, 465.

Davis, M. & Peebles, P.J.E., 1983b. *Ann. Rev. Astr. Astro*, **2**, 109.

de Vaucouleurs, G., de Vaucouleurs, A. & Corwin, H.G., Jr., 1976. *Second Reference Catalogue of Bright Galaxies* (Austin: University of Texas Press).

de Lapparant, V., Kurtz, M.J. & Geller M.J., 1986. *Astrophys. J.*, **267**, 465.

Dekel, A. & Rees, M.J., 1987. *Nayure*, **326**, 455.

Dressler, A., 1980. *Astrophys. J.*, **236**, 351.

Disney, M., 1976. *Nature*, **263**, 573.

Disney, M. & Phillipps, S., 1983. *Mon. Not. R. astr. Soc.*, **205**, 1253.

Disney, M. & Phillipps, S., 1987. *Nature*, **329**, 203.

Eder, J.A., Schombert, J.M., Dekel, A. & Oemler, A., 1989. *Astrophys. J.*, **340**, 29.

Efstathiou, G., Bond, J.R. & White, S.D.M., 1992. *Mon. Not. R. astr. Soc.*, **258**, 1P.

Efstathiou, G., Ellis, R.S. & Peterson, B.A., 1988a. *Mon. Not. R. astr. Soc.*, **232**, 43.

Efstathiou, G., Frenk, C.S., White, S.D.M. & Davis, M., 1988b. *Mon. Not. R. astr. Soc.*, **235**, 715(EFWD).

Efstathiou, G., Kaiser, N., Saunders, W., Lawrence, A., Rowan-Robinson, M., Ellis, R.S. & Frenk, C.S., 1990. *Mon. Not. R. astr. Soc.*, **247**, 10P.

Einasto, J., Saar, E., Kaasik, A. & Charin, A.D., 1974. *Nature*, **252**, 111.

Erickson, K., Gottesman, S.T. & Hunter, J.H., Jr., 1987. *Nature*, **325**, 779.

Fall, S.M., 1979. *Rev. Mod. Phys.*, **51**, 21.

Ferguson, H.C. & Sandage, A., 1991. *Astr. J.*, **101**, 765.

Freeman, K., 1970. *Astrophys. J.*, **160**, 811.

Frenk, C.S., White, S.D.M., Davis, M. & Efstathiou, G., 1985. *Nature*, **317**, 595.

Frenk, C.S., White, S.D.M., Davis, M. & Efstathiou, G., 1988. *Astrophys. J.*, **327**, 507.

Frenk, C.S., White, S.D.M., Efstathiou, G. & Davis, M., 1990. *Astrophys. J.*, **351**, 10.

Geller, M.J., de Lapparant, V. & Kurtz, M.J., 1984. *Astrophys. J.*, **287**, L55.

Groth, E.J. & Peebles, P.J.E., 1977. *Astrophys. J.*, **217**, 385.

Groth, E.J. & Peebles, P.J.E., 1986a. *Astrophys. J.*, **310**, 499.

Groth, E.J. & Peebles, P.J.E., 1986b. *Astrophys. J.*, **310**, 507.

Guth, A.H., 1981. *Phys. Rev. D*, **23**, 347.

Hamilton, A.J.S., 1988. *Astrophys. J.*, **331**, L59.

Hamilton, A.J.S., Kumar, P., Lu, E. & Matthews, A., 1991. *Astrophys. J.*, **374**, L1.

Henry, J.P., 1991. in *Observational Tests of Cosmological Inflation* , ed. Shanks, T., Banday, A.J., Ellis, R.S., Frenk, C.S. & Wolfendale, A.W. (Kluwer, Dordrecht).

Holmberg, E., 1969. *Ark. Astr.*, **5**, 305.

Huchra, J.P., 1990. *The Huchra Catalogue.*

Huchra, J.P., Henry, J.P., Postman, M. & Geller, M. J., 1990. *Astrophys. J.*, **365**, 66.

Huchtmeier, W.K. & Richter, O-G, 1989. *HI Observations of Galaxies* (New York: Springer-Verlag).

Impey, C., Bothun, G. & Malin, D., 1988. *Astrophys. J.*, **330**, 634.

Irwin, M.J., 1985. *Mon. Not. R. astr. Soc.*, **214**, 575.

Irwin, M.J., Davies, J.I., Disney, M.J. & Phillipps, S., 1990. *Mon. Not. R. astr. Soc.*, **245**, 289.

Kaiser, N., 1984. *Astrophys. J.*, **284**, L9.

Kaiser, N., 1991. *Astrophys. J.*, **383**, 104.

Kaiser, N., Efstathiou, G., Ellis, R.S., Frenk, C.S., Lawrence, A., Rowan-Robinson, M. & Saunders, W., 1991. *Mon. Not. R. astr. Soc.*, **252**, 1.

Kashlinsky, A., 1986. *Astrophys. J.*, **317**, 19.

Kashlinsky, A., 1991. *Astrophys. J.*, **376**, L5.

Kaufmann, G., White, S.D.M. & Guideroni, B., 1993. *Submitted to Mon. Not. R. astr. Soc.*.

Kennicutt, R.C., 1989. *Astrophys. J.*, **344**, 685.

Kibblewhite, E.J., 1980. *APM Manual* (SERC).

Kibblewhite, E.J., Bridgeland, M.J., Bunclark, P. & Irwin, M.J., 1984. in *Proc. Astronomical Microdensitometry Conf.*, ed. Kinglesmith, D.A. (NASA).

Lacey, C. & Cole, S.M., 1993. *Preprint.*

Lacey, C. & Silk, J., 1991. *Astrophys. J.*, **381**, 14.

Lake, G. & Tremaine, S., 1980. *Astrophys. J.*, **238**, L13.

Lilje, P.B. & Efstathiou, G., 1988. *Mon. Not. R. astr. Soc.*, **231**, 635.

Limber, D.N., 1953. *Astrophys. J.*, **117**, 134.

Little, B. & Tremaine, S., 1980. *Astrophys. J.*, **238**, L13.

Loveday, J., Efstathiou, G., Peterson, B.A. & Maddox, S.J., 1992b. *Astrophys. J.*, **400**, 43.

Loveday, J., Peterson, B.A., Efstathiou, G. & Maddox, S.J., 1992a. *Astrophys. J.*, **390**, 338.

Lucey, J.R., 1983. *Mon. Not. R. astr. Soc.*, **204**, 33.

Lynden-Bell, D., 1967. *Mon. Not. R. astr. Soc.*, **136**, 101.

McGaugh, S.S., 1992. *PhD Thesis*, University of Michigan.

Maddox, S.J., 1988. *PhD Thesis*, University of Cambridge.

Maddox, S.J., Efstathiou, G., Sutherland, W.J. & Loveday, J., 1990. *Mon. Not. R. astr. Soc.*, **242**, 43P.

Malin, D.F., 1978. *Nature*, **276**, 591.

Marshall, H.L., 1987. *Astrophys. J.*, **316**, 84.

Matthewson, D.S., Ford, V.L. & Buchhorn, M., 1992. *Astrophys. J. Suppl.*, **81**, 413.

Meszaros, P., 1974. *Astr. Astrophys.*, **37**, 225.

Mo, H.J., Miralda-Escude, J. & Rees, M.J., 1993. *Submitted to Mon. Not. R. astr. Soc.*.

Moore, B., 1991. *PhD Thesis*, University of Durham.

Moore, B., Frenk C.S. & White, S.D.M., 1993. *Submitted to Mon. Not. R. astr. Soc.*.

Nusser, A., 1993. *PhD Thesis*, Hebrew University.

Nusser, A. & Dekel, A., 1993. *Astrophys. J.*, **405**, 437.

Ostriker, J.P. & Tremaine, S.D., 1975. *Astrophys. J.*, **202**, L113.

Parry, I.R. & Gray, P.M., 1986. *Proc. of SPIE*, **627**, 118.

Parry, I.R. & Sharples, R.M., 1988. *PASP conference series*, **3**, 93.

Peacock, J.A. & Heavens, A.F., 1990. *Mon. Not. R. astr. Soc.*, **243**, 133.

Peebles, P.J.E., 1980. *The Large Scale Structure of the Universe* (Princeton University Press).

Peebles, P.J.E., 1993. *The Principles of Physical Cosmology* (Princeton University Press).

Peletier, R. & Willner, S., 1992. *Astr. J.*, **103**, 1761.

Phillipps, S., 1985. *Mon. Not. R. astr. Soc.*, **212**, 657.

Phillipps, S., Davies, J.I. & Disney, M.J., 1988. *Mon. Not. R. astr. Soc.*, **233**, 485.

Phillipps, S. & Disney, M.J., 1986. *Mon. Not. R. astr. Soc.*, **221**, 1039.

Phillipps, S., Disney, M.J., Kibblewhite, E.J. & Cawson, M.G.M., 1987. *Mon. Not. R. astr. Soc.*, **229**, 505.

Phillipps, S. & Shanks, T., 1987a. *Mon. Not. R. astr. Soc.*, **227**, 115.

Phillipps, S. & Shanks, T., 1987b. *Mon. Not. R. astr. Soc.*, **229**, 621.

Pierce, M.J. & Tully, R.B., 1992. *Astrophys. J.*, **387**, 47.

Postman, M. & Geller, M., 1984. *Astrophys. J.*, **281**, 95.

Press, W.H., Flannery, B.P., Teukolsky, S.A. & Vetterling,W.T., 1986. *Numerical Recipes* (CUP).

Press, W.H. & Schechter, P., 1974. *Astrophys. J.*, **187**, 425(PS).

Rice, S.O., 1954. in *Selected Papers on Noise and Stochastic Processes*, ed. Wax, N. (New York: Dover).

Roche, N., Shanks, T., Metcalfe, N. & Fong R., 1992. *Submitted to Mon. Not. R. astr. Soc.*.

Romer, A.K. & Collins, C.A., 1993. *In preparation.*

Rubin, V.C., Burstein, D. & Thonnard, N., 1980. *Astrophys. J.*, **242**, 1149.

Rubin, V.C. & Ford, W.K., Jr., 1970. *Astrophys. J.*, **159**, 379.

Rubin, V.C., Ford, W.K., Jr. & Thonnard, N., 1978. *Astrophys. J.*, **225**, L107.

Sandage, A., Bingelli, B. & Tammann, G.A., 1985. *Astr. J.*, **90**, 1759.

Sanders, D.B., Soifer, B.T., Elias, J.H., Madore, B.F., Matthews, K., Neugebauer, G. & Scoville, N.Z., 1988. *Astrophys. J.*, **325**, 74.

Saunders, W., Frenk, C.S., Rowan-Robinson, M., Efstathiou, G., Lawrence, A., Kaiser, N., Ellis, R.S., Crawford, J., Xia, X.Y. & Parry, I.R., 1991. *Nature*, **349**, 32.

Schechter, P.L., 1976. *Astrophys. J.*, **203**, 297.

Schombert, J.M., Bothun, G.D., Impey, C.D. & Mundy, L.G., 1990. *Astr. J.*, **100**, 1523.

Schneider, S., Thuan, T., Magri, C. & Wadiak, J., 1990. *Astrophys. J. Suppl.*, **72**, 245.

Schweizer, F., Seitzer, P., Faber, S., Burnstein, D., Dalle Ore, C. & Gonzalez, J., 1990. *Astrophys. J.*, **364**, L33.

Shortridge, K., 1990. *The FIGARO users Manual* (STARLINK).

Smoot, G.F., Bennett, C.L., Cogut, A., Wright, E.L., Aymon, J., Boggess, N.W., Cheng, E.S., de Amici, G., Gulkis, S., Hauser, M.G., Hinshaw, G., Lineweaver, C., Loewenstein, K., Jackson, P.D., Janssen, M., Kaita, E., Kelsall, T., Keegstra, P., Lubin, P., Mather, J., Meyer, S.S., Moseley, S.H., Murdoch, T., Rokke, L., Silverberg, R.F., Tenorio, L., Weiss, R. & Wilkinson, D.T., 1992. *Astrophys. J.*, **396**, L1.

Shane, C.D. & Wirtanen, C.A., 1967. *Publs. Lick Obs.*, **22**, part 1.

Sutherland, W.J., 1991. in *Observational Tests of Cosmological Inflation* , ed. Shanks, T., Banday, A.J., Ellis, R.S., Frenk, C.S. & Wolfendale, A.W. (Kluwer, Dordrecht).

Tamman, G.A. & Sandage, A., 1985. *Astrophys. J.*, **294**, 81.

Thuan, T., Gott, R., & Schneider, S., 1987. *Astrophys. J.*, **315**, L93.

Trümper, J., 1983. *Adv. Space Res.*, **2(4)**, 241.

Tully, R.B. & Fisher, J.R., 1977. *Astr. Astrophys.*, **54**, 661.

Vader, J.P. & Sandage A., 1991. *Astrophys. J.*, **379**, L1.

van den Bergh, S., 1980. in *The Structure and Evolution of Normal Galaxies*, ed. Fall, S.M. & Lynden-Bell, D. (Cambridge: Cambridge University Press).

van der Hulst, T., Skillman, E., Smith, T., Bothun, G. & McGaugh, S., 1993. *Preprint.*

Walker, T.P., Steigman, G., Schramm, D.N., Olive, K.A. & Hkoang, H-S, 1991. *Astrophys. J.*, **376**, 51.

White, S.D.M., 1981. *Mon. Not. R. astr. Soc.*, **195**, 1037.

White, S.D.M., Davis, M., Efstathiou, G., Frenk, C.S., 1987a. *Nature*, **330**, 451.

White, S.D.M. & Frenk, C.S., 1992. *Astrophys. J.*, **379**, 52.

White, S.D.M., Frenk, C.S., Davis, M. & Efstathiou, G., 1987b. *Astrophys. J.*, **313**, 505.

White, S.D.M. & Rees, M.J., 1978. *Mon. Not. R. astr. Soc.*, **209**, 27P.

White, S.D.M., Tully, R.B. & Davis M., 1988. *Astrophys. J.*, **333**, L45.

White, S.D.M. & Zaritsky, D., 1992. *Astrophys. J.*, **394**, 1.

Yahil, A., 1985. *Observatory*, **105**, 165.

Zaritsky, D., 1991. *PhD Thesis*, University of Arizona.

Zaritsky, D., 1992. *Astrophys. J.*, **400**, 74.

Zaritsky, D., Smith, R.M., Frenk, C.S. & White, S.D.M., 1993. *Astrophys. J.*, **405**, 464(ZSFW).

Zaritsky, D. & Lorrimer S.J., 1992. in *The Third Teton Summer School: Evolution of Galaxies and Their Environment – The Contributed Papers*, ed. Hollenbach, D. (Universities of Colarado & Wyoming).

Zaritsky, D., Olszewski, E.W., Schommer, R.A., Peterson, R. & Aaronson, M., 1989. *Astrophys. J.*, **345**, 759.

Zepf, S., 1993. *Astrophys. J.*, **407**, 448.

Appendix

In this appendix we give a table of all Primaries drawn from the CfA survey found in the region of POSS plates used in the analysis of Chapter 2. In each case we give the RA and Dec of the galaxy (columns (1) and (2)), its apparent magnitude (column (3)), its morphological type (column (4)) and its recession velocity corrected for Virgocentric infall.

RA	Dec	m_B	T	v (km s^{-1})
(1)	(2)	(3)	(4)	(5)
		Plate 1019		
$13^h44^m31^s$	$16°31^m0^s$	14.3	5	6064
$13^h49^m43^s$	$17°13^m0^s$	14.1	−3	7003
$13^h35^m10^s$	$16°14^m0^s$	14.5	−2	7981
$13^h31^m44^s$	$18°7^m0^s$	14.0	−7	7177
		Plate 1032		
$10^h31^m36^s$	$35°31^m0^s$	14.1	8	1739
$10^h33^m5^s$	$37°35^m0^s$	12.4	5	1802
		Plate 104		
$12^h47^m24^s$	$5°35^m0^s$	12.3	7	857
$12^h46^m35^s$	$3°40^m0^s$	12.9	6	919
$12^h53^m18^s$	$4°34^m0^s$	12.6	6	963
$12^h45^m11^s$	$4°37^m0^s$	12.7	6	1187
$12^h52^m42^s$	$3°10^m0^s$	14.4	2	3001
$12^h48^m42^s$	$5°8^m0^s$	14.3	5	7732
$12^h50^m42^s$	$4°44^m0^s$	12.9	15	970
		Plate 1146		
$21^h58^m8^s$	$0°41^m0^s$	14.0	4	3686
$22^h0^m42^s$	$0°20^m0^s$	14.4	3	9004

Table 6.1

RA	Dec	m_B	T	v (km s^{-1})
(1)	(2)	(3)	(4)	(5)
	Plate 1157			
$22^h30^m36^s$	$7^o50^m0^s$	14.2	10	1939
$22^h31^m36^s$	$5^o19^m0^s$	13.4	2	4447
$22^h37^m45^s$	$7^o47^m34^s$	14.3	1	7453
$22^h32^m6^s$	$5^o33^m0^s$	14.5	3	8243
	Plate 1161			
$22^h58^m41^s$	$16^o7^m0^s$	13.6	−5	1999
$23^h0^m36^s$	$16^o20^m0^s$	14.0	−5	2080
$22^h55^m5^s$	$19^o31^m0^s$	15.2	−6	5695
	Plate 1201			
$1^h18^m48^s$	$6^o45^m0^s$	14.2	6	2094
$1^h19^m12^s$	$5^o0^m0^s$	11.4	3	2102
$1^h19^m11^s$	$8^o56^m0^s$	13.4	5	2329
$1^h20^m11^s$	$8^o47^m0^s$	13.8	−2	2343
$1^h13^m23^s$	$4^o55^m0^s$	13.9	−1	5105
$1^h11^m48^s$	$5^o40^m0^s$	14.0	0	5132
$1^h13^m29^s$	$4^o2^m0^s$	13.8	−2	5269

RA	Dec	m_B	T	v (km s^{-1})
(1)	(2)	(3)	(4)	(5)
		Plate 1202		
$1^h56^m37^s$	$18°46^m0^s$	11.4	3	2385
$1^h56^m31^s$	$18°43^m0^s$	14.2	−5	2439
$2^h4^m48^s$	$16°58^m0^s$	13.9	0	4378
$1^h59^m41^s$	$18°8^m0^s$	14.0	−3	8116
		Plate 1274		
$1^h0^m34^s$	$13°47^m15^s$	15.1	5	12122
$1^h0^m34^s$	$13°47^m0^s$	15.3	5	12454
$0^h50^m58^s$	$12°25^m20^s$	14.0	−6	18005
		Plate 1300		
$2^h36^m33^s$	$10°38^m0^s$	13.8	2	3311
$2^h33^m37^s$	$11°26^m0^s$	13.9	−7	3352
$2^h36^m57^s$	$10°35^m0^s$	14.1	0	3473
$2^h32^m36^s$	$12°36^m0^s$	14.1	−2	5858
$2^h23^m53^s$	$11°56^m0^s$	14.5	5	8107

RA	Dec	m_B	T	v (km s^{-1})
(1)	(2)	(3)	(4)	(5)
		Plate 1331		
$9^h58^m26^s$	$55°52^m0^s$	13.8	−3	1316
$10^h4^m36^s$	$52°6^m0^s$	13.9	7	1346
$9^h59^m30^s$	$55°55^m0^s$	11.4	5	1374
$10^h4^m45^s$	$53°20^m0^s$	13.8	5	1378
$10^h28^m59^s$	$54°39^m0^s$	13.2	10	1705
		Plate 1351		
		No Primaries		
		Plate 1358		
		No Primaries		

RA	Dec	m_B	T	v (km s^{-1})
(1)	(2)	(3)	(4)	(5)
		Plate 1359		
$9^h57^m24^s$	$5°34^m0^s$	12.2	10	365
$10^h11^m23^s$	$7°16^m0^s$	14.4	5	1313
$10^h10^m7^s$	$3°23^m0^s$	13.2	−2	1361
$10^h11^m43^s$	$3°43^m0^s$	11.5	1	1367
$10^h10^m55^s$	$3°38^m0^s$	14.5	10	1384
$10^h11^m13^s$	$3°40^m0^s$	11.4	0	1406
$9^h57^m47^s$	$3°37^m0^s$	14.5	7	2134
$9^h57^m53^s$	$4°39^m0^s$	14.2	3	4244
$10^h9^m36^s$	$5°10^m0^s$	14.5	4	8541
		Plate 1371		
$14^h50^m36^s$	$43°56^m0^s$	14.4	5	2858
$15^h13^m7^s$	$42°14^m0^s$	12.8	5	2913
$15^h11^m44^s$	$42°9^m0^s$	14.1	3	5740
$14^h52^m36^s$	$42°45^m0^s$	13.7	−2	5821
$15^h4^m41^s$	$42°50^m0^s$	14.2	−6	5855
$14^h53^m34^s$	$42°42^m0^s$	14.1	0	5854
$15^h11^m13^s$	$41°27^m0^s$	14.3	3	9096

RA	Dec	m_B	T	v (km s^{-1})
(1)	(2)	(3)	(4)	(5)
	Plate 1386			
$13^h52^m48^s$	$41°34^m0^s$	13.2	3	2524
$13^h55^m5^s$	$42°6^m0^s$	12.1	3	2606
$13^h51^m7^s$	$40°37^m0^s$	12.7	3	2661
$13^h53^m28^s$	$40°42^m0^s$	11.6	4	2906
$13^h58^m41^s$	$41°14^m0^s$	14.1	3	4111
$13^h58^m0^s$	$39°9^m0^s$	13.1	4	5495
$14^h9^m38^s$	$39°53^m0^s$	13.9	−3	5648
$13^h58^m32^s$	$39°23^m0^s$	14.5	−2	5776
$14^h1^m25^s$	$39°17^m0^s$	14.4	3	6168
$14^h14^m35^s$	$39°44^m0^s$	14.5	1	6197
$14^h10^m42^s$	$39°32^m0^s$	13.7	2	7951
$14^h14^m40^s$	$39°49^m0^s$	13.4	5	8047
$13^h51^m6^s$	$40°31^m0^s$	12.4	−2	2515
$13^h51^m25^s$	$40°34^m0^s$	14.0	0	2713
$13^h51^m13^s$	$40°33^m0^s$	12.9	0	2758

RA	Dec	m_B	T	v (km s^{-1})
(1)	(2)	(3)	(4)	(5)
		Plate 1392		
$11^h18^m30^s$	$3°31^m0^s$	11.8	−5	1429
$11^h21^m49^s$	$3°36^m0^s$	13.0	9	1500
$11^h17^m42^s$	$3°14^m0^s$	13.0	−2	1639
$11^h14^m54^s$	$4°50^m0^s$	13.0	1	1750
$11^h18^m36^s$	$3°28^m0^s$	14.0	−7	1885
$11^h17^m54^s$	$3°51^m0^s$	14.3	1	2681
$11^h8^m43^s$	$6°6^m0^s$	14.4	−2	6507
$11^h12^m54^s$	$5°23^m0^s$	14.1	5	7931
$11^h13^m35^s$	$3°9^m0^s$	14.5	4	9077
		Plate 1399		
$10^h24^m5^s$	$4°7^m0^s$	13.8	8	2231
$10^h19^m47^s$	$4°15^m0^s$	14.2	3	6902
$10^h36^m54^s$	$5°22^m0^s$	14.2	3	7899

RA	Dec	m_B	T	v (km s^{-1})
(1)	(2)	(3)	(4)	(5)
		Plate 14		
$1^h39^m42^s$	$13°43^m0^s$	13.9	10	640
$1^h40^m6^s$	$12°54^m0^s$	14.3	10	707
$1^h40^m24^s$	$13°23^m0^s$	11.9	1	727
$1^h39^m30^s$	$12°20^m0^s$	13.6	3	2853
$1^h30^m54^s$	$12°19^m0^s$	14.5	10	4057
$1^h50^m12^s$	$12°28^m0^s$	14.0	1	4473
$1^h46^m30^s$	$12°48^m0^s$	14.3	−7	4965
$1^h45^m43^s$	$11°17^m0^s$	13.3	5	5030
$1^h46^m48^s$	$12°15^m0^s$	14.2	0	5083
$1^h46^m8^s$	$10°15^m0^s$	14.2	−1	5205
$1^h42^m19^s$	$10°10^m0^s$	13.5	−2	5272
$1^h44^m18^s$	$12°52^m0^s$	14.3	4	5326
$1^h45^m48^s$	$12°21^m0^s$	14.0	1	5337
		Plate 15		
$2^h51^m6^s$	$12°38^m0^s$	14.1	3	3425
$2^h50^m54^s$	$12°48^m0^s$	13.2	2	3444

RA	Dec	m_B	T	v (km s^{-1})
(1)	(2)	(3)	(4)	(5)
	Plate 154			
$13^h23^m21^s$	$43^o31^m0^s$	13.6	0	1565
$13^h47^m15^s$	$39^o45^m0^s$	14.3	5	2746
$13^h42^m58^s$	$41^o45^m0^s$	13.5	2	2860
$13^h43^m8^s$	$41^o58^m0^s$	13.0	3	2927
$13^h47^m3^s$	$40^o14^m0^s$	13.7	0	3036
$13^h38^m34^s$	$39^o2^m0^s$	14.3	3	6279
$13^h35^m31^s$	$39^o24^m31^s$	14.2	4	6361
$13^h30^m38^s$	$42^o8^m0^s$	14.4	5	8526
$13^h21^m23^s$	$43^o20^m0^s$	13.5	5	8604

RA	Dec	m_B	T	v (km s^{-1})
(1)	(2)	(3)	(4)	(5)
	Plate 1560			
$12^h32^m5^s$	$7°26^m0^s$	14.2	10	774
$12^h31^m29^s$	$7°58^m0^s$	11.0	−2	805
$12^h21^m8^s$	$7°22^m0^s$	13.9	−3	908
$12^h22^m26^s$	$7°43^m0^s$	14.1	1	983
$12^h37^m50^s$	$3°24^m0^s$	13.7	−2	973
$12^h35^m55^s$	$4°36^m0^s$	12.9	1	1009
$12^h26^m24^s$	$3°51^m0^s$	12.0	0	1074
$12^h35^m18^s$	$5°39^m0^s$	12.9	1	1194
$12^h23^m11^s$	$7°29^m30^s$	14.4	6	1197
$12^h21^m8^s$	$7°14^m0^s$	13.7	3	1205
$12^h19^m44^s$	$7°25^m0^s$	14.3	−1	1246
$12^h24^m36^s$	$6°9^m0^s$	14.4	8	1282
$12^h33^m1^s$	$3°19^m0^s$	14.4	4	1308
$12^h22^m42^s$	$6°1^m0^s$	13.9	10	1344
$12^h21^m56^s$	$7°36^m0^s$	11.2	−5	1435
$12^h24^m54^s$	$6°32^m0^s$	13.4	3	1664
$12^h19^m21^s$	$4°45^m6^s$	10.3	4	1765
$12^h20^m36^s$	$5°32^m0^s$	12.6	−1	1866

RA	Dec	m_B	T	v (km s^{-1})
(1)	(2)	(3)	(4)	(5)
	Plate 1560 cont			
$12^h34^m23^s$	$7°31^m0^s$	12.2	−2	1933
$12^h23^m59^s$	$4°14^m0^s$	13.2	3	1916
$12^h31^m48^s$	$6°44^m0^s$	12.6	10	2208
$12^h19^m6^s$	$5°39^m0^s$	13.9	1	2494
$12^h27^m54^s$	$4°31^m0^s$	13.4	5	2607
$12^h36^m41^s$	$6°17^m0^s$	14.1	1	2649
$12^h22^m48^s$	$5°12^m0^s$	12.3	1	2729
$12^h18^m56^s$	$6°56^m0^s$	14.0	−2	4417
$12^h26^m54^s$	$7°3^m0^s$	14.2	10	793
$12^h21^m37^s$	$6°53^m0^s$	14.2	10	956
$12^h21^m1^s$	$6°22^m0^s$	12.8	−5	1476
$12^h19^m23^s$	$4°45^m0^s$	10.9	4	1754
$12^h29^m6^s$	$4°13^m0^s$	12.0	9	1947
	Plate 1561			
$13^h14^m42^s$	$6°18^m0^s$	14.2	3	6486
$13^h10^m12^s$	$5°0^m0^s$	14.5	9	6612
$13^h20^m53^s$	$6°39^m0^s$	14.4	5	7201

RA	Dec	m_B	T	v (km s^{-1})
(1)	(2)	(3)	(4)	(5)
		Plate 1611		
$12^h5^m36^s$	$3°9^m0^s$	12.0	5	1490
$12^h13^m23^s$	$6°41^m0^s$	13.0	−1	2252
$12^h14^m37^s$	$3°58^m0^s$	13.6	8	2248
$12^h12^m0^s$	$6°5^m0^s$	13.8	6	2263
$12^h10^m29^s$	$7°19^m0^s$	13.2	2	2306
$12^h14^m33^s$	$7°54^m0^s$	13.4	−1	2416
$12^h14^m52^s$	$6°58^m0^s$	13.6	0	2422
$12^h14^m34^s$	$7°28^m9^s$	12.9	1	2786
$12^h11^m16^s$	$7°28^m0^s$	13.9	−2	2821
$12^h13^m57^s$	$7°44^m0^s$	13.2	1	2841
$12^h1^m11^s$	$3°50^m0^s$	14.0	1	5963
$11^h59^m48^s$	$4°37^m0^s$	14.1	3	6627
		Plate 209		
$2^h5^m43^s$	$10°46^m0^s$	12.6	−5	1563
$1^h57^m30^s$	$12°24^m0^s$	14.0	3	3342
$2^h1^m7^s$	$14°30^m0^s$	14.2	−3	3510
$2^h1^m1^s$	$14°28^m0^s$	14.3	−2	3517
$2^h5^m35^s$	$14°44^m0^s$	14.3	3	4275
$2^h5^m35^s$	$14°6^m0^s$	13.7	3	4292
$1^h56^m56^s$	$13°46^m0^s$	14.4	−2	4462

RA	Dec	m_B	T	v (km s^{-1})
(1)	(2)	(3)	(4)	(5)
		Plate 21		
$1^h46^m18^s$	$5°40^m0^s$	10.5	0	1342
$1^h47^m54^s$	$5°54^m0^s$	13.5	0	1419
$1^h34^m41^s$	$5°37^m0^s$	13.5	−2	2981
$1^h34^m35^s$	$4°38^m0^s$	14.5	4	2983
$1^h37^m0^s$	$6°58^m0^s$	14.4	−5	3014
$1^h37^m36^s$	$5°28^m0^s$	13.8	4	3140
$1^h38^m49^s$	$8°15^m0^s$	14.3	5	4141
$1^h49^m12^s$	$6°3^m0^s$	13.2	5	4819
$1^h40^m36^s$	$8°38^m0^s$	14.2	3	5342
$1^h48^m52^s$	$8°0^m0^s$	14.2	−7	5375
		Plate 233		
$9^h43^m42^s$	$5°56^m0^s$	13.5	5	3250
$9^h43^m0^s$	$5°10^m0^s$	13.9	2	3786
$9^h36^m19^s$	$7°11^m0^s$	13.8	4	5010
$9^h43^m24^s$	$4°38^m0^s$	14.0	−2	5065
$9^h38^m19^s$	$7°10^m0^s$	14.5	6	8634
		Plate 28		
		No Primaries		

RA	Dec	m_B	T	v (km s^{-1})
(1)	(2)	(3)	(4)	(5)
	Plate 316			
$23^h12^m11^s$	$4°16^m0^s$	12.8	4	2525
$23^h11^m59^s$	$4°14^m0^s$	14.1	4	2566
$23^h19^m9^s$	$8°36^m48^s$	13.7	−2	3084
$23^h17^m12^s$	$8°18^m9^s$	14.3	−2	3162
$23^h17^m6^s$	$7°47^m0^s$	13.9	0	3315
$23^h18^m10^s$	$7°56^m36^s$	12.9	−5	3382
$23^h10^m41^s$	$6°9^m29^s$	14.5	1	3460
$23^h13^m24^s$	$6°25^m0^s$	13.2	−5	3536
$23^h17^m58^s$	$8°7^m20^s$	14.2	−1	3607
$23^h18^m48^s$	$7°56^m0^s$	13.8	3	3673
$23^h17^m42^s$	$7°55^m57^s$	12.8	−5	3679
$23^h15^m44^s$	$6°18^m45^s$	13.8	3	4889
$23^h16^m54^s$	$5°38^m0^s$	14.5	8	6039
$23^h25^m22^s$	$8°30^m0^s$	13.6	4	8591
	Plate 495			
$11^h45^m24^s$	$4°46^m0^s$	14.4	1	6136
$11^h47^m59^s$	$6°51^m0^s$	13.8	3	6308
	Plate 552			
	No Primaries			

RA	Dec	m_B	T	v (km s^{-1})
(1)	(2)	(3)	(4)	(5)
	Plate 635			
$1^h21^m24^s$	$12°39^m0^s$	12.6	5	2352
$1^h17^m18^s$	$14°31^m0^s$	14.0	−2	4025
$1^h23^m26^s$	$11°11^m0^s$	14.2	5	5676
$1^h22^m39^s$	$14°36^m0^s$	14.3	−7	6241
$1^h16^m7^s$	$14°45^m0^s$	14.2	6	6792
$1^h15^m30^s$	$11°7^m0^s$	14.3	6	4931
$1^h24^m26^s$	$14°31^m0^s$	14.2	6	6203
	Plate 642			
	No Primaries			
	Plate 662			
$10^h44^m23^s$	$63°29^m0^s$	11.3	5	1307
$10^h34^m45^s$	$64°32^m0^s$	14.4	−2	1916
$10^h29^m5^s$	$65°18^m0^s$	13.0	4	2033
$10^h29^m47^s$	$65°1^m0^s$	13.5	−2	2190
$10^h17^m3^s$	$65°25^m0^s$	14.1	5	3582
$10^h11^m19^s$	$65°23^m0^s$	14.4	5	3598
$10^h46^m54^s$	$65°59^m0^s$	13.1	5	3701
$10^h44^m35^s$	$66°37^m0^s$	14.5	3	6802

RA	Dec	m_B	T	v (km s^{-1})
(1)	(2)	(3)	(4)	(5)
	Plate 673			
$11^h7^m36^s$	$55°57^m0^s$	10.9	6	993
$10^h35^m48^s$	$53°46^m0^s$	11.2	4	1268
$11^h4^m58^s$	$53°54^m0^s$	14.1	−2	1546
$10^h51^m42^s$	$54°34^m0^s$	12.4	0	1643
$11^h4^m34^s$	$51°30^m0^s$	14.2	5	2491
$11^h8^m2^s$	$53°40^m0^s$	12.8	5	3160
$10^h48^m34^s$	$55°39^m0^s$	14.4	5	3153
$10^h57^m23^s$	$51°12^m0^s$	14.3	−1	3193
$10^h48^m39^s$	$51°18^m0^s$	14.1	−5	7819
	Plate 692			
	No Primaries			

RA	Dec	m_B	T	v (km s^{-1})
(1)	(2)	(3)	(4)	(5)
	Plate 700			
$11^h33^m42^s$	$45°34^m0^s$	14.2	10	503
$11^h30^m35^s$	$49°31^m0^s$	13.9	10	548
$11^h34^m58^s$	$48°11^m0^s$	12.7	3	1022
$11^h36^m51^s$	$46°47^m0^s$	13.3	6	1036
$11^h30^m37^s$	$47°18^m0^s$	11.1	5	1155
$11^h11^m42^s$	$48°35^m0^s$	12.2	3	2415
$11^h12^m40^s$	$47°43^m0^s$	13.0	−1	2532
$11^h15^m20^s$	$46°1^m0^s$	12.4	5	2621
$11^h38^m28^s$	$47°58^m0^s$	13.0	6	3403
$11^h10^m54^s$	$47°51^m0^s$	13.6	−5	5688
$11^h23^m30^s$	$47°15^m0^s$	13.5	−1	7833
$11^h30^m59^s$	$49°20^m0^s$	14.2	−7	9736

RA	Dec	m_B	T	v (km s^{-1})
(1)	(2)	(3)	(4)	(5)
		Plate 709		
$10^h52^m4^s$	$49°59^m0^s$	14.0	10	1630
$10^h37^m0^s$	$48°11^m0^s$	14.5	5	1798
$10^h59^m23^s$	$45°30^m0^s$	13.4	5	6245
$11^h6^m9^s$	$45°24^m0^s$	14.0	1	6446
$10^h57^m27^s$	$46°11^m0^s$	14.5	−7	6683
$11^h2^m12^s$	$45°24^m0^s$	13.0	5	6785
$10^h59^m30^s$	$46°9^m0^s$	14.5	3	6823
$10^h51^m2^s$	$49°55^m0^s$	13.9	−2	6853
$10^h56^m42^s$	$46°23^m0^s$	13.0	4	6939
$10^h58^m55^s$	$45°55^m22^s$	14.1	1	9050
$10^h57^m28^s$	$46°0^m0^s$	14.4	3	11581
		Plate 711		
$10^h15^m17^s$	$41°40^m0^s$	10.6	6	831
$10^h0^m52^s$	$41°0^m0^s$	14.2	10	837
$10^h9^m47^s$	$43°24^m0^s$	13.8	0	2501
$10^h17^m11^s$	$43°16^m0^s$	14.2	1	6932
$10^h17^m40^s$	$43°14^m0^s$	14.3	1	6932
$10^h17^m40^s$	$43°14^m0^s$	14.3	1	7230
$10^h17^m29^s$	$43°13^m0^s$	14.4	0	7273
$10^h15^m1^s$	$41°22^m0^s$	14.2	−2	7488

RA	Dec	m_B	T	v (km s^{-1})
(1)	(2)	(3)	(4)	(5)
		Plate 719		
$11^h23^m56^s$	$43°52^m0^s$	11.1	3	1053
$11^h47^m26^s$	$42°20^m0^s$	14.2	−6	1326
		Plate 722		
$10^h46^m31^s$	$7°11^m0^s$	14.2	0	839
$10^h48^m36^s$	$6°6^m0^s$	11.9	6	1124
$10^h58^m43^s$	$3°54^m0^s$	12.6	7	1257
$10^h49^m24^s$	$4°4^m0^s$	13.4	3	3692
$10^h50^m24^s$	$4°54^m0^s$	14.1	−6	5902
$10^h44^m49^s$	$6°19^m0^s$	14.4	0	5948
$10^h52^m42^s$	$7°58^m0^s$	13.4	−2	6512
$10^h49^m55^s$	$7°30^m0^s$	13.9	5	6722
$11^h0^m37^s$	$3°36^m0^s$	14.4	5	7666
$11^h2^m7^s$	$4°33^m0^s$	14.5	3	7677
$11^h1^m48^s$	$5°6^m0^s$	14.0	4	7766
$10^h45^m36^s$	$5°11^m0^s$	13.7	−2	7924
$10^h44^m50^s$	$7°31^m0^s$	14.5	3	8246

RA	Dec	m_B	T	v (km s^{-1})
(1)	(2)	(3)	(4)	(5)
		Plate 731		
$10^h49^m42^s$	$36°53^m0^s$	11.9	9	852
$10^h48^m35^s$	$33°2^m0^s$	13.1	−2	856
$10^h48^m59^s$	$33°10^m0^s$	13.2	3	1722
$10^h45^m35^s$	$34°58^m0^s$	12.8	3	1841
$10^h46^m56^s$	$33°15^m0^s$	12.5	6	1855
$10^h47^m2^s$	$33°15^m0^s$	12.9	10	1875
$10^h50^m19^s$	$34°11^m0^s$	13.2	1	1971
$10^h57^m4^s$	$33°39^m0^s$	13.3	9	2092
$10^h43^m5^s$	$35°14^m0^s$	14.3	−1	2263
$10^h38^m53^s$	$37°34^m0^s$	14.1	−1	7437
$10^h47^m14^s$	$36°36^m0^s$	14.4	−2	7468
$10^h49^m24^s$	$33°13^m0^s$	12.4	5	1813
		Plate 796		
$23^h44^m24^s$	$6°35^m0^s$	13.9	−5	3144
$23^h50^m53^s$	$7°36^m0^s$	13.6	0	5057
$23^h32^m55^s$	$7°3^m0^s$	14.4	6	5122
$23^h50^m41^s$	$7°36^m0^s$	13.8	−7	5146
$23^h32^m59^s$	$4°57^m0^s$	14.5	2	5681
$23^h35^m53^s$	$4°32^m0^s$	14.3	5	6040

RA	Dec	m_B	T	v (km s^{-1})
(1)	(2)	(3)	(4)	(5)
		Plate 821		
$23^h0^m40^s$	$8°36^m0^s$	13.1	1	4730
		Plate 823		
$0^h24^m29^s$	$11°18^m0^s$	14.0	5	2089
$0^h19^m38^s$	$10°13^m0^s$	13.4	5	4788
$0^h22^m42^s$	$12°36^m0^s$	14.1	2	5198
		Plate 860		
$21^h37^m15^s$	$6°3^m0^s$	14.0	3	4873
		Plate 877		
$0^h45^m32^s$	$8°3^m0^s$	13.7	6	5079
		Plate 90		
$13^h45^m43^s$	$4°12^m0^s$	12.0	5	1404
$13^h50^m26^s$	$3°4^m0^s$	14.5	3	4911
$13^h35^m42^s$	$4°47^m0^s$	14.5	−2	7149
$13^h47^m7^s$	$4°29^m0^s$	14.4	2	7249

RA	Dec	m_B	T	v (km s^{-1})
(1)	(2)	(3)	(4)	(5)
		Plate 915		
$0^h28^m54^s$	$5^o56^m0^s$	14.3	7	1923
$0^h35^m22^s$	$8^o22^m0^s$	14.3	4	5128
$0^h32^m59^s$	$8^o51^m0^s$	13.9	1	5180
$0^h31^m24^s$	$6^o59^m0^s$	14.5	−2	5321
		Plate 924		
		No Primaries		
		Plate 940		
		No Primaries		

RA	Dec	m_B	T	v (km s^{-1})
(1)	(2)	(3)	(4)	(5)
		Plate 96		
$14^h8^m30^s$	$6°36^m0^s$	13.9	5	971
$14^h4^m0^s$	$6°16^m0^s$	14.5	3	1264
$13^h55^m1^s$	$6°21^m0^s$	13.7	4	4533
$13^h55^m49^s$	$6°35^m0^s$	13.7	0	4535
$13^h55^m43^s$	$6°30^m0^s$	14.0	−2	4551
$13^h59^m49^s$	$7°56^m0^s$	14.4	3	4791
$13^h55^m43^s$	$6°46^m0^s$	14.0	−2	5343
$14^h6^m0^s$	$7°18^m0^s$	14.5	5	6175
$13^h58^m44^s$	$7°57^m0^s$	14.5	7	7169
$14^h11^m10^s$	$7°54^m0^s$	14.5	7	7593
$14^h12^m19^s$	$3°21^m0^s$	14.4	−7	7799
$14^h12^m1^s$	$3°25^m0^s$	14.8	2	8300
$14^h12^m55^s$	$4°38^m0^s$	14.3	7	12536

RA	Dec	m_B	T	v (km s^{-1})
(1)	(2)	(3)	(4)	(5)
	Plate 982			
$9^h12^m41^s$	$53°3^m0^s$	14.0	10	826
$9^h8^m28^s$	$51°28^m0^s$	14.5	5	2404
$9^h14^m15^s$	$53°12^m0^s$	13.4	1	2550
$8^h56^m9^s$	$55°53^m0^s$	13.8	3	2764
$8^h53^m13^s$	$52°16^m0^s$	14.1	1	3993
$9^h6^m12^s$	$54°46^m0^s$	14.5	5	4184
$8^h52^m55^s$	$52°18^m0^s$	13.6	1	4244
$9^h1^m5^s$	$51°49^m0^s$	13.6	−2	4960
$8^h53^m8^s$	$51°32^m0^s$	13.4	−5	5075
$9^h10^m1^s$	$53°11^m0^s$	14.2	−3	7843
$9^h15^m21^s$	$52°43^m0^s$	14.0	−7	7850
$8^h56^m39^s$	$52°42^m0^s$	13.7	3	9252
$9^h5^m20^s$	$54°3^m0^s$	13.2	98	1095
$8^h55^m26^s$	$53°58^m0^s$	12.7	5	2547

ACKNOWLEDGMENTS

I must first thank my supervisor, Carlos Frenk. Throughout my time at Durham he has never been short of comments and ideas and many times has spurred me on when I had all but given up. There have been many other people in Durham, and elsewhere, whose help and encouragement were invaluable. I must in particular thank Richard Bower, not only for his help, but for his friendship. 'Doc Ricky' is always fun to be with and challenging to work with. I must also thank my other collaborators: Rodney Smith, for putting up with me having seen all the videos at the AAT and teaching me about POSS plates; Simon White, for having such good ideas; Dennis Zaritsky, for hassling me just enough to get the work done.

No Durham Thesis would be complete without thanking Alan Lotts. His proficient management of the computer systems allows us to get on with our work (semi-)efficiently. I'm sure I've made him use his infamous exasperated 'eye-roll' more than most. And, I'm sorry about all the processes! I must also thank Mike Irwin of the APM laboratory for providing a large number of APM scans. Without his help there would have been no Thesis.

There are many other people in Durham who have helped to make my time in Durham so much fun. There are far too many to thank individually and I'm sure they know who they are. Thank you!

Next I must thank my former school Physics teacher, Derek Fry. He sparked my interest in Astronomy with his lunchtime lessons in 'O'-level Astronomy. That I became an Astronomy postgrad is mostly his fault. Finally I must thank my parents, my sister, Sue, and my fiancée, Karen, for all their love and support. This Thesis is as much the result of their efforts as my own.